PERFORMANCE EVALUATION OF DECT IN DIFFERENT RADIO ENVIRONMENTS

by
Kevin J. Saldanha

Thesis submitted to the Faculty of the
Virginia Polytechnic Institute and State University
in partial fulfillment of the requirements for the degree of

MASTER OF SCIENCE
in
Electrical Engineering

Approved:

Dr. Jeffrey H. Reed
(Chairman)

Dr. Brian D. Woerner

Dr. Theodore S. Rappaport

August 1996
Blacksburg, Virginia

PERFORMANCE EVALUATION OF DECT IN DIFFERENT RADIO ENVIRONMENTS

by

Kevin J. Saldanha

Committee Chairman: Dr. Jeffrey H. Reed

Electrical Engineering

Abstract

DECT is a cordless telephone standard whose applications are broadening with the advent of PCS services, wireless local loop (WLL), and the increasing demand for high data-rate wireless local area networks (WLANs).

This thesis investigates the performance of DECT in different channel conditions. DECT is simulated using the Signal Processing WorkSystem (SPW) software in different channels including the additive white Gaussian noise (AWGN) channel, the flat faded Rayleigh channel, the frequency selective faded Rayleigh channel, and the Ricean channel. The effect of cochannel and adjacent channel interference is also investigated.

In order to quantify the RF channel dispersive properties, and other parameters that determine performance in a radio channel, channel impulse response measurements at 1.9 GHz are made. Parameters that help describe the radio channel are identified and calculated from the recorded power delay profile measurements.

Finally, a mean-opinion-score (MOS) rating was performed for National Semiconductor Corporation's implementation of DECT in the indoor, indoor-to-outdoor, and outdoor environments. A comparison is made between the MOS and propagation measurements. It is found that the performance of DECT is very closely related to the RMS delay spread and the path loss in the RF channel.

Acknowledgements

I am deeply indebted to Dr. Jeffrey Reed who besides being an excellent advisor has been a steadfast source of encouragement during my thesis work. I am very grateful.

I am grateful to Dr. Theodore Rappaport who provided me an excellent opportunity to understand the fundamentals of RF propagation. His support by way of the channel sounder used in making measurements, as well as in the review of this manuscript is much appreciated. I am also thankful to Dr. Brian Woerner for his advice and suggestions in his review of this report. I would like to express my gratitude to Prab Koushik for his advice, technical support, and patience while I ran these simulations.

I thank Mike Schwartz, T. P. Subramanian, Carsten Andersen, and Dennis Rose at the Wireless Communications Group at National Semiconductor Corporation for their support of the DECT systems used for the project.

I would also like to thank in a special way Francis Dominique for the helping me in this endeavor. Keith Blankenship helped immensely in the measurement section of this endeavor. I also recognize the help of my friends and colleagues at MPRG.

Throughout my education I have relied on the love and support of my parents – Dominic and Lyra, and my three younger brothers Colin, Vernon, and Ian. I am truly blessed in that they have always supported me in every way. I also acknowledge my Aunt Olive and my other relative and friends for their encouragement over the years.

Contents

List of Figures

List of Tables

Chapter 1

Introduction

1.1 Introduction

Cordless radio telephone communication systems are used extensively today. Cordless technology primarily offers access technology rather than fully specified networks. The first generation cordless telephone systems were analog Frequency Modulation (FM) systems with limited range and no multiple access capability within a channel. Present cordless systems are fully digital, and provide enhanced features and advanced services compared to a conventional analog cordless system.

One of the first digital cordless telephone standards implemented is the Digital European Cordless Telecommunications (DECT) standard. DECT standard is a high performance wireless communications system suitable for the two-way transfer of voice, data and video information. This Pan-European standard, was approved by the European Telecommunications Standards Institute (ETSI) in 1992. It is capable of inter-working with all types of networks: PSTN, ISDN, GSM, PABXs, X.25, and IEEE LANs [1]. It employs a frequency division multiple access (FDMA), time division multiple access (TDMA), time division duplexed (TDD) multi-purpose telecommunication system based on low power, portable telephones (or data terminals) that access a fixed micro-cellular infrastructure. DECT accommodates multiple users by assigning different time slots to different users. An effective range of up to 100 meters is possible indoors, 300 meters outdoors [1]. DECT is designed to provide full, on site, mobile telecommunications for both voice and data services.

DECT has been simulated and tested in low dispersive indoor radio channels [2],

but tests of a commercial implementation in typical indoor/outdoor radio channels has not been completely quantified. National Semiconductor Corporation (NSC) produces a state-of-the-art chip set which implements the DECT standard. The chip set performs well in static tests [3], but NSC desires a performance evaluation of its DECT chip set in an actual mobile environment with the added impairment of adjacent and co-channel interference (ACI and CCI).

The research focus of this thesis is directed towards performing a subjective and objective analysis of the DECT (based on the NSC DECT solution) in outdoor and indoor radio propagation environments. In order to quantify the radio channel at 1.88 - 1.9 GHz, a sliding correlator measurement system has been used to obtain power delay profiles of the channel at each measurement location. In addition, the performance of DECT is simulated in SPW using different channel models. A mean–opinion–score (MOS) rating on the voice quality of the DECT cordless phones is also performed.

1.2 Presentation Format of the Thesis

The thesis is organized as follows:

Chapter 2 describes the technical details of the physical layer of the DECT system and National Semiconductor's implementation of a DECT transceiver. It also provides an summary of different measurement campaigns carried out in the frequency spectrum of 1.8 - 1.9 GHz.

In Chapter 3, SPW models of the DECT system that have been developed are explained in detail. While the design concentrates on modeling National Semiconductor Corporation's implementation of DECT, through prudent choice of different parameters (which are detailed in this chapter), any modification or derivative of DECT can be simulated.

The performance of DECT is simulated under different channel conditions. The development of these channel models and the various models used in the simulation are explained in Chapter 4. This chapter also details the different factors that influenced the choice of measurement locations and describes the measurement set-up used.

Chapter 5 describes the spread spectrum sliding correlator measurement system that has been used to make channel impulse response measurements. Included in

this chapter are calibration and post-processing procedures. A description of the measurement locations is included at the end of this chapter.

Chapter 6 summarizes the results of the simulations of DECT, as well as the channel impulse response measurements. The MOS ratings for the phone are listed for the different locations.

Chapter 7 concludes the work of this thesis. It outlines applications based on the simulated system performance and measured RF channel propagation studies and suggests possible directions for future studies on DECT.

The contributions of this research endeavor are in simulating the performance of DECT for different channel conditions such as the AWGN channel, the Rayleigh flat fading channel, the Rayleigh frequency selective channel, and the Ricean channel. Performance measures are the bit-error-rate (BER) and the frame-erasure-rate (FER). Furthermore, the channel impulse response measurements made at different locations provide a good basis for understanding the nature of the RF channel at frequencies used for DECT transmission. National Semiconductor Corporation's DECT solution is evaluated in different radio environments, and with varied levels of interference. This thesis could therefore provide a stepping stone to the launch of new and interesting applications for DECT.

Chapter 2

DECT and Radio Channels at 1.9 GHz

2.1 Introduction to the DECT System

The Digital European Cordless Telecommunications (DECT) standard [4] was approved by European Telecommunications Standards Institute (ETSI) in 1992. DECT is a cordless access technology, that allows wireless access for a wide variety of services to any public or private communication network. The standard has a modular design, allowing manufacturers flexibility to produce optimal solutions for different applications (e.g. voice, data and video) and different application areas (e.g. business, and residential service).

DECT uses the Open System Interconnect (OSI) principles for its architecture [5, 6]. The complete DECT air interface corresponds to the first three ISO OSI layers; however, DECT defines four layers of protocol: physical, medium access control, data link, and network. This is shown in Figure 2.1. A control plane (C-plane) and a user plane (U-plane) utilize the services offered by the physical layer and the medium access control (MAC) layer. DECT also has provision for the data link control (DLC) and network layer protocols but these layers are not detailed here because of the complexity involved in their implementation and the scope of this thesis. Literature which discusses the functionality of these layers can be found in [4, 5, 6].

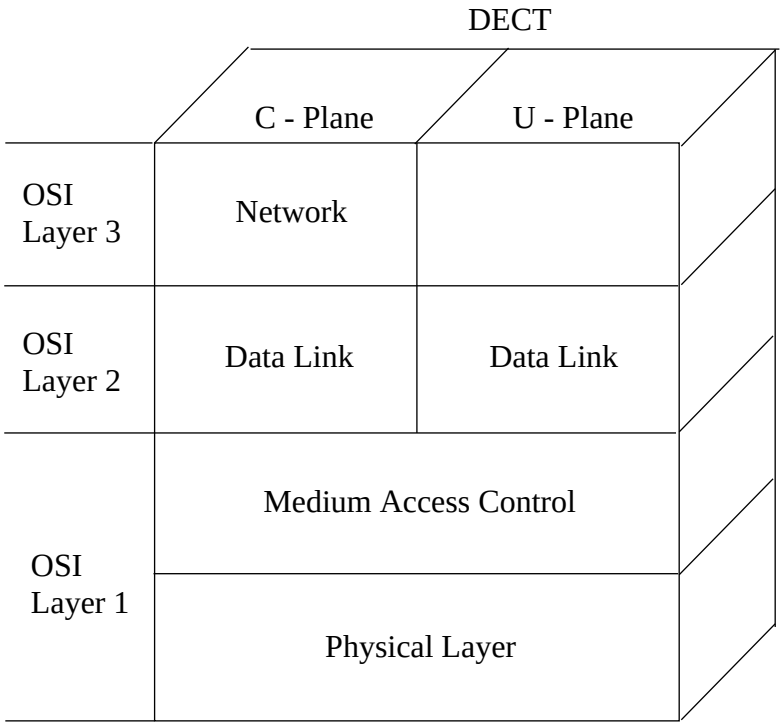

Figure 2.1: DECT protocol layers

2.2 Physical Layer of DECT

The DECT system is based on a micro-cellular system architecture, with cell sizes ranging from 50 to 300 meters in diameter. Ten radio carrier frequencies in the 1.88 - 1.9 GHz range, each 1.728 MHz wide, carry 12 full duplex channels organized in a Time Division multiplex, Time Division Duplex (TDM/TDD) manner. Each frame of transmission is of 10 ms duration and is composed of 24 time slots. The first 12 of these are used for transmission on the down-link, and the remaining 12 time slots are used for transmission from the handset to the base station. The DECT time slot and frame structures are shown in Figure 2.2 [6].

2.3 Medium Access Control Layer of DECT

The DECT Medium Access Control (MAC) layer provides a paging channel and a control channel for the transfer of signaling information to the control plane. The

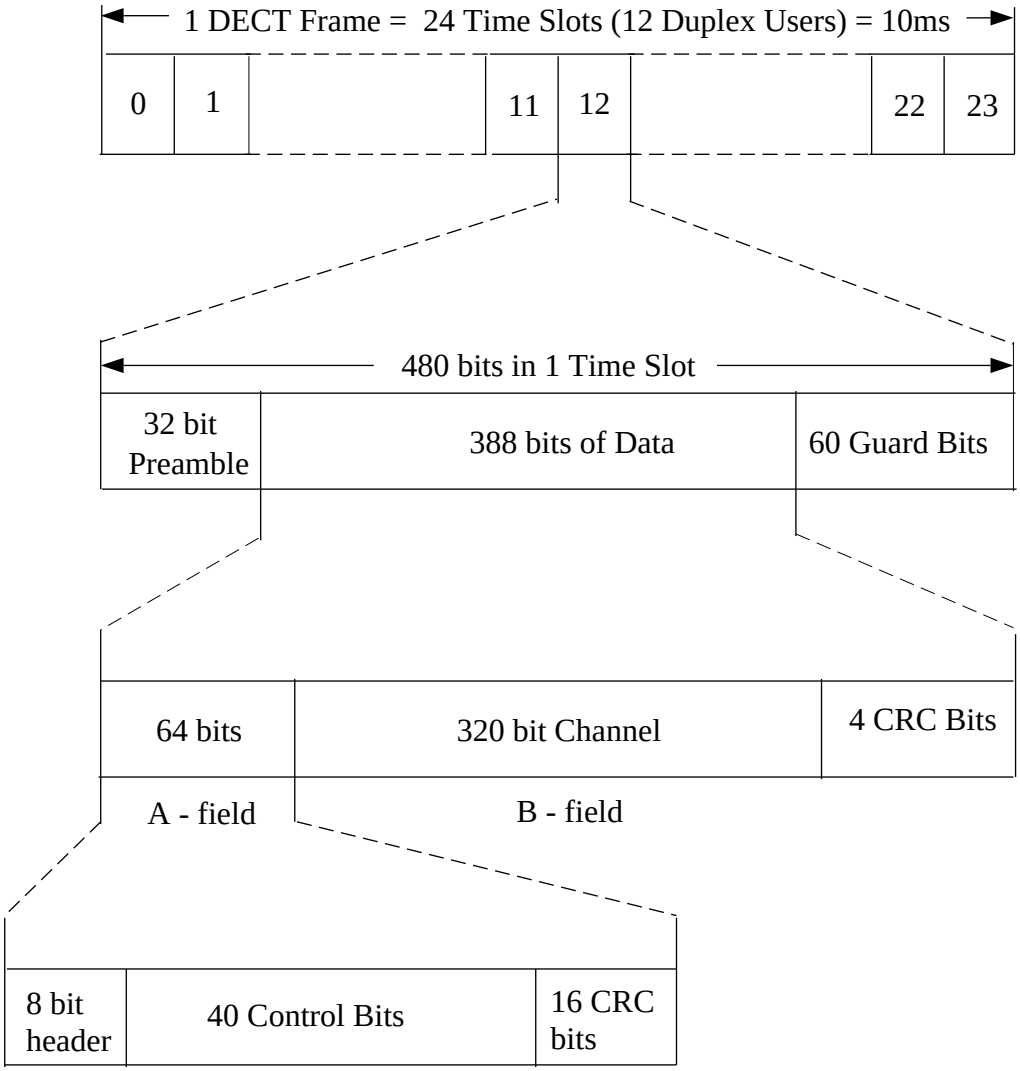

Figure 2.2: DECT frame structure

Table 2.1: DECT system technical specifications

Parameter	Specification
Frequency band	1880 - 1900 MHz
Channel Access	FDMA/TDMA/TDD
Number of Carriers	10
Channel Spacing	1.728 MHz
Number of Timeslots/Carrier	24 (12 duplex)
Modulation Principle	GFSK with BT = 0.5
Modulation Data Rate	1.152 Mbit/sec
Peak Transmit Power	$<$ 250 mW (24 dBm)
Average Transmit Power	10 mW (10 dBm)
Speech Coding	32 kbit/s ADPCM
Frame Length	10 ms
Nominal FM Deviation	288 kHz
Channel Assignment Method	Dynamic Channel Allocation

MAC layer superimposes a multi-frame structure on the TDMA structure of the DECT frame. Apart from basic MAC layer functions such as the establishment of the connection, the DECT MAC layer supports two specific functions: MAC hand-over and the provision of a "beacon" [7].

The MAC hand-over is initiated by the portable. This decision is based on the received signal strength indicator (RSSI) that is incorporated in the DECT solution. The DECT MAC layer provides a virtually seamless hand-over. In order for seamless hand-over to take place, it is necessary for the base stations to be time synchronized to each other [8]. This is accomplished via a Radio Exchange (RE) which interfaces with several base stations and in turn interconnects with the PSTN.

The base station (or fixed radio) transmits on at least one channel. This is similar to each base station acting as a beacon. The radio fixed part (RFP) broadcasts system information and base station identification [5]. The idle portables can then monitor the signal levels from each of these base stations, find the best one and lock on it. This allows for very fast connection set-up times.

Table 2.1 summarizes the technical specifications of the DECT standard.

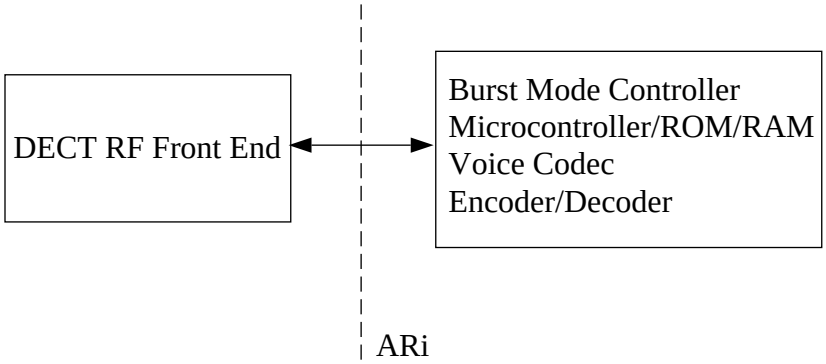

Figure 2.3: NSC DECT implementation

2.4 NSC Implementation of DECT

The National Semiconductor solution for DECT is composed of two subsections namely the RF front-end subsystem, and the Burst Mode Controller (BMC) with the ARi^{1TM} dividing line between them as shown in Figure 2.3 [9].

2.4.1 The Burst Mode Controller (BMC)

The Burst Mode Controller performs all the time critical control functions as well as the audio interface to the transducers. The interface to the transducers (microphone and earpiece) consists of the codec internally in the BMC and external passive components to decouple the low frequency and the RF noise. The Sierra Semiconductor SC14401 DECT Terminal Processor with Codec used in the National Semiconductor implementation, contains all the digital processing including the ADPCM CODEC, burst mode logic, scrambler/de-scrambler, encryptor/decryptor and CRC logic. The SC14401 encodes/decodes linear or PCM A-law coded voice samples down to 32 kbit/sec. The prescribed ADPCM technique is used. It is possible to select the input or output format for the ADPCM data as either A-law coded or as 16-bit sign extended, 14 bit linear data. Receive and transmit burst timing information is controlled via instructions in the sequencer RAM. The BMC is capable of detecting the synchronization field (S-field) pattern. The BMC also automatically adjusts the frame timing [10]. The SC14401 will only write the received B-field in the case that

the A-field CRC is correctly received. In this way the last frame is repeated and erroneously received frames will not disturb the ADPCM. In case of double slot diversity, the second slot is selected in case the A-field CRC is incorrect in the first slot.

2.4.2 The RF Front-End

The block diagram of NSC's implementation of the RF front-end is shown in Figure 2.4 [11]. Although the LMX2411 baseband controller is not included in the front-end, its functions are inherent to the operation of the front-end and is therefore included.

The Transmit Path

The transmit path of the RF front-end is composed of two parts

The Gaussian Filter: A frame of data constructed by the burst mode controller enters the LMX2411 baseband controller via the Tx_Data pin [12]. The LMX2411 uses a mask-programmable Read-Only Memory (ROM) look-up table to construct pulse responses of a Gaussian filter shape. For DECT this filter is half the bandwidth of the bit rate ($B_bT = 0.5$). The output of the ROM filter, addresses an eight bit digital-to-analog converter (DAC). The LMX2411 ROM filter supports three different system clocks selected by two external pins. The transmit DAC uses a voltage mode output. The Gaussian filter ROM DAC uses a three bit memory to represent the filter's pulse response. The result is an effective 3 bit time delay from input of the first bit to when that bit is actually output from the filter. In addition, the end of the information data stream must be padded by 3 bits to push the last data bit through the filter. When the Tx_PD pin goes low, the ROM filter output will be at the mid-band voltage until the first edge of Tx_Data, which is used for synchronizing the internal clock with the transmitted data. The ROM DAC output voltage is capable of directly modulating a VCO to produce a GMSK signal.

The Frequency Modulator: Most of the blind-slot synthesizer plans for DECT fall under two categories, open loop and closed loop modulation. In open loop modulation, the VCO output is directly at the channel frequency during transmission. Just before the beginning of a transmit RF burst, the synthesizer is switched off, and the VCO is made free running. The baseband Gaussian filtered ROM DAC output directly modulates the VCO. In closed loop modulation, the RF VCO always works

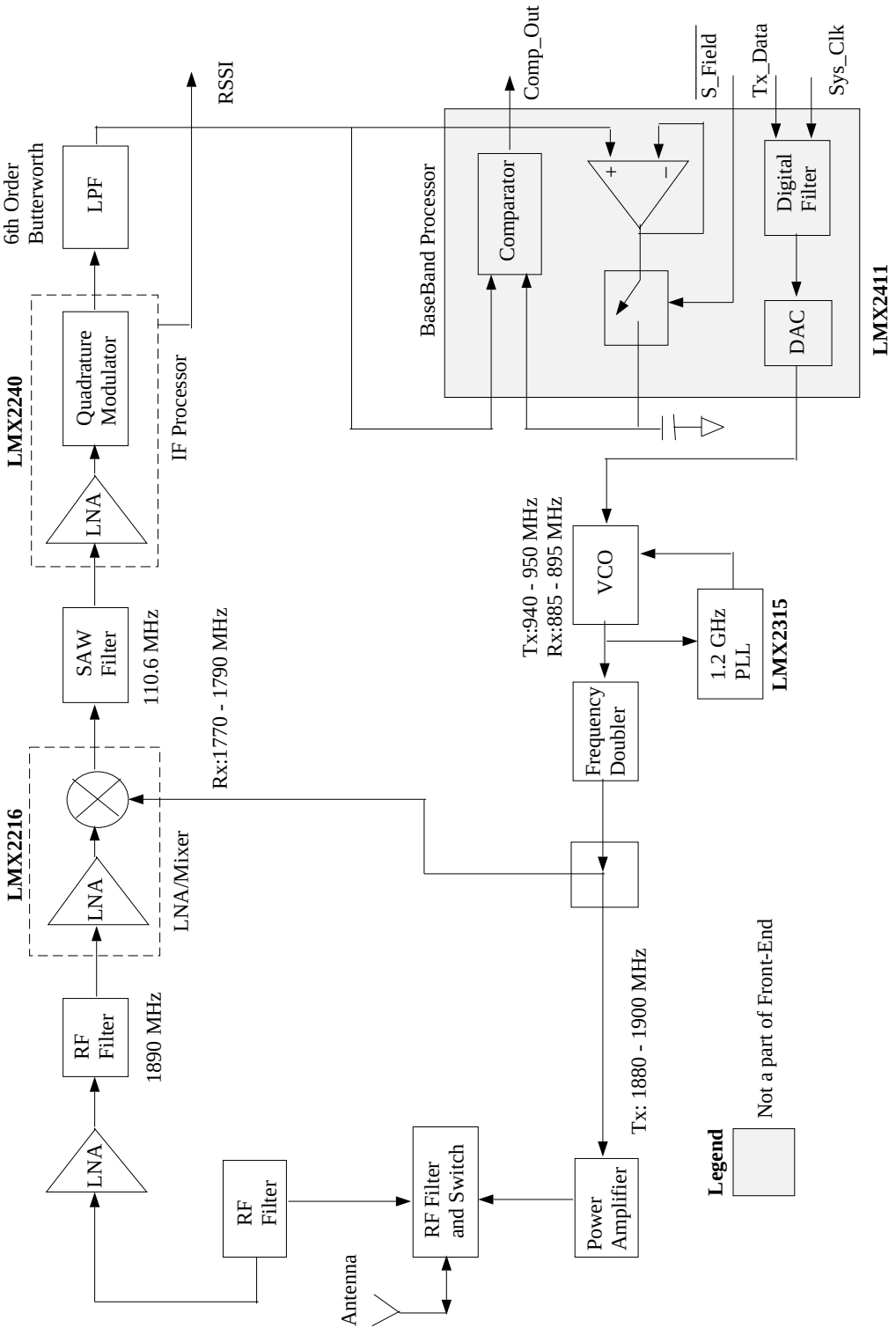

Figure 2.4: NSC DECT transceiver front end

in closed loop. This modulation has two possibilities. The first is where the VCO is directly modulated at the transmit frequency in closed loop. The other possibility is in using a second VCO at IF for modulation, and mixing it with an RF VCO signal up to the transmit frequency. The IF VCO can work in open loop modulation [13].

National Semiconductor uses open-loop modulation in their DECT implementation. Open loop modulation is a technique that allows for relatively simple implementation as long as frequency pushing and load pulling effects can be controlled. The loop is opened by powering down the PLL, which in the LMX2315 results in a TRI-STATE at the charge pump output [14]. The modulating voltage is then added to the VCO center frequency voltage using a resistive adder. Since DECT is bursty in nature for its transmissions, the loop filter (in the NSC implementation of DECT) will not lose its charge, and the center frequency will not drift over the duration of a time slot. The LMX2315 can be programmed so that the PLL can switch to any one of the 10 available carrier frequencies.

The output of the VCO is fed to a frequency doubler circuit which translates the GMSK signal to 1.88 - 1.9 GHz. The signal is then amplified and fed the antenna through the antenna switch (which determines whether the transmit or receive section is active).

The Receive Path

The received signal passes through the following stages before it is converted to the baseband signal.

RF Front End Filter: From the antenna the signal passes through a lowpass filter and TR-switch into a 2 pole dielectric bandpass filter, with center frequency at approximately 1890 MHz. After amplification in a bipolar transistor, the signal is via a second 1890 MHz filter fed to the amplifier and mixer of the LMX2216.

LMX2216 LNA and Mixer: The Low Noise Amplifier (LNA) is a common emitter stage with active feedback. This feedback network allows for wide bandwidth operation while providing the necessary optimal input impedance for low noise performance [15]. The mixer is a Gilbert cell architecture, with the RF input signal modulating the local oscillator (LO) signal and single ended output taken from the collector of one of the upper four transistors of the cell. The LO signal is generated by the LMX2315 frequency synthesizer in conjunction with the VCO.

IF Filter: The output of the LMX2216 contains the desired intermediate frequency as well as higher order frequency terms. The IF bandpass surface acoustic wave (SAW) filter which follows the mixer is centered at 110.592 MHz (which is the IF frequency for DECT) and has a bandwidth of approximately 1 MHz. The filter is used to add the main adjacent channel selectivity.

LMX2240 Intermediate Frequency Receiver: The LMX2240 consists of a high gain limiting amplifier, a frequency discriminator, and a received signal strength indicator (RSSI) [16]. The high gain limiting amplifier has a gain of approximately 70 dB and a sensitivity of about -75 dBm. The output of the limiter is connected off chip to an external quadrature tank circuit as well as connected internally to the discriminator. The frequency discriminator is a Gilbert cell mixer that requires an external tank circuit to create a 90^o phase shift at the desired frequency. This type of implementation is commonly used in mobile communications because of its relative ease of construction and low cost.

Low Pass Filter: The output of the LMX2240 limiter discriminator is lowpass filtered using a sixth order Butterworth lowpass filter to remove the double the frequency terms and harmonics. A 3 dB bandwidth of about 1 MHz is used.

LMX2411 Baseband Processor: In the receive mode, the baseband processor acts as a high speed comparator and as an analog DC compensation circuit. The function of the comparator is to convert the shaped output stream of the low pass filter into a rectangular 1 and 0 pattern. The high speed comparator's threshold can be set either by an external voltage or by using the internal DC compensation circuit.

The DC compensation circuit allows control over DC drift due to temperature, frequency drift, component tolerance, and aging. The sample and hold buffer allows a single RC filter to average the DC value of the received signal without distorting it. This DC value is an input to the comparator. The DC compensation circuit can acquire the DC voltage during the preamble of DECT (16 bits of alternating ones and zeros), and then hold it for the duration of the burst. This solution avoids the problem of long strings of 1's and 0's that conventional continuous average circuits have while still reacting quickly to acquire the proper DC average at the beginning of a burst.

2.5 Channel Characterization at 1.8–1.9 GHz

This section describes various RF channel impulse response measurements that have been performed at 1.8–2 GHz and the different measurement systems used. There are three different ways for making channel measurements using either a direct pulse channel sounder, a sliding correlator measurement system, or a frequency domain measurement system. The direct RF pulse system suffers from several drawbacks and is now rarely used in making channel characterization measurements. The direct RF pulse system is highly susceptible to interference and noise. It also requires a strong line-of-sight component to serve as a trigger for the oscilloscope. Further, the width of the sounding pulse determines the resolution of such a system, and this is found to be a severe limitation. Earlier work done at the frequency of 1.8–2 GHz is classified according to the type of measurement system used.

2.5.1 Measurements using a Sliding Correlator System

The advantage of using a spread spectrum channel sounding system lies in its ability to reject passband noise. This is because while the probing signal may be wideband, it is possible to detect the transmitted signal using a narrowband receiver preceded by a wideband mixer. This also improves the dynamic range of the system. Furthermore, processing gain of spread spectrum signals reduces the required transmit power for a given T-R separation [17]. The transmitter and receiver no longer need to synchronized with each other (the clocks for these circuits are assumed to be highly stable with negligible drift).

Heath [18], used a channel sounder with a measurement resolution of 100 ns. Sleeve dipoles were used for both transmitter and receiver. The presence of a strong direct path between the transmitter and receiver is known to significantly reduce the delay spread [19, 20]. Measurements were made outdoors in a Piazza (a paved area approximately 85×35 m) enclosed by buildings on all sides. The nature of the measurement site ensured that almost all locations had a clear path between the transmitter and the receiver. In this measurement study, almost half of the average profiles measured had delay spread greater than 100ns. A cumulative distribution function (CDF) of delay spread showed that 47% of the average profiles had delay spreads in excess of 100ns, 10% in excess of 137 ns and 5% in excess of 145 ns. While

the maximum path loss for these measurements was 91 dB, path loss measurements in excess of 100 dB (up to 120 dB) have also been reported [19]. The path loss exponent was calculated to be 2.15 which is very close to the free space decay law. This is because of the open nature of the measurement site, where most areas had a clear line-of-sight path between the transmitter and receiver.

Lopes [2] performed simulations to analyze performance of DECT in different propagation environments. His study shows that RSSI-driven two-branch diversity would be able to improve coverage and capacity of DECT, as well as extend the range of delay spread that it could withstand. In Lopes [21], simulation results estimate that RSSI-driven diversity could provide gains of about 10 dB in flat fading channels. However, the results show that as the delay spread rises above 100 ns, DECT performance degrades further from the flat fading case. He suggests that propagation work would be necessary to determine whether antenna diversity on its own would be sufficient to reduce dispersion effects.

In order to analyze the performance of DECT in canyon type urban streets, where lots of people have their homes and might use such a telephone system as a PCS application, Kauschke performed different simulations and compared these with measurements [22]. It was observed that path loss exponent had values between 1.6 and 2.0. This was explained as being due to the wave-guiding effect under canyon type conditions. The calculated received power appears to be larger than the one received under free space conditions because power is reflected back into the canyon. However, beyond the first Fresnel zone (calculated to be 350 m for the experiment), the path loss exponent increases to 3.5. For the simulation runs, 5000 DECT frames were considered. It has been found that it is feasible for DECT to operate in delay spread environments of 85 ns ($S/N > 27$ dB). The radio zone for DECT is fairly limited to the first Fresnel zone. By increasing the distance out to the first Fresnel zone (by increasing antenna height), it is possible to increase the range of DECT. However, this assumes that the canyon structure of the radio environment is preserved.

In the analysis of the Siemens DECT prototype Gigaset 95x, delay spreads as large as 200 ns were simulated by using a tapped delay line. This study concentrated on examining the performance of DECT of different values of RMS delay spread. The performance of DECT was found to be significantly improved through the use of antenna diversity (to combat the problem of delay spread) [23]. However, these

measurements were simulated in a laboratory setup and so provide little information on the actual nature of radio environments at 1.8 GHz. Furthermore, the effect of path loss on DECT performance was neglected as the SNR was maintained greater than 60 dB.

Devasirvatham and Murray [20] conducted measurements at both 850 MHz and 1900 MHz using a sliding correlator measurement system. From measurements obtained, it is found that RMS time delay spread doubled, statistically for every 18 dB increase in path loss at 1900 MHz. For path loss up to 80 dB (relative to path loss at 1m), the RMS delay spread was of the order of 200 ns. For measurement locations which had a direct line-of-sight path, a free space path loss exponent ($n = 2$) was used along with a linear attenuation factor (dB/m). This fitted the measured data well. For non line-of-sight paths, the path loss exponent is of the order of 4.9. This study also concluded that RMS time delay spreads, statistically, are the same at the two frequencies.

2.5.2 Measurements using a Frequency Domain Measurement System

Frequency domain measurements provide both phase and amplitude information about the transmitted signal. This necessitates the requirement that the measurement system be calibrated to compensate for phase and amplitude variations caused by the amplifier, cables, measurement equipment and antennas. The drawback of this type of a measurement system is that cable needs to be run between the transmitter, the receiver and the measurement set-up. As the frequency increases, the cable losses increase significantly, and thereby introduce additional constraints on the range of the measurement plan. This restricts the use of frequency domain measurements primarily to indoor applications. Another limitation of this system is the non–real–time nature of the measurement. For time–varying channels, the channel frequency response can change rapidly during a sweep period, giving an erroneous impulse response measurement.

In the first approach which dealt with measurements up to 20 GHz, Nobles et. al. used a vector network analyzer [24]. The third harmonic IF of the received signal is interpreted by the VNA for phase and magnitude data by comparison with the

reference channel.

The time domain response can be obtained from frequency domain measurements through use of the Inverse Fast Fourier Transform (due to its high speed of operation and ease of implementation). The sweep bandwidth of 500 MHz and a 1024 point FFT provided a time domain resolution of 1 ns. For the floor plan (laboratory and adjacent corridor), the RMS delay spread had a mean of about 35 ns. Using linear regression on the path loss data obtained, the path loss exponent was found to be 1.5 [24].

Howard and Pahlavan conducted coherent wide-band frequency-domain measurements that provide magnitude and phase information about the frequency response of the channel [25]. In time-domain measurements the ratio of the peak to average transmitted power is large. However, in frequency domain measurements, the transmitted signal has a constant envelope. This fact allows a larger area to be measured and reduces the effects of nonlinearities.

Measurements were made using a 200 MHz bandwidth in the frequency domain which provides an equivalent resolution of 5 ns in the time domain. Analysis of the data provided a path loss exponent of 2.5. The RMS delay spread in the mean was on the order of 25 ns and had a standard deviation of about 5 ns. The relationship between the 3-dB width of the frequency correlation function (B_c in MHz) and the RMS delay spread (τ_{RMS} in ns) was determined. This relationship is of the form given in equation 2.1.

$$B_c = C\tau_{RMS}^{-\beta} \tag{2.1}$$

For the experiments, β is around 1.9. The value of the constant C depends on the nature of the indoor environment and is in the range of 1800–4200. This can then be used to arrive at an estimate for the maximum data rate without diversity or equalization for the channel.

2.6 DECT Performance in Indoor and Outdoor Radio Channels

Since DECT systems are based on a cordless telephone standard, they perform well in indoor channels. However, in outdoor environments, the RMS delay spread becomes a significant fraction of a bit period, resulting in frequency selective fading and inter-symbol interference (ISI). A bit error rate (BER) of 10^{-3} or a frame erasure rate (FER) of 10^{-2} is used as a criteria for acceptable performance [2, 26]. Since ISI causes an irreducible BER for GMSK [17], a limit for delay spread may be established beyond which the maximum tolerable error rate will be exceeded regardless of the received signal SNR. Even in the case of indoor radio channels (wherein flat fading is predominant), a fade margin of 15 dB [8, 27] to 18 dB [22] is specified for DECT to ensure proper operation.

Several studies have attempted to quantify the amount of delay spread which is tolerable using DECT. Kauschke [22] presents results for DECT in a micro-cellular urban canyon. He assumes a two ray Rayleigh fading environment with a fade margin of 30 dB. The channel is modeled assuming a mobile velocity of $v = 1$ m/s (average walking speed). Results showed that typical delay spreads of about 80 ns were obtained for distances less than the first Fresnel zone. For these delay spreads, a BER of 8.6×10^{-4} were observed. For delay spreads in excess of 90 ns the BER increases to 1.3×10^{-3}.

Lopes [2] also used a simple two-path model, with equal powers in both paths and random phase. He reports that the CRC failure rate can be as high as 0.5 at RMS delay spreads of 400 ns (approximately half the bit period). When modeling the channel by using power delay profiles, the CRC failure rate is found to be unacceptable for even 100 ns delay spread (without antenna diversity). Van de Berg [8] gives simulation results for outdoor environments. He found that the range of DECT for acceptable BER performance is between 220 to 280 m for base station antenna gains ranging between 3 dBi and 9 dBi.

There are significant discrepancies among the authors regarding the allowable delay spreads in DECT. This may be due in part to the different implementations of DECT. Lopes has postulated that the differences may be to certain extent due to timing recovery schemes in various papers [28]. He finds a significant degradation in

performance when a fixed timing point (synchronized to the first arriving component in the channel's power delay profile) is used rather than a standard bit-by-bit adaptive recovery scheme. He concludes the allowable RMS delay spread increases from 38 ns to 94 ns for a BER of 10^{-3} when adaptive recovery is used. Adaptive timing recovery tries to acquire a timing point a half-bit away from the zero crossings of the eye pattern using the initial 16 bits of the DECT packet. Even under low dispersive conditions, the performance of DECT using standard (adaptive clock recovery) is better than that using fixed timing recovery.

Chapter 3

SPW Models for DECT

3.1 Introduction

Signal Processing WorkSystem (SPW) [29] is used to model the performance of DECT in different propagation environments. SPW is a powerful software package used in for developing, simulating, debugging, and evaluating DSP and communication systems. SPW modeling of DECT has been split into three blocks: the transmitter, the receiver, and the RF channel. For each block, there exist a set of default parameters and those that are editable. The editable parameter values can be changed in accordance with new design specifications, and its effect on system performance can be observed.

For most of the SPW blocks in this chapter, there are a list of default parameter settings. Some of these parameters can be changed whereas others are constant for the simulations. The important parameters for a particular SPW block are listed in the respective section. Other default parameters of lesser significance are included Appendix A.

3.2 The Transmitter

3.2.1 System Executive

The system executive performs frame formatting, synchronization, and other housekeeping tasks required to operate the transceiver. In this section, its operation as related to the transmit function are delineated. As explained in Section 2.3, each

Table 3.1: Parameters for system executive – transmit path

Parameter	Default Value	Editable
Sampling frequency	18432000.0 Hz	Yes
Bit rate	1.152 Mbps	Yes
Number of bits/frame	480	Yes
Length of sync. sequence	16	Yes

DECT time-slot comprises 480 bits, the first 32 of which form the header. The primary function of the transmit executive is to format a block of data that is sent in a time-slot. The system executive has been implemented as a custom coded block written in 'C'. The executive also controls the antenna switch (which determines whether the transmit or receive path of the transceiver is active). The parameters used in the SPW simulation of this block are given in Table 3.1.

The data generation and transmission is performed in two stages. The block diagram of these operations is shown in Figure 3.1. The 32 bit header pattern – 10101010101010101110100110001010 is stored in an ASCII file. The header pattern is stored as 1s and 0s without any line breaks between successive bits. The remaining 448 bits of the time-slot are generated by the program using the generator polynomial [30]

$$g(D) = D^3 + D^{30} \tag{3.1}$$

After each time-slot, the state of the generator polynomial is stored and data for subsequent frames use the previously stored polynomial. In this way, data in successive frames have a low cross-correlation. A plot of the autocorrelation function of data in a frame, and the cross–correlation between data in successive frames is shown in Figure 3.2.

The code has been optimized so as be computationally efficient [31]. By generating the data during program execution, file server requests to the Solaris OS are reduced which reduces the time for simulations. After the data for a time-slot has been transmitted, the system executive will wait for its next allocated slot before transmitting again. There are two modes of operation. In the first approach, the transmitter sends out 480 bits of data, then switches to the receive mode and performs functions that

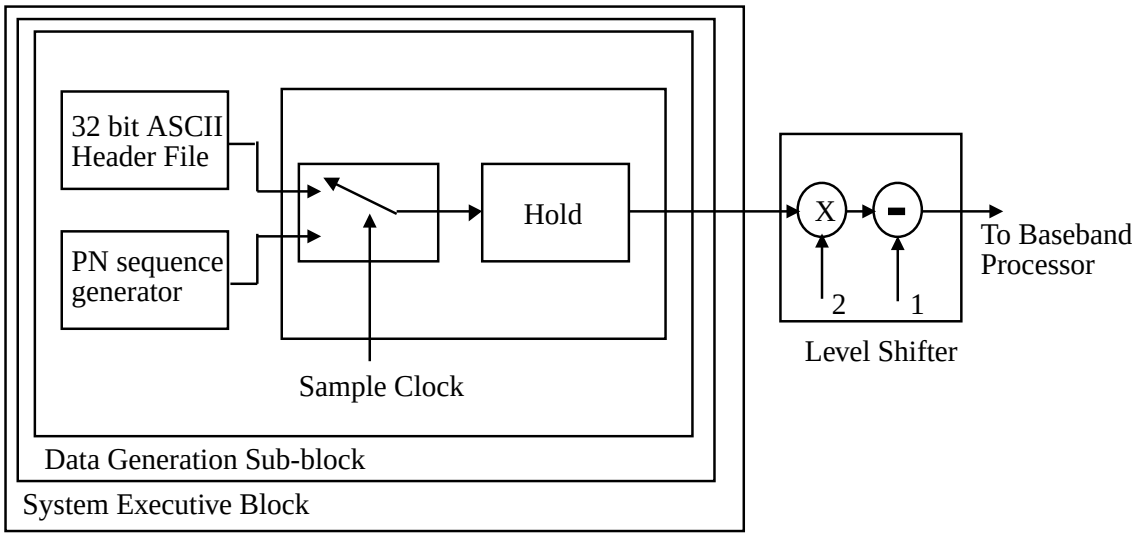

Figure 3.1: Block diagram for data generation

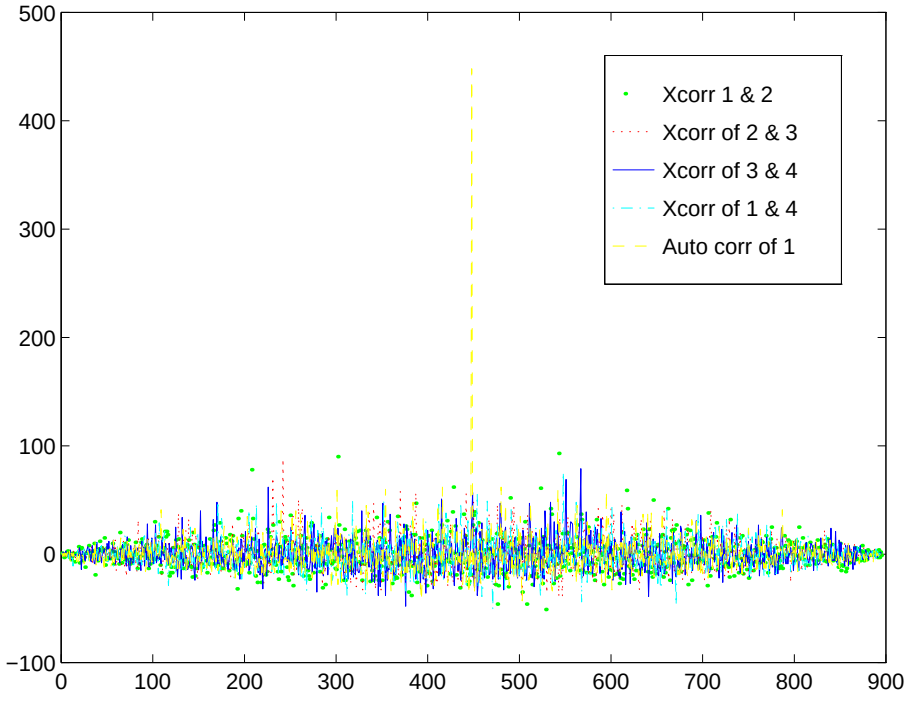

Figure 3.2: Autocorrelation of data in 1 frame, and its cross–correlation to data in successive frames

would correspond to a normal DECT receiver operation. The other way that operation can be simulated is that the transceiver transmits for the duration of a time-slot, and then waits in an idle mode until its next transmit time-slot occurs (no receiver functions are implemented). Since DECT has been commercially implemented using a blind-slot approach, the second mode of transmission is used in the simulation. There exist provision in the custom coded block which support both methods.

3.2.2 The Level Shifter – Type 1

The level shifter is a hierarchical block that is constructed using SPW blocks. The input to the level shifter is a binary data stream represented by 1s and 0s. The level shifter converts the 1s and 0s pattern into a bi-level NRZ data stream. The amplitude of the output signal can be changed by changing the scaling constant to the multiplier block. The input to the adder/subtracter block determines the amount of level translation. Parameter values used for this block in the simulations are given in Table 3.2.

Table 3.2: Parameters for the level shifter – type 1

Parameter	Default Value	Editable
Output signal amplitude	+1 to -1 volt	Yes
Mean signal level	0 volt	Yes

3.2.3 LMX2411 Baseband Processor – Transmit Section

The transmit section of the LMX2411 baseband processor implements the Gaussian pulse-shaping of the NRZ baseband data stream. As described in section 2.4.2, the Gaussian filter has been configured as a ROM based filter in National Semiconductors Corporation's hardware implementation. In SPW, a hierarchical block exists which performs the Gaussian pulse-shaping. This provides the flexibility of changing the bandwidth of the filter. The 3 dB bandwidth of the filter is half the bit rate. Since the bit rate for DECT is 1.152 Mb/s, the filter bandwidth is chosen as 576 kHz. The tap length of the complex Gaussian filter must be a power of 2. Since the sampling rate is 16 times the bit rate, the number of taps (filter order) have been set to 16. Only

Table 3.3: Parameters for the LMX2411 baseband processor – transmit path

Parameter	Default Value	Editable
3 dB frequency of Gaussian filter	576 kHz	Yes
Bandwidth of IIR filter	2.304 MHz	Yes

the real part of the output of the filter is used (since the system has been simulated at IF rather than at baseband).

The Gaussian filter output has been scaled by a suitable factor and then passed through a quantizer to simulate the effects of finite precision representation of the Gaussian pulse samples. The scaling factor is chosen such that the peak frequency deviation of the frequency synthesizer block that follows is 288 kHz (this is determined from the specifications of the DECT standard). The quantized output is then passed through a first order IIR Butterworth filter to smooth the quantized values. The bandwidth of the filter is chosen as twice the bit rate. The parameter values used for the baseband processor block on the transmit path are as given in Table 3.3. The sequence of operations performed by the transmit section of the LMX2411 is summarized in the block diagram of Figure 3.3.

3.2.4 LMX2316 Frequency Synthesizer

The frequency synthesizer has been modeled as shown in Figure 3.4. The VCO which exists as a hierarchical block in SPW does not undergo any frequency drift unless specifically programmed. Hence there is no need for a PLL to stabilize the center frequency of the frequency synthesizer. This reduces the simulation complexity. Further, due to blind-slot implementation, the need for modeling the settling time of the PLL is neglected. By adjusting the voltage at the tuning voltage port, an appropriate carrier frequency can be chosen. The modulation control switch determines whether the output of the VCO is just a carrier frequency (when connected to no modulating voltage) or a GMSK DECT signal (when the data stream is allowed to modulate the carrier). There are two ways in which the synthesizer is implemented. The first method described above is used for simulation of DECT in a channel with white Gaussian noise. In order to simulate the effects of Rayleigh fading, the complex baseband representation of the DECT GMSK signal is required. For this purpose,

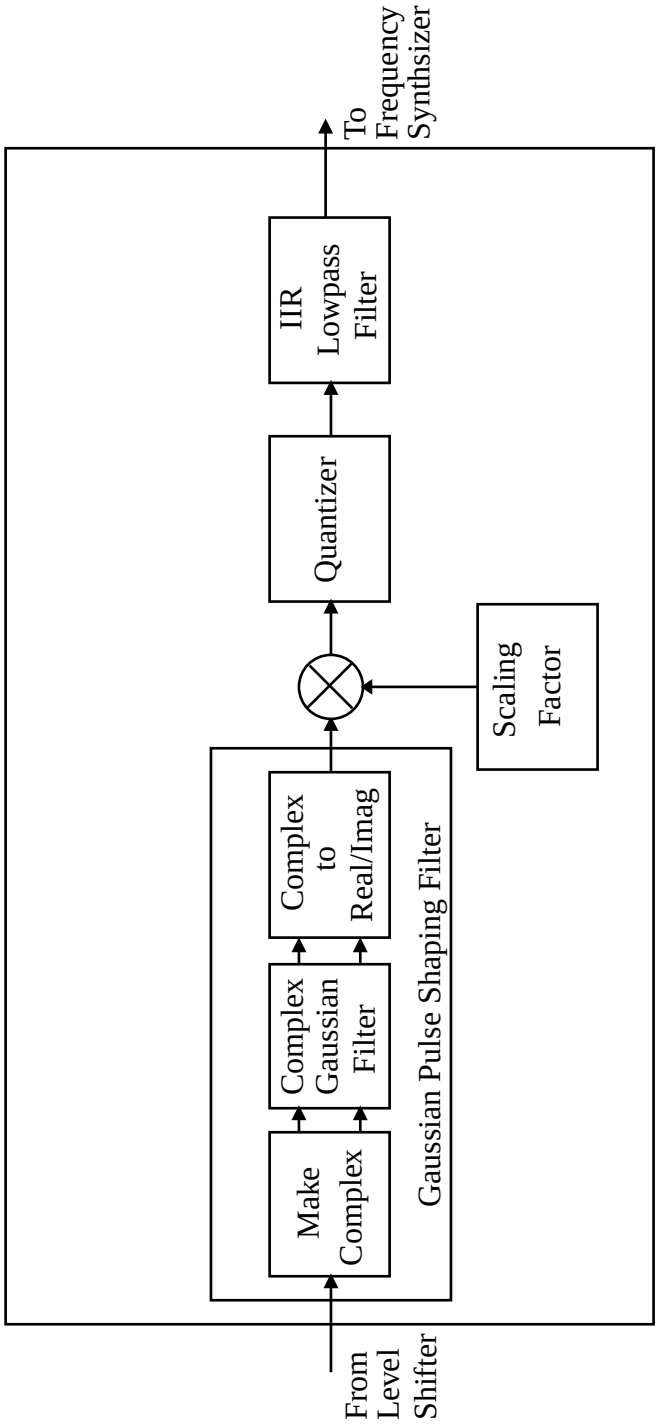

Figure 3.3: Block diagram of the LMX2411 – transmit section

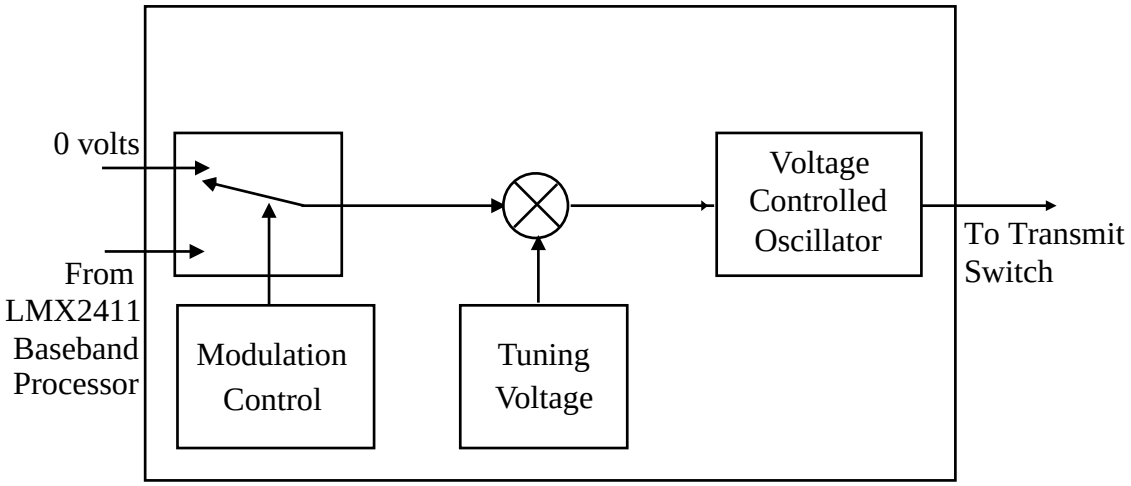

Figure 3.4: Block diagram of the LMX2316

Table 3.4: Parameters for the LMX2416 frequency synthesizer

Parameter	Default Value	Editable
Quiescent frequency	0 Hz	Yes
VCO gain	1.152 MHz/volt	Yes

the complex signal output of the VCO is directly taken as the output of the frequency synthesizer block. The parameters for the LMX2416 are listed in Table 3.4.

3.3 The Receiver

The receive segment of the simulated DECT system is comprised of the IF filter, IF limiter discriminator, lowpass baseband filter, receive section of the baseband processor, symbol timing recovery, and receive section of the system executive. The LNA/Mixer has not been included, since the entire system has been modeled at an IF of 2.304 MHz (rather than 1.88 GHz). The reason for simulating the system at an IF rather than the RF for DECT, is that the required sampling rate at RF would be at least 4 GHz, and hence simulation time would be extremely long.

3.3.1 The IF filter

The IF filter bandwidth is critical to determining the performance of the modeled system in the presence of adjacent channel interference and additive white Gaussian noise (AWGN). In order that the signal remain undistorted after passing through the filter, its phase response should be linear. Taking these design issues into consideration, the filter is modeled as an FIR filter. FIR filters are linear phase filters with constant group delay across the filter bandwidth. The magnitude response of the FIR filter closely resembles that of the hardware implementation. The FIR filter operation can be modeled in SPW using the existing SPW block. This requires filter coefficients to be specified in a separate data file. The filter has been designed using custom code in MATLAB developed by Dominique [32]. The MATLAB program can be used to design any bandpass FIR filter. The input to this program is the lower and upper cut-off 3 dB cut-off points, the filter order, and the sampling frequency. The magnitude and phase response of the filter are shown in Figures 3.5 and 3.6. As seen from these plots, the center frequency is 2.304 MHz. The parameters used for the IF filter block are listed in Table 3.5.

Table 3.5: Parameters for the IF filter

Parameter	Default Value	Editable
Center frequency of filter	2.304 MHz	Yes
IF filter bandwidth	1.728 MHz	Yes

3.3.2 LMX2240 IF Limiter Discriminator

The block diagram of the modeled LMX2240 is shown in Figure 3.7. The limiter is designed to saturate at +1 or -1 volt. The frequency discriminator used is a quadrature detector. The frequency discriminator provides an output voltage that is a function of the input instantaneous frequency (or the rate of phase change). Optimum performance is achieved when a 180^o phase shift is introduced across the frequency band of interest. Under ideal performance conditions, the phase shift should be $90^o \pm 90^o$. The fixed phase shift of 90^o is obtained by using the Hilbert transform block of SPW. The frequency dependent phase shift is modeled by a FIR filter of

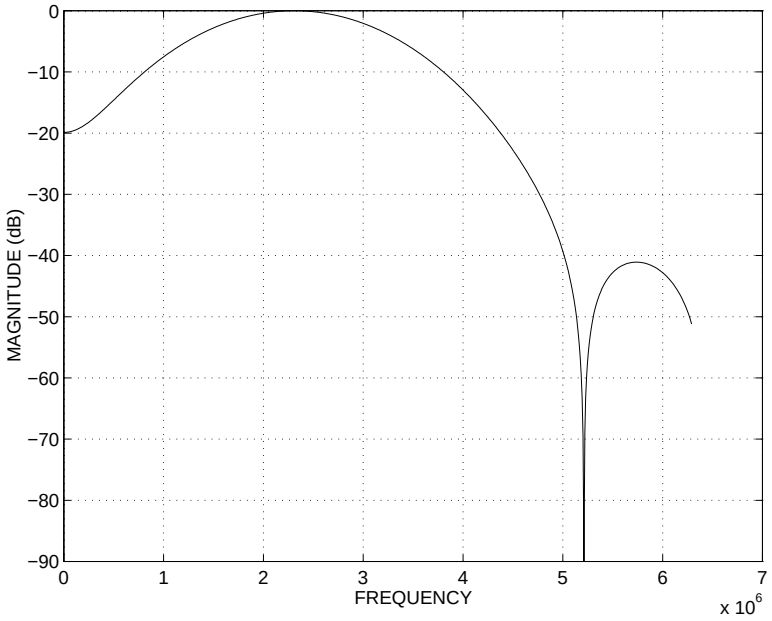

Figure 3.5: Magnitude response of the IF filter

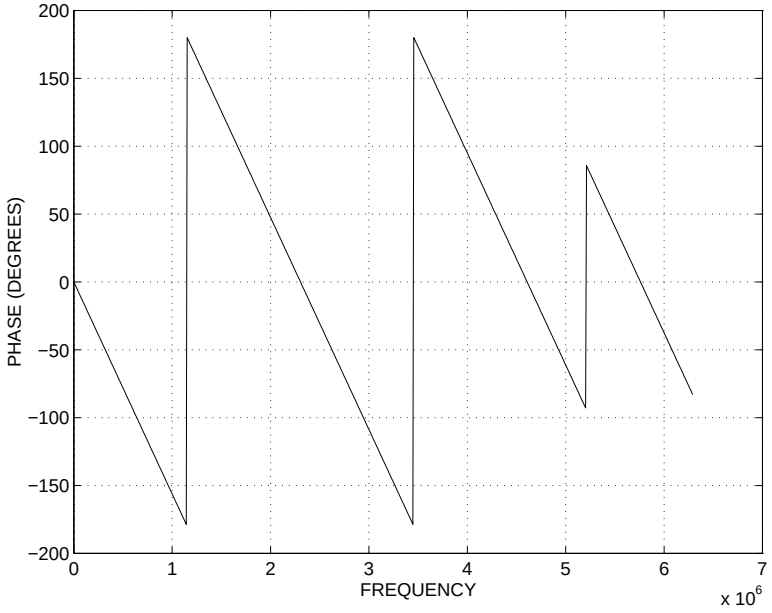

Figure 3.6: Phase response of the IF filter

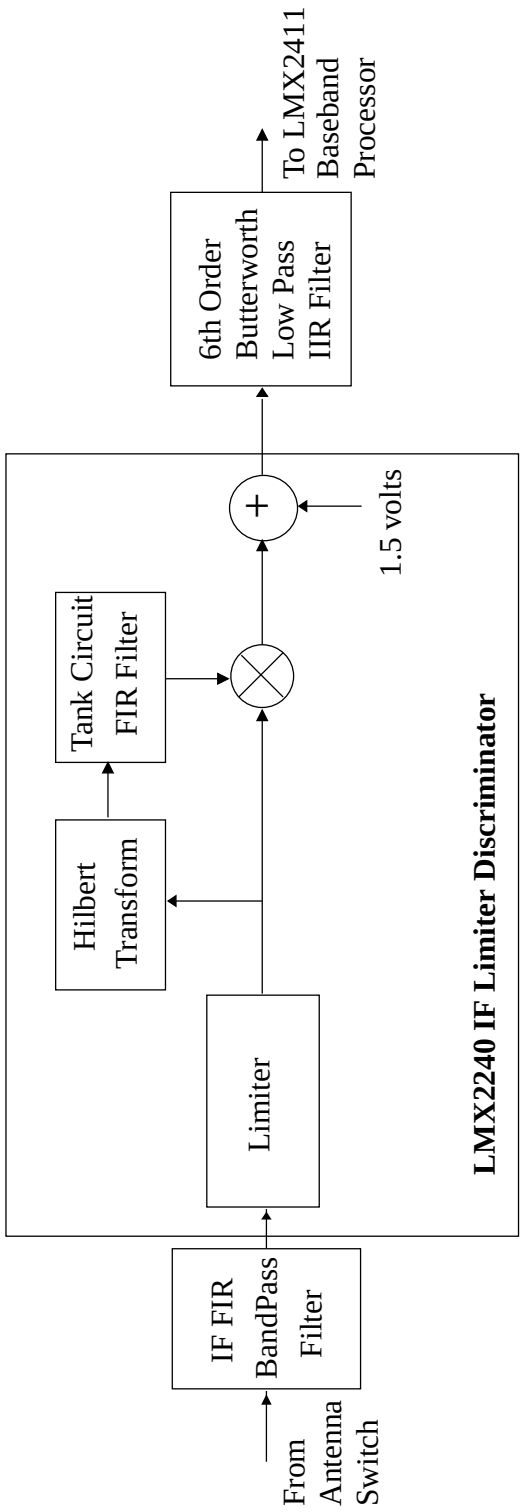

Figure 3.7: Block diagram of the LMX2240

suitable order so as to obtain a phase shift of about 50^o across the band of interest. The FIR filter provides the linear phase response. An important parameter of the tank circuit is the quality factor (called Q–factor) of the circuit. Ideally the Q–factor should be high, so that the phase shift versus frequency will be steep and linear [33]. The SPW model for an FIR filter requires that the filter co-efficients be stored in a data file. MATLAB was used to design the FIR filter. The magnitude and phase response of the filter are shown in Figures 3.8 and 3.9. The parameters used in the SPW simulation of this block are given in Table 3.6.

Table 3.6: Parameters for the LMX2240 limiter discriminator

Parameter	Default Value	Editable
Center frequency of tank filter	2.304 MHz	Yes
Tank filter bandwidth	1.728 MHz	Yes

3.3.3 The Lowpass Filter

In its implementation of DECT, NSC has used a sixth order lowpass Butterworth filter. This block has been modeled in SPW by a sixth order IIR Butterworth filter and the parameters used are given in Table 3.7.

Table 3.7: Parameters for the lowpass filter

Parameter	Default Value	Editable
3 dB bandwidth	1.152 MHz	Yes
Filter order	6	Yes

3.3.4 LMX2411 Baseband Processor – Receive Section

The baseband processor on the receive path recovers the DC level of the signal, and uses this voltage to shape the analog lowpass signal into a NRZ digital data stream. The first 16 bits of the DECT header are an alternating 1 and 0 pattern. During this period, a capacitor is allowed to charge to the average incoming signal DC voltage, which is then held constant for the remaining duration of the time-slot.

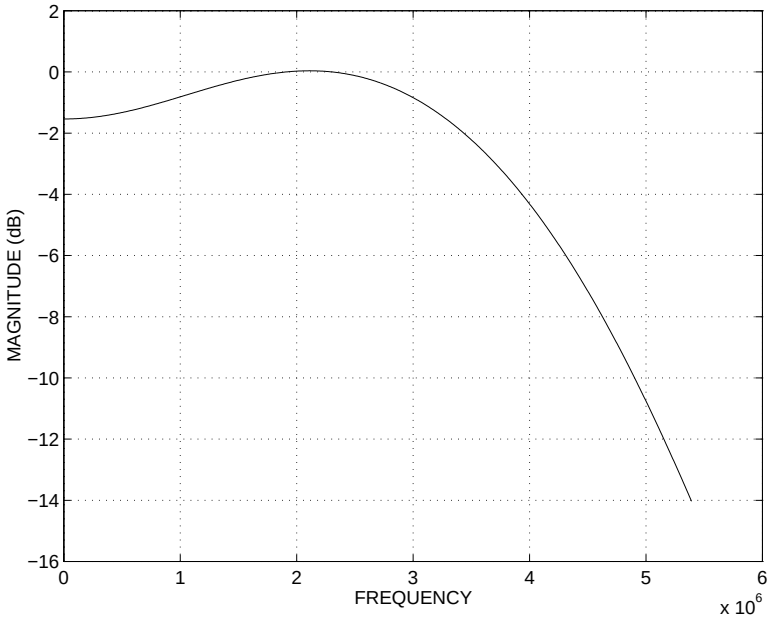

Figure 3.8: Magnitude response of the tank filter circuit

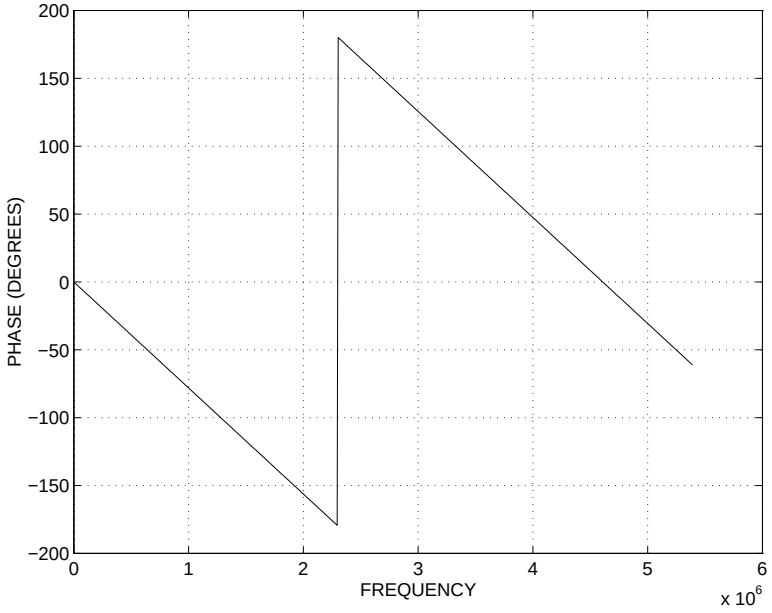

Figure 3.9: Phase response of the tank filter circuit

Table 3.8: Parameters for the LMX2411 baseband processor – receive path

Parameter	Default Value	Editable
3 dB bandwidth	35 kHz	Yes
Filter order	1	Yes

Table 3.9: LMX2411 Control Signals

Mode of operation	H_Field	S_Field	Control	External Voltage
External compensation	'X'	1	0	V_{ext}
Internal compensation over 16 bit preamble	From 'Hold' of System Executive	0	From 'Hold' of System Executive	'X'
Continuous internal compensation	0	0	'X'	'X'

It is also possible to operate the DC recovery circuit in a continuous update mode. If external DC compensation is used, then the internal circuit should be disabled, and the external voltage should be connected to the pin marked 'External Voltage'. The first order integrator used to average the DC value is modeled by a first order Butterworth filter. The block diagram of the baseband processor is shown in Figure 3.10. The parameters used for the SPW simulations are listed in Table 3.8. For different modes of operation, the control signals used are listed in Table 3.9.

3.3.5 Symbol Timing Recovery

Symbol timing recovery has been implemented using the squaring loop technique shown in Figure 3.11. The input signal is delayed by half the data bit period (which corresponds to 8 samples). The delay is accomplished using the bulk delay block in SPW. The signal input to the block is multiplied with the delayed version using an XOR gate to generate a discrete spectral line at the bit rate. The output of the XOR gate is TTL logic. It is level shifted to obtain the polar NRZ signal required from the remaining section of the block. The spectrum at the output consists of a discrete spectral line at multiples of the bit rate, a continuous component and a DC

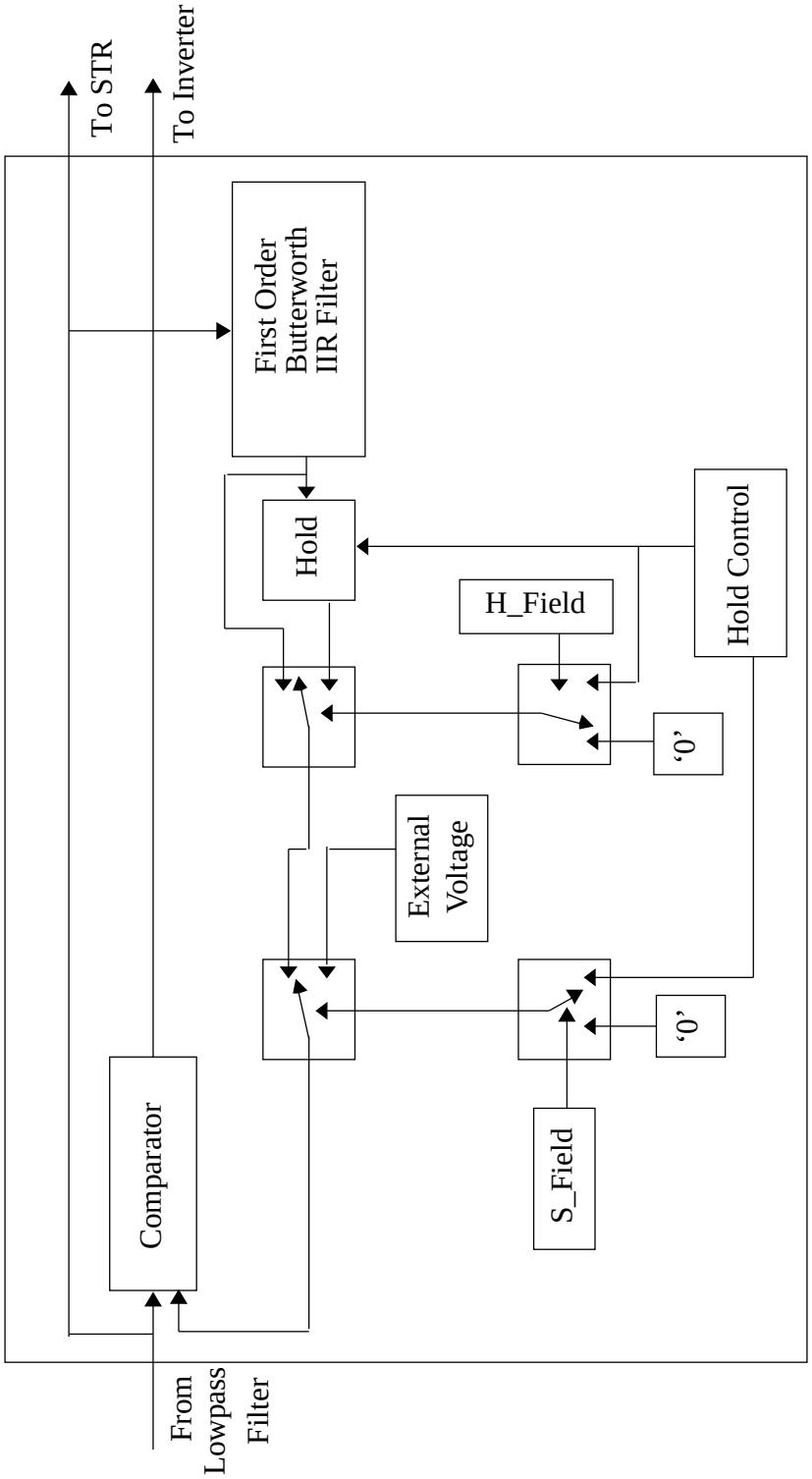

Figure 3.10: Block diagram of the LMX2411 – Receive Section

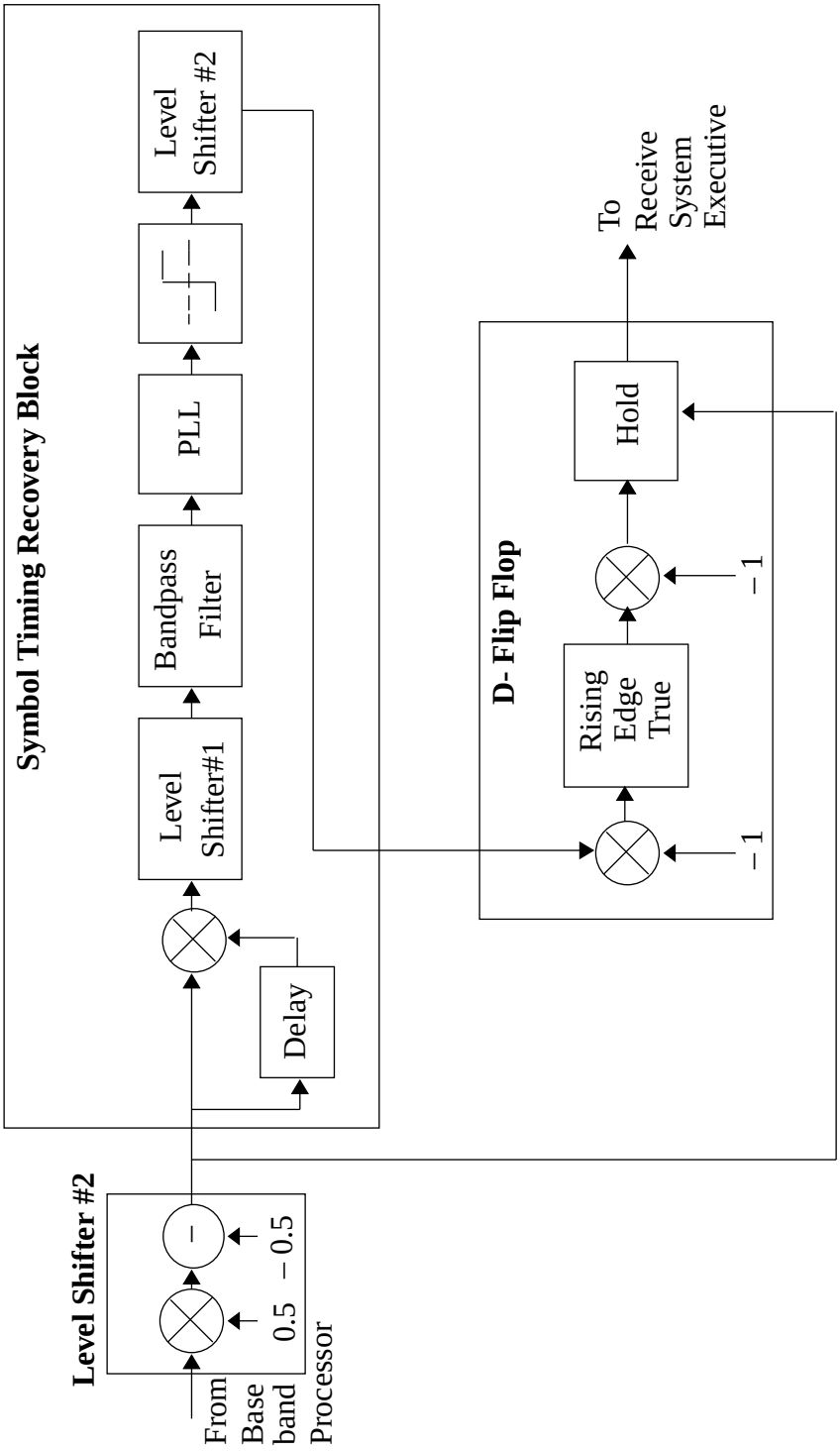

Figure 3.11: Block diagram for Symbol Timing Recovery

Table 3.10: Parameters for the symbol timing recovery block

Parameter	Default Value	Editable
Amount of delay	8 samples	Yes
Filter order of BPF	4	Yes
Center frequency of BPF	1.152 MHz	Yes
3 dB bandwidth of loop filter	10 kHz	Yes
PLL center frequency	1.152 MHz	Yes
Lock range of PLL	10 kHz	Yes

component. The discrete component at the data rate is then tracked by a second order PLL. The lock range of the PLL is 10 kHz. The PLL tracks the phase of the discrete spectral component at the bit rate. The sinusoidal output of the PLL is sent to a zero crossing detector to shape the recovered clock into a digital signal.

3.3.6 System Executive – Receive Section

The receive section of the system executive performs three functions: it detects the start of a DECT time slot; it deformats the received frame i.e., it recovers the data bits from the received DECT frame; and it calculates the BER for the system under the specified channel conditions.

In order to detect the start of frame, the system executive performs a matched filter correlation operation. It continuously compares the received signal with the sixteen bit synchronization PN sequence of DECT. When the correlation score of the input sequence with the synchronization sequence is above the value specified by the threshold parameter (in the default parameter value settings), the correlation operation is discontinued, and the frame deformating begins. At the same time, a control signal is sent to the LMX2411 baseband processing receiver section to hold the value of the DC compensation circuit for the remaining duration of the frame. The parameters for the system executive at the receiver are given in Table 3.11.

The BER analysis is performed by the BER sub-block shown in Figure 3.12. It compares the received signal with the copy of the transmitted signal. A count is maintained of the number of bits in error as well as the number of bits transmitted. These values are stored in an output file.

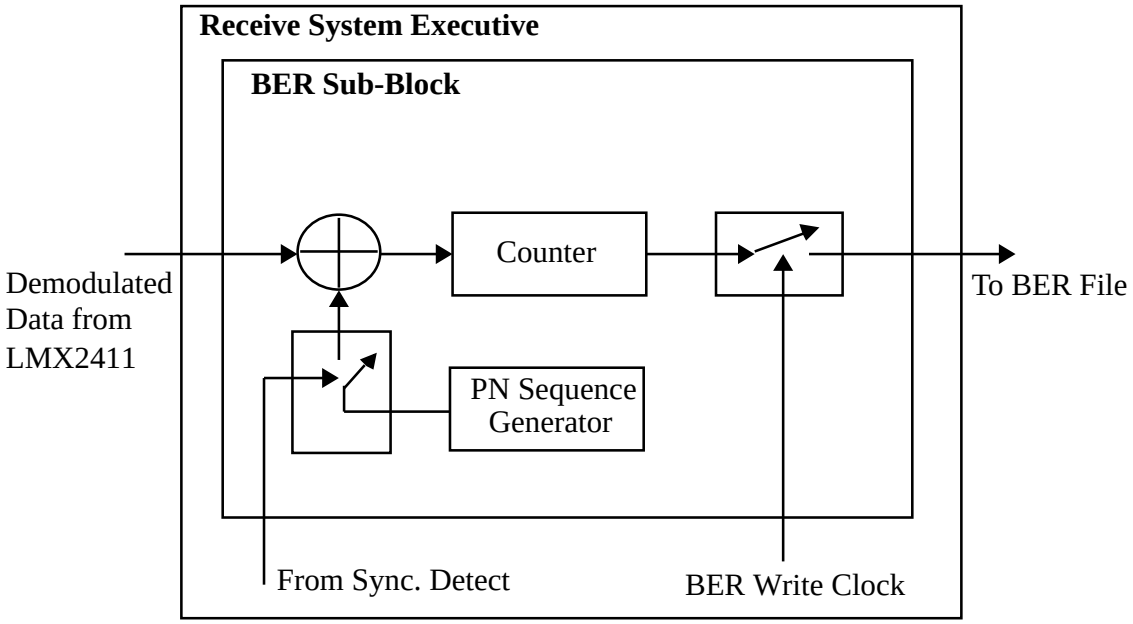

Figure 3.12: BER sub-block of System Executive

Table 3.11: Parameters for the system executive – receive path

Parameter	Default Value	Editable
Bit Rate	1.152 Mbps	Yes
Number of bits/frame	480	Yes
Length of Sync. sequence	16	Yes

Chapter 4

Channel Models

4.1 Introduction

The performance of DECT is modeled for different radio channel conditions. These are the additive white Gaussian noise (AWGN) channel, the Rayleigh flat faded channel, the Rayleigh frequency selective faded channel, and the Ricean channel. The performance is quantified by the bit-error-rate (BER) and the frame-erasure-rate (FER). The impairements caused by cochannel and adjacent channel interference on system performance are also included in these channel models.

4.2 Cochannel Interference

In frequency division multiple access (FDMA) schemes, cochannel users introduce interference which tends to degrade the performance of the system. Cochannel interference is introduced when two users (the desired signal and the interfering signal) are assigned the same channel frequency for communication. DECT uses a FDMA/TDMA/TDD multiple access scheme, and hence the cochannel interferer can be assigned to the same base station.

In order to model a cochannel interferer, a pseudo random sequence generator is used to generate a random 1's and 0's bit stream at the same data rate as DECT. The PN sequence generator exists as a hierarchical block in SPW. The length of the shift register determines the length of the PN code, i.e., the number of bits before the

Table 4.1: Parameters for PN sequence generator

Parameter	Default Value	Editable
Sampling frequency	18432000.0 Hz	Yes
Bit rate	1.152 Mbps	Yes
Shift register length	20	Yes

PN sequence repeats itself. This is given as

$$\text{Length of code} = 2^n - 1 \tag{4.1}$$

where n is the length of the shift register. The parameters used to simulate the PN sequence generator in SPW are given in Table 4.1.

The bit stream is then passed through the level shifter which converts the 1 and 0 pattern to a NRZ waveform. Gaussian filtering is performed through use of the transmit section of the baseband processor LMX2411. The Gaussian filtered data stream then modulates the VCO in the LMX2316 frequency synthesizer. The frequency synthesizer has the same carrier frequency as the desired DECT signal. The output of the synthesizer is scaled by a suitable factor to obtain the desired cochannel interference level. The block diagram of the implementation of the cochannel interferer is shown in Figure 4.1. The default parameters of the various blocks used to model the cochannel interference are the same as the desired DECT transmission values. These values may be changed as explained in Sections 3.2.2 to 3.2.4. The system has been modeled for a worst-case scenario where the cochannel interferer transmits in the same time-slot as the desired user (and at the same frequency). This would represent performance of a fully loaded DECT system.

4.3 Adjacent Channel Interference

DECT being an FDMA/TDMA/TDD system, it is necessary to understand the effects of adjacent channel interference on the performance of the system. The adjacent channel interferer is modeled using the same blocks as for cochannel interference as shown in Figure 4.1. By changing the voltage at the tuning port of the frequency synthesizer (see section 3.2.4, the carrier frequency can be changed thereby modeling

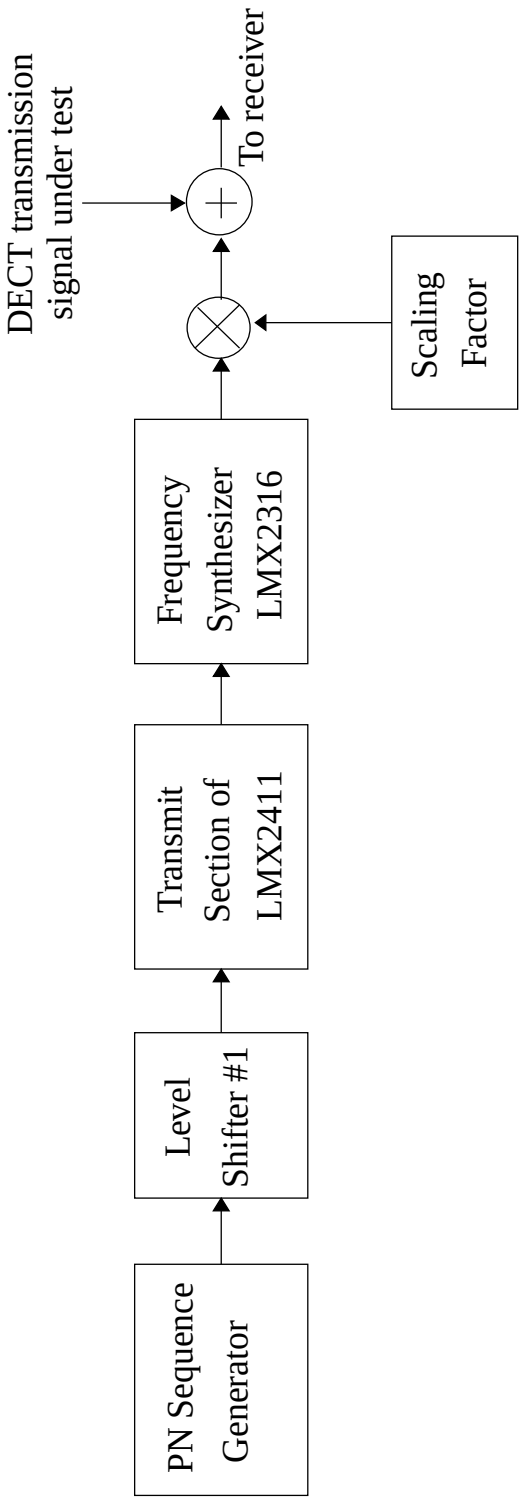

Figure 4.1: Block diagram for cochannel and adjacent channel interference

adjacent channel interference. The scaling factor can be chosen so that the power level of the interferer is scaled accordingly. Thus the performance of DECT can be simulated for different level of ACI.

4.4 The AWGN Channel

In order to model white Gaussian noise, we assume that the noise has a constant double–sided power spectral density for all frequencies

$$S_{NN}(f) = N_o/2 \quad -\infty < f < \infty. \tag{4.2}$$

Consider that the filter at the front end of the receiver, has a bandwidth B, and the sampling rate for simulation is $f_s > 2B$. Now, if we use band-limited white Gaussian noise with a constant PSD over the simulation bandwidth $-f_s/2 < f < f_s/2$,

$$S_{N_sN_s}(f) = N_o/2 \quad -f_s/2 < f < f_s/2, \tag{4.3}$$

then the response of the system is the same whether the input has the PSD $S_{NN}(f)$ or $S_{N_sN_s}(f)$ [34]. This is illustrated in Figure 4.2.

A hierarchal block exists in SPW which generates white Gaussian noise. However, this block requires that the mean and variance of the noise be given as parameters. In order to relate E_b/N_o required for a particular simulation run to the noise variance, we use the following relationships

$$E_b = S\,T_b, \tag{4.4}$$

where S is the incoming signal power, and T_b is the bit duration. Also,

$$N_o/2 = \sigma_o^2\,T_s, \tag{4.5}$$

where σ_o^2 is the noise power, and T_s is the sampling period. Combining equations 4.4 and 4.5,

$$\frac{E_b}{N_o} = \frac{S\,T_b}{2\,\sigma_o^2\,T_s}. \tag{4.6}$$

Thus through the selection of different values for σ_o^2, the performance of DECT in an AWGN channel can be simulated.

The effects of cochannel and adjacent channel interference are incorporated as shown in Figure 4.3.

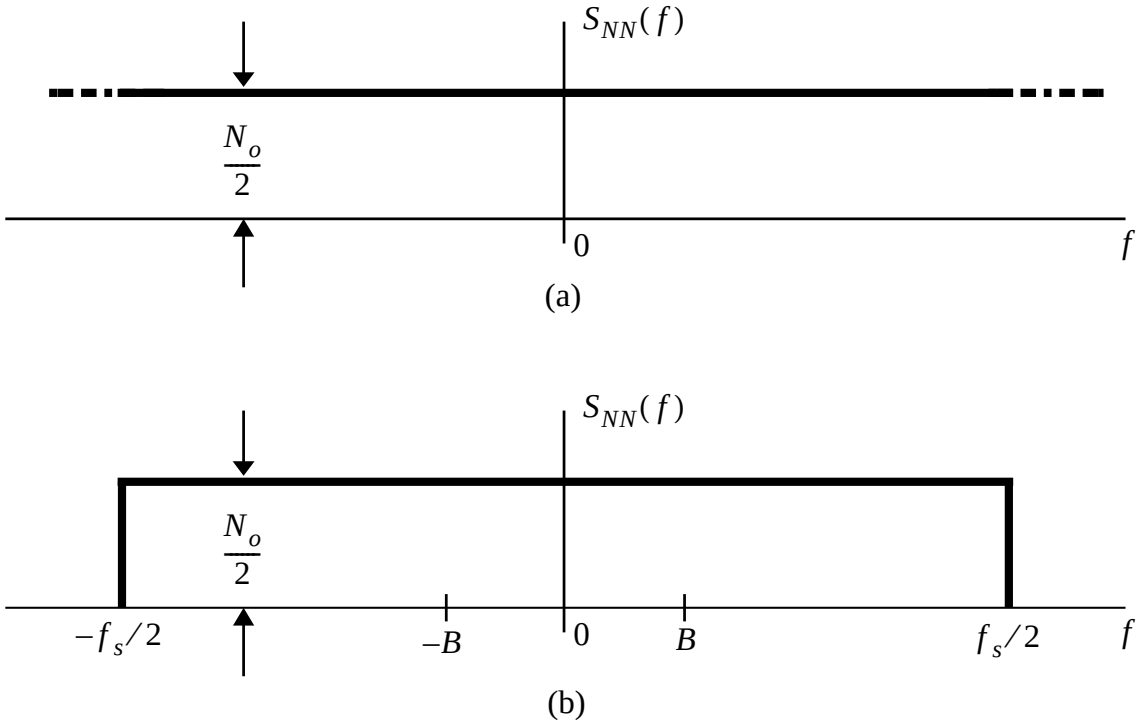

Figure 4.2: Simulation model for white noise (a) noise PSD (b) simulated PSD

4.5 The Rayleigh Flat Faded Channel

Due to reflections, scattering, and diffraction of the transmitted signal in a mobile channel, multiple versions of the transmitted signal arrive at the receiver with different amplitudes and phases. This time dispersion of the transmitted signal results in either flat or frequency selective fading.

A flat fading mobile channel has a constant gain and linear phase response over a bandwidth greater than that of the transmitted signal [17, 34]. In a flat fading channel, the spectral characteristics of the transmitted signal are preserved, but the received signal strength changes in magnitude with time.

Rayleigh fading models are commonly used in mobile communications to model the effects of multiple point scatters in the neighborhood of a mobile receiver. The Rayleigh distribution assumes that there is no dominant non-fading signal component present. If a non-obstructed line-of-sight path exists between the transmitter and receiver, then the Ricean model is appropriate.

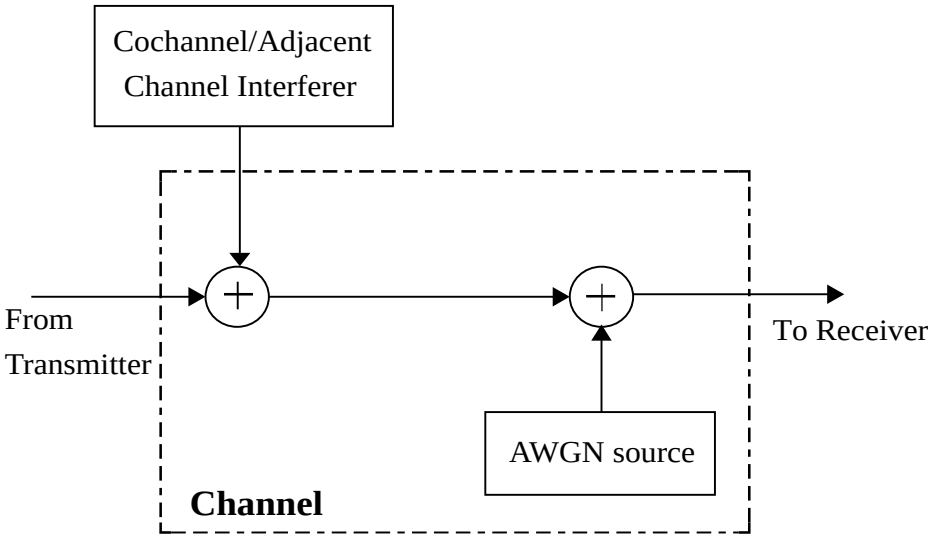

Figure 4.3: Simulation model for an AWGN channel

If a mobile is moving with a velocity v towards the base-station (reference point), then the maximum Doppler frequency shift is

$$f_d = \frac{v}{\lambda}. \tag{4.7}$$

Depending on the value of the Doppler frequency spread, and the baseband signaling, channels are classified as slow fading or fast fading. The DECT standard has a relatively wide channel bandwidth, and is intended for use at walking speeds. At the carrier frequency of 1880 MHz, and for a velocity $v = 1$ m/s, using equation 4.7, the maximum Doppler frequency is $f_d = 8.7$ Hz.

The Rayleigh fading simulator is modeled in SPW as shown in Figure 4.4.

Complex Gaussian white noise is passed through a Doppler filter. The Doppler fading filter also known as the spectrum fading filter has a frequency response given by equation 4.8 [35].

$$H(f) = \begin{cases} \dfrac{A}{\sqrt{1-(\dfrac{f}{f_d})^2}} & for \quad |f| \leq f_d \\ 0 & for \quad |f| > f_d \end{cases} \tag{4.8}$$

where f_d is the Doppler frequency. Because the Doppler frequency is usually much less than the sampling frequency, the fading filter response $H(f)$ is usually a very

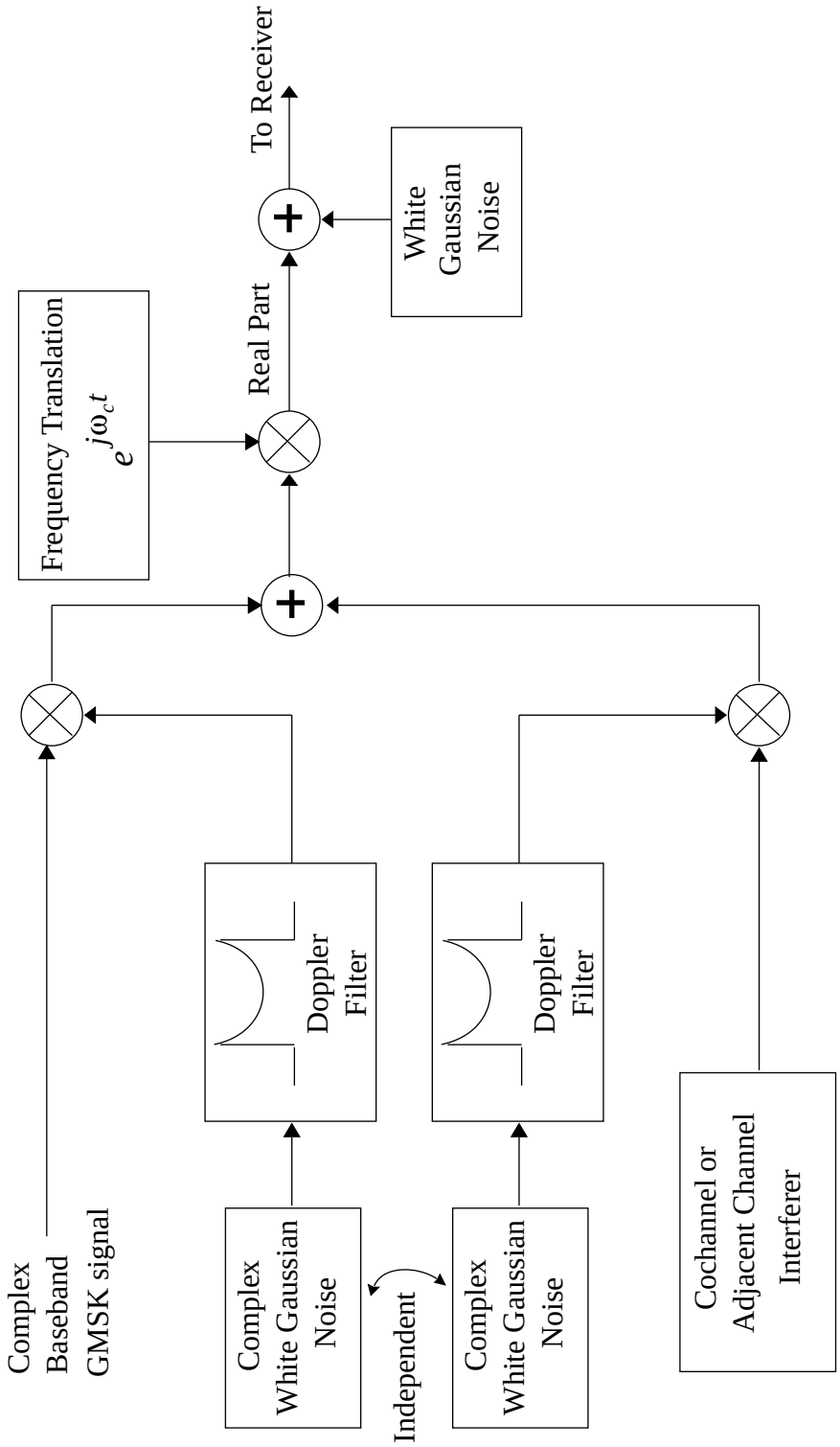

Figure 4.4: Simulation model for a flat faded Rayleigh channel

Table 4.2: Parameters for the Doppler filter

Parameter	Default Value	Editable
Sampling frequency	18432000.0 Hz	Yes
Fading filter length	100	Yes
Doppler frequency	8.7 Hz	Yes
Normalized output power	1.0 W	Yes
Interpolation factor	200	Yes
Number of points used in interpolation	11	Yes

narrow lowpass filter. The output of the fading filter is interpolated using a hamming windowed sinc function. The Doppler filter exists as a hierarchical block in SPW [36]. The parameters used for the Doppler fading filter block in SPW are summarized in Table 4.2.

In order to model the cochannel interferer in a flat faded channel, the block diagram of Figure 4.1 is used. The output of this cochannel interferer block (attenuated by a suitable factor to obtain the desired C/I) is multiplied by the output of the Rayleigh fading simulator and then added to the desired user's signal. To the composite signal (the summation of the desired user's signal and the cochannel interferer's signal) white Gaussian noise is added and the resultant signal is input to the DECT receiver.

Two independent Rayleigh fading simulator outputs multiply the desired user's signal, and the interferer's signal. The reason for this is understood by considering the manner in which a signal undergoes fading. In a flat faded channel, the multipath components that combine to form the composite signal arrive from different scattering, reflecting, and or diffracting sources, and hence have different amplitudes and phases for each user. Thus the Rayleigh envelope that multiplies the transmitted signal will be different for each user. The independence of the two Rayleigh fading simulators is implemented by using two independent complex white Gaussian noise sources as input to the Doppler filters.

4.6 The Rayleigh Frequency Selective Channel

When the channel possesses a constant gain and linear phase response over a bandwidth that his smaller than the bandwidth of the transmitted signal, then the transmitted signal undergoes frequency selective fading in the channel. The received signal contains multiple versions of the transmitted signal that are time–delayed, phase–shifted, and attenuated. The net result is a time dispersion of the transmitted signal which at the receiver manifests itself as inter-symbol interference (ISI). The 2–ray Rayleigh fading model is often used to described the multipath channel. The impulse response of the channel is then given as [37]

$$h_b(t) = \alpha_1 \, e^{j\phi_1} \, \delta(t) + \alpha_2 \, e^{j\phi_2} \, \delta(t - \tau) \tag{4.9}$$

where α_1 and α_2 are independent and Rayleigh distributed, ϕ_1 and ϕ_2 are independent and uniformly distributed over $[0, 2\pi)$, and τ is the delay spread (or the excess delay).

The model for Rayleigh frequency selective channel implementation in SPW is shown in Figure 4.5. Each arm of the Rayleigh fading signal is generated by passing complex white Gaussian noise through the Doppler filter as explained in section 4.5. The Rayleigh faded branches are independent of each other. In this model it is possible to have variable delay spreads between the direct and delayed arm (this delay spread τ is represented by the bulk delay block in Figure 4.5). It is also possible to change the power level of the two incoming Rayleigh faded signals relative to each other. These parameters are listed in Table 4.3.

For the two–ray Rayleigh frequency selective channel model, when the direct and delayed signals have the same power, the delay spread is related to the RMS delay spread as $\sigma_\tau = \tau/2$ [2, 26].

In order to model the cochannel interferer in a frequency selective channel, the block diagram of Figure 4.1 is used. The output of this cochannel interferer block (attenuated by a suitable factor to obtain the desired C/I) is multiplied by the output of the Rayleigh fading simulator and then added to the desired user's signal. The Rayleigh fading block that multiplies the cochannel interferer's signal is generated independent of both the direct path and the delay multipath component of the desired user's signal. To this signal white Gaussian noise is added and the resultant signal is detected by the DECT receiver thereby modeling the performance of DECT in a frequency selective Rayleigh faded channel with the impairments of cochannel

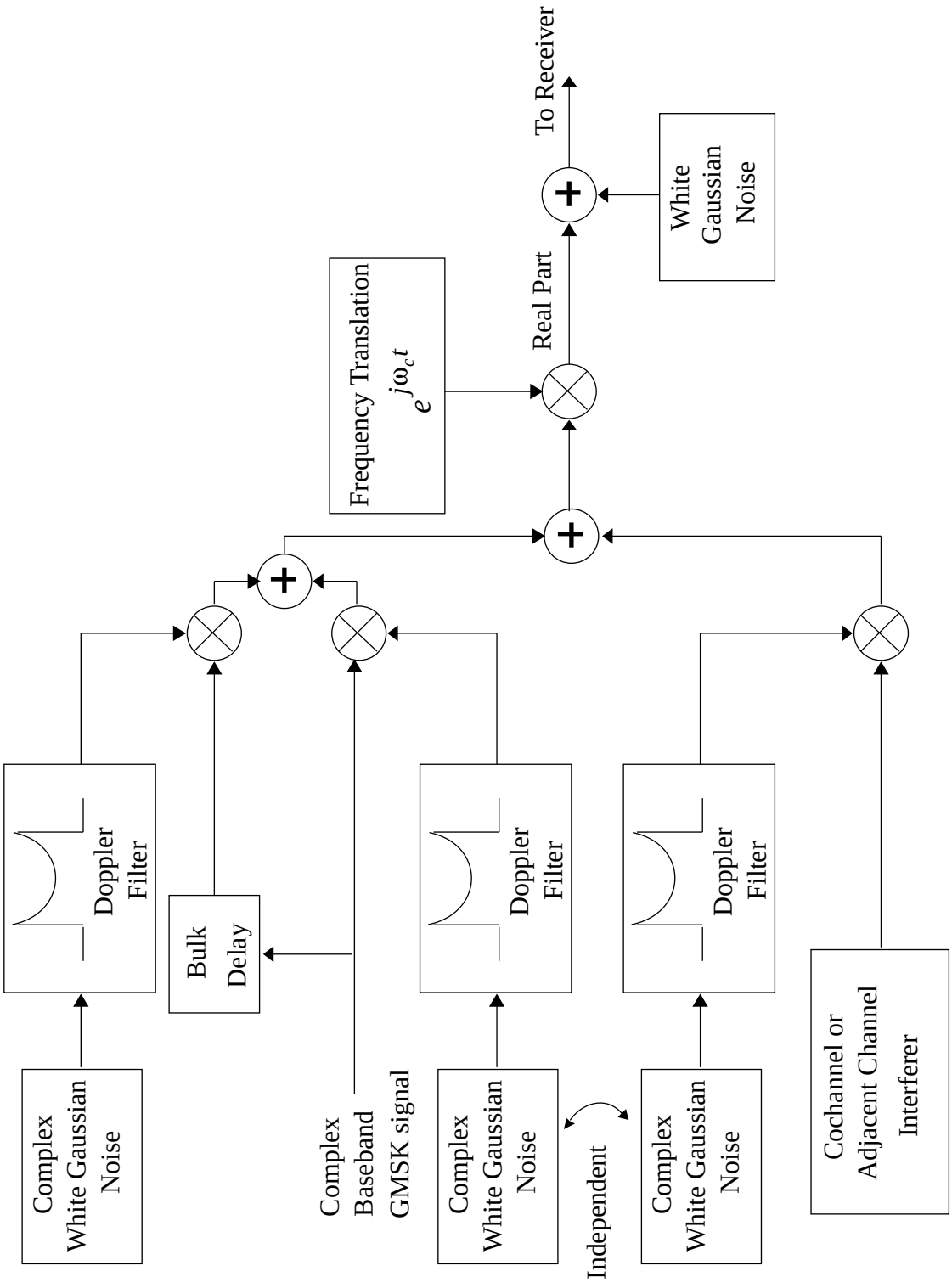

Figure 4.5: Simulation model for a frequency selective faded Rayleigh channel

Table 4.3: Parameters for the Rayleigh frequency selective channel

Parameter	Default Value	Editable
Sampling frequency	18432000.0 Hz	Yes
Fading filter length	100	Yes
Doppler frequency	8.7 Hz	Yes
Normalized output power	1.0 W	Yes
Interpolation factor	200	Yes
Number of points used in interpolation	11	Yes
Delay spread or bulk delay	2 samples	Yes
Relative strength of multipath	1.0	Yes

interference and white Gaussian noise.

4.7 The Ricean Faded Channel

In some propagation environments, there exists a line-of-sight (LOS) path between the transmitter and receiver, in addition to the multipath received from reflections, scattering, and diffraction. If this LOS component is the dominant component of the received signal and non-fading, then the small-scale fading envelope distribution is described by the Ricean distribution [17, 38]. Thus the random multipath components are superimposed on the stationary dominant signal. As the LOS signal weakens in comparison to the multipath, the Ricean faded channel reduces to the case of a Rayleigh faded channel.

The pdf of the Ricean distribution is given by

$$p(r) = \begin{cases} \frac{r}{\sigma^2}\, e^{\frac{-(r^2+A^2)}{2\,\sigma^2}}\, I_o(\frac{A\,r}{\sigma^2}) & for \quad A \geq 0, r \geq 0 \\ 0 & for \quad r < 0 \end{cases} \tag{4.10}$$

where A is the peak amplitude of the dominant LOS signal, $I_o(\bullet)$ is the modified Bessel function of the first kind and zero order, and σ^2 is the variance of the multipath. The Ricean distribution is described by a Ricean factor K that completely specifies the distribution. It is given by equation 4.11.

$$K\ (\text{dB}) = 10\ \log\,(\frac{A^2}{2\,\sigma^2})\ (\text{dB}) \tag{4.11}$$

Table 4.4: Parameters for the Ricean channel model

Parameter	Default Value	Editable
Sampling frequency	18432000.0 Hz	Yes
Fading filter length	100	Yes
Doppler frequency	8.7 Hz	Yes
Normalized output power	1.0 W	Yes
Interpolation factor	200	Yes
Number of points used in interpolation	11	Yes
Delay spread or bulk delay	2 samples	Yes
Relative strength of multipath	1.0	Yes
Ricean factor	6 dB	Yes

From the above equation we note that as the dominant component begins to vanish, $A \rightarrow 0, K \rightarrow -\infty$ dB, and the Rayleigh distribution results [17].

The SPW block diagram for simulation of a Ricean channel is shown in Figure 4.6. As can be expected, the implementation of the Ricean channel is virtually the same as the Rayleigh flat faded channel with the exception that there now exists a non-faded LOS path in addition to the Rayleigh faded signal. By varying the variance of the multipath, the performance of DECT can be simulated in a Ricean channel for different values of Ricean factor K. The parameters that are used in the SPW simulations are given in Table 4.4.

In order to model the cochannel interferer in a Ricean faded channel, the block diagram of Figure 4.1 is used. The output of this cochannel interferer block (attenuated by a suitable factor to obtain the desired C/I) is multiplied by the output of the Rayleigh fading simulator and then added to a non-faded LOS component of the interfering signal. This Ricean faded cochannel interfering signal is then added to the desired user's signal. To the composite signal (the summation of the desired user's signal and the cochannel interferer's signal – both Ricean faded) white Gaussian noise is added and the resultant signal is input to the DECT receiver.

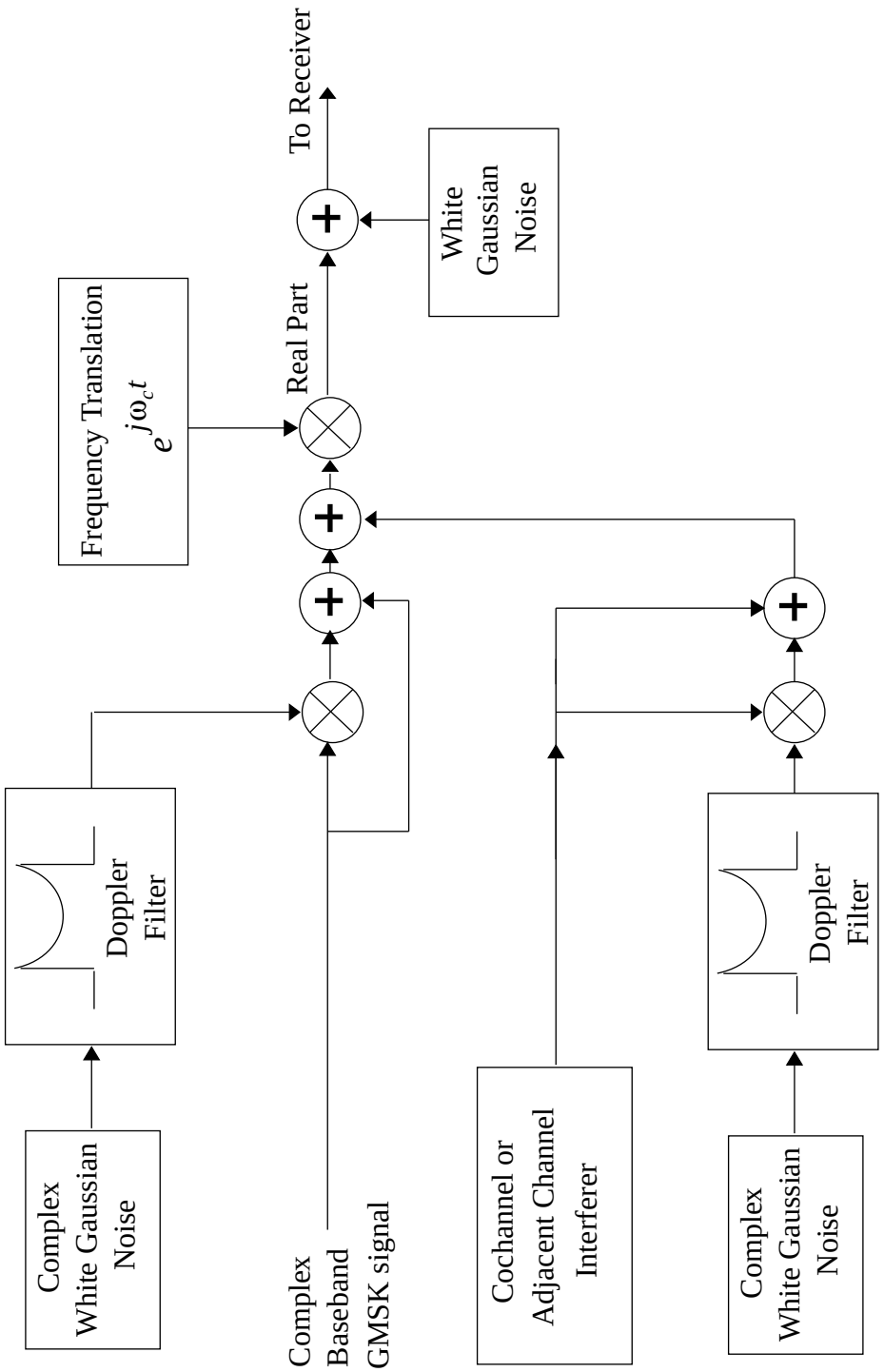

Figure 4.6: SPW Block diagram for simulation of a Ricean faded channel

Chapter 5

RF Channel Measurements

5.1 Introduction

The design of a wireless communication system is dependent upon the propagation environment in which the system is to be used. In order to characterize the mobile channel for DECT, channel impulse response measurements were made using a spread spectrum sliding correlator measurement system. This chapter begins with a brief description of the measurement system used, and the parameters under which measurements are performed. Next a description of the measurement locations chosen is provided. The chapter concludes with results obtained from the measurement campaign.

5.2 The Spread Spectrum Sliding Correlator

The reasons that influenced the use of a spread spectrum sliding correlator were outlined in Chapter 2 (section 2.5.1). The block diagram of the transmitter is shown in Figure 5.1 [39].

The frequency synthesizer generates a CW signal at 1900 MHz. Using the rubidium frequency standards (at 10 MHz) as a reference, and a frequency multiplier circuit, the transmit PN sequence generator is clocked at a rate of 100 Mchip/s. This PN sequence is used to spread the CW signal to a bandwidth of 200 MHz at a center

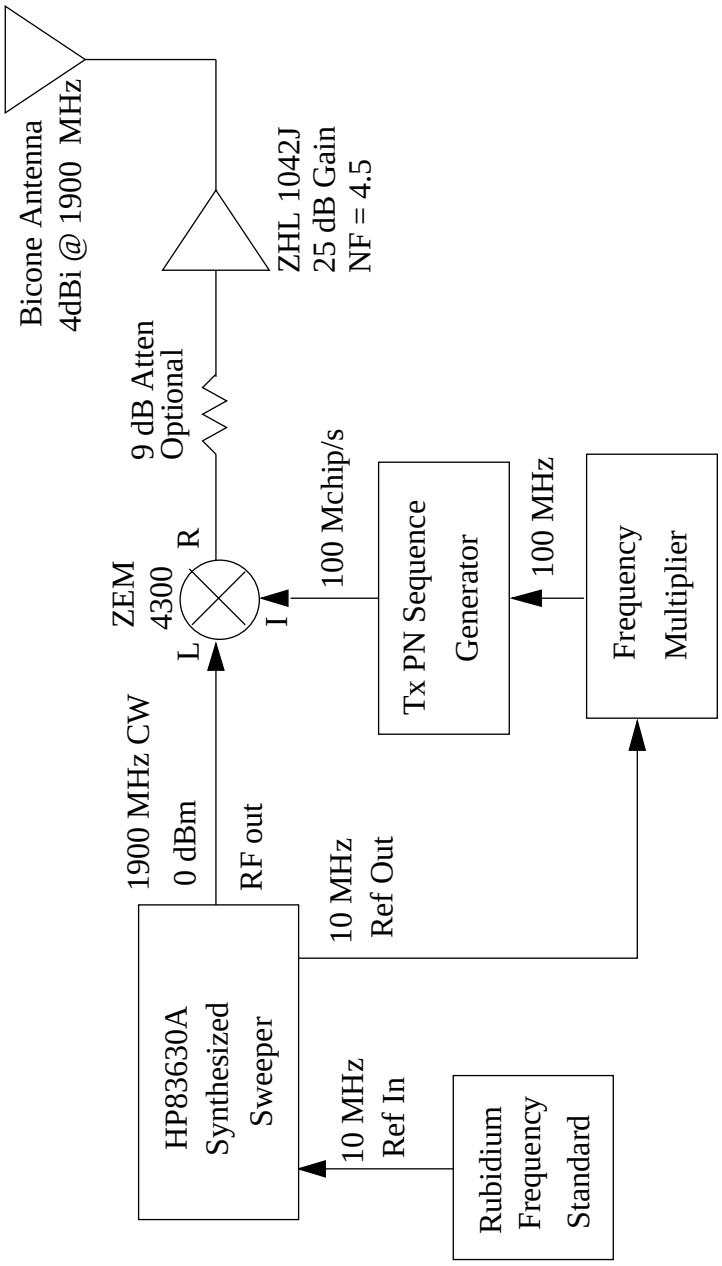

Figure 5.1: Sliding correlator measurement system transmitter at 1.9 GHz. Adapted from [39, 40].

frequency of 1900 MHz. Thus the time resolution of the system is

$$\Delta\tau \approx 2\,T_c = \frac{2}{R_c} = 20ns \tag{5.1}$$

where T_c is the chip period and R_c is the chip rate.

A block diagram of the receiver is shown in Figure 5.2. The receiver uses a PN sequence identical to that at the transmitter to despread the received signal. The transmitter chip clock is run slightly faster than the receiver chip clock. When the PN code of the transmitter is aligned with the PN code at the receiver, a correlation peak occurs. When the two sequences are not maximally correlated, mixing the incoming spread spectrum signal with the unsynchronized receiver chip sequence spreads this signal into a bandwidth at least as large as the receiver's reference PN sequence. Thus the narrowband filter that follows the correlator can reject almost all of the incoming signal power. This realization of processing gain allows the receiver to reject passband interference [17].

The slip rate is defined as the difference between the transmitter and receiver chip rates. If α is the transmitter chip rate, and β is the receiver chip rate, then

$$R_{slip} = \alpha - \beta \tag{5.2}$$

The slide factor which relates the observed multipath delay time at the receiver to the actual propagation delay time is defined as:

$$\gamma = \frac{\alpha}{\alpha - \beta} \tag{5.3}$$

Using the slide factor, we can relate the actual propagation time $t_{propagation}$ to the observed oscilloscope time $t_{observed}$ by

$$t_{propagation} = \frac{t_{observed}}{\gamma} \tag{5.4}$$

The spectrum analyzer is used to realize the narrowband filter by setting its resolution bandwidth to that of the desired bandwidth. The resolution bandwidth is chosen as [17]

$$ResBW = 2\,(\alpha - \beta) \tag{5.5}$$

For the measurement campaign conducted at Virginia Tech, the parameter settings used are summarized in Table 5.1. Keith Blankenship was an immense help in conducting this measurement campaign.

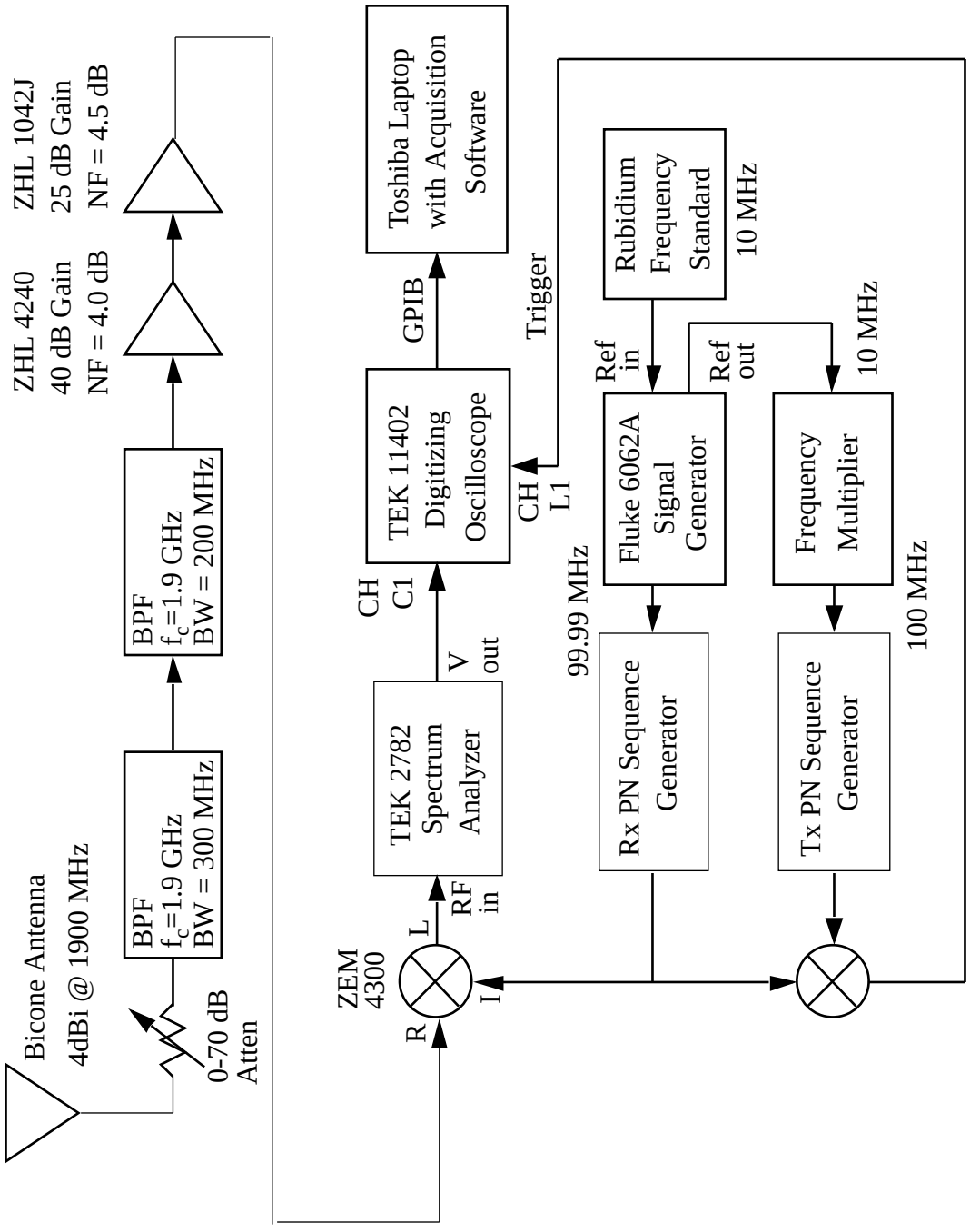

Figure 5.2: Sliding correlator measurement system receiver at 1.9 GHz. Adapted from [39, 40].

Table 5.1: Measurement parameters for Virginia Tech

Parameter Name	Symbol	Value	Units
Transmitter Chip Rate	α	100.00	Mchip/s
Receiver Chip Rate	β	99.99	Mchip/s
PN sequence length	M	2047	chips
Slip rate	R_{slip}	10.0	kHz
Slide factor	γ	10000	unitless
Spectrum Analyzer ResBW	ResBW	30	kHz
Spectrum Analyzer Video BW	VideoBW	30	kHz
Transmitter Antenna Gain	G_t	4	dBi
Receiver Antenna Gain	G_r	4	dBi
Transmitter Antenna Height	h_{Tx}	1.75 or 3	m
Receiver Antenna Height	h_{Rx}	1.75	m

5.3 Calibration Procedure

In order to calculate RMS delay spread σ_τ and path loss PL from data recorded from the receiver oscilloscope, the system needs to be calibrated. Calibration is required in order to convert the oscilloscope voltage to an absolute power level in dBm. Calibration also accounts for changes in component specifications. This is performed both at the start of measurements and at its completion. Calibration data consists of several power delay profiles taken when the transmitter and receiver are connected back-to-back through a coaxial cable and attenuator. A total of 70 dB of attenuation is used between the output cable of the transmitter and input cable of receiver connected to bandpass filters. The frequency synthesizer output is set at a value such that the correlation peak observed on the oscilloscope at the receiver just peaked above the correlation noise. Then the carrier power is increased in steps of 2 dB and at each stage, the power delay profile is recorded at the receiver. The spectrum analyzer resolution bandwidth is set at 30 kHz. Calibration is performed at the start and completion of measurement recording at each site.

From these calibration profiles, the sensitivity parameter D expressed in dB/V is determined. This parameter relates a voltage recorded on the oscilloscope to a received power level in dBm. The sensitivity parameter D is set equal to the slope of the best-fit line through the calibration points on the graph.

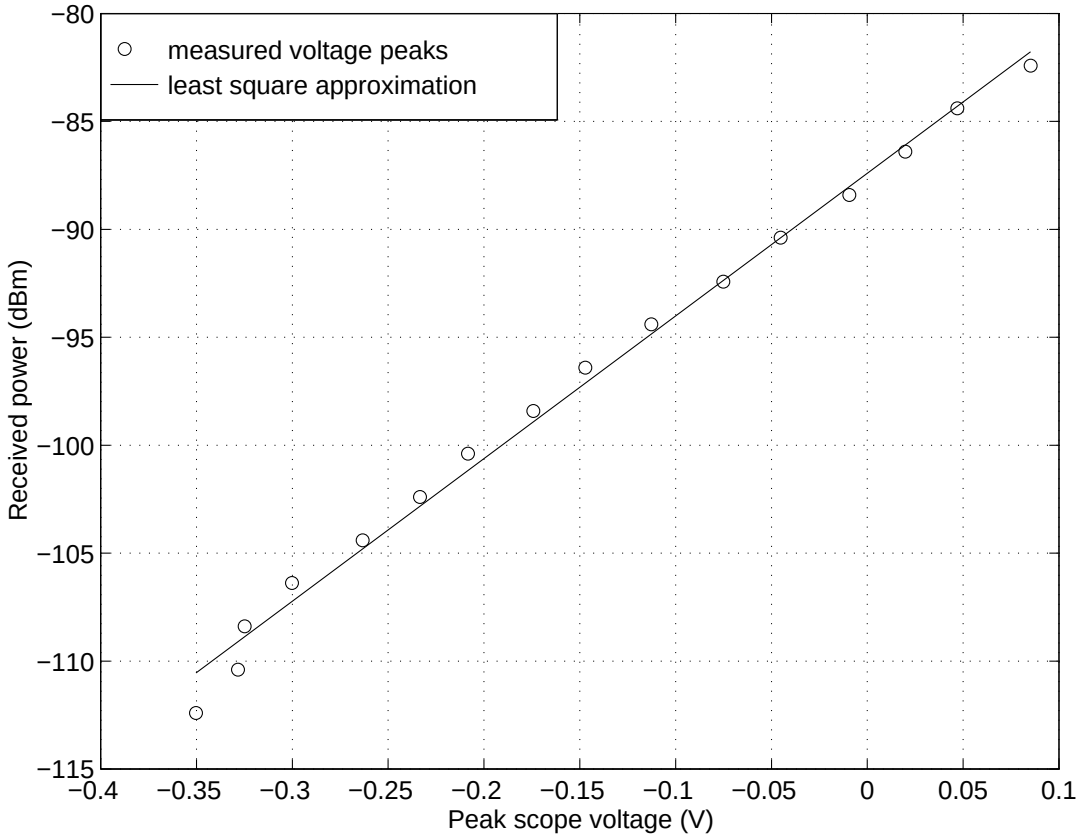

Figure 5.3: Received power versus peak scope voltage

As an example, the calibration curve used for the indoor measurements is shown in Figure 5.3. From the graph, the slope yields the sensitivity parameter as $D = 63.08$ dB/V. During measurements at all locations, the transmitter was maintained at 0 dBm. From this, the received calibration power off the graph is determined as $P_{calc} = -87.39$ dB. The area under the single component that corresponds to this power level is denoted as A_{calc}.

5.4 Post–Processing of Data

There are different parameters of interest like RMS delay spread (σ_τ), path loss (PL), path loss exponent (n), and the standard deviation (σ) of the log-normal shadowing model, whose values are calculated from the power delay profiles recorded in the field. The calculation of these values from the data recorded at the various receiver

locations is described below.

5.4.1 Received Power and Path Loss

From the power delay profile, the noise threshold is determined. The noise threshold is set as the peak value of noise observed in the first 10% of the power delay profile. This is because there is no multipath observed in the first 10% of the power delay profile. The location of the first arriving component in the power delay profile can be adjusted by triggering the oscilloscope at the desired instant. By ensuring that the first 10% of the power delay profile does not contain any multipath components, we are able to determine the noise floor of the system. All data points below the noise threshold are assigned a power of 0 Watts. The area under the power delay profile curve is now calculated. This area is then related to power in dBm using the relationship

$$P_r \text{ (dBm)} = P_{calc} \text{ (dBm)} + 10 \log (\frac{A_{rec}}{A_{calc}}), \tag{5.6}$$

where A_{rec} is the area under the points of the received power delay profile which lie above the noise threshold, and A_{calc} is the area under the points on the calibration power delay profile. It is important to note that the area must be calculated on a linaer (not dB) scale. If $P_{w_{ABS}}(k)$ is the power at point k and $\Delta\, t$ is the time between two data points on the power delay profile expressed in seconds, then

$$A_{rec} = \sum_k P_{w_{ABS}}\, \Delta\, t, \tag{5.7}$$

where k includes all data points which lie above the noise threshold.

Further, the received power is related to the transmitted power by

$$P_r = P_t + G_t + G_r - \text{PL}. \tag{5.8}$$

Using this equation, the path loss can be determined for each measurement location. The return loss of the transmitter is negligible and has been omitted in the above equation. The justification for this lay in a simple measurement. The output of the signal generator was connected through a directional coupler to the transmitter. A 20 dBm CW signal at 1.9 GHz was sent to the transmitter. A reflected signal of 6 dBm strength was observed. Thus return loss is

$$RL = P_{CW} - P_{reflected} = 20\text{dBm} - 6\text{dBm} = 14\text{dB}. \tag{5.9}$$

Thus, the reflection co-efficient is

$$|\rho|^2 = 10^{-\frac{RL}{10}} = 10^{-1.4} = 0.04. \tag{5.10}$$

Hence the radiated power is

$$P_{radiated} = (1 - |\rho|^2)\ P_{CW} = 0.998\, P_{CW}. \tag{5.11}$$

The voltage standing wave ratio (VSWR) is

$$VSWR = \frac{1 + |\rho|^2}{1 - |\rho|^2} = \frac{1.04}{0.96} = 1.083. \tag{5.12}$$

From equations 5.11 and 5.12, we can conclude that we had a perfect match between the output of the transmitter and the transmitting antenna.

5.4.2 Path Loss Exponent Calculation

Given that received power at some distance d from the transmitter falls off as d^n past some reference distance d_o, then the received power at distance d is

$$P_r(d) = P_r(d_o) - 10\, n\ \log\,(\frac{d}{d_o}), \tag{5.13}$$

where $P_r(d)$ and $P_r(d_o)$ are in dBm, and n is the path loss exponent. For this measurement campaign the reference distance $d_o = 1$ m is chosen as it lies in the far-field of the antenna. At 1.9 GHz, a distance of 1m corresponds to a free-space path loss of 38 dB, where path loss is calculated as

$$PL_{fs} = 10\ \log\,(\frac{4\,\pi\,d}{\lambda})^2. \tag{5.14}$$

Using $P_r(d_o) = 38$ dB (from equation 5.14),

$$PL(d) = 38 + 10\, n\ \log\,(\frac{d}{1\text{ m}}). \tag{5.15}$$

Equation 5.15 is the mean path loss. Path loss is often considered to be log-normally distributed about the mean path loss. Linear regression is used to determine the best-fit line through the data points and the reference path loss represents the best estimate of n. The standard deviation σ of the measured path loss can be used in a log-normal statistical model.

5.4.3 Time Delay Spread

Wide band multipath channels are grossly quantified by their mean excess delay ($\bar{\tau}$) and their RMS delay spread (σ_τ). The former is the first moment of the power delay profile and is defined to be [17]

$$\bar{\tau} = \frac{\sum_k \alpha_k^2 \tau_k}{\sum_k \alpha_k^2}, \tag{5.16}$$

where α_k and τ_k is the amplitude and excess delay of the kth multipath component respectively. The RMS delay spread is the second central moment of the power delay profile, and is defined as

$$\sigma_\tau = \sqrt{\overline{\tau^2} - \bar{\tau}^2}, \tag{5.17}$$

where

$$\overline{\tau^2} = \frac{\sum_k \alpha_k^2 \tau_k^2}{\sum_k \alpha_k^2}, \tag{5.18}$$

and

$$\alpha_k^2 = P_{w_{ABS}}(k), \tag{5.19}$$

where k includes all data points above the established noise threshold, and $P_{w_{ABS}}(k)$ is the received power in watts at point k. The excess delay τ_k is the time difference between the data point k and the instant of the trigger pulse (reference time zero). Actually, RMS delay spread can be calculated by using any point as the reference for τ_k, and is therefore independent of the reference point.

5.5 Measurement Sites Description

Three different types of propagation environments were chosen for this study. The first is an indoor setting. The RMS delay spread for indoor locations is small when compared to that obtained in an outdoor setting. Thus, it may be feasible for DECT to operate indoors without the need for any equalizer to undo the effects of inter-symbol interference (ISI). The second location is chosen with the intention of studying the effect of having a DECT transmitter located indoors, and then moving the receiver to different outdoor locations. This type of setting would be encountered when trying to extend the range of DECT by using it as a cordless phone with extended coverage area. The third measurement location was chosen to see whether it would be possible

for DECT to operate outdoors, and the conditions under which such propagation would be feasible.

5.5.1 Indoor Propagation Measurements

The performance of DECT has been simulated extensively for indoor environments. In addition, there exists a wealth of indoor channel impulse response measurements. The objective of performing this first measurement study was to verify the validity of our measurements in comparison to earlier work.

The first measurement location was chosen inside the MPRG building, Suite 4 located at 840 University City Boulevard, Blacksburg. The floor plan for the first floor of MPRG is shown in Figure 5.4. In the floor plan, the bold lines denote walls, whereas the dashed lines are cubicle partitions which extend from the floor up to 1.7m (called soft partitions). Partitions that are part of the building structure are called hard partitions, and partitions that may be moved and which do not span to the ceiling are called soft partitions [17]. The path loss exponent for offices with hard partitions are higher than those with soft partitions [17, 49]. Both the transmitter and receiver antennas were at 1.75m above ground level. The transmitter was placed in the printer room (marked as Tx1), and the receiver was moved around the laboratory area. All channel impulse response measurements at this site were made in the late evening when there were no people around. Thereby the channel was quite static for the duration of measurements. Channel impulse response profiles were recorded along tracks labeled Paths A, B, C, and D. Profiles were recorded every 1 foot. The transmitter and receiver were kept stationary for the duration of a measurement. Path A in Figure 5.4 has no direct line–of–sight (LOS) path between the transmitter and receiver. There are a few locations along paths B, C, and D that have LOS paths to the receiver. There are a total of 83 power delay profiles recorded along these four paths.

5.5.2 Indoor to Outdoor Propagation Measurements

Since DECT and DCS-1800 are both based on the Open System Interconnect (OSI) Reference model, it is possible that with minor modification, these two standards

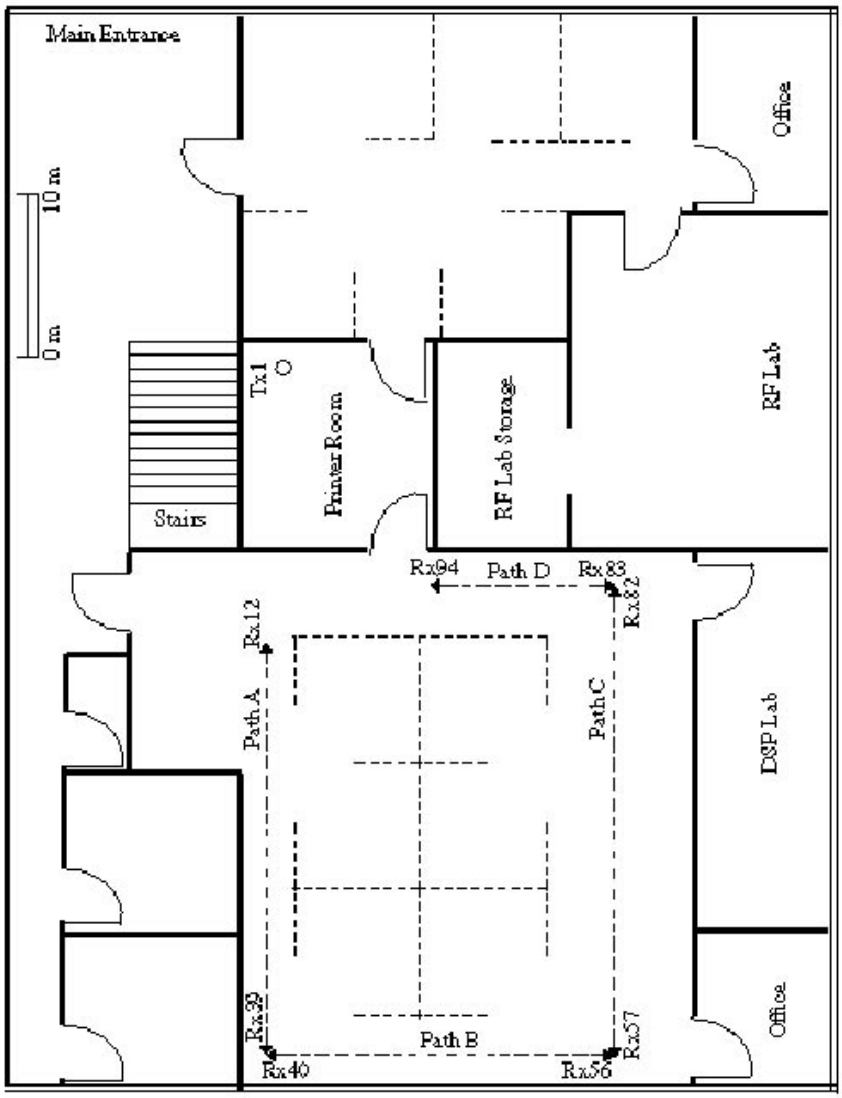

Figure 5.4: Floor plan of MPRG first floor used for indoor measurements

could be integrated into a dual-mode phone. Thus the phone could operate as a cordless telephone based on the DECT standard indoors, and then at a certain radius from the indoor office/home environment, the phone could switch to the DCS-1800 cellular telephone mode of operation. In order to understand the propagation conditions that exist in such an event, the set–up of site 2 is chosen.

For this site, the transmitter was located inside the MPRG building on the staircase at a height of 3m. A photograph of the transmitter is shown in Figure 5.6. This photograph shows the transmitter on the staircase with the antenna at a height of 3m. The transmitter and receiver carts are also shown in the picture. They are placed next to each other for calibration. The height of the receiver antenna was kept at 1.7m. The receiver was placed at locations marked Rx1 through Rx11 which are on the paved side-walk around the MPRG building. These receiver positions are separated by 3.048m (10 feet). Power delay profiles were also recorded at receiver locations Rx12 through Rx17. These receiver positions too are separated by 3.048m. In addition, measurements were made at positions Rx18, Rx19, Rx20 and Rx21, which are estimated to have larger values of RMS delay spread.

At each receiver location, four power delay profiles were recorded. This was done in order to obtain a local average power delay profile. As an example consider the measurement location marked Rx1 in Figure 5.7. The power delay profiles for this site are recorded at positions labeled 'a', 'b', 'c', and 'd'. The locations 'a' and 'c' are diagonally across and are separated by 0.3m.

Thus for this measurement site, a total of 84 power delay profiles were recorded. This is in addition to the calibration data recorded at the start and completion of impulse response measurements. Figure 5.8 is a photograph of the MPRG building. The receiver cart is at location Rx12 shown in Figure 5.5.

5.5.3 Outdoor Propagation Measurements

In order to characterize the RF channel at 1.9 GHz in an outdoor radio environment, channel impulse response measurements were recorded at site 3. The site chosen is a parking lot (with side-walks) that is enclosed by Robeson Hall, Pamplin Hall, B. J. Student Center, and Derring Hall. This is shown in Figure 5.9.

For this set of measurements, the transmitter position was kept the same at position labeled Tx3. Receiver locations are marked Rx1 through Rx14 and are placed at

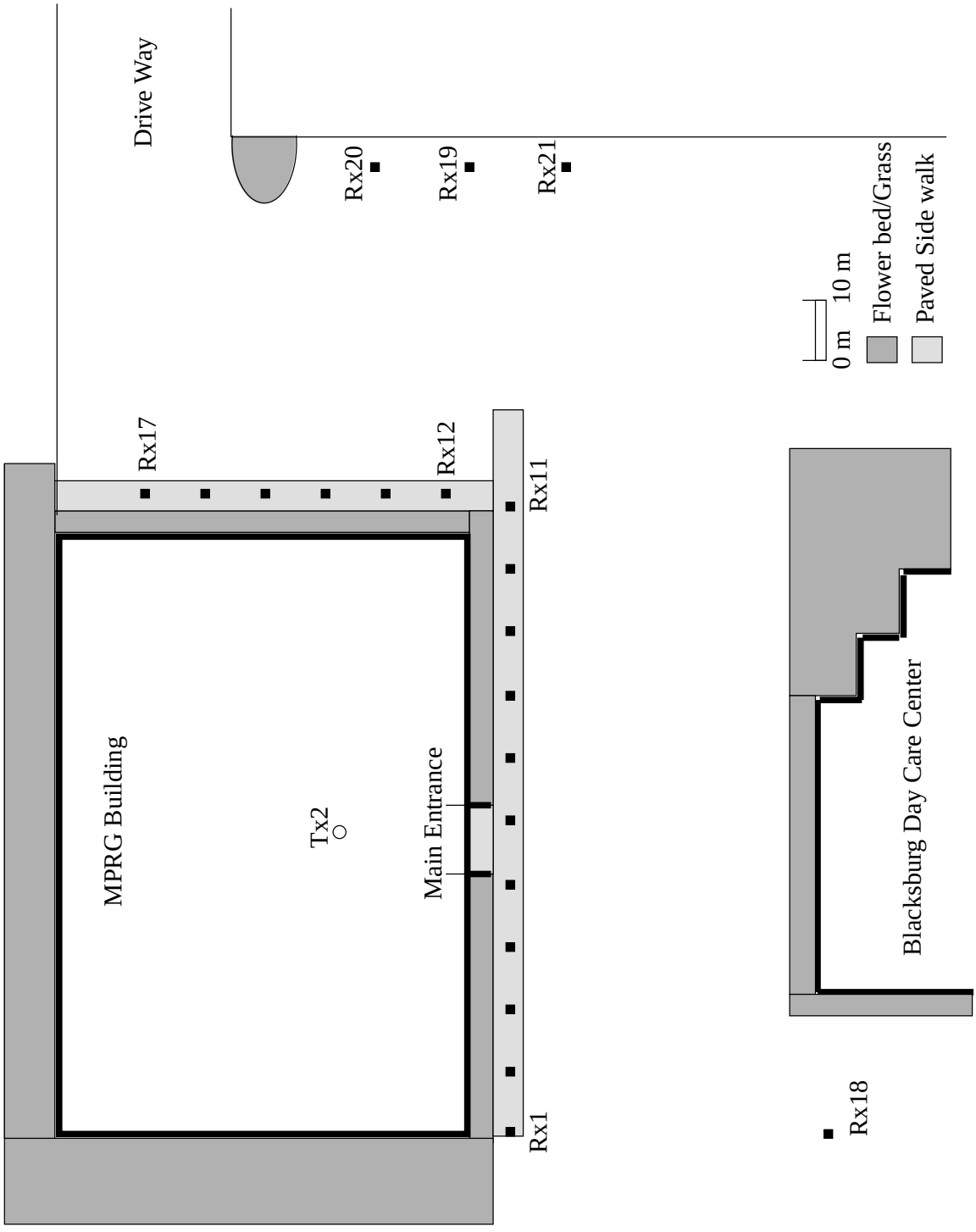

Figure 5.5: Map of MPRG and surrounding area used for indoor-to-outdoor measurements

Figure 5.6: Photograph of the transmitter for site 2

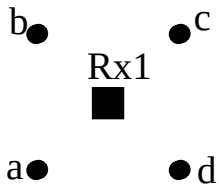

Figure 5.7: Local averaging of measurements

Figure 5.8: Photograph of the receiver at Site 2 measurement location Rx12

different position in the parking lot. When the receiver was positioned at Rx1, Rx2, Rx8, Rx9, and Rx12, there was no line-of-sight path between the transmitter and receiver. For the other locations, a LOS path was present, though in some cases it was attenuated by obstructing foliage (receiver locations Rx4, Rx5, and Rx6). Receiver locations Rx10, Rx11, and Rx12 are approximately 100m away from the transmitter and would represent the boundary of the performance of DECT.

As with measurements at site 2, four power delay profiles were recorded at each receiver location. Thus a total of 56 power delay profiles were recorded at site 3. A photograph of the transmitter set up at measurement site 3 is shown in Figure 5.10. The height of the transmitter was set at 3m.

Receiver location Rx13 is shown in Figure 5.11. As seen this site has a LOS path between the transmitter and receiver. Referring this back to Figure 5.9, the receiver is placed beside Derring Hall with the B. J. Student center in the background and Pamplin Hall on the right.

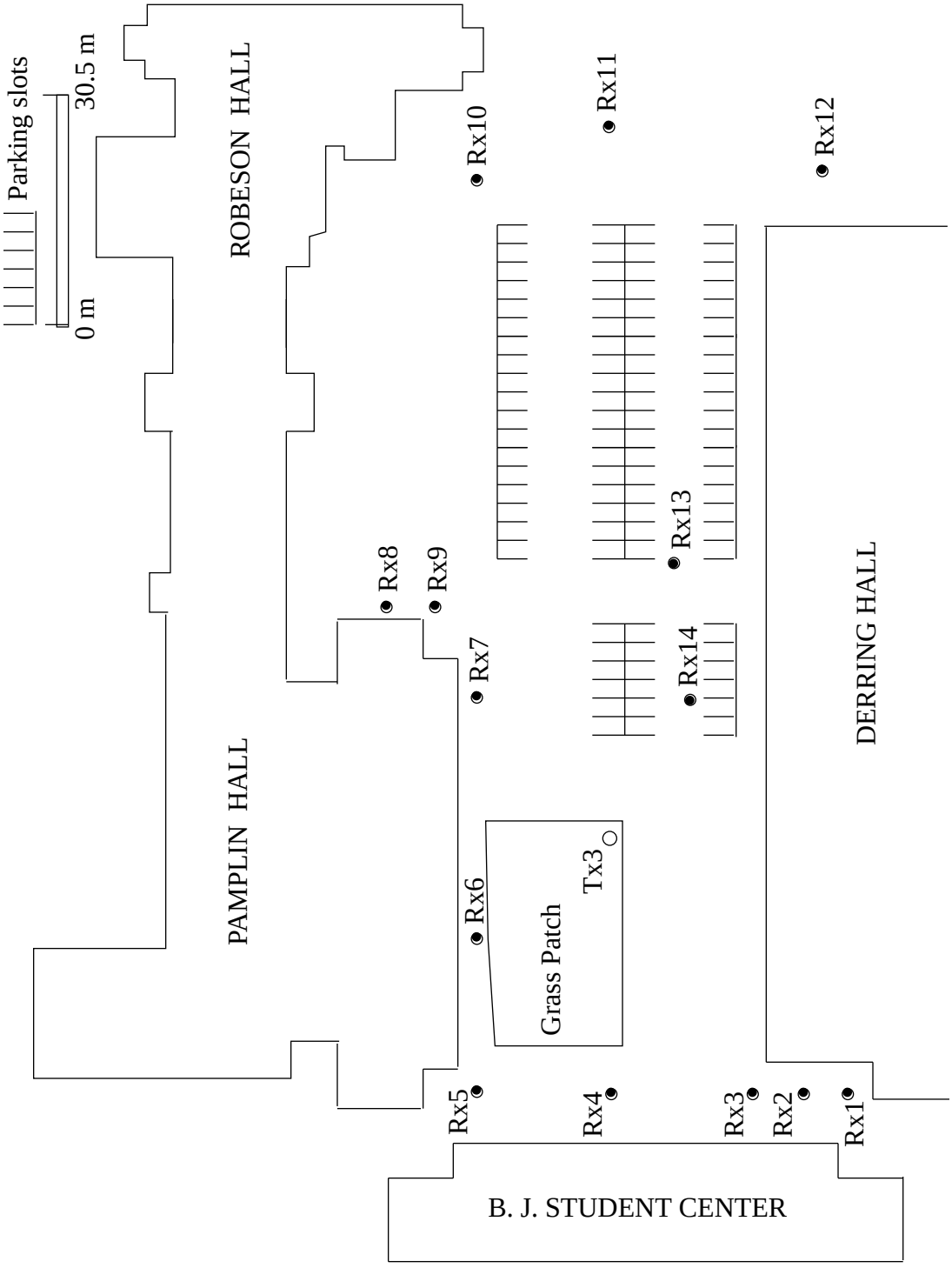

Figure 5.9: Map of site 3 outdoor measurement locations

Figure 5.10: Photograph of transmitter at Site 3

Figure 5.11: Measurement location Rx13 at Site 3

Chapter 6

Results

6.1 Introduction

This chapter summarizes the results obtained through SPW simulations, as well as the results from the measurement campaign. As mentioned in the earlier chapters, all the simulations were performed using SPW on a Sun UltraSPARC/SPARCstation 20. The results first focus on the simulated BER performance of DECT, and then on the FER in the different modeled channels.

6.2 Performance in the AWGN

The performance of DECT was simulated in an AWGN for different channel conditions. Simulations were first run without the presence of any interferer. The simulation results were then compared with theoretical results for non-coherent frequency shift keying (NFSK) and GMSK (using a limiter discrimator receiver structure). This is shown in Figure 6.1. The performance in an AWGN for a non-coherent reception of FSK is given by [17, 41]

$$P_e = \frac{1}{2}\, e^{-\frac{1}{2}\,\frac{E_b}{N_o}} \tag{6.1}$$

M. Simon and C. Wang [42] quantified the BER for differential detection of GMSK in different mobile environments. It was found that for an optimum 1 bit differential detector receiver, the BER in an AWGN traces the curve labeled as "Theoretical GMSK" in Figure 6.1. Without the presence of any cochannel or adjacent channel

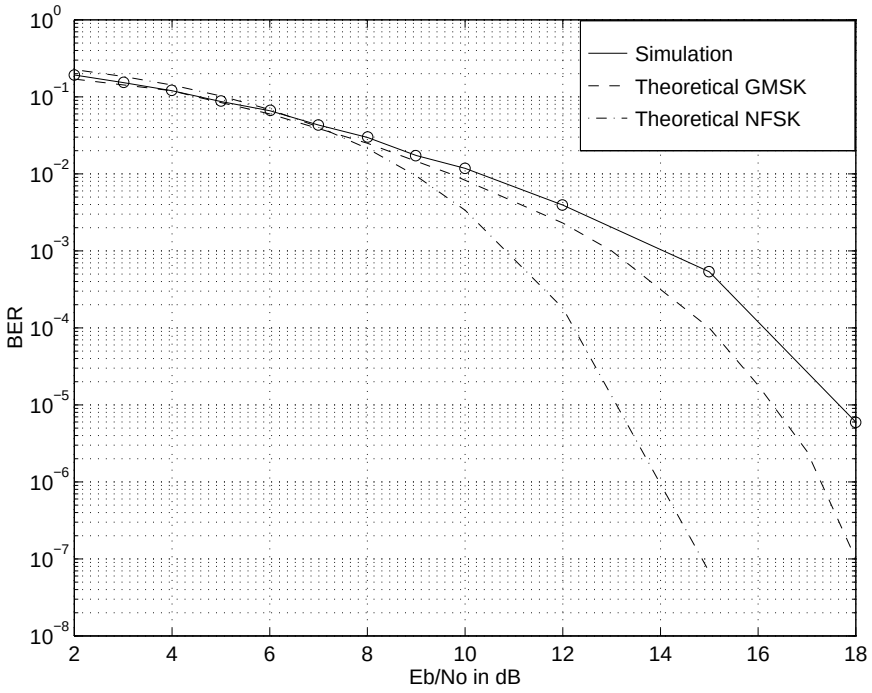

Figure 6.1: BER versus E_b/N_o in an AWGN channel

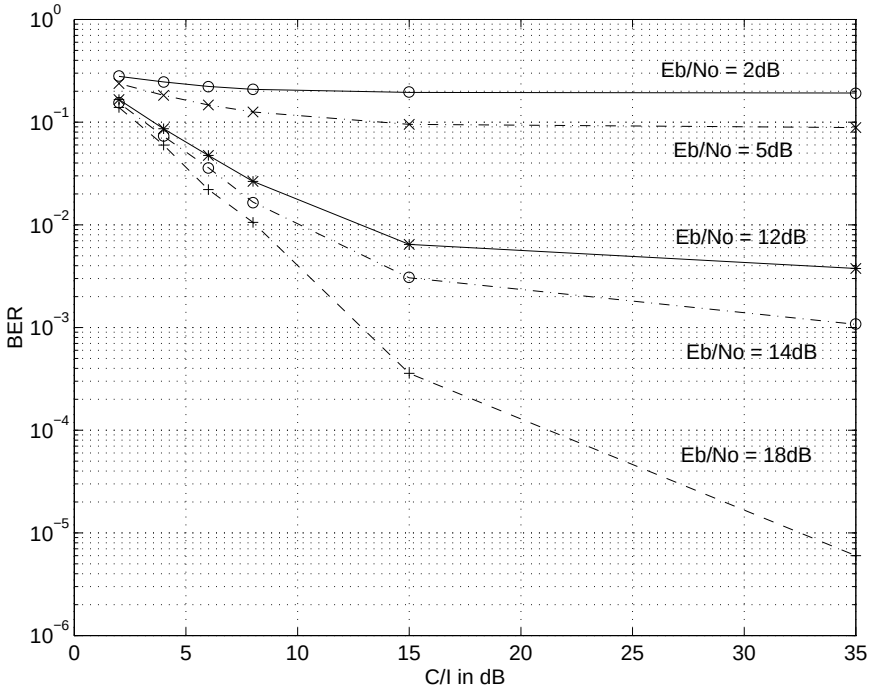

Figure 6.2: BER versus C/I in an AWGN channel for different values of E_b/N_o

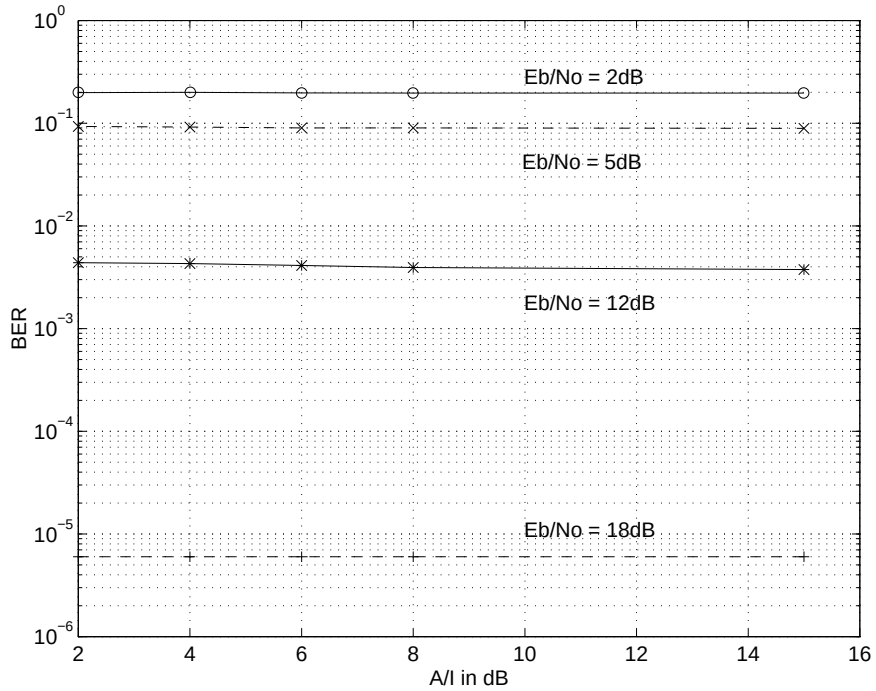

Figure 6.3: BER versus A/I in an AWGN channel for different values of E_b/N_o

interferer, as seen from Figure 6.1, for a BER of 10^{-3}, the simulated system requires an E_b/N_o of 14 dB. This result is exactly the same as that obtained by Schultes [43].

The performance curves for DECT with the added impairment of cochannel interference is given in Figure 6.2 different values of E_b/N_o. As seen from this graph, cochannel interference has a significant impact on the performance of DECT. Relatively high values of C/I ratio are required to achieve acceptable performance.

The impact of adjacent channel interference is of minimal effect. This is seen in Figure 6.3. Because the DECT standard is very robust in its ability to operate in the presence of a strong adjacent channel interferer, its performance is not modelled for other channel types.

6.3 Performance in a Flat Faded Rayleigh Channel

The performance of DECT for a flat faded Rayleigh channel corrupted by white

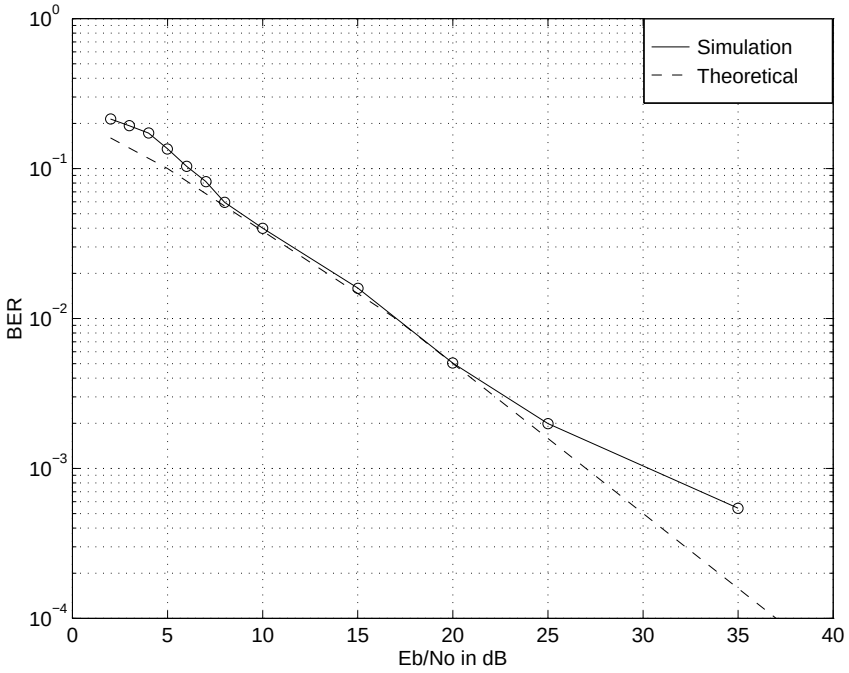

Figure 6.4: BER versus E_b/N_o in an flat faded Rayleigh channel with AWGN

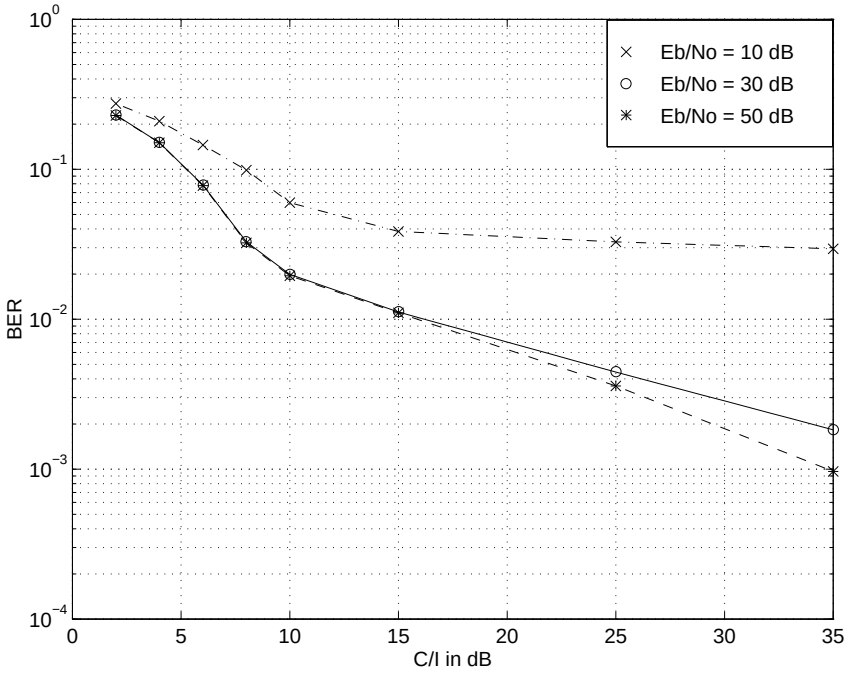

Figure 6.5: BER versus C/I in a flat faded Rayleigh channel for different values of E_b/N_o with cochannel interference and AWGN

Gaussian noise is shown in Figure 6.4. The simulations are for a walking speed of $v = 1\,\mathrm{m/s}$. The performance matches well compared to the theoretical curve [42]. From the graph, it is seen that an E_b/N_o of 30 dB is required to maintain a BER of 10^{-3}.

When cochannel interference is introduced to the flat faded Rayleigh channel, the graph of Figure 6.5 is obtained. Cochannel interference is seen to severely degrade the performance in a flat faded Rayleigh channel. For large values of C/I (above 25 dB), the there is only a marginal reduction in BER when the C/I increases. This trend is observed at high E_b/N_o ($>$ 30 dB). Thus a C/I of 25–30 dB can be considered adequate for this channel.

6.4 Performance in a Frequency Selective Rayleigh Channel

Random FM and time dispersion–caused errors generally result in irreducible errors or error floors, since they appear even in high signal-to-noise conditions. In high bit–rate systems, the irreducible error is dominated by time dispersion while random FM becomes negligible [44].

Crohn, et.al. [45], derived a first–order approximation for the average error probability in a frequency selective channel for a MSK system using 1 bit differential detector receiver under conditions of high E_b/N_o. If S is the RMS delay spread, and $T = 868\,\mathrm{ns}$ is the bit duration for DECT, then the average error probability is given by

$$P_e \cong \frac{1}{2}\,(\frac{S}{T})^2. \tag{6.2}$$

S/T is referred to as the normalized delay spread. This first order approximation is found to be valid for $S/T \leq 0.2$.

Molisch [46] calculated the BER for MSK modulation using two independently Rayleigh faded paths. It is a more accurate expression for the BER than that calculated by Crohn [45], and is given by

$$P_e \cong \frac{1}{2}\,(\frac{\pi}{4})^2\,(\frac{S}{T})^2 \tag{6.3}$$

and is valid for $S/T \leq 0.3$, and is reasonably accurate for $S/T \leq 0.6$. The results obtained in this work are in close agreement with equation 6.3. The BER

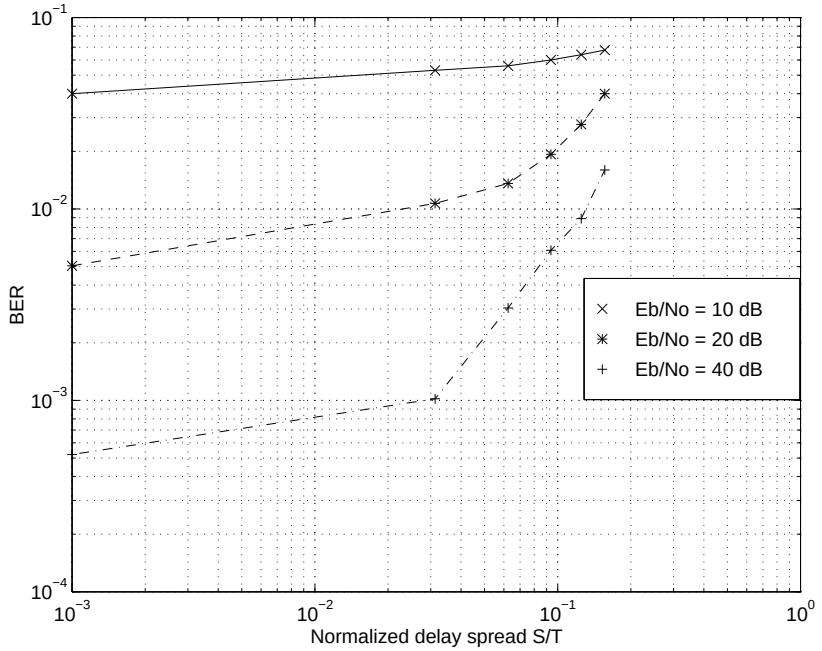

Figure 6.6: BER versus normalized RMS delay spread in an frequency selective Rayleigh channel for different values of E_b/N_o

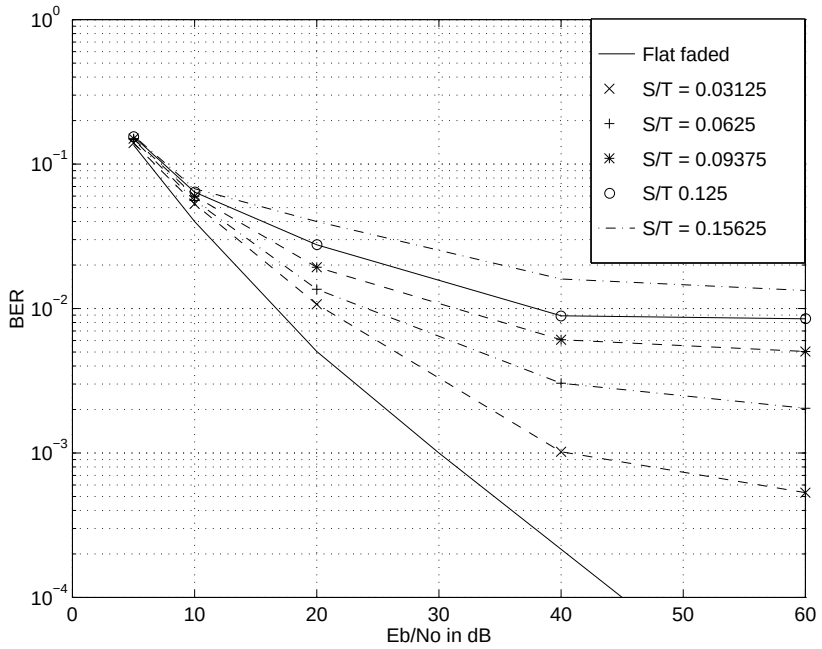

Figure 6.7: BER versus E_b/N_o in a frequency selective Rayleigh channel for different values of normalized RMS delay spread S/T

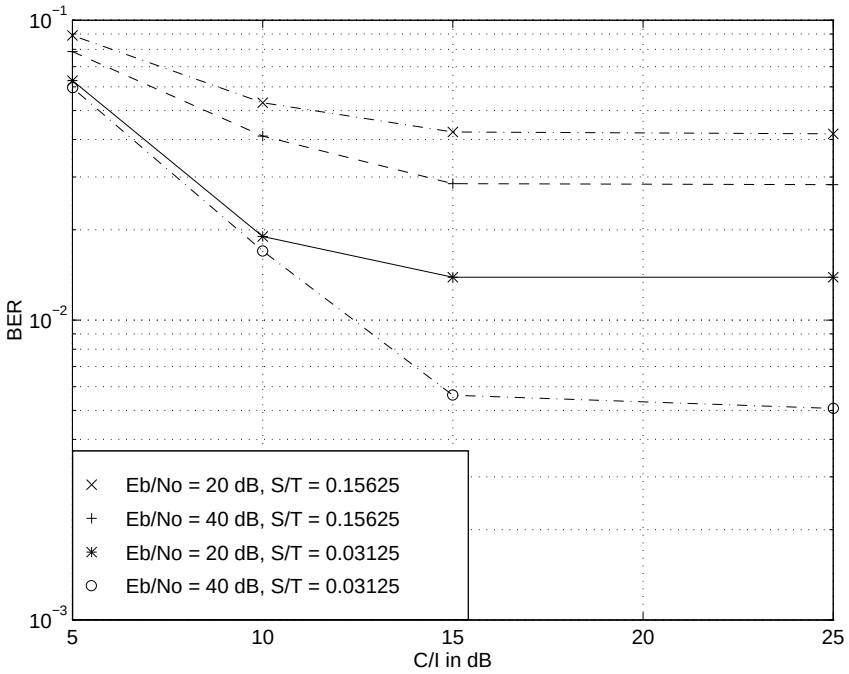

Figure 6.8: BER versus C/I in a frequency selective Rayleigh channel with cochannel interference for different values of E_b/N_o and normalized RMS delay spread

performance of DECT in a frequency selective Rayleigh faded channel as a function of the normalized RMS delay spread S/T is shown in Figure 6.6. The BER is measured under different E_b/N_o conditions. For the simulations performed, each bit was represented by 16 samples. Thus, the minimum delay spread is 1/16 the bit period. Hence, the minimum normalized RMS delay spread that could be simulated is $S/T = 0.5(1/16) = 0.03125$ [2, 26]. Since the minimum value of normalized delay spread simulated is $S/T = 0.03125$, the values of BER for delay spreads of $S/T = 0.001$ were those obtained from the Rayleight flat faded channel simulation. This would be the upper bound on performance in a frequency selective Rayleigh faded channel. Under the condition of high $E_b/N_o = 40\,\text{dB}$, an acceptable BER of 10^{-3} is achieved for a maximum normalized RMS delay spread of $S/T = 0.031$ which corresponds to a maximum tolerable RMS delay spread of 26.9 ns. Thus it is seen that DECT is highly susceptible to failure in high RMS delay spread environments. Even large values of E_b/N_o do not ensure acceptable levels of performance.

Figure 6.7 is a plot of the BER versus E_b/N_o for different values of normalized

RMS delay spread. From these simulation results, at low values of E_b/N_o, the BER is determined by the noise in the system. However, as the E_b/N_o ratio increases, the performance is now determined by the delay spread of the multipath. Finally for high E_b/N_o, the BER settles down to a value determined by the irreducible error floor of the GMSK system.

With the added impairment of cochannel interference, the BER performance curves are shown in Figure 6.8. It is seen that no further improvement in BER is achieved for $C/I > 15$ dB.

6.5 Performance in a Ricean Channel

The BER performance of DECT in a Ricean faded channel is shown in Figure 6.9. The performance curves in an AWGN channel and a flat faded Rayleigh channel are also included as a comparison. From the BER curved traced in a Ricean channel (with a Ricean factor defined in equation 4.11 of $K = 6\,\text{dB}$), it is seen that the performance of DECT is much better than in a channel that is Rayleigh flat faded in nature. The Ricean channel therefore may be viewed a transition from the AWGN channel to the Rayleigh flat faded channel. From the simulation results, an additional 2.44 dB of E_b/N_o is required over that in an AWGN channel in order to achieve the 10^{-3} acceptable BER. This however is far less than the 16 dB required to maintain the 10^{-3} in a Rayleigh flat faded channel.

Figure 6.10 is the BER curve for the Ricean faded channel. First, it is seen that for $C/I > 20\,\text{dB}$, the performance improvement is marginal. Thus, for low values of C/I, the cochannel interferer's signal level determines the BER in the system. However, at higher C/I this changes, and performance is determined by the E_b/N_o. A comparison with the performance in a flat faded Rayleigh channel clearly emphasizes the enhanced performance of DECT in the presence of a strong LOS path. For the flat faded Rayleigh channel a BER of 10^{-3} is only achieved for $E_b/N_o = 50\,\text{dB}$ and $C/I = 35\,\text{dB}$ (see Figure 6.5), whereas in the Ricean faded channel, a E_b/N_o of 20dB and a $C/I = 22\,\text{dB}$ are sufficient.

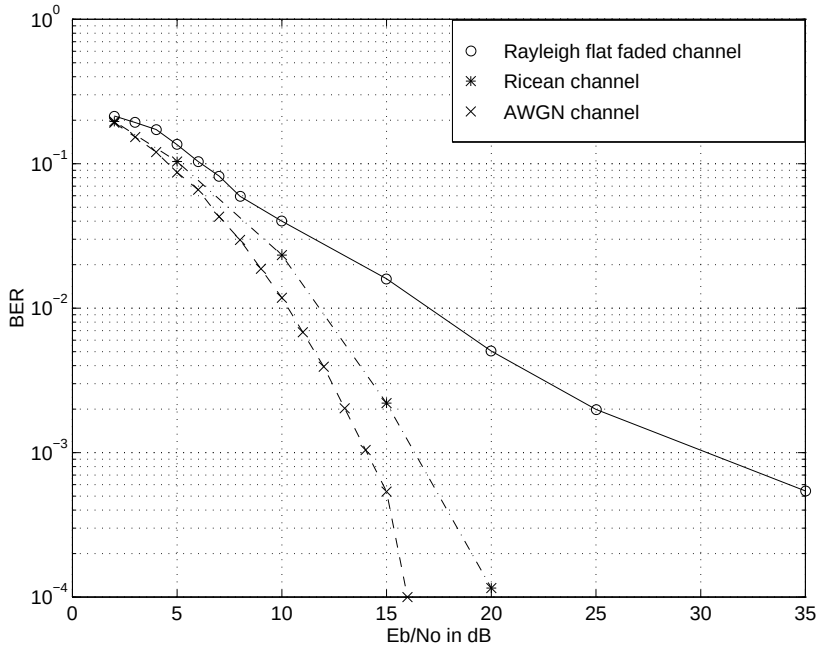

Figure 6.9: BER versus E_b/N_o in a Ricean channel corrupted by AWGN. The curves for an AWGN channel and a Rayleigh flat faded channel are included for comparison.

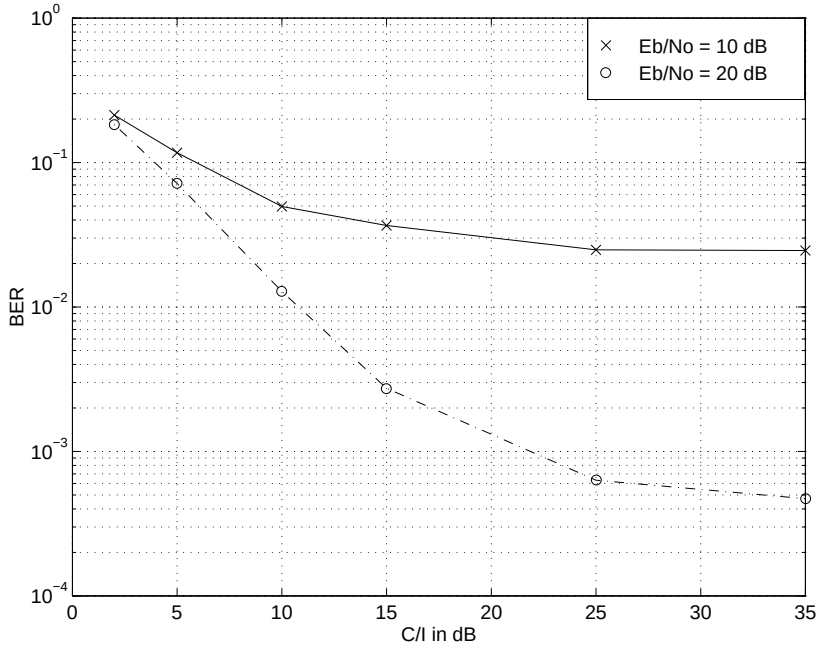

Figure 6.10: BER versus E_b/N_o in a Ricean channel corrupted by AWGN and cochannel interference

6.6 FER in the Simulated Channel Conditions

The frame–erasure–rate is another measure that is used to quantify the performance of the DECT system. While a BER of 10^{-3} is deemed acceptable voice quality, a frame erasure rate (FER) of 10^{-2} is required to maintain proper operation [2, 26]. A frame erasure occurs when there is one bit in error in the 16 bit DECT PN synchronization header pattern. The FER is defined as

$$\text{FER} = 1 - \frac{\text{Number of frames received}}{\text{Number of frames transmitted}} \tag{6.4}$$

Figure 6.11 is the simulated FER performance under all the different channel conditions. The curve for the Rayleigh frequency selective channel is for a normalized delay spread of $S/T = 0.03125$ or 27.1 ns. From this curve it is seen that an E_b/N_o of approximately 15 dB is required for FER of 10^{-2} in an AWGN channel. This requirement increases as the channel conditions deteriorate from the AWGN case to the Ricean channel, the Rayleigh flat faded channel, and finally the Rayleigh frequency selective faded channel.

Considering the frequency selective Rayleigh faded channel, the FER for different delay spreads is graphed in Figure 6.12. An E_b/N_o of 31dB is required under RMS delay spread conditions of $S/T = 0.03125$ which corresponds to a RMS delay spread of 27.1 ns.

When the FER is plotted as a function of the normalized RMS delay spread for different values of E_b/N_o, it is seen that a FER of 10^{-2} is obtained for RMS delay spreads up to 21.9 ns under $E_b/N_o = 30$ dB, and up to 47.7 ns for $E_b/N_o = 40$ dB. From Figure 6.12 and 6.13, we can conclude that relatively high E_b/N_o is required in a frequency selective Rayleigh faded channel. In Figure 6.13, the FER values for normalized RMS delay spreads of 10^{-3} are those obtained from the Rayleigh flat fading channel. This is because, the minimum S/T simulated by a Rayleigh frequency selective channel is $S/T = 0.03125$. This is derived from the sampling frequency which is 16 times the bit rate, and thus a minimum delay between the direct and delayed signal is 1/16 of a bit period. Lopes [21] and Safavi [47] had simulated the FER in a frequency selective Rayleigh channel. The results presented in these papers are in close agreement to that of Figure 6.12.

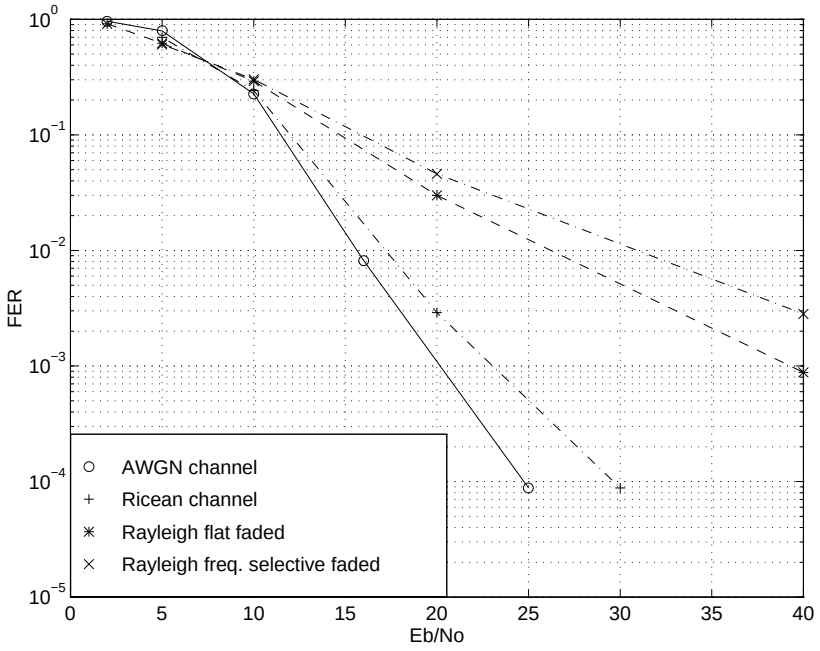

Figure 6.11: FER versus E_b/N_o under different channel conditions.

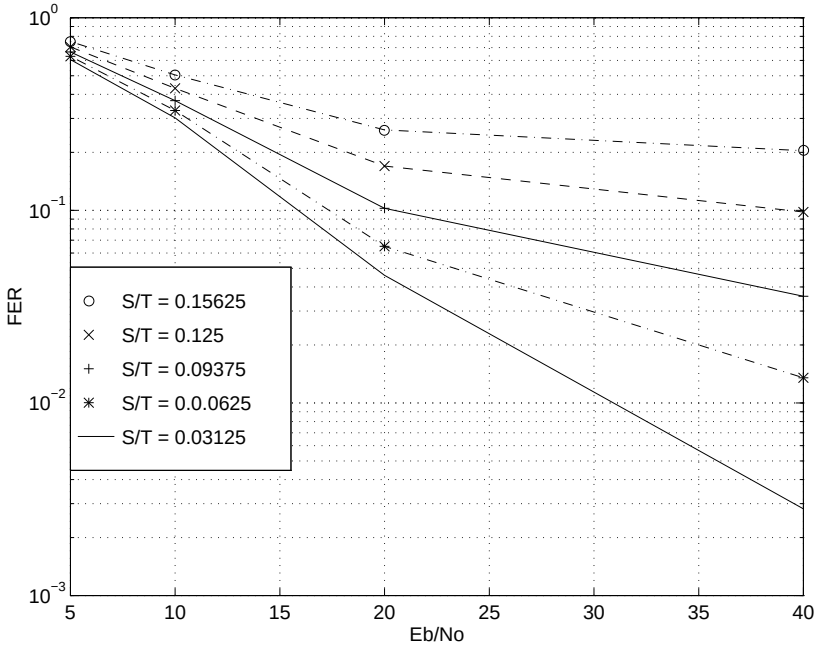

Figure 6.12: FER versus E_b/N_o in a Rayleigh frequency selective channel for different values of normalized RMS delay spread S/T

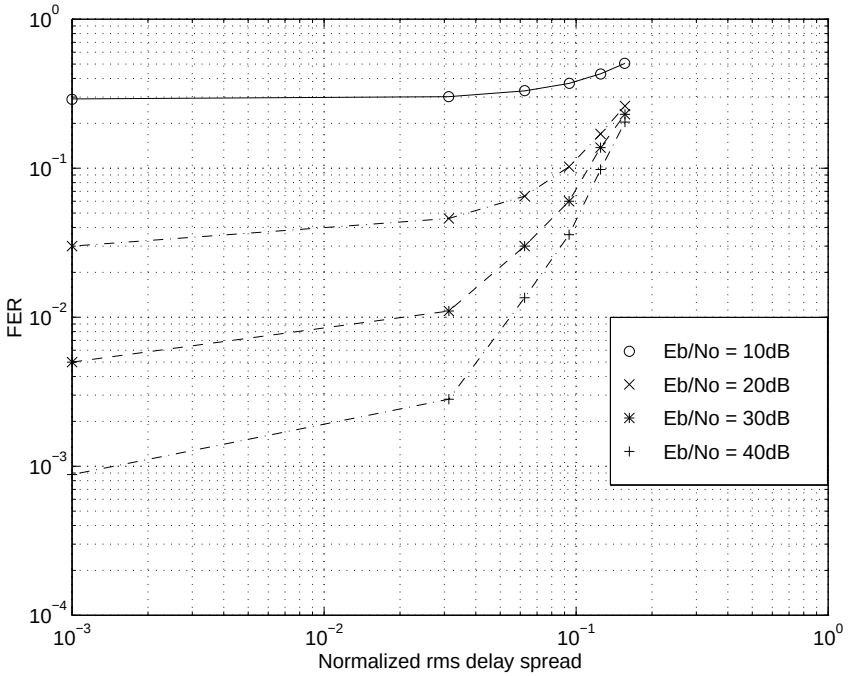

Figure 6.13: FER versus normalized RMS delay spread S/T for different E_b/N_o

6.7 Channel Impulse Response Measurement Results

The three different measurement sites were described in detail in Chapter 5. Chapter 5 also detailed the measurement system, and parameters used during the measurement campaign. In this section, the results of the channel impulse response measurements are presented. For each of the power delay profiles recorded, the received power, path loss, and RMS delay spread are calculated. Best estimates for the path loss exponent n are calculated for each site. The log-normal standard deviation (σ) was also calculated for each estimate of n. The average RMS delay spread, maximum RMS delay spread, and standard deviation of the measured RMS delay spreads are calculated for all of the sites.

The power delay profiles for the three measurement sites, and the various receiver locations are included in the Appendices. Appendix B has the power delay profiles for the channel impulse response profiles at site 1, Appendix C contains those captured at site 2, and Appendix D contains those recorded at site 3. At the top of each of

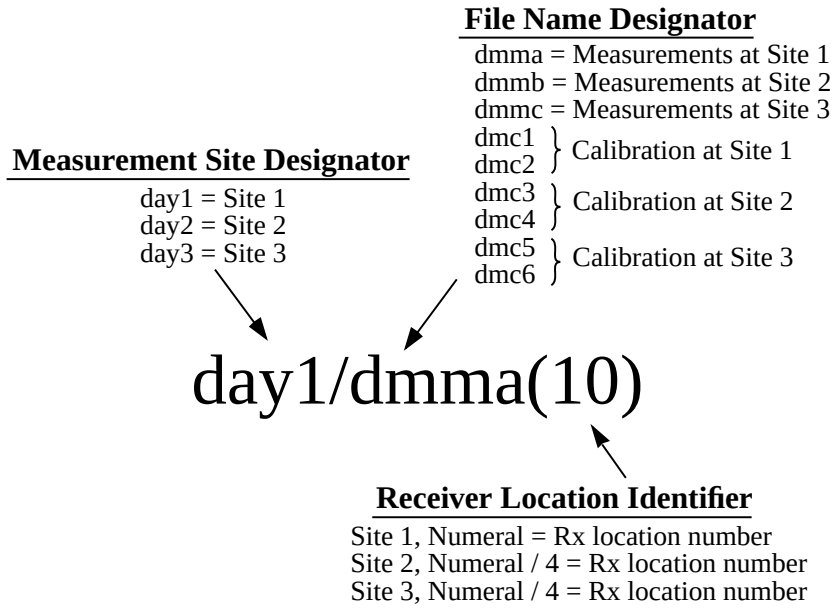

Figure 6.14: File naming convention for power delay profiles

Table 6.1: Statistical results of RF propagation measurements at 1.9 GHz

Location	n	σ (dB)	Avg. σ_τ (ns)	Max. σ_τ (ns)	Std.Dev. σ_τ (ns)	Number of measurements
Site 1	2.79	4.57	15.78	30.69	4.67	83
Site 2	3.78	6.76	46.23	111.51	22.5	84
Site 3	2.69	5.57	63.37	162.21	36.13	60

these profiles is a header which is used to index the location and site at which the profile was recording. The convention used is as shown in Figure 6.14.

Table 6.1 summarizes the results of the measurement campaign at the three different locations.

Figure 6.15 is a plot of the path loss at different receiver locations for measurements at site 1. The x-axis is the sequence number of the receiver location. For measurements at site 1 (inside the MPRG building), the path loss exponent is $n = 2.79$. This value is in the range of 2 – 3 which is a typical value found in literature [48]. Propagation measurement studies done by Anderson [49] have yielded similar results to those obtained for the indoor environment at MPRG. Howard [25] reported mean

RMS delay spreads of approximately 24 ns with a standard deviation of 5 ns, and a path loss exponent of about 2.5.

The cumulative distribution function of the RMS delay spread is shown in Figure 6.16. 50% of the locations have a delay spread of approximately 15ns and 90% have delay spreads less than 20ns. The standard deviation of the RMS delay spread is only 4.67 ns. Thus the RMS delay spread at the different receiver locations for measurements at site 1 are comparable. Relating these observed values of the RMS delay spread to the performance from simulations in the Rayleigh frequency selective channel, we conclude that DECT will operate at the acceptable level of a BER of 10^{-3} in the indoor environment (without any form of equalization of diversity implementations).

The power delay profiles for the individual measurement locations are included in Appendix B. Profiles labeled "day1/dmma(12)" through "day1/dmma(39)" are measurements made along Path A in Figure 5.4. Power delay profiles recorded along Path B are labeled as "day1/dmma(40)" to "day1/dmma(56)". Along Path C these are "day1/dmma(57)" to "day1/dmma(82)", and along Path D, "day1/dmma(83)" to "day1/dmma(94)" record the measurements. By comparing the individual power delay profiles with the receiver locations, one can gain insight into the nature of RF propagation in the indoor environment studied.

For the data obtained at site 2 (the indoor-to-outdoor radio link), the path loss at different receiver locations is shown in Figure 6.17. At each receiver location shown in Figure 5.5, four power delay profiles are recorded, and each point on the graph represents a local averaged received power. The path loss exponent for this site was found to be the highest among the three measurement sites. This is because with the exception of a couple of receiver locations, no others had a LOS path to the transmitter, and were heavily shadowed.

Figure 6.18 is a plot of the CDF of the RMS delay spread for site 2. There is an increase in the average delay spread to 46.23ns, with a maximum observed delay spread of 116.5ns. 50% of the locations have a delay spread of approximately 46 ns and 90% have delay spreads less than 70 ns. The standard deviation of the RMS delay spread is 22.5 ns. From these observed values of the RMS delay spread, we can conclude that DECT will not be able to maintain the acceptable BER of 10^{-3} or the FER of 10^{-2}, and equalization or diversity techniques would need to be incorporated

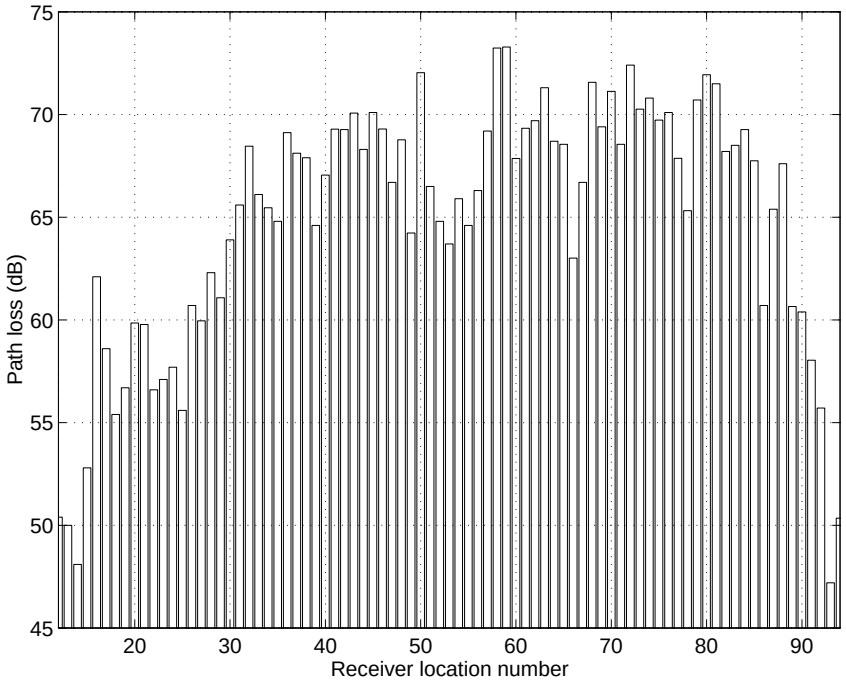

Figure 6.15: Path loss as a function of receiver location for Site 1

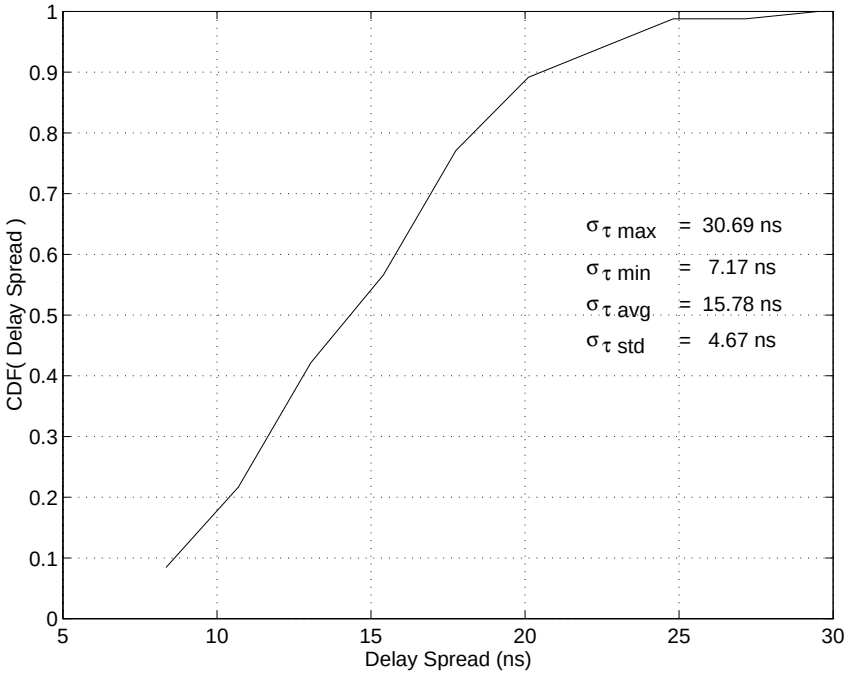

Figure 6.16: CDF of RMS delay spread for measurements at site 1

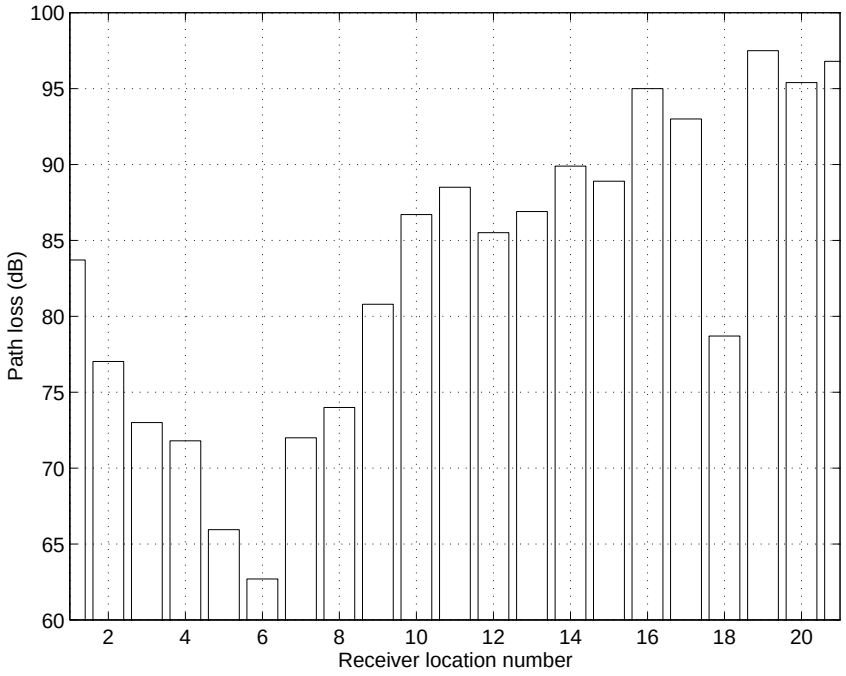

Figure 6.17: Path loss as a function of receiver location for site 2

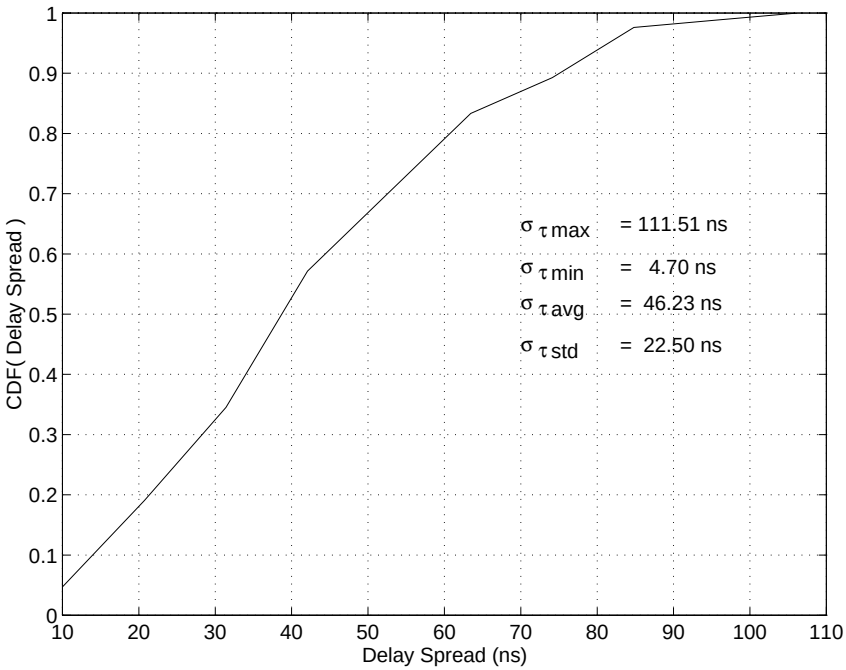

Figure 6.18: CDF of RMS delay spread for measurements at site 2

for these environments.

The power delay profiles for this site are included in Appendix C. In order to determine the receiver location number, using the convention of Figure 6.14, the receiver location number is the quotient of numeral inclosed in braces divided by four (since four power delay profiles are recorded at each location). As an example, "day2/dmmb(14)" would correspond to receiver location $14/4 = \text{Rx3}$ and this would be same for profile labeled as "day2/dmmb(12)", "day2/dmmb(13)", and "day2/dmmb(15)".

The data analysis for site 3 resulted in the path loss at the 14 measurement locations being and is shown in Figure 6.19. Very large values of path loss are observed for Rx8 (which is heavily shadowed), Rx11, and Rx12 (approximately 100m from transmitter). The path loss exponent of 2.69 is lower than typical values for an outdoors environment. However, this can be explained on the basis that the measurement locations at site 3 are enclosed by tall buildings. Kauschke [22] observed a value of $n = 1.4$ of an outdoor environment which had a canyon type setting. The maximum RMS delay spread was 162.21ns. This is at receiver location Rx8 (see power delay profile for Rx8 labeled day3/dmmc(29) through day3/dmmc(32) in Appendix D). The variance of the observed RMS delay spread is also very high. The CDF of the RMS delay spread is shown in Figure 6.20. The values of observed RMS delay spread and path loss are similar to those measured by Schaubach [50] who also recorded channel impulse response measurements at different locations on the Virginia Tech campus.

6.8 Mean–Opinion–Score (MOS) Ratings

The mean–opinion–score rating was performed in the indoor setting and the indoor-to-outdoor link at the MPRG building. A group of nine people were chosen as the test group. The average height of the group of people who evaluated the voice quality of the phones was 1.7 m. The grading of the voice quality is on a scale of 0–5. The lower limit of 0 represents the inability of the DECT system to establish a call. A score of 5 would represent voice quality which is obtained when using a land-line telephone system.

For site 1, shown in Figure 5.4, the DECT radio-fixed-part (RFP) or base station, was placed at Tx1. Four locations were chosen along Path A spaced 1.8 m apart.

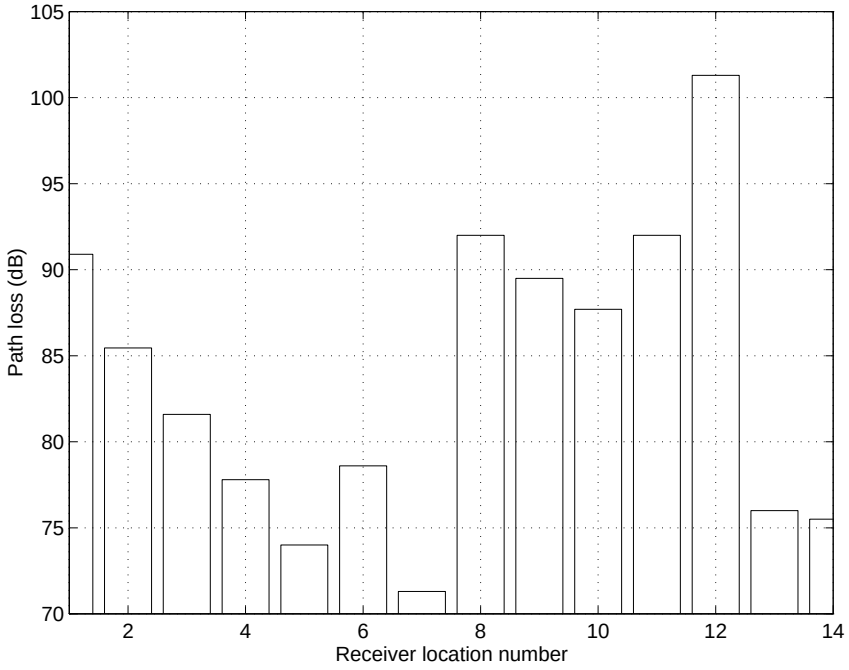

Figure 6.19: Path loss as a function of receiver location for site 3

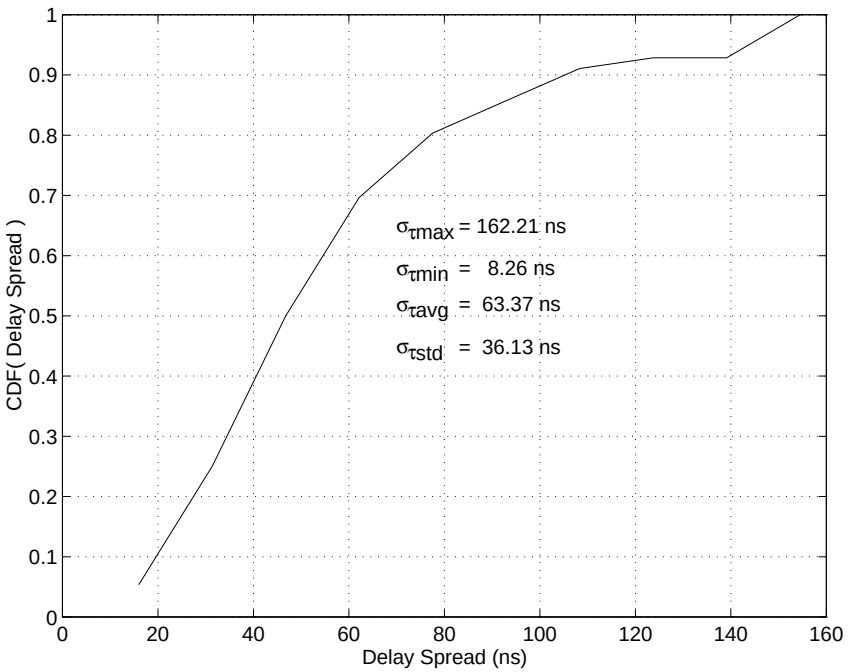

Figure 6.20: CDF of RMS delay spread for measurements at site 3

Table 6.2: MOS results of Site 1.

Location	Number of users	MOS	Variance(MOS)	RMS Delay Spread (ns)	Path Loss (dB)
A1	9	4.7	0.20	12.24	50.37
A2	9	4.7	0.20	12.89	55.44
A3	9	4.4	0.53	15.36	60.66
A4	9	4.4	0.49	17.34	68.12
B1	9	4.0	0.57	19.27	69.29
B2	9	4.1	0.69	15.70	70.11
B3	9	4.1	0.57	10.36	64.89
B4	9	4.0	0.28	13.78	65.90
B5	9	4.3	0.49	12.90	66.30
C1	9	4.3	0.49	17.74	69.24
C2	9	4.3	0.20	15.39	69.33
C3	9	4.4	0.49	15.42	68.55
C4	9	4.4	0.25	19.49	69.38
C5	9	4.7	0.20	18.74	70.26
C6	9	4.6	0.25	17.36	67.87
C7	9	4.6	0.25	25.71	71.50
D1	9	4.6	0.25	22.44	68.50
D2	9	4.6	0.25	23.33	67.75
D3	9	4.7	0.20	14.66	65.39
D4	9	4.9	0.12	11.89	60.39
D5	9	4.9	0.12	7.17	47.21

Along Path B, five receiver locations spaced 1.2 m apart, and along Path C, the seven locations have a separation of 1 m between them. Finally, along Path D, the five receiver locations are 0.6 m apart.

The results of the MOS test are given in Table 6.2. The receiver locations are labeled A1–A4, B1–B5, C1–C7, and D1–D5 respectively. The variance of the MOS at each location is also included in Table 6.2. The average MOS for all the indoor locations is 4.5. From these results, it is evident that DECT performs very well in the indoor environment under study. The call quality was poorest along Path B where the average MOS was 4.05. Along this path, the separation between the transmitter and receiver was greatest, as well as there being no line-of-sight path for most of the test group at these locations. There is a close agreement between the MOS results and

the value of RMS delay spread recorded at the particular receiver location. Although the RMS delay spread at receiver locations C1–C5 is high, these locations have a LOS path between the base station and handset and are therefore seen to be more tolerant to the multipath environment.

In order to study the effect of a cochannel interferer on the voice quality, MOS tests were performed for varying levels of C/I. A cochannel interfering signal is simulated by generating an FM signal with a frequency deviation of 288 kHz, and the rate of FM deviation is 1 MHz. The center frequency of the FM interfering signal was kept the same as the carrier frequency of the DECT transmission. The transmitting antenna for the cochannel interference is place immediately below the DECT base station antenna.

The results of the MOS for different C/I are summarized in Table 6.3.

Figure 6.21 is a graph of the average MOS results for the indoor locations as a function of the C/I ratio. From this graph it is seen that a C/I of approximately 32 dB is required for an MOS of 4.0. The MOS drops off rapidly for lower values of C/I. For C/I of about 24 dB, the ability for DECT to maintain a call depends on the person using the phone and the location of measurement. For people who are taller than the height of the soft-partition (such that a line-of-sight path exists between the base station and handset) a call would be established with very low voice quality. At those same locations shorter people could not receive the call.

For the indoor-to-outdoor radio link performance evaluation, the same receiver locations were chosen as shown in Figure 5.5. The DECT RFP was placed on the stairwell at a height of 3 m.

The results of the MOS test for site 2 are given in Table 6.4. Receiver locations Rx5 and Rx6 are seen to have the best reception. These locations are on the sidewalk approximately 9m in front of the transmitter, and since the main entrance to the MPRG building is glass paneled, there is very little signal attenuation for the line-of-sight path between the base station and cordless phone handset. Subsequently, these receiver locations obtained the highest score on the test of 4.7. As the receiver locations moved away from the doorway – either decreasing towards Rx1 or increasing towards Rx11, the RMS delay spread, and path loss increases and the reception deteriorates rapidly in quality. After about 9m the voice quality is incoherent, and the call breaks up. Further, there is no reception at receiver locations Rx10 through

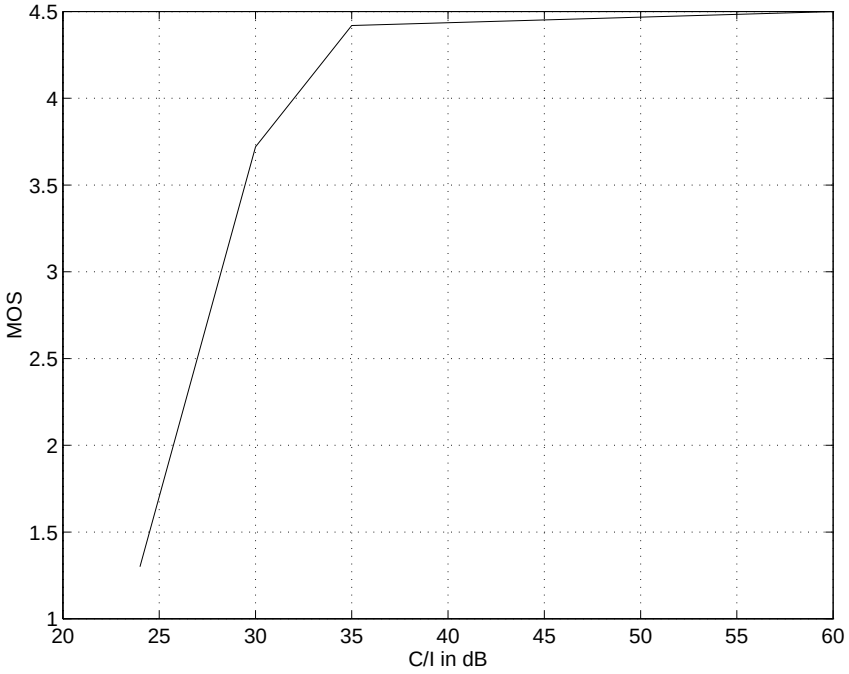

Figure 6.21: MOS as a function of C/I at site 1

Rx21. From these MOS results at site 2, for acceptable voice quality a maximum path loss of approximately 70 dB is tolerable. It is also seen that RMS delay spreads in excess of 35 ns cause severe degradation in telephone call voice quality.

MOS tests are not performed at site 3 because NSC's DECT implementation requires an analog telephone line whereas the telephone network at Virginia Tech is digital.

Table 6.3: MOS results of Site 1 with cochannel interference.

Location	Number of users	MOS for C/I level of			
		∞dB	35 dB	30 dB	24 dB
A1	9	4.7	4.7	4.1	2.1
A2	9	4.7	4.7	4.1	2.2
A3	9	4.4	4.4	4.0	1.7
A4	9	4.4	4.4	4.0	1.3
B1	9	4.0	4.0	3.3	1.0
B2	9	4.1	4.0	3.2	0.0
B3	9	4.1	4.0	3.2	0.0
B4	9	4.0	4.0	3.1	0.6
B5	9	4.3	4.2	3.2	0.9
C1	9	4.3	4.3	3.5	1.0
C2	9	4.3	4.3	3.6	1.0
C3	9	4.4	4.4	3.7	1.0
C4	9	4.4	4.4	3.7	1.1
C5	9	4.7	4.5	3.7	1.1
C6	9	4.6	4.6	3.8	1.3
C7	9	4.6	4.5	3.8	1.3
D1	9	4.6	4.5	4.0	1.3
D2	9	4.6	4.5	4.0	1.8
D3	9	4.7	4.7	4.0	2.1
D4	9	4.9	4.8	4.0	2.1
D5	9	4.9	4.9	4.2	2.5
Average		4.5	4.42	3.72	1.3

Table 6.4: MOS results of Site 2.

Location	Number of users	MOS	Variance(MOS)	RMS Delay Spread (ns)	Path Loss (dB)
Rx1	9	0.6	0.53	43.73	83.71
Rx2	9	2.3	2.49	25.45	77.03
Rx3	9	3.4	1.39	35.54	73.06
Rx4	9	4.1	0.98	33.46	71.83
Rx5	9	4.7	0.20	53.64	65.95
Rx6	9	4.7	0.49	24.46	62.68
Rx7	9	4.0	0.57	31.05	71.98
Rx8	9	3.3	0.98	29.79	74.21
Rx9	9	1.1	2.41	38.15	80.77
Rx10	9	0.0	0.00	52.65	86.65
Rx11	9	0.0	0.00	41.85	88.45
Rx12	9	0.0	0.00	47.65	85.51
Rx13	9	0.0	0.00	56.81	86.92
Rx14	9	0.0	0.00	47.05	89.93
Rx15	9	0.0	0.00	40.72	88.87
Rx16	9	0.0	0.00	68.75	94.96
Rx17	9	0.0	0.00	75.75	93.08
Rx18	9	0.0	0.00	20.78	78.74
Rx19	9	0.0	0.00	72.48	97.55
Rx20	9	0.0	0.00	68.26	95.41
Rx21	9	0.0	0.00	71.43	96.79

Chapter 7

Conclusions and Future Directions

This chapter presents a summary of the research performed for this thesis. A review of the results presented in Chapter 6 is also presented. Topics for future areas of research are suggested in this chapter.

7.1 Summary of Research

From the simulations performed for DECT, it is seen that an E_b/N_o of approximately 14 dB is required for BER of 10^{-3} in an AWGN channel. This requirement increases as cochannel interference is introduced. The effect of adjacent channel interference appears to be quite minimal. For an $E_b/N_o = 12$ dB, the BER improves from 4.38×10^{-3} to 3.75×10^{-3} as the carrier to adjacent channel interference ratio increases from 2 dB to 15 dB.

The performance degrades in a Rayleigh flat faded channel and the Rayleigh frequency selective channel. In the Rayleigh frequency selective channel, as the normalized RMS delay spread increases, the BER becomes unacceptably high. Under the condition of high $E_b/N_o = 40$ dB, an acceptable BER of 10^{-3} is achieved for a maximum RMS delay spread of 26.9 ns. The addition of cochannel interference results in even more degradation of the BER tolerance. For an $E_b/N_o = 40$ dB, the BER $= 10^{-3}$ without cochannel interference, and this reduces to a BER $= 1.7 \times 10^{-3}$ when $C/I = 10$ dB.

The Ricean channel was used to model propagation conditions wherein there exists a strong line-of-sight path between the transmitter and receiver. The degradation for

a typical Ricean channel appears to be less severe than for a typical Rayleigh flat fading channel and a typical Rayleigh frequency selective fading channel.

FER simulations performed under different channel conditions followed the same trends as for the BER analysis. The FER criterion for acceptable performance is 10^{-2}, and the minimum E_b/N_o for an AWGN channel is found to be 15.5 dB. The FER in a Rayleigh frequency selective channel for different values of RMS delay spreads, and different E_b/N_o values is also simulated. An E_b/N_o of 31 dB is required for a FER of 10^{-2} in a channel with an RMS delay spread of 27.1 ns.

The channel impulse response measurements provide insights in to the nature of the RF channel at 1.88–1.9GHz. For the indoor propagation environment, the path loss exponent is calculated to be 2.79, and the standard deviation (σ) for the log-normal shadowing model is 4.57 dB. RMS delay spreads in the channel are small for the indoor environment (site 1), the average being 15.78 ns.

For the indoor-to-outdoor radio link (site 2), the path loss exponent is 3.78. This is higher than the indoor environment because the majority of receiver locations are shadowed. The standard deviation (σ) for the log-normal shadowing model is 6.76 dB. For site 2, the average RMS delay spread is 46.23 ns.

For measurements made at site 3 on campus, the path loss exponent is 2.69. Large values of RMS delay spread are observed for receiver locations on campus. The average RMS delay spread at site 3 is 63.37 ns with a maximum value of 162.21 ns recorded at a shadowed receiver location.

Mean-opinion-score ratings taken for the indoor and indoor-to-outdoor link affirmed that DECT performs well in the interference free indoor setting. As the cochannel interference level increases, the call quality reduces rapidly and becomes incoherent. It is also observed that the voice quality drops rapidly as one moves away from the base station on the indoor-to-outdoor measurement locations. The performance of DECT qualified by the MOS results correspond well to those derived based on the values of RMS delay spread recorded at the different receiver locations using the channel sounder. The key results are summarized in Table 7.1. Criterion for acceptable performance are a BER of 10^{-3} and a FER of 10^{-2}.

In conclusion from the simulation results and measurements, it is seen that a LOS path between the base station and handset improves the performance of DECT especially when there exists cochannel interference. It is hence prudent to choose

Table 7.1: Summary of threshold conditions for DECT

Channel Condition	Parameter value
AWGN channel	$E_b/N_o = 15.5\,\text{dB}$
Rayleigh flat faded channel Doppler frequency $f_d = 8.7\text{Hz}$	$E_b/N_o = 30\,\text{dB}$
Rayleigh frequency selective channel for $\sigma_\tau = 26.9\text{ns}$, $f_d = 8.7\,\text{Hz}$	$E_b/N_o = 40\,\text{dB}$
Ricean channel for Ricean factor $K = 6\,\text{dB}$, $f_d = 8.7\,\text{Hz}$	$E_b/N_o = 17.2\,\text{dB}$
AWGN channel with $E_b/N_o = 18\,\text{dB}$	$C/I = 12.7\,\text{dB}$
Rayleigh flat faded channel with $E_b/N_o = 50\,\text{dB}$, $f_d = 8.7\,\text{Hz}$	$C/I = 35\,\text{dB}$
Ricean channel for $K = 6\,\text{dB}$, $E_b/N_o = 20\,\text{dB}$, and $f_d = 8.7\,\text{Hz}$	$C/I = 21.8\,\text{dB}$

locations for base stations such that there are LOS paths for most of the conceivable receiver locations. For the wireless private exchange (WPBX) office application, by locating the base station near the ceiling of the room and maintaining a handset and battery charging unit (with minimal functionality) at each desk, performance improvements can be realized.

7.2 Future Work

Research has been done to investigate the performance and feasibility of DECT in Radio Local Loop (RLL) and Wireless Local Area Network (WLAN) type applications [5, 8, 51, 52]. These earlier publications investigated issues like PCS implementations, WLL network connectivity and other related problems. The work in this thesis when combined with the higher level networking functions of the Open System Interconnect (OSI) protocol could lay the foundation for deployment strategies of such systems.

Possible future directions include the study of the integration of DECT and PCS–1900 to provide PCS services in the recently auctioned PCS band in the USA. For DECT to combat the problem of RMS delay spread in outdoor environments it is imperative that cheap and efficient equalizer structures be incorporated into the system. This could provide a stepping stone towards increasing the range of DECT thereby

making it better suited for the WLL. Mogensen [51, 53] considered antenna diversity techniques to improve the performance of DECT in indoor and micro-cellular applications. Similar work was also performed by Safavi et. al. [47]. Wigard [54] considered optimum diversity combining as a solution to the problem of large RMS delay spreads. Based on these and other related studies, a suitable technique to mitigate the effects of RMS delay spread must be implemented for DECT to be a viable choice for WLL applications.

Appendix A

SPW Parameters for DECT System Models

This Appendix lists the default and editable parameters for the models used in the simulation of the DECT system. These parameters are in addition to the ones of primary importance given in Chapter 3.

A.1 System Executive – Transmit Path

The sampling rate used throughout the simulations was 18432000.0 Hz. The other default parameters for the system executive operating in the transmit mode are listed below.

	Default Parameter Value
1. Bit Count	1
2. Frame Count	1000
3. Frame Counter	1
4. Total number of bits	480
5. Initial1	0
6. Start of header detection	0
7. Threshold	16
8. Flag for transmit or receive	1
9. Flag for full or half rate	0
10. Seed for PN data	105

11. Counter1	1
12. Counter2	1
13. Counter3	1
14. Header Data File	'/home/u5/kevin/alatadata/caedata/kevin/header.dat'
15. Delay Line File	'/home/u5/kevin/alatadata/caedata/kevin/delay.dat'
16. Data File	'/home/u5/kevin/alatadata/caedata/kevin/data.dat'

Editable Parameters

1. Frame Count
2. Total number of bits
3. Number of bits/frame
4. Length of synchronization sequence
5. Flag for full or half rate
6. Header Data File
7. Delay Line File
8. Data File

A.2 LMX2411 Baseband Processor – Transmit Path

The LMX2411 uses a sixteenth order filter to perform the complex Gaussian pulse shaping. A scaling factor of 0.25 is used to limit the frequency deviation of the GMSK signal to 288 kHz.

Default Parameter Value

1. Filter order	16
2. Scaling factor	0.25
3. Number of bits used in quantization	8
4. Order of the smoothing IIR filter	1

Editable Parameters

1. Order of the complex Gaussian filter
2. Scale factor

3. Number of bits used in quantization
4. Order of the smoothing IIR filter

A.3 LMX2316 – Frequency Synthesizer

The IF at which the DECT simulations are carried out is 2.304 MHz. This frequency is an editable parameter and can be changed by increasing or decreasing the value of the tuning voltage.

Default Parameter Value

1. Sampling frequency	18432000 Hz
2. Value of tuning voltage	2 volts

Editable Parameters

1. Sampling frequency
2. Value of tuning voltage

A.4 IF Filter

The IF filter at the receiver is a sixteenth order FIR filter. SPW accepts the filter coefficients from a data file. The filter order and coefficients are editable parameters.

Default Parameter Value

1. Sampling frequency	18432000 Hz
2. Filter order	16
3. Data file name	'home/u5/kevin/altadata/caedata/kevin/if_filter_ber.ascfilt'

Editable Parameters

1. Sampling frequency
2. Filter order
3. Data file name

A.5 LMX2240 – IF Limiter Discriminator

The tank circuit filter is an eighth order FIR filter. The Hilbert transform filter is used to obtain a fixed 90^o phase shift.

Default Parameter Value

1. Sampling frequency	18432000 Hz
2. Tank filter order	8
3. Data file name	'home/u5/kevin/altadata/caedata/kevin/tank_ber.ascfilt'
4. Order of the Hilbert transform	32

Editable Parameters

1. Sampling frequency
2. Center frequency of filter
3. Tank filter bandwidth
4. Tank Filter order
5. Data file name
6. Order of the Hilbert transform

A.6 System Executive – Receive Path

The default parameter values for the system executive on the receive path are given below. The BER is stored to a file labelled "BER.dat".

Default Parameter Value

1. Bit Count	1
2. Frame Count	1000
3. Frame Counter	1
4. Total number of bits	480
5. Initial1	0
6. Start of header detection	0
7. Threshold	16
8. Flag for transmit or receive	1
9. Flag for full or half rate	0
10. Seed for PN data	105

11. Counter1	1
12. Counter2	1
13. Counter3	1
14. Header Data File	'/home/u5/kevin/alatadata/caedata/kevin/header.dat'
15. Delay Line File	'/home/u5/kevin/alatadata/caedata/kevin/delay.dat'
16. Data File	'/home/u5/kevin/alatadata/caedata/kevin/data.dat'

Editable Parameters

1. Frame Count
2. Total number of bits
3. Number of bits/frame
4. Length of synchronization sequence
5. Flag for full or half rate
6. Header Data File
7. Delay Line File
8. Data File

Appendix B

Power Delay Profiles at Measurement Site 1

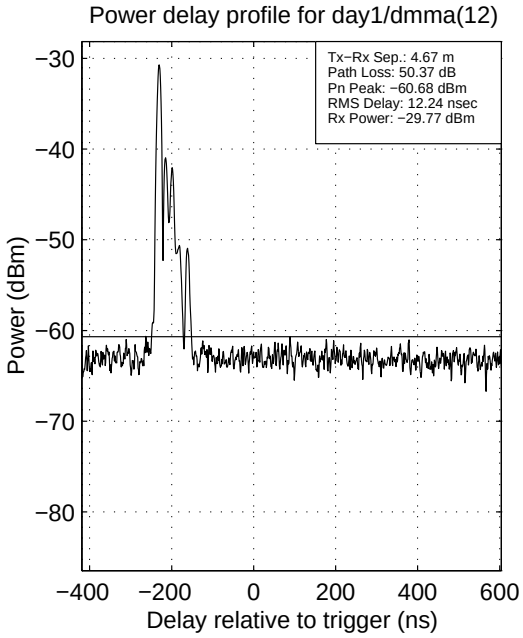
Power delay profile for day1/dmma(12)
Tx−Rx Sep.: 4.67 m
Path Loss: 50.37 dB
Pn Peak: −60.68 dBm
RMS Delay: 12.24 nsec
Rx Power: −29.77 dBm
Power (dBm)
−30
−40
−50
−60
−70
−80
−400
−200
0
200
400
600
Delay relative to trigger (ns)

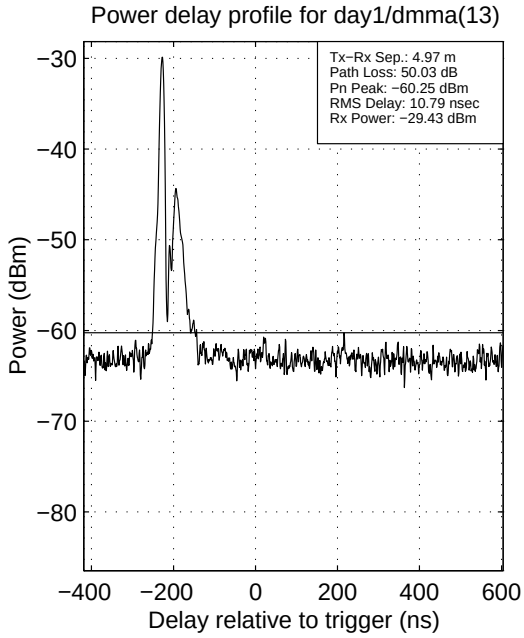
Power delay profile for day1/dmma(13)
Tx−Rx Sep.: 4.97 m
Path Loss: 50.03 dB
Pn Peak: −60.25 dBm
RMS Delay: 10.79 nsec
Rx Power: −29.43 dBm
Power (dBm)
−30
−40
−50
−60
−70
−80
−400
−200
0
200
400
600
Delay relative to trigger (ns)

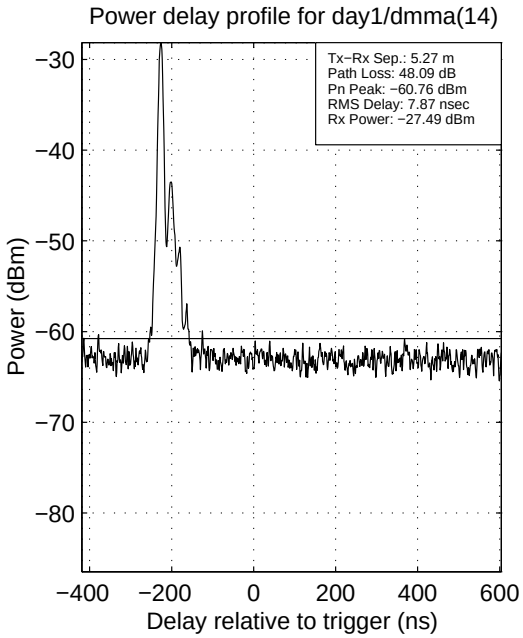
Power delay profile for day1/dmma(14)
Tx−Rx Sep.: 5.27 m
Path Loss: 48.09 dB
Pn Peak: −60.76 dBm
RMS Delay: 7.87 nsec
Rx Power: −27.49 dBm
Power (dBm)
−30
−40
−50
−60
−70
−80
−400
−200
0
200
400
600
Delay relative to trigger (ns)

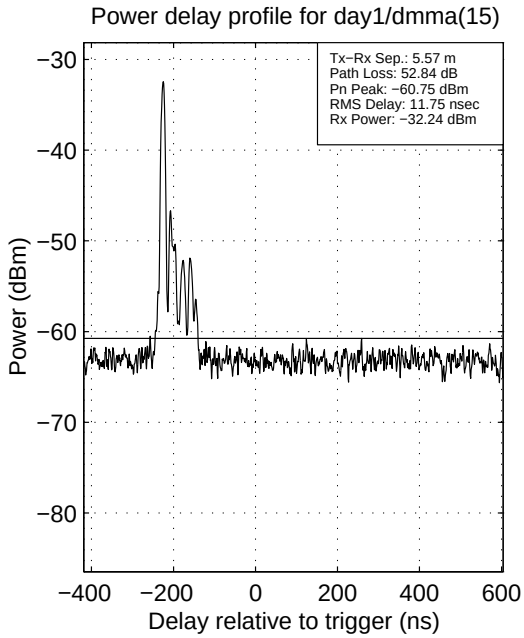
Power delay profile for day1/dmma(15)
Tx−Rx Sep.: 5.57 m
Path Loss: 52.84 dB
Pn Peak: −60.75 dBm
RMS Delay: 11.75 nsec
Rx Power: −32.24 dBm
Power (dBm)
−30
−40
−50
−60
−70
−80
−400
−200
0
200
400
600
Delay relative to trigger (ns)

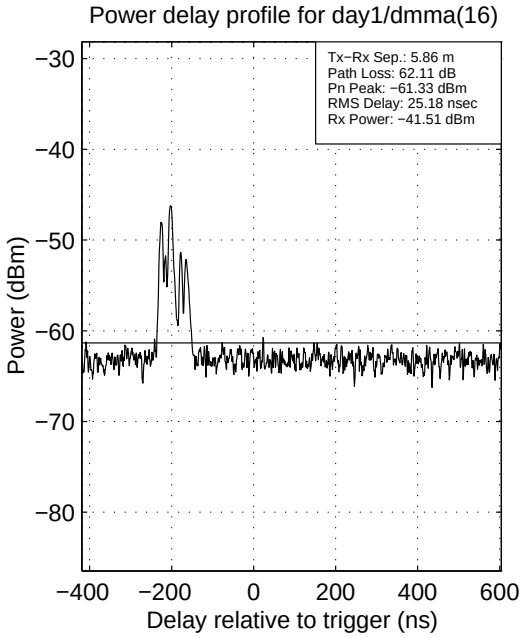
Power delay profile for day1/dmma(16)
Tx−Rx Sep.: 5.86 m
Path Loss: 62.11 dB
Pn Peak: −61.33 dBm
RMS Delay: 25.18 nsec
Rx Power: −41.51 dBm
Power (dBm)
−30
−40
−50
−60
−70
−80
−400
−200
0
200
400
600
Delay relative to trigger (ns)

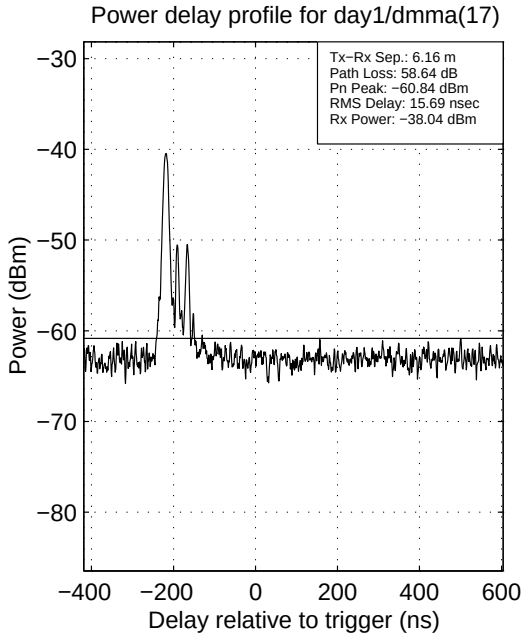
Power delay profile for day1/dmma(17)
Tx−Rx Sep.: 6.16 m
Path Loss: 58.64 dB
Pn Peak: −60.84 dBm
RMS Delay: 15.69 nsec
Rx Power: −38.04 dBm
Power (dBm)
−30
−40
−50
−60
−70
−80
−400
−200
0
200
400
600
Delay relative to trigger (ns)

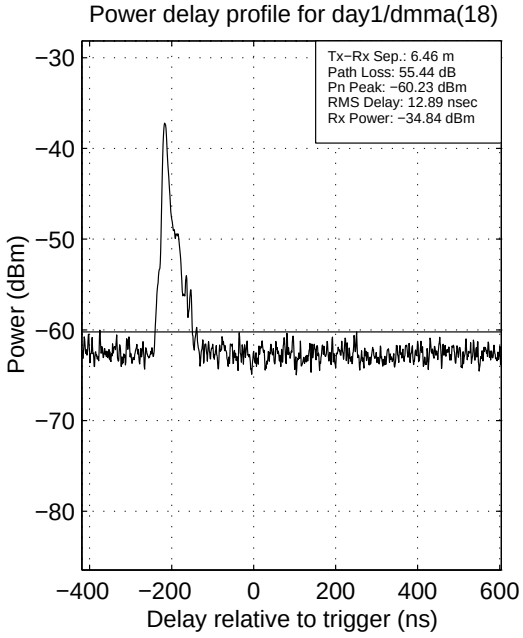
Power delay profile for day1/dmma(18)
Tx−Rx Sep.: 6.46 m
Path Loss: 55.44 dB
Pn Peak: −60.23 dBm
RMS Delay: 12.89 nsec
Rx Power: −34.84 dBm
Power (dBm)
−30
−40
−50
−60
−70
−80
−400
−200
0
200
400
600
Delay relative to trigger (ns)

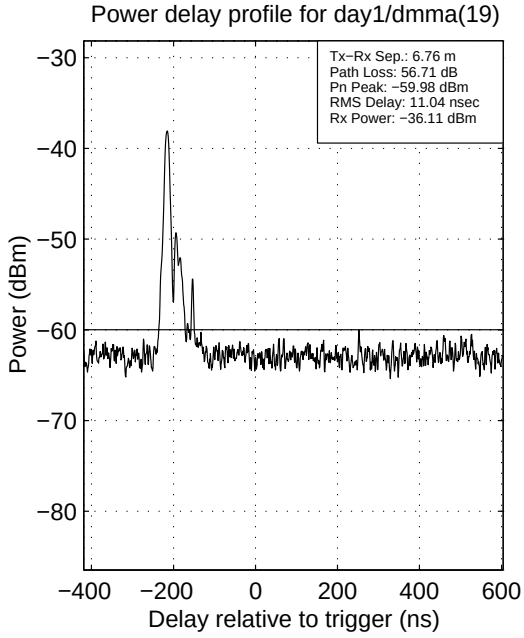
Power delay profile for day1/dmma(19)
Tx−Rx Sep.: 6.76 m
Path Loss: 56.71 dB
Pn Peak: −59.98 dBm
RMS Delay: 11.04 nsec
Rx Power: −36.11 dBm
Power (dBm)
−30
−40
−50
−60
−70
−80
−400
−200
0
200
400
600
Delay relative to trigger (ns)

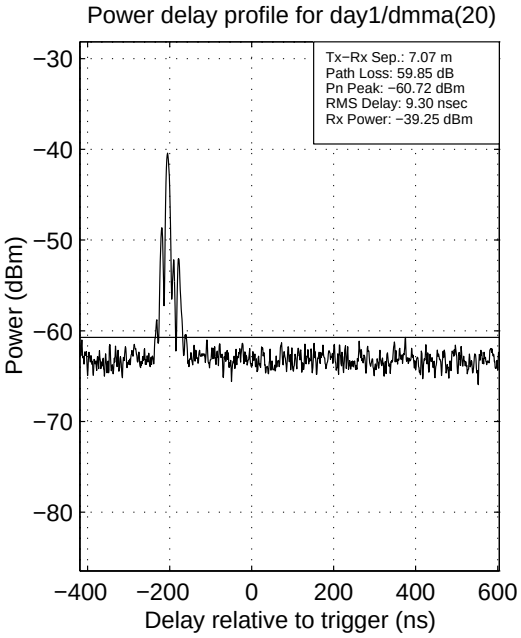
Power delay profile for day1/dmma(20)
Tx−Rx Sep.: 7.07 m
Path Loss: 59.85 dB
Pn Peak: −60.72 dBm
RMS Delay: 9.30 nsec
Rx Power: −39.25 dBm
Power (dBm)
−30
−40
−50
−60
−70
−80
−400
−200
0
200
400
600
Delay relative to trigger (ns)

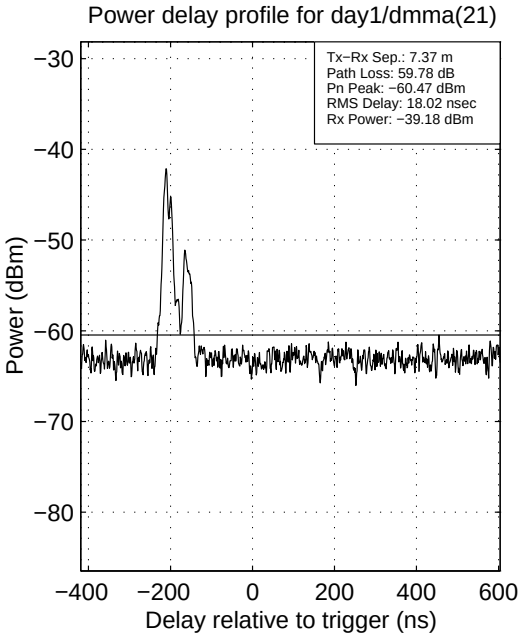
Power delay profile for day1/dmma(21)
Tx−Rx Sep.: 7.37 m
Path Loss: 59.78 dB
Pn Peak: −60.47 dBm
RMS Delay: 18.02 nsec
Rx Power: −39.18 dBm
Power (dBm)
−30
−40
−50
−60
−70
−80
−400
−200
0
200
400
600
Delay relative to trigger (ns)

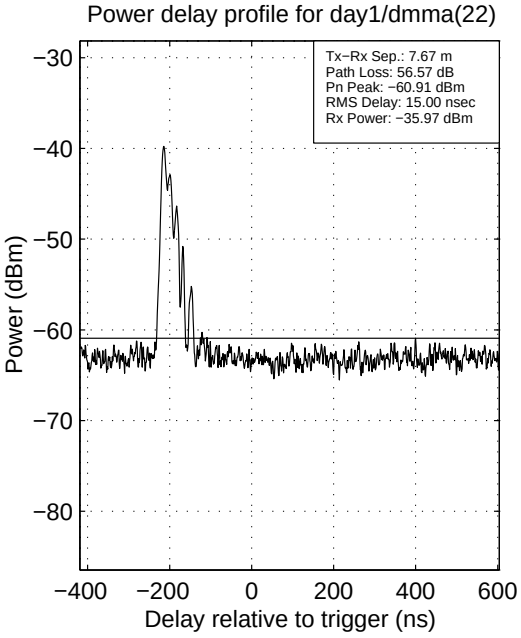
Power delay profile for day1/dmma(22)
Tx−Rx Sep.: 7.67 m
Path Loss: 56.57 dB
Pn Peak: −60.91 dBm
RMS Delay: 15.00 nsec
Rx Power: −35.97 dBm
Power (dBm)
−30
−40
−50
−60
−70
−80
−400
−200
0
200
400
600
Delay relative to trigger (ns)

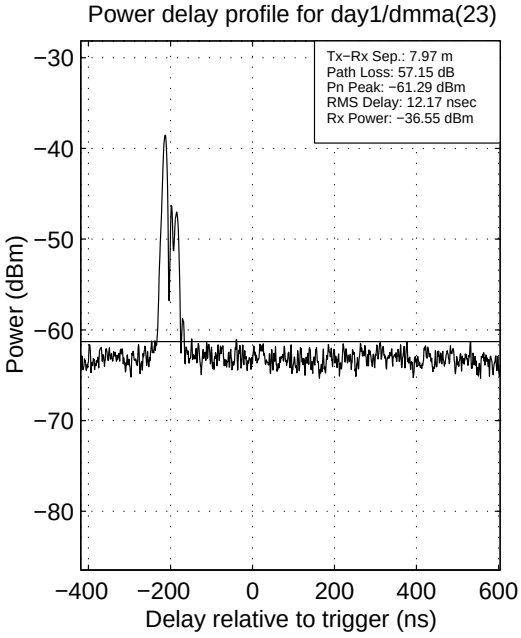
Power delay profile for day1/dmma(23)
Tx−Rx Sep.: 7.97 m
Path Loss: 57.15 dB
Pn Peak: −61.29 dBm
RMS Delay: 12.17 nsec
Rx Power: −36.55 dBm
Power (dBm)
−30
−40
−50
−60
−70
−80
−400
−200
0
200
400
600
Delay relative to trigger (ns)

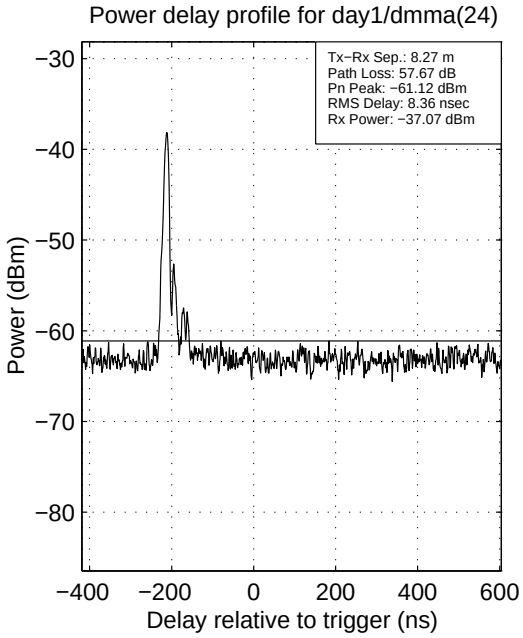
Power delay profile for day1/dmma(24)
Tx−Rx Sep.: 8.27 m
Path Loss: 57.67 dB
Pn Peak: −61.12 dBm
RMS Delay: 8.36 nsec
Rx Power: −37.07 dBm
Power (dBm)
−30
−40
−50
−60
−70
−80
−400
−200
0
200
400
600
Delay relative to trigger (ns)

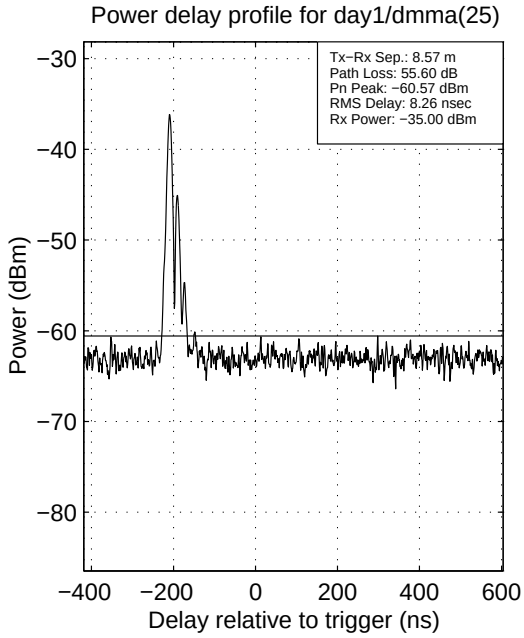
Power delay profile for day1/dmma(25)
Tx−Rx Sep.: 8.57 m
Path Loss: 55.60 dB
Pn Peak: −60.57 dBm
RMS Delay: 8.26 nsec
Rx Power: −35.00 dBm
Power (dBm)
−30
−40
−50
−60
−70
−80
−400
−200
0
200
400
600
Delay relative to trigger (ns)

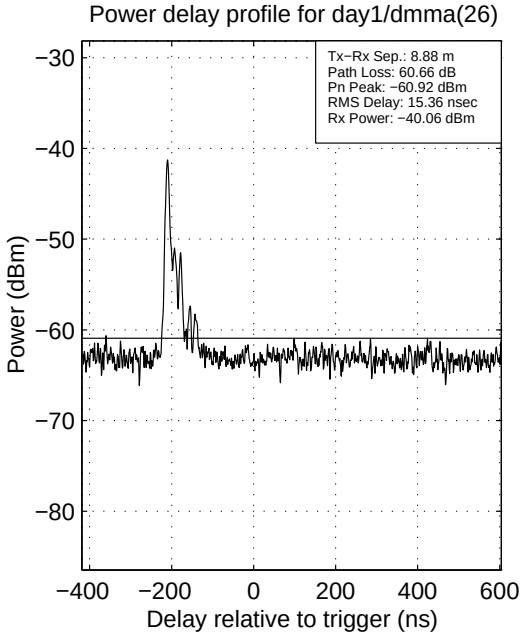
Power delay profile for day1/dmma(26)
Tx−Rx Sep.: 8.88 m
Path Loss: 60.66 dB
Pn Peak: −60.92 dBm
RMS Delay: 15.36 nsec
Rx Power: −40.06 dBm
Power (dBm)
−30
−40
−50
−60
−70
−80
−400
−200
0
200
400
600
Delay relative to trigger (ns)

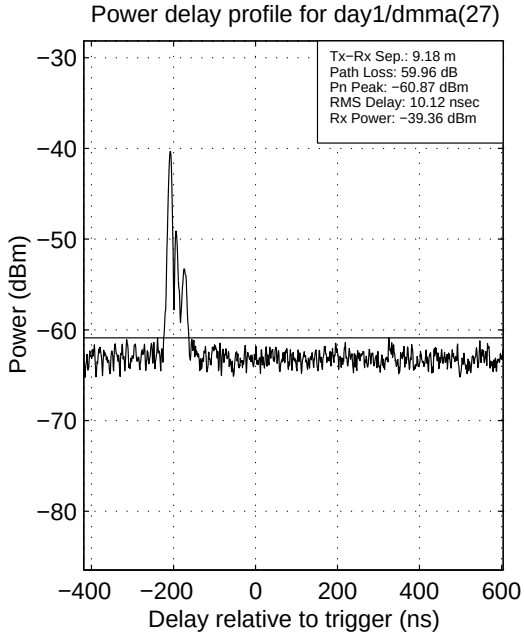
Power delay profile for day1/dmma(27)
Tx−Rx Sep.: 9.18 m
Path Loss: 59.96 dB
Pn Peak: −60.87 dBm
RMS Delay: 10.12 nsec
Rx Power: −39.36 dBm
Power (dBm)
−30
−40
−50
−60
−70
−80
−400
−200
0
200
400
600
Delay relative to trigger (ns)

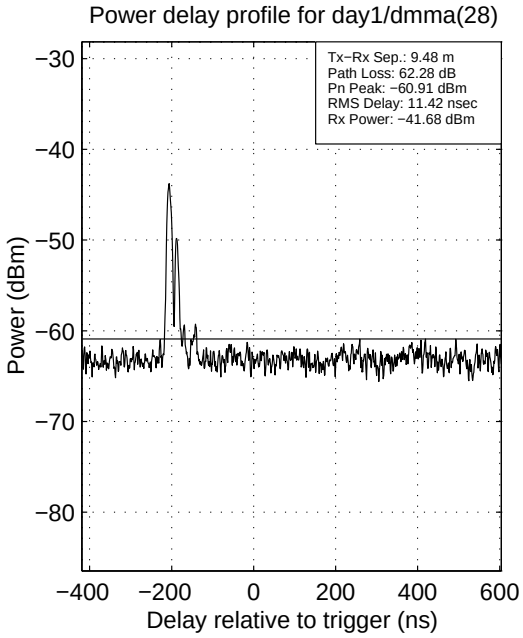
Power delay profile for day1/dmma(28)
Tx−Rx Sep.: 9.48 m
Path Loss: 62.28 dB
Pn Peak: −60.91 dBm
RMS Delay: 11.42 nsec
Rx Power: −41.68 dBm
Power (dBm)
−30
−40
−50
−60
−70
−80
−400
−200
0
200
400
600
Delay relative to trigger (ns)

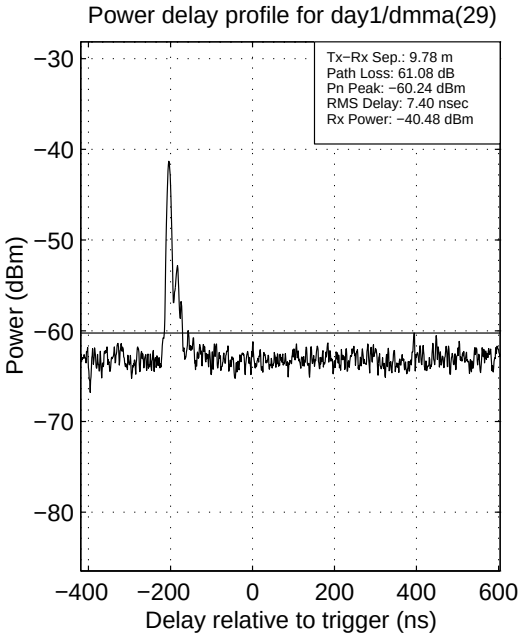
Power delay profile for day1/dmma(29)
Tx−Rx Sep.: 9.78 m
Path Loss: 61.08 dB
Pn Peak: −60.24 dBm
RMS Delay: 7.40 nsec
Rx Power: −40.48 dBm
Power (dBm)
−30
−40
−50
−60
−70
−80
−400
−200
0
200
400
600
Delay relative to trigger (ns)

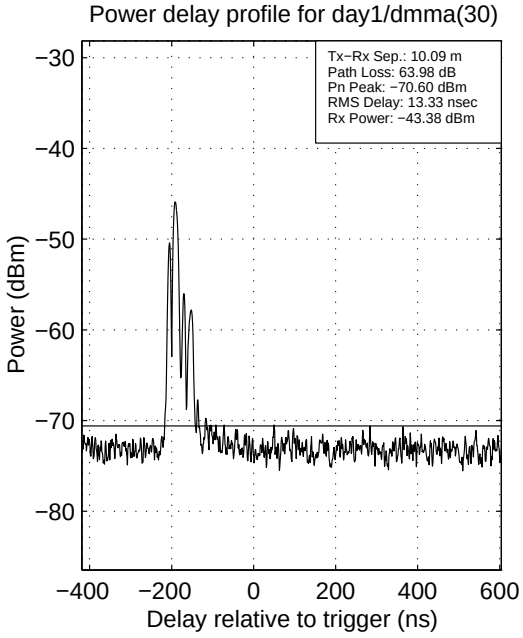
Power delay profile for day1/dmma(30)
Tx−Rx Sep.: 10.09 m
Path Loss: 63.98 dB
Pn Peak: −70.60 dBm
RMS Delay: 13.33 nsec
Rx Power: −43.38 dBm
Power (dBm)
−30
−40
−50
−60
−70
−80
−400
−200
0
200
400
600
Delay relative to trigger (ns)

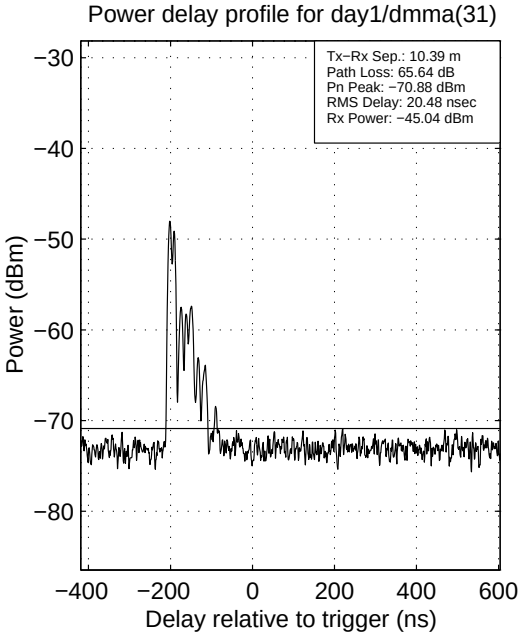
Power delay profile for day1/dmma(31)
Tx−Rx Sep.: 10.39 m
Path Loss: 65.64 dB
Pn Peak: −70.88 dBm
RMS Delay: 20.48 nsec
Rx Power: −45.04 dBm
Power (dBm)
−30
−40
−50
−60
−70
−80
−400
−200
0
200
400
600
Delay relative to trigger (ns)

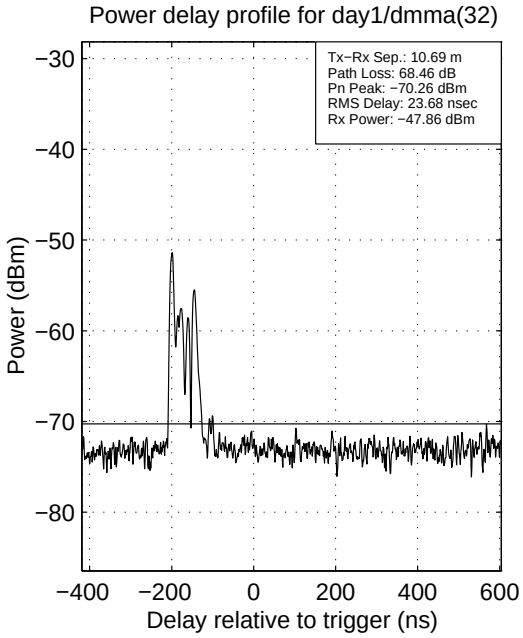
Power delay profile for day1/dmma(32)
Tx−Rx Sep.: 10.69 m
Path Loss: 68.46 dB
Pn Peak: −70.26 dBm
RMS Delay: 23.68 nsec
Rx Power: −47.86 dBm
Power (dBm)
−30
−40
−50
−60
−70
−80
−400
−200
0
200
400
600
Delay relative to trigger (ns)

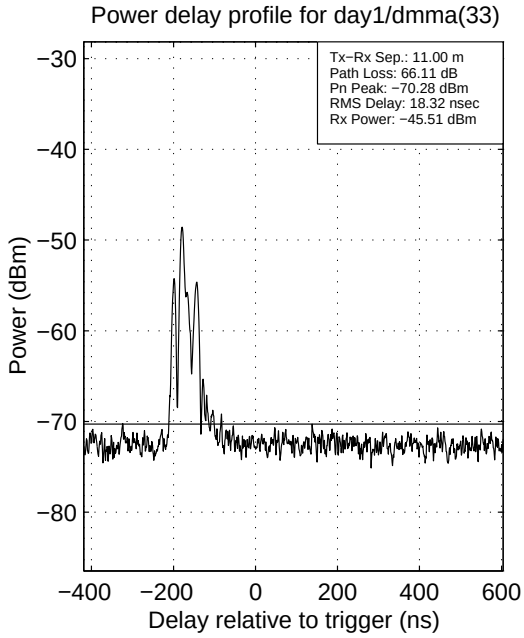
Power delay profile for day1/dmma(33)
Tx−Rx Sep.: 11.00 m
Path Loss: 66.11 dB
Pn Peak: −70.28 dBm
RMS Delay: 18.32 nsec
Rx Power: −45.51 dBm
Power (dBm)
−30
−40
−50
−60
−70
−80
−400
−200
0
200
400
600
Delay relative to trigger (ns)

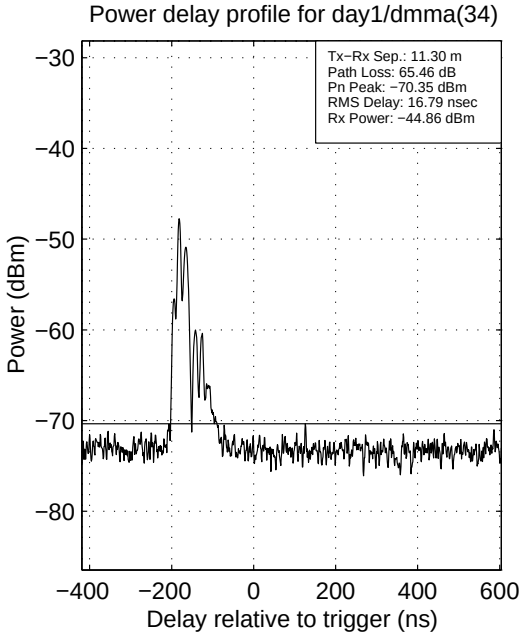
Power delay profile for day1/dmma(34)
Tx−Rx Sep.: 11.30 m
Path Loss: 65.46 dB
Pn Peak: −70.35 dBm
RMS Delay: 16.79 nsec
Rx Power: −44.86 dBm
Power (dBm)
−30
−40
−50
−60
−70
−80
−400
−200
0
200
400
600
Delay relative to trigger (ns)

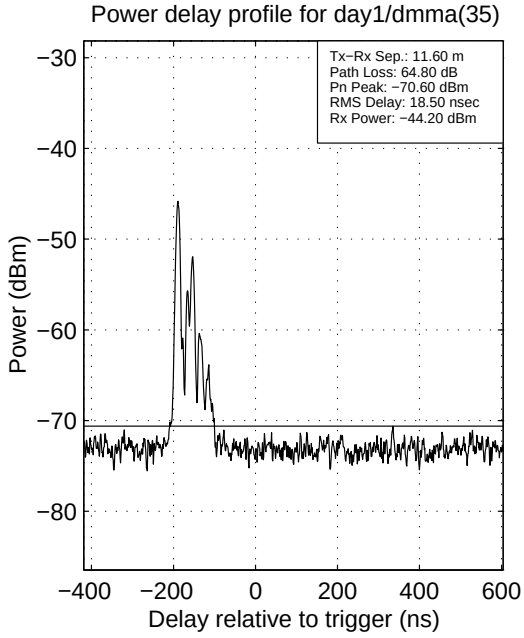
Power delay profile for day1/dmma(35)
Tx−Rx Sep.: 11.60 m
Path Loss: 64.80 dB
Pn Peak: −70.60 dBm
RMS Delay: 18.50 nsec
Rx Power: −44.20 dBm
Power (dBm)
−30
−40
−50
−60
−70
−80
−400
−200
0
200
400
600
Delay relative to trigger (ns)

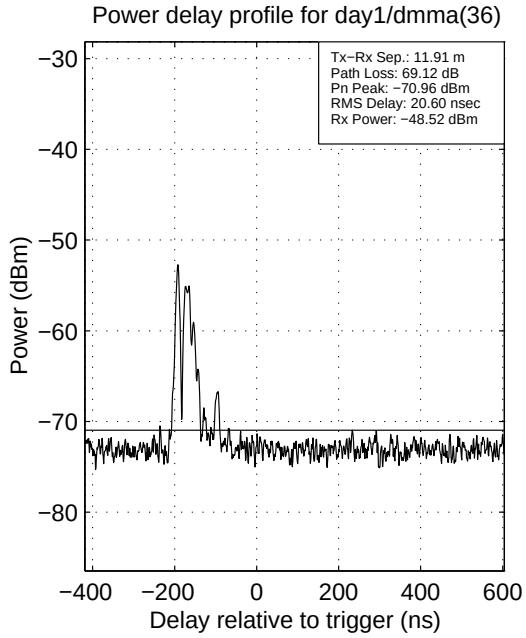
Power delay profile for day1/dmma(36)
Tx−Rx Sep.: 11.91 m
Path Loss: 69.12 dB
Pn Peak: −70.96 dBm
RMS Delay: 20.60 nsec
Rx Power: −48.52 dBm
Power (dBm)
−30
−40
−50
−60
−70
−80
−400
−200
0
200
400
600
Delay relative to trigger (ns)

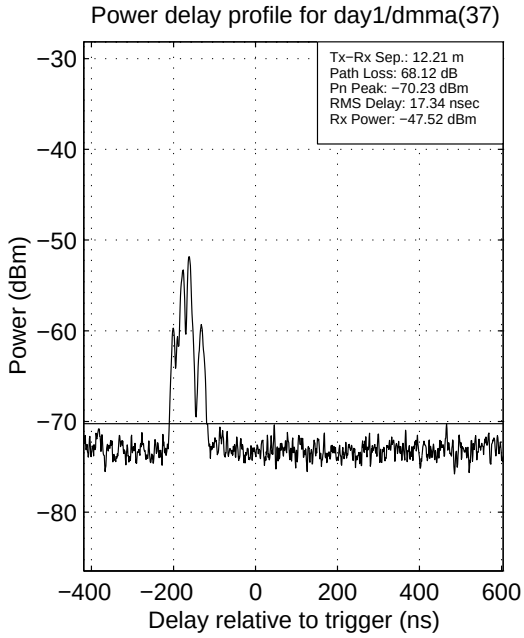
Power delay profile for day1/dmma(37)
Tx−Rx Sep.: 12.21 m
Path Loss: 68.12 dB
Pn Peak: −70.23 dBm
RMS Delay: 17.34 nsec
Rx Power: −47.52 dBm
Power (dBm)
−30
−40
−50
−60
−70
−80
−400
−200
0
200
400
600
Delay relative to trigger (ns)

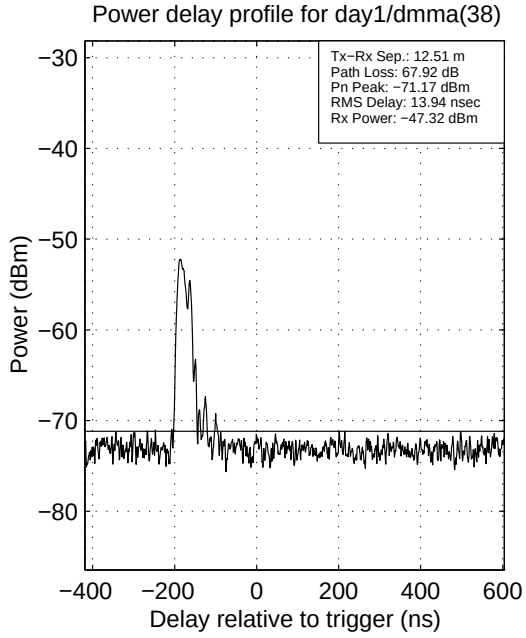
Power delay profile for day1/dmma(38)
Tx−Rx Sep.: 12.51 m
Path Loss: 67.92 dB
Pn Peak: −71.17 dBm
RMS Delay: 13.94 nsec
Rx Power: −47.32 dBm
Power (dBm)
−30
−40
−50
−60
−70
−80
−400
−200
0
200
400
600
Delay relative to trigger (ns)

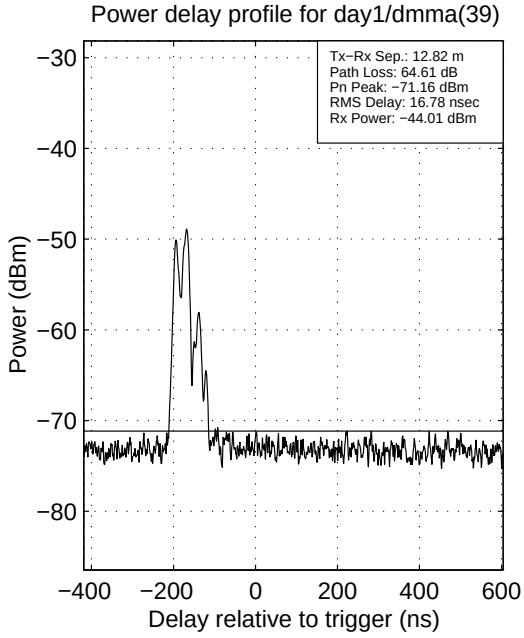
Power delay profile for day1/dmma(39)
Tx−Rx Sep.: 12.82 m
Path Loss: 64.61 dB
Pn Peak: −71.16 dBm
RMS Delay: 16.78 nsec
Rx Power: −44.01 dBm
Power (dBm)
−30
−40
−50
−60
−70
−80
−400
−200
0
200
400
600
Delay relative to trigger (ns)

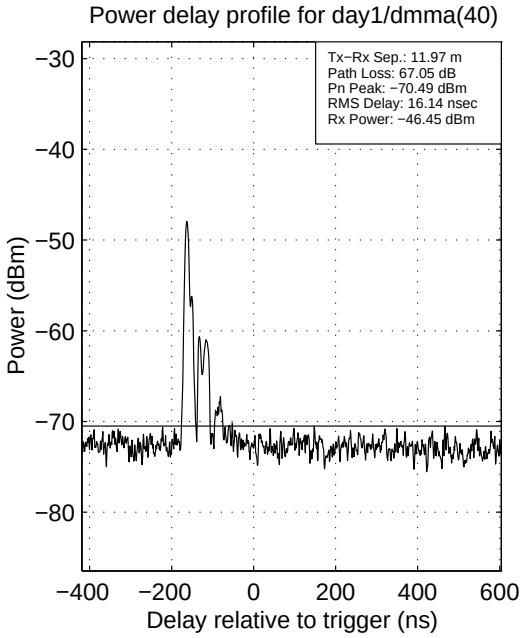
Power delay profile for day1/dmma(40)
Tx−Rx Sep.: 11.97 m
Path Loss: 67.05 dB
Pn Peak: −70.49 dBm
RMS Delay: 16.14 nsec
Rx Power: −46.45 dBm
Power (dBm)
−30
−40
−50
−60
−70
−80
−400
−200
0
200
400
600
Delay relative to trigger (ns)

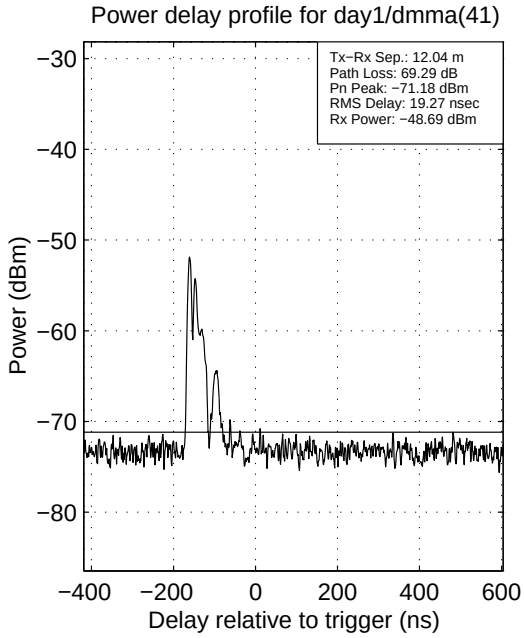
Power delay profile for day1/dmma(41)
Tx−Rx Sep.: 12.04 m
Path Loss: 69.29 dB
Pn Peak: −71.18 dBm
RMS Delay: 19.27 nsec
Rx Power: −48.69 dBm
Power (dBm)
−30
−40
−50
−60
−70
−80
−400
−200
0
200
400
600
Delay relative to trigger (ns)

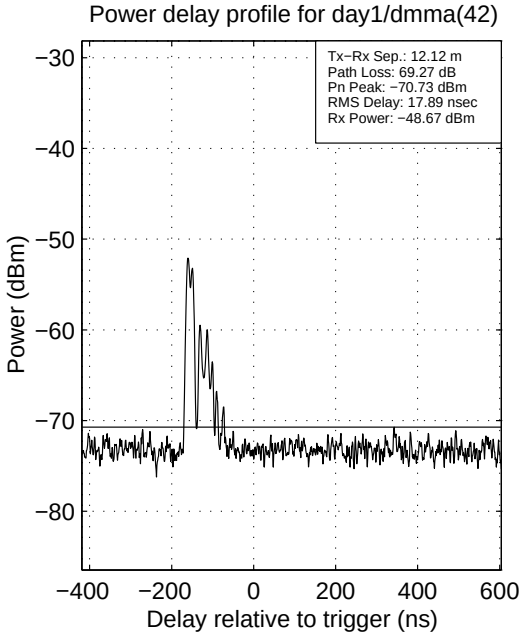
Power delay profile for day1/dmma(42)
Tx−Rx Sep.: 12.12 m
Path Loss: 69.27 dB
Pn Peak: −70.73 dBm
RMS Delay: 17.89 nsec
Rx Power: −48.67 dBm
Power (dBm)
−30
−40
−50
−60
−70
−80
−400
−200
0
200
400
600
Delay relative to trigger (ns)

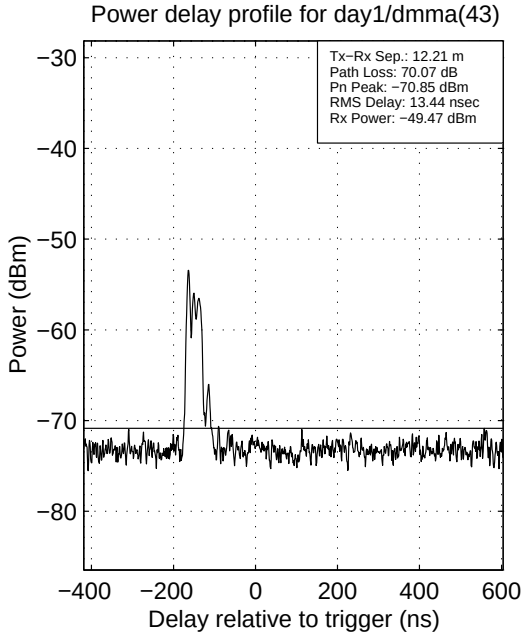
Power delay profile for day1/dmma(43)
Tx−Rx Sep.: 12.21 m
Path Loss: 70.07 dB
Pn Peak: −70.85 dBm
RMS Delay: 13.44 nsec
Rx Power: −49.47 dBm
Power (dBm)
−30
−40
−50
−60
−70
−80
−400
−200
0
200
400
600
Delay relative to trigger (ns)

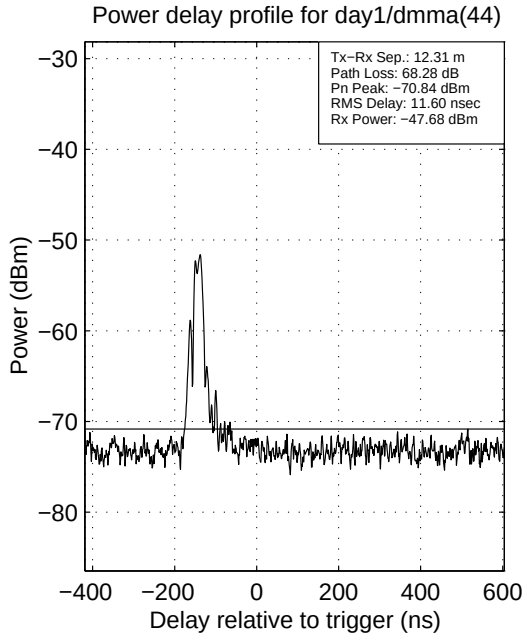
Power delay profile for day1/dmma(44)
Tx−Rx Sep.: 12.31 m
Path Loss: 68.28 dB
Pn Peak: −70.84 dBm
RMS Delay: 11.60 nsec
Rx Power: −47.68 dBm
Power (dBm)
−30
−40
−50
−60
−70
−80
−400
−200
0
200
400
600
Delay relative to trigger (ns)

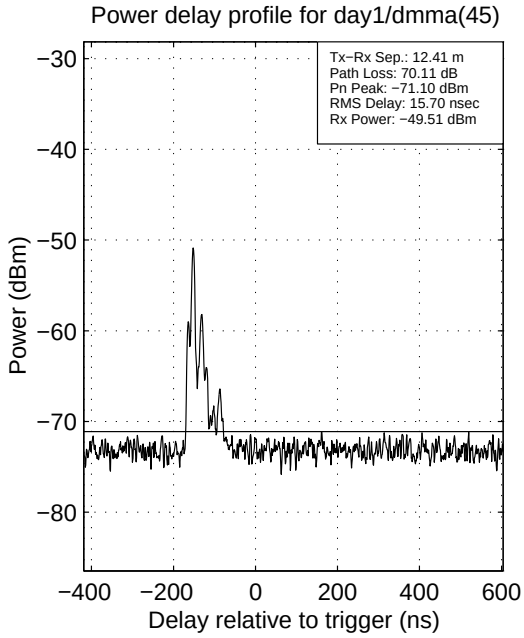
Power delay profile for day1/dmma(45)
Tx−Rx Sep.: 12.41 m
Path Loss: 70.11 dB
Pn Peak: −71.10 dBm
RMS Delay: 15.70 nsec
Rx Power: −49.51 dBm
Power (dBm)
−30
−40
−50
−60
−70
−80
−400
−200
0
200
400
600
Delay relative to trigger (ns)

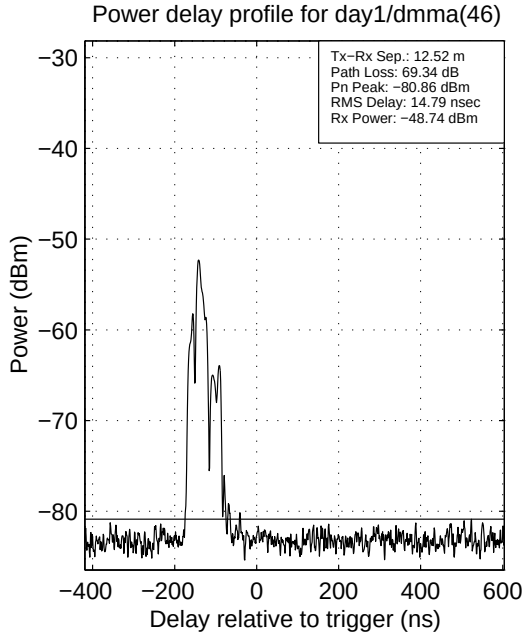
Power delay profile for day1/dmma(46)
Tx−Rx Sep.: 12.52 m
Path Loss: 69.34 dB
Pn Peak: −80.86 dBm
RMS Delay: 14.79 nsec
Rx Power: −48.74 dBm
Power (dBm)
−30
−40
−50
−60
−70
−80
−400
−200
0
200
400
600
Delay relative to trigger (ns)

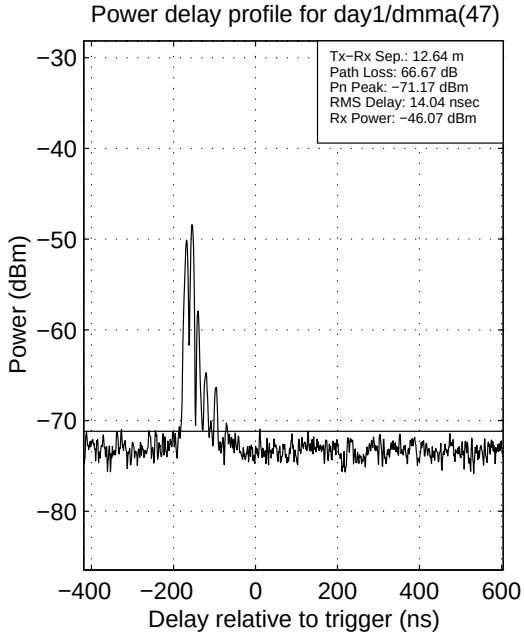
Power delay profile for day1/dmma(47)
Tx−Rx Sep.: 12.64 m
Path Loss: 66.67 dB
Pn Peak: −71.17 dBm
RMS Delay: 14.04 nsec
Rx Power: −46.07 dBm
Power (dBm)
−30
−40
−50
−60
−70
−80
−400
−200
0
200
400
600
Delay relative to trigger (ns)

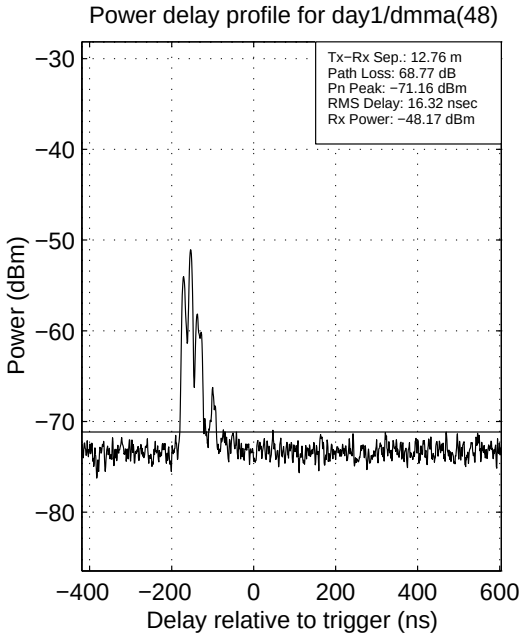
Power delay profile for day1/dmma(48)
Tx−Rx Sep.: 12.76 m
Path Loss: 68.77 dB
Pn Peak: −71.16 dBm
RMS Delay: 16.32 nsec
Rx Power: −48.17 dBm
Power (dBm)
−30
−40
−50
−60
−70
−80
−400
−200
0
200
400
600
Delay relative to trigger (ns)

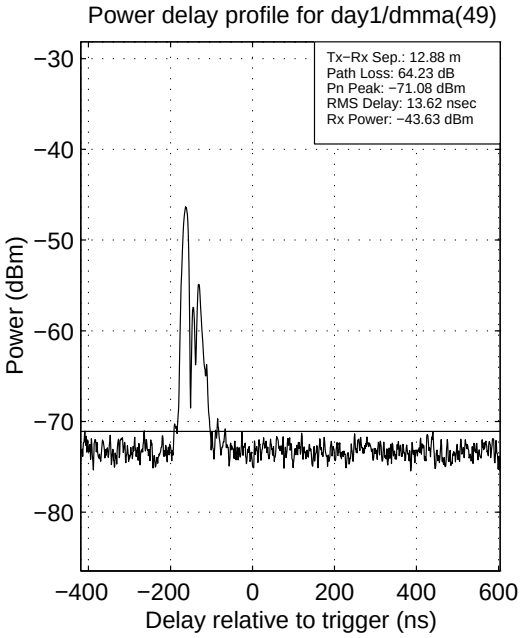
Power delay profile for day1/dmma(49)
Tx−Rx Sep.: 12.88 m
Path Loss: 64.23 dB
Pn Peak: −71.08 dBm
RMS Delay: 13.62 nsec
Rx Power: −43.63 dBm
Power (dBm)
−30
−40
−50
−60
−70
−80
−400
−200
0
200
400
600
Delay relative to trigger (ns)

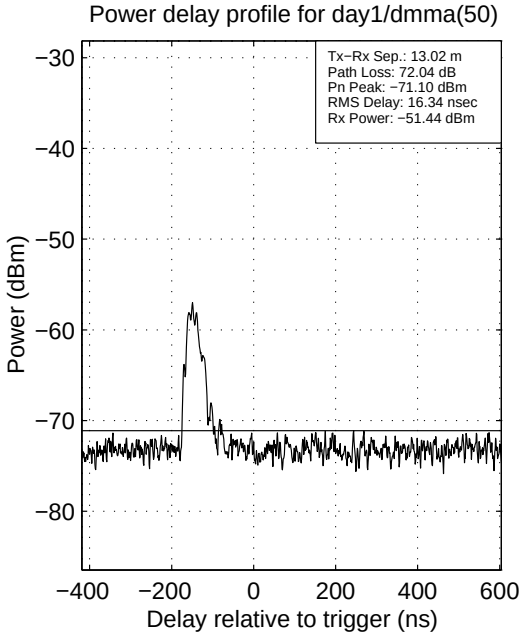
Power delay profile for day1/dmma(50)
Tx−Rx Sep.: 13.02 m
Path Loss: 72.04 dB
Pn Peak: −71.10 dBm
RMS Delay: 16.34 nsec
Rx Power: −51.44 dBm
Power (dBm)
−30
−40
−50
−60
−70
−80
−400
−200
0
200
400
600
Delay relative to trigger (ns)

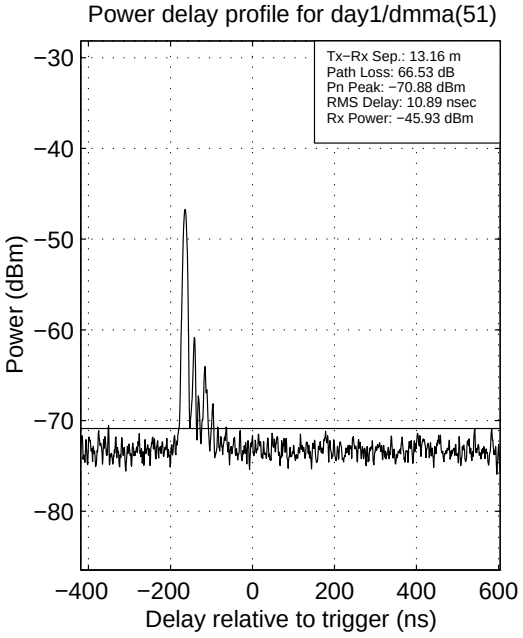
Power delay profile for day1/dmma(51)
Tx−Rx Sep.: 13.16 m
Path Loss: 66.53 dB
Pn Peak: −70.88 dBm
RMS Delay: 10.89 nsec
Rx Power: −45.93 dBm
Power (dBm)
−30
−40
−50
−60
−70
−80
−400
−200
0
200
400
600
Delay relative to trigger (ns)

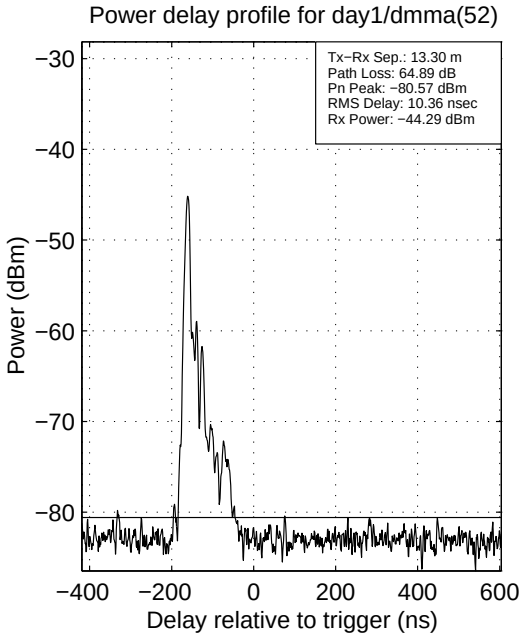
Power delay profile for day1/dmma(52)
Tx−Rx Sep.: 13.30 m
Path Loss: 64.89 dB
Pn Peak: −80.57 dBm
RMS Delay: 10.36 nsec
Rx Power: −44.29 dBm
Power (dBm)
−30
−40
−50
−60
−70
−80
−400
−200
0
200
400
600
Delay relative to trigger (ns)

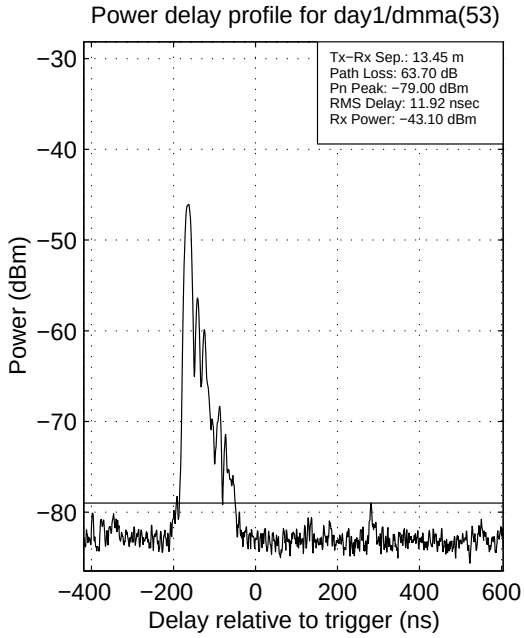
Power delay profile for day1/dmma(53)
Tx−Rx Sep.: 13.45 m
Path Loss: 63.70 dB
Pn Peak: −79.00 dBm
RMS Delay: 11.92 nsec
Rx Power: −43.10 dBm
Power (dBm)
−30
−40
−50
−60
−70
−80
−400
−200
0
200
400
600
Delay relative to trigger (ns)

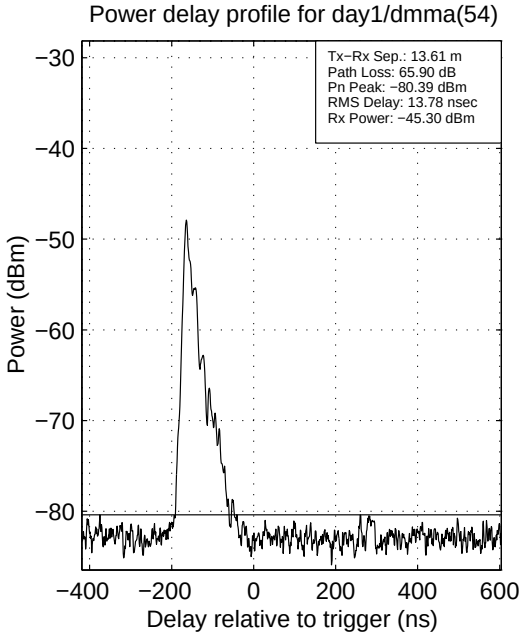
Power delay profile for day1/dmma(54)
Tx−Rx Sep.: 13.61 m
Path Loss: 65.90 dB
Pn Peak: −80.39 dBm
RMS Delay: 13.78 nsec
Rx Power: −45.30 dBm
Power (dBm)
−30
−40
−50
−60
−70
−80
−400
−200
0
200
400
600
Delay relative to trigger (ns)

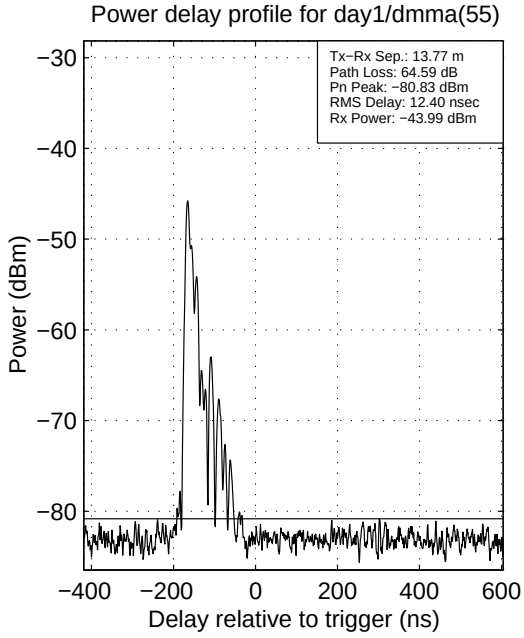
Power delay profile for day1/dmma(55)
Tx−Rx Sep.: 13.77 m
Path Loss: 64.59 dB
Pn Peak: −80.83 dBm
RMS Delay: 12.40 nsec
Rx Power: −43.99 dBm
Power (dBm)
−30
−40
−50
−60
−70
−80
−400
−200
0
200
400
600
Delay relative to trigger (ns)

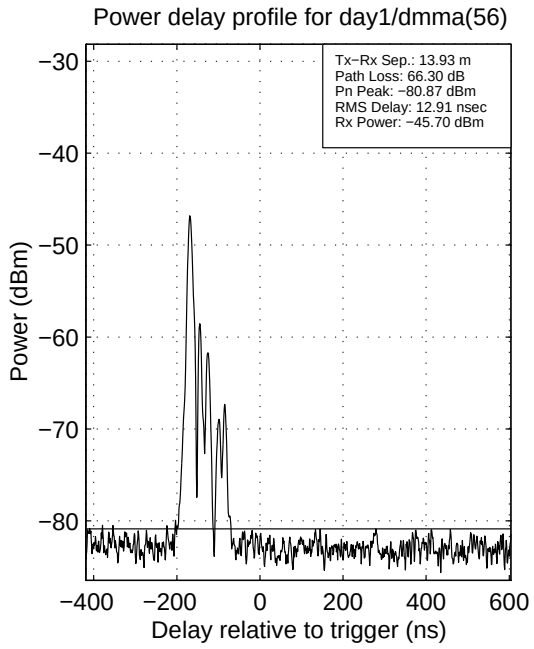
Power delay profile for day1/dmma(56)
Tx−Rx Sep.: 13.93 m
Path Loss: 66.30 dB
Pn Peak: −80.87 dBm
RMS Delay: 12.91 nsec
Rx Power: −45.70 dBm
Power (dBm)
−30
−40
−50
−60
−70
−80
−400
−200
0
200
400
600
Delay relative to trigger (ns)

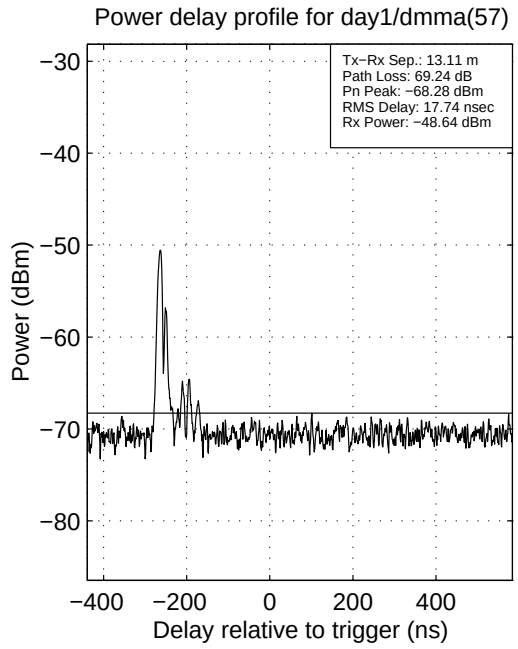
Power delay profile for day1/dmma(57)
Tx−Rx Sep.: 13.11 m
Path Loss: 69.24 dB
Pn Peak: −68.28 dBm
RMS Delay: 17.74 nsec
Rx Power: −48.64 dBm
Power (dBm)
−30
−40
−50
−60
−70
−80
−400
−200
0
200
400
Delay relative to trigger (ns)

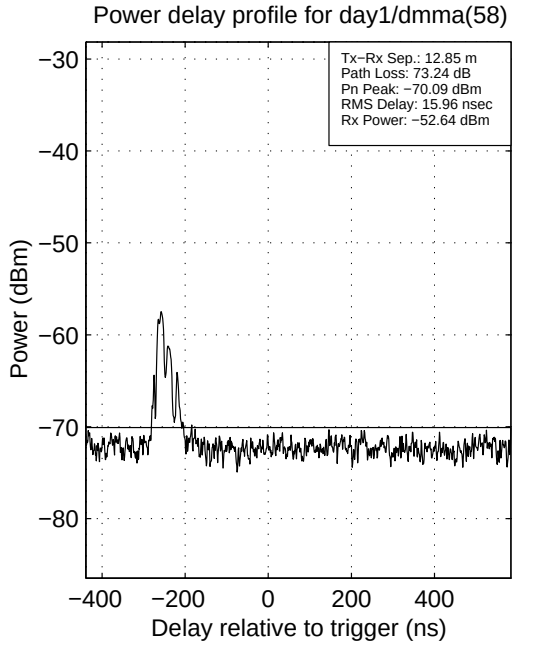
Power delay profile for day1/dmma(58)
Tx−Rx Sep.: 12.85 m
Path Loss: 73.24 dB
Pn Peak: −70.09 dBm
RMS Delay: 15.96 nsec
Rx Power: −52.64 dBm
Power (dBm)
−30
−40
−50
−60
−70
−80
−400
−200
0
200
400
Delay relative to trigger (ns)

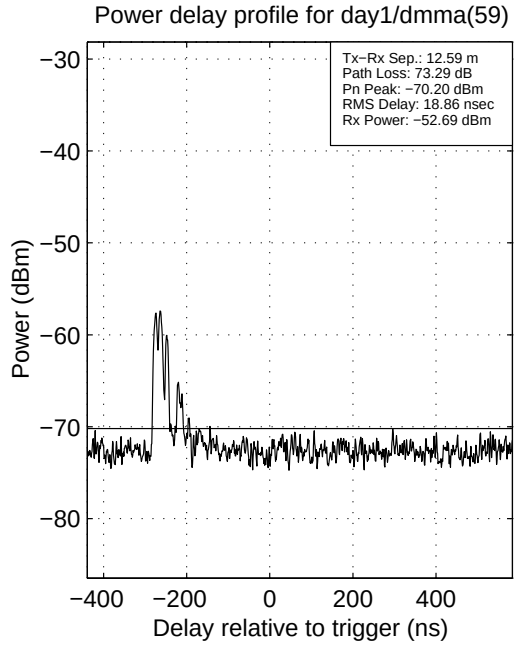
Power delay profile for day1/dmma(59)
Tx−Rx Sep.: 12.59 m
Path Loss: 73.29 dB
Pn Peak: −70.20 dBm
RMS Delay: 18.86 nsec
Rx Power: −52.69 dBm
Power (dBm)
−30
−40
−50
−60
−70
−80
−400
−200
0
200
400
Delay relative to trigger (ns)

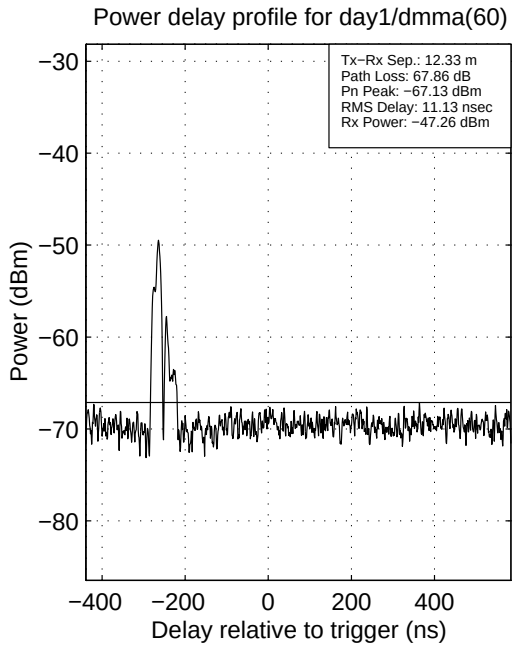
Power delay profile for day1/dmma(60)
Tx−Rx Sep.: 12.33 m
Path Loss: 67.86 dB
Pn Peak: −67.13 dBm
RMS Delay: 11.13 nsec
Rx Power: −47.26 dBm
Power (dBm)
−30
−40
−50
−60
−70
−80
−400
−200
0
200
400
Delay relative to trigger (ns)

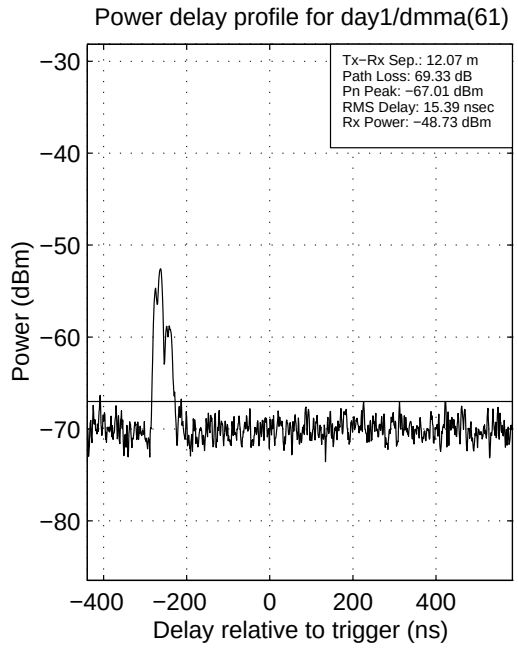
Power delay profile for day1/dmma(61)
Tx−Rx Sep.: 12.07 m
Path Loss: 69.33 dB
Pn Peak: −67.01 dBm
RMS Delay: 15.39 nsec
Rx Power: −48.73 dBm
Power (dBm)
−30
−40
−50
−60
−70
−80
−400
−200
0
200
400
Delay relative to trigger (ns)

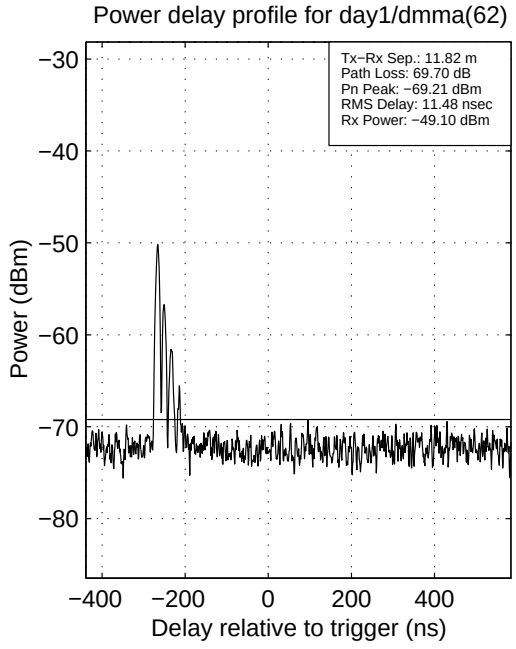
Power delay profile for day1/dmma(62)
Tx−Rx Sep.: 11.82 m
Path Loss: 69.70 dB
Pn Peak: −69.21 dBm
RMS Delay: 11.48 nsec
Rx Power: −49.10 dBm
Power (dBm)
−30
−40
−50
−60
−70
−80
−400
−200
0
200
400
Delay relative to trigger (ns)

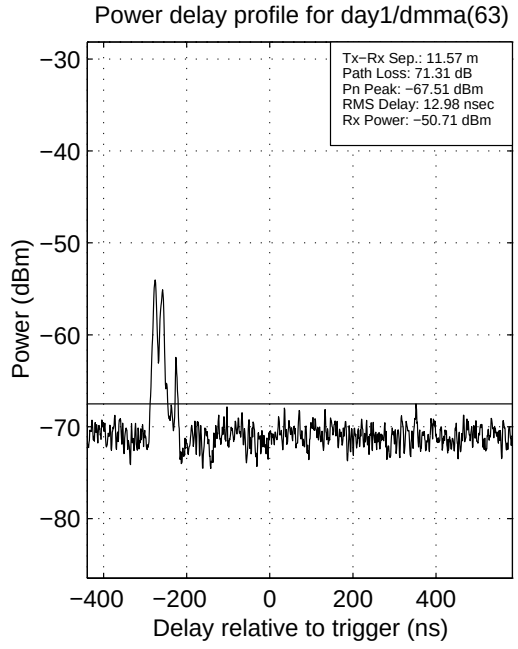
Power delay profile for day1/dmma(63)
Tx−Rx Sep.: 11.57 m
Path Loss: 71.31 dB
Pn Peak: −67.51 dBm
RMS Delay: 12.98 nsec
Rx Power: −50.71 dBm
Power (dBm)
−30
−40
−50
−60
−70
−80
−400
−200
0
200
400
Delay relative to trigger (ns)

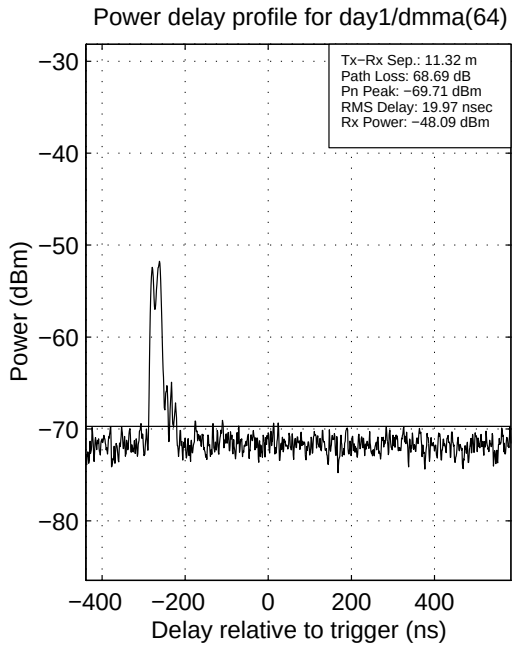
Power delay profile for day1/dmma(64)
Tx−Rx Sep.: 11.32 m
Path Loss: 68.69 dB
Pn Peak: −69.71 dBm
RMS Delay: 19.97 nsec
Rx Power: −48.09 dBm
Power (dBm)
−30
−40
−50
−60
−70
−80
−400
−200
0
200
400
Delay relative to trigger (ns)

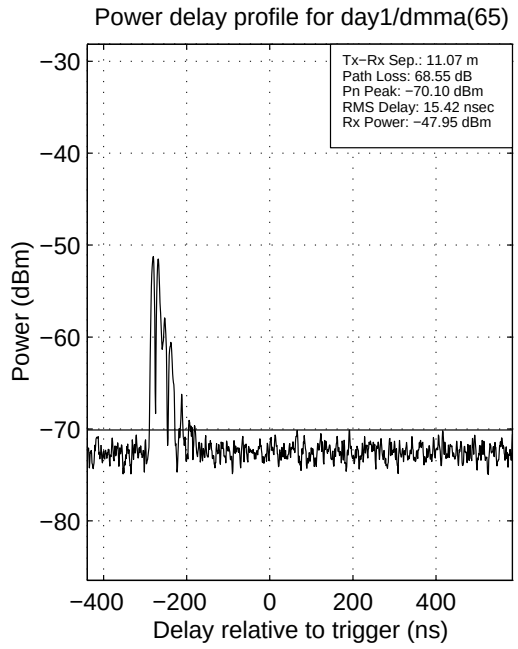
Power delay profile for day1/dmma(65)
Tx−Rx Sep.: 11.07 m
Path Loss: 68.55 dB
Pn Peak: −70.10 dBm
RMS Delay: 15.42 nsec
Rx Power: −47.95 dBm
Power (dBm)
−30
−40
−50
−60
−70
−80
−400
−200
0
200
400
Delay relative to trigger (ns)

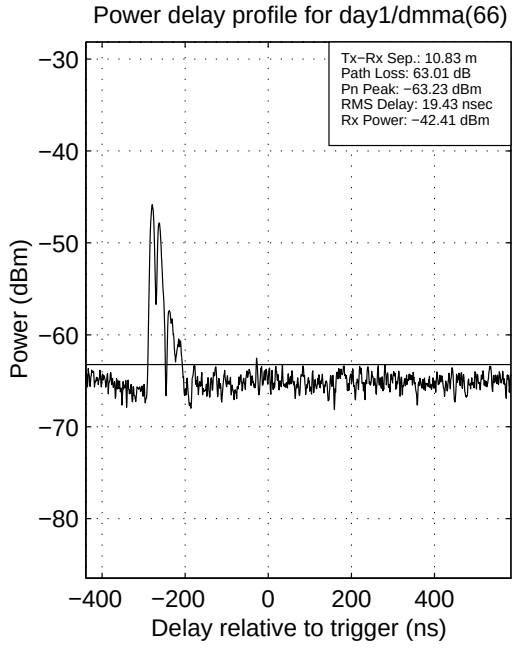
Power delay profile for day1/dmma(66)
Tx−Rx Sep.: 10.83 m
Path Loss: 63.01 dB
Pn Peak: −63.23 dBm
RMS Delay: 19.43 nsec
Rx Power: −42.41 dBm
Power (dBm)
−30
−40
−50
−60
−70
−80
−400
−200
0
200
400
Delay relative to trigger (ns)

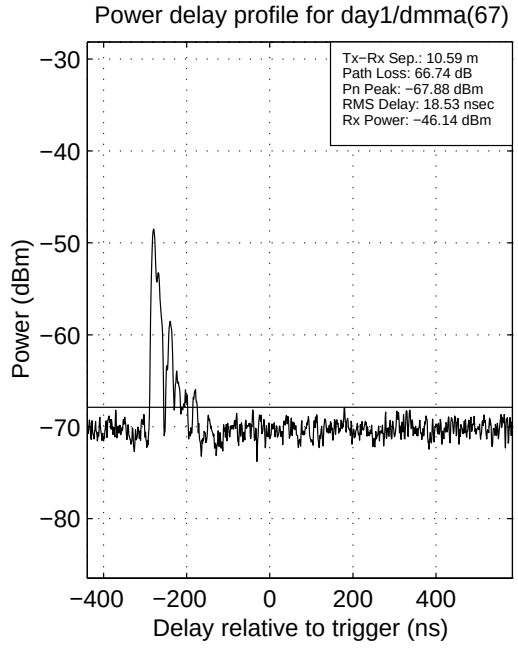
Power delay profile for day1/dmma(67)
Tx−Rx Sep.: 10.59 m
Path Loss: 66.74 dB
Pn Peak: −67.88 dBm
RMS Delay: 18.53 nsec
Rx Power: −46.14 dBm
Power (dBm)
−30
−40
−50
−60
−70
−80
−400
−200
0
200
400
Delay relative to trigger (ns)

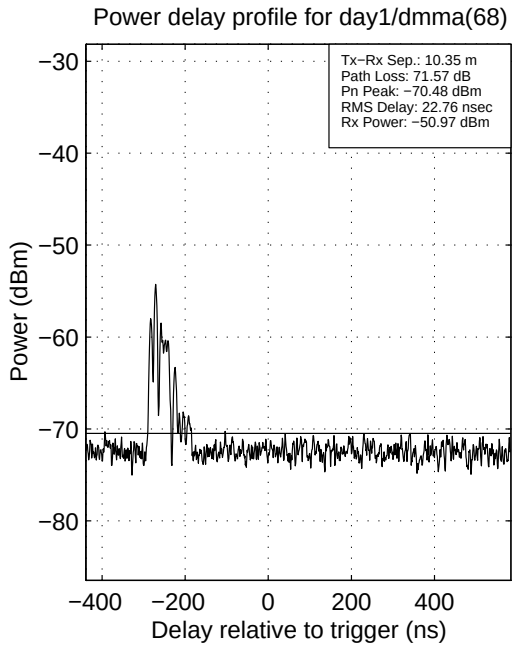
Power delay profile for day1/dmma(68)
Tx−Rx Sep.: 10.35 m
Path Loss: 71.57 dB
Pn Peak: −70.48 dBm
RMS Delay: 22.76 nsec
Rx Power: −50.97 dBm
Power (dBm)
−30
−40
−50
−60
−70
−80
−400
−200
0
200
400
Delay relative to trigger (ns)

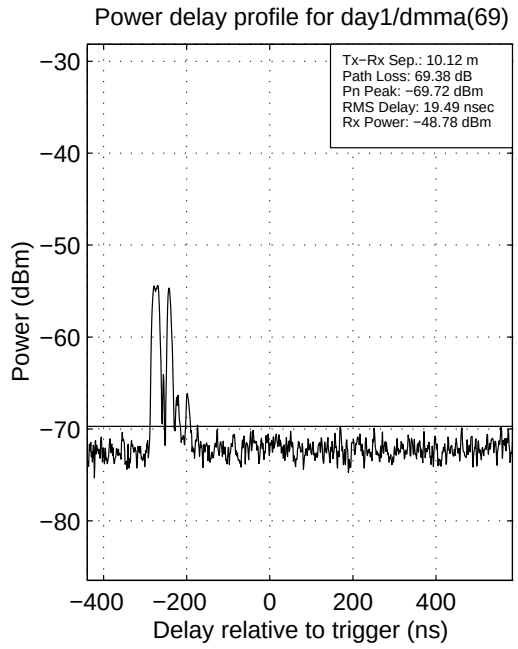
Power delay profile for day1/dmma(69)
Tx−Rx Sep.: 10.12 m
Path Loss: 69.38 dB
Pn Peak: −69.72 dBm
RMS Delay: 19.49 nsec
Rx Power: −48.78 dBm
Power (dBm)
−30
−40
−50
−60
−70
−80
−400
−200
0
200
400
Delay relative to trigger (ns)

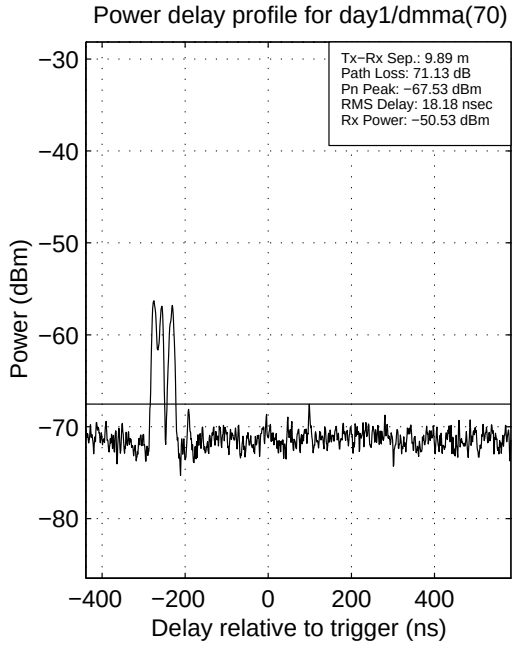
Power delay profile for day1/dmma(70)
Tx−Rx Sep.: 9.89 m
Path Loss: 71.13 dB
Pn Peak: −67.53 dBm
RMS Delay: 18.18 nsec
Rx Power: −50.53 dBm
Power (dBm)
−30
−40
−50
−60
−70
−80
−400
−200
0
200
400
Delay relative to trigger (ns)

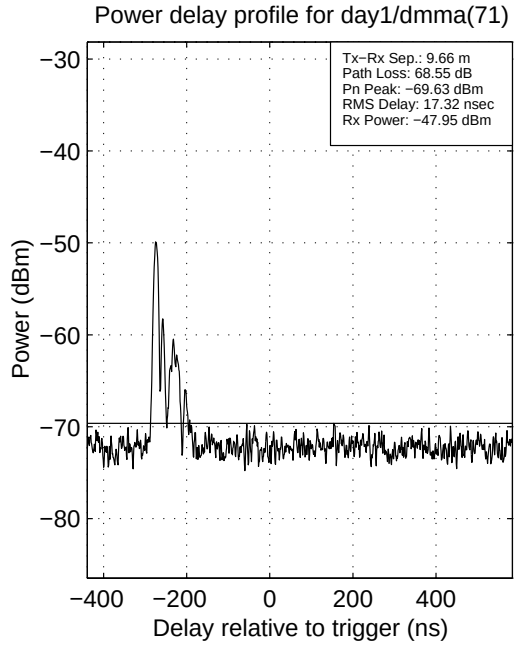
Power delay profile for day1/dmma(71)
Tx−Rx Sep.: 9.66 m
Path Loss: 68.55 dB
Pn Peak: −69.63 dBm
RMS Delay: 17.32 nsec
Rx Power: −47.95 dBm
Power (dBm)
−30
−40
−50
−60
−70
−80
−400
−200
0
200
400
Delay relative to trigger (ns)

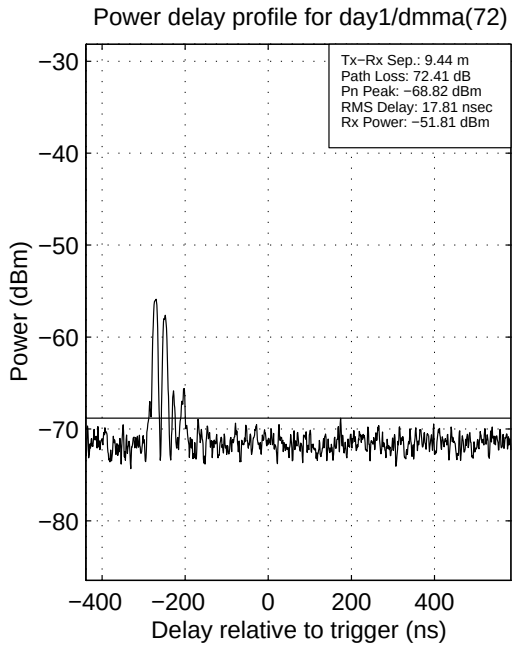
Power delay profile for day1/dmma(72)
Tx−Rx Sep.: 9.44 m
Path Loss: 72.41 dB
Pn Peak: −68.82 dBm
RMS Delay: 17.81 nsec
Rx Power: −51.81 dBm
Power (dBm)
−30
−40
−50
−60
−70
−80
−400
−200
0
200
400
Delay relative to trigger (ns)

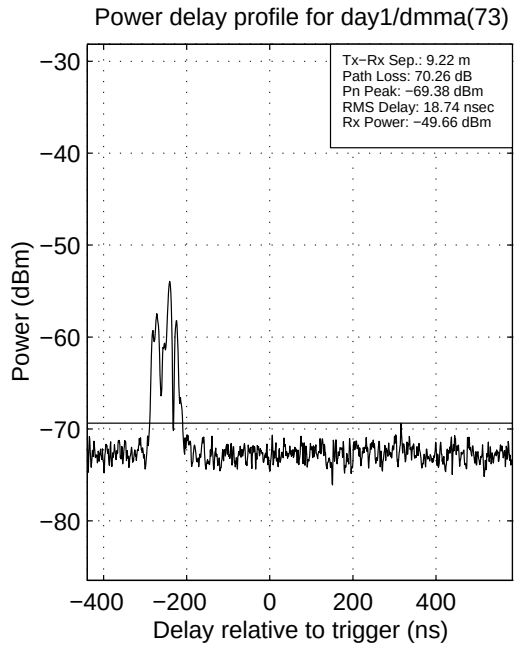
Power delay profile for day1/dmma(73)
Tx−Rx Sep.: 9.22 m
Path Loss: 70.26 dB
Pn Peak: −69.38 dBm
RMS Delay: 18.74 nsec
Rx Power: −49.66 dBm
Power (dBm)
−30
−40
−50
−60
−70
−80
−400
−200
0
200
400
Delay relative to trigger (ns)

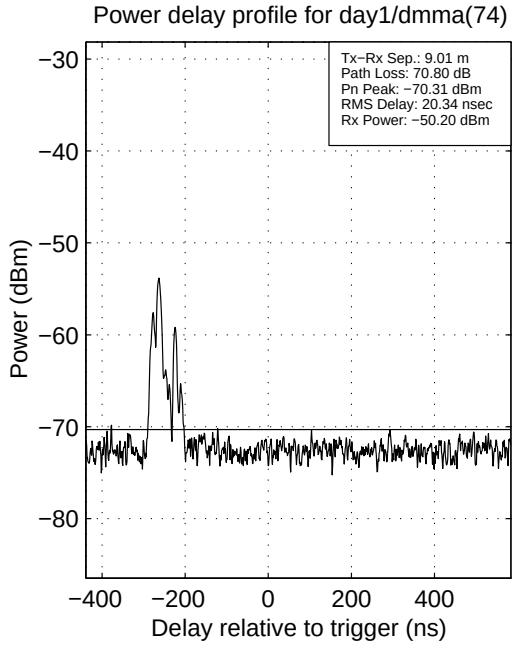
Power delay profile for day1/dmma(74)
Tx−Rx Sep.: 9.01 m
Path Loss: 70.80 dB
Pn Peak: −70.31 dBm
RMS Delay: 20.34 nsec
Rx Power: −50.20 dBm
Power (dBm)
−30
−40
−50
−60
−70
−80
−400
−200
0
200
400
Delay relative to trigger (ns)

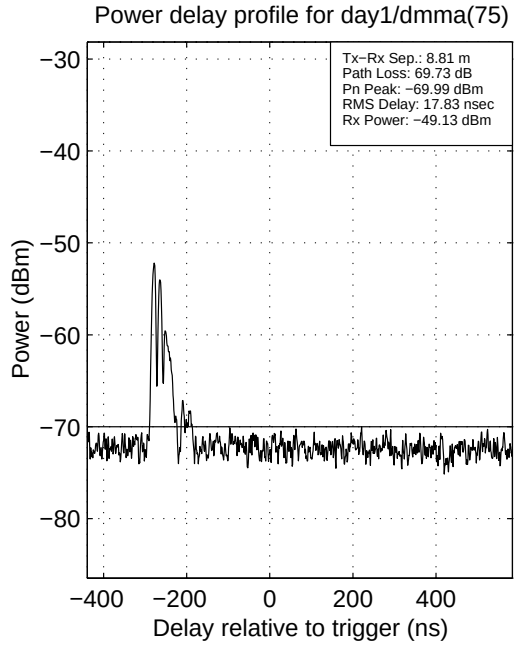
Power delay profile for day1/dmma(75)
Tx−Rx Sep.: 8.81 m
Path Loss: 69.73 dB
Pn Peak: −69.99 dBm
RMS Delay: 17.83 nsec
Rx Power: −49.13 dBm
Power (dBm)
−30
−40
−50
−60
−70
−80
−400
−200
0
200
400
Delay relative to trigger (ns)

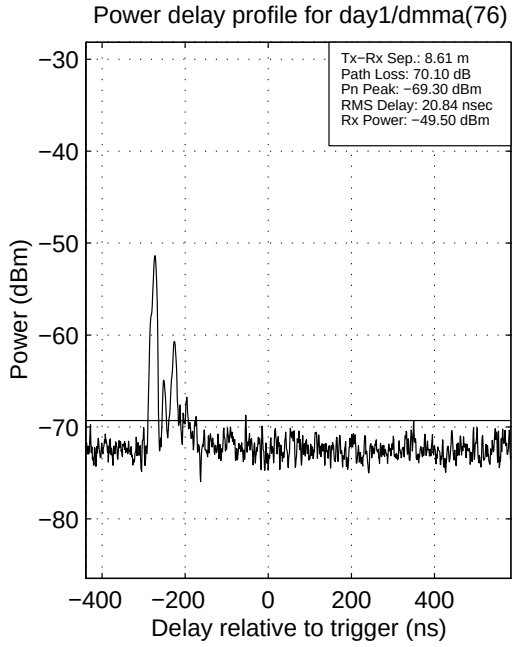
Power delay profile for day1/dmma(76)
Tx−Rx Sep.: 8.61 m
Path Loss: 70.10 dB
Pn Peak: −69.30 dBm
RMS Delay: 20.84 nsec
Rx Power: −49.50 dBm
Power (dBm)
−30
−40
−50
−60
−70
−80
−400
−200
0
200
400
Delay relative to trigger (ns)

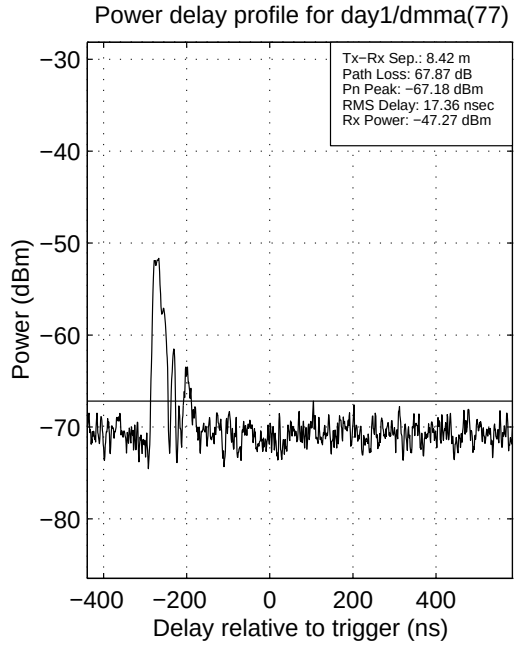
Power delay profile for day1/dmma(77)
Tx−Rx Sep.: 8.42 m
Path Loss: 67.87 dB
Pn Peak: −67.18 dBm
RMS Delay: 17.36 nsec
Rx Power: −47.27 dBm
Power (dBm)
−30
−40
−50
−60
−70
−80
−400
−200
0
200
400
Delay relative to trigger (ns)

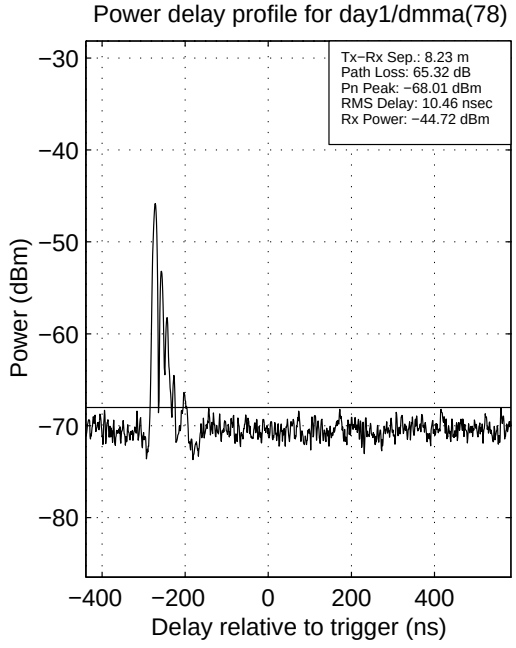
Power delay profile for day1/dmma(78)
Tx−Rx Sep.: 8.23 m
Path Loss: 65.32 dB
Pn Peak: −68.01 dBm
RMS Delay: 10.46 nsec
Rx Power: −44.72 dBm
Power (dBm)
−30
−40
−50
−60
−70
−80
−400
−200
0
200
400
Delay relative to trigger (ns)

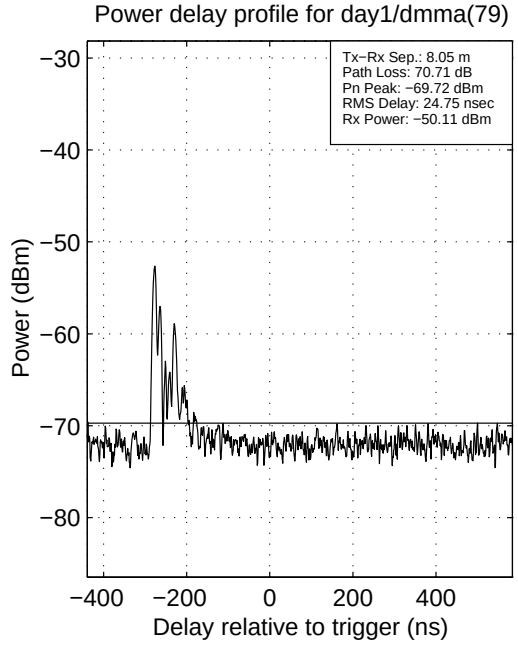
Power delay profile for day1/dmma(79)
Tx−Rx Sep.: 8.05 m
Path Loss: 70.71 dB
Pn Peak: −69.72 dBm
RMS Delay: 24.75 nsec
Rx Power: −50.11 dBm
Power (dBm)
−30
−40
−50
−60
−70
−80
−400
−200
0
200
400
Delay relative to trigger (ns)

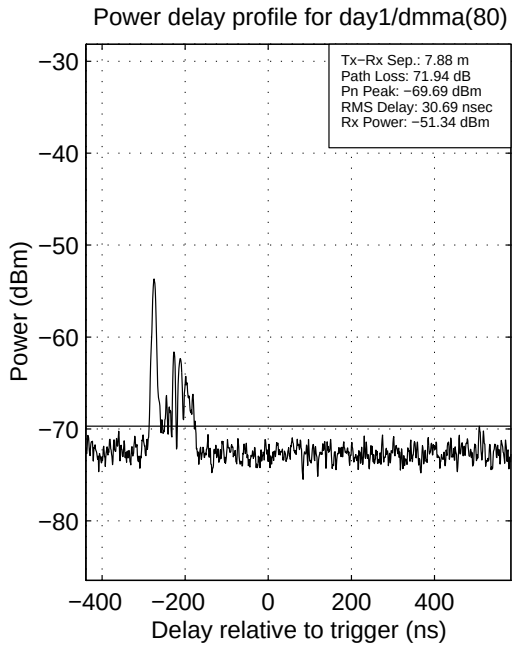
Power delay profile for day1/dmma(80)
Tx−Rx Sep.: 7.88 m
Path Loss: 71.94 dB
Pn Peak: −69.69 dBm
RMS Delay: 30.69 nsec
Rx Power: −51.34 dBm
Power (dBm)
−30
−40
−50
−60
−70
−80
−400
−200
0
200
400
Delay relative to trigger (ns)

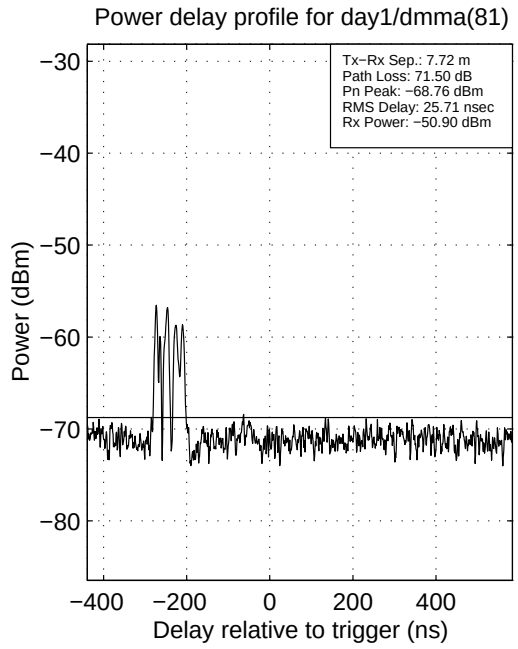
Power delay profile for day1/dmma(81)
Tx−Rx Sep.: 7.72 m
Path Loss: 71.50 dB
Pn Peak: −68.76 dBm
RMS Delay: 25.71 nsec
Rx Power: −50.90 dBm
Power (dBm)
−30
−40
−50
−60
−70
−80
−400
−200
0
200
400
Delay relative to trigger (ns)

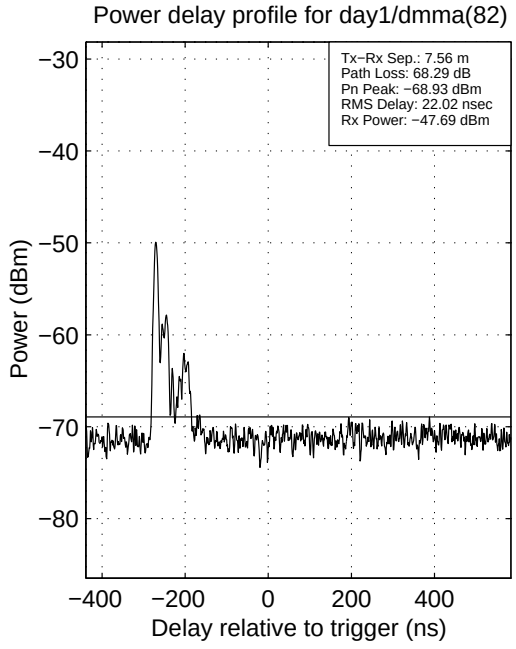
Power delay profile for day1/dmma(82)
Tx−Rx Sep.: 7.56 m
Path Loss: 68.29 dB
Pn Peak: −68.93 dBm
RMS Delay: 22.02 nsec
Rx Power: −47.69 dBm
Power (dBm)
−30
−40
−50
−60
−70
−80
−400
−200
0
200
400
Delay relative to trigger (ns)

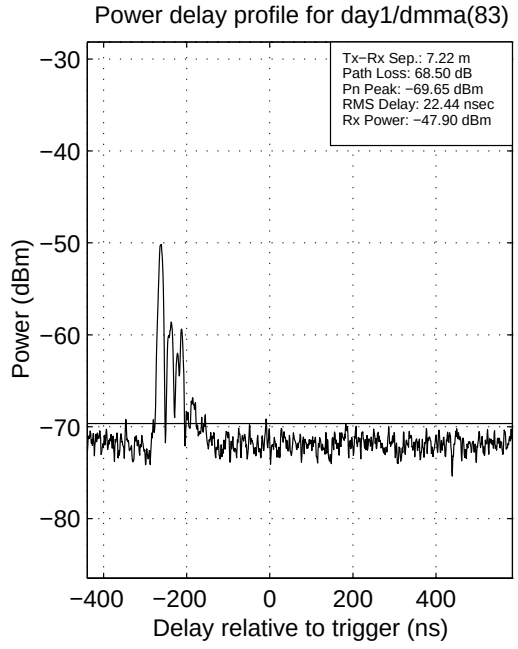
Power delay profile for day1/dmma(83)
Tx−Rx Sep.: 7.22 m
Path Loss: 68.50 dB
Pn Peak: −69.65 dBm
RMS Delay: 22.44 nsec
Rx Power: −47.90 dBm
Power (dBm)
−30
−40
−50
−60
−70
−80
−400
−200
0
200
400
Delay relative to trigger (ns)

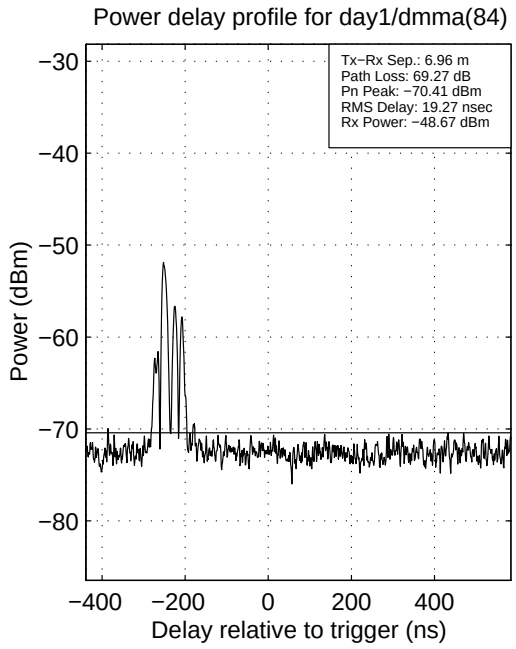
Power delay profile for day1/dmma(84)
Tx−Rx Sep.: 6.96 m
Path Loss: 69.27 dB
Pn Peak: −70.41 dBm
RMS Delay: 19.27 nsec
Rx Power: −48.67 dBm
Power (dBm)
−30
−40
−50
−60
−70
−80
−400
−200
0
200
400
Delay relative to trigger (ns)

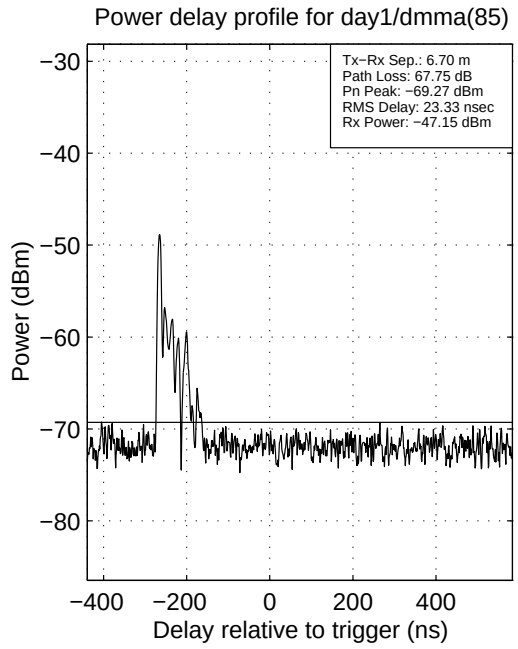
Power delay profile for day1/dmma(85)
Tx−Rx Sep.: 6.70 m
Path Loss: 67.75 dB
Pn Peak: −69.27 dBm
RMS Delay: 23.33 nsec
Rx Power: −47.15 dBm
Power (dBm)
−30
−40
−50
−60
−70
−80
−400
−200
0
200
400
Delay relative to trigger (ns)

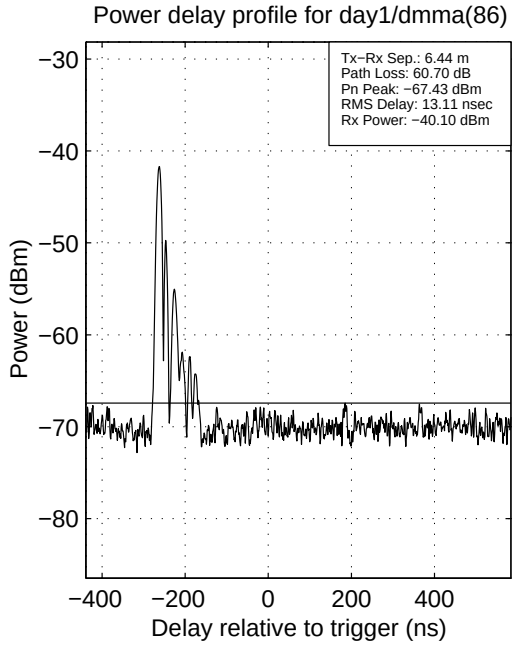
Power delay profile for day1/dmma(86)
Tx−Rx Sep.: 6.44 m
Path Loss: 60.70 dB
Pn Peak: −67.43 dBm
RMS Delay: 13.11 nsec
Rx Power: −40.10 dBm
Power (dBm)
−30
−40
−50
−60
−70
−80
−400
−200
0
200
400
Delay relative to trigger (ns)

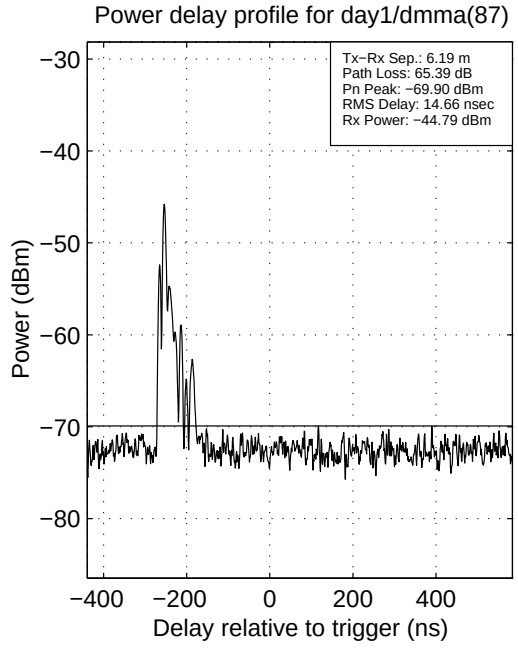
Power delay profile for day1/dmma(87)
Tx−Rx Sep.: 6.19 m
Path Loss: 65.39 dB
Pn Peak: −69.90 dBm
RMS Delay: 14.66 nsec
Rx Power: −44.79 dBm
Power (dBm)
−30
−40
−50
−60
−70
−80
−400
−200
0
200
400
Delay relative to trigger (ns)

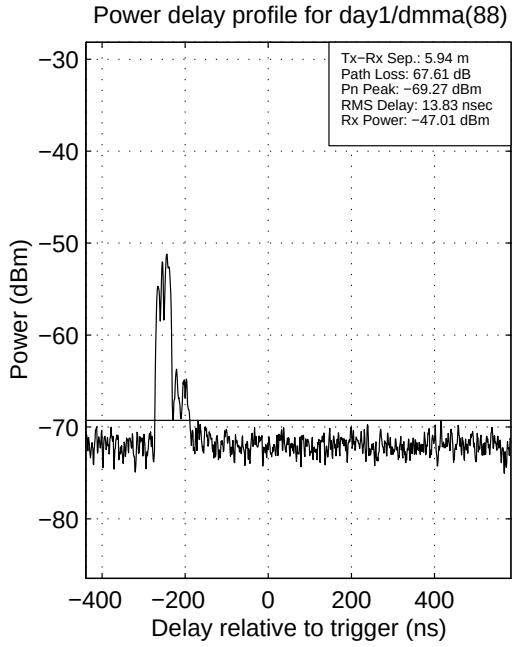
Power delay profile for day1/dmma(88)
Tx−Rx Sep.: 5.94 m
Path Loss: 67.61 dB
Pn Peak: −69.27 dBm
RMS Delay: 13.83 nsec
Rx Power: −47.01 dBm
Power (dBm)
−30
−40
−50
−60
−70
−80
−400
−200
0
200
400
Delay relative to trigger (ns)

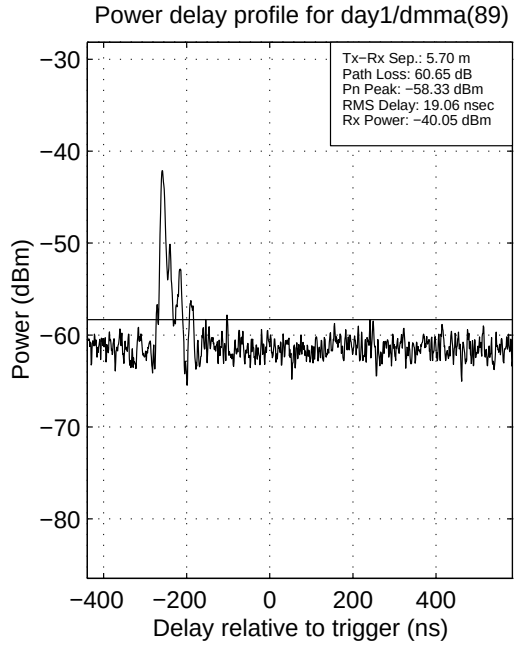
Power delay profile for day1/dmma(89)
Tx−Rx Sep.: 5.70 m
Path Loss: 60.65 dB
Pn Peak: −58.33 dBm
RMS Delay: 19.06 nsec
Rx Power: −40.05 dBm
Power (dBm)
−30
−40
−50
−60
−70
−80
−400
−200
0
200
400
Delay relative to trigger (ns)

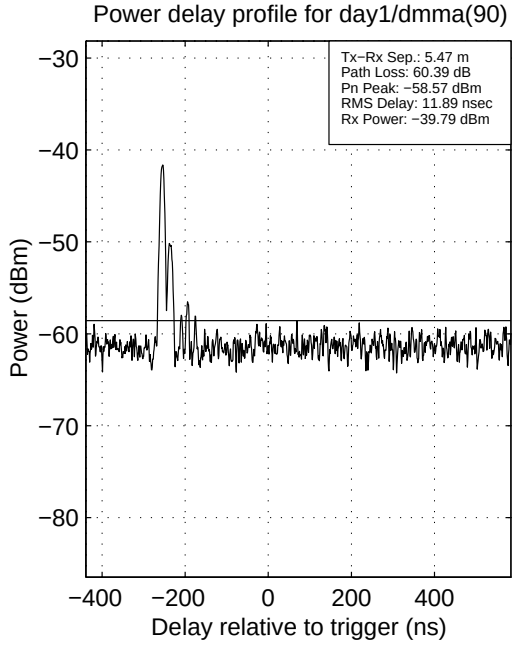
Power delay profile for day1/dmma(90)
Tx−Rx Sep.: 5.47 m
Path Loss: 60.39 dB
Pn Peak: −58.57 dBm
RMS Delay: 11.89 nsec
Rx Power: −39.79 dBm
Power (dBm)
−30
−40
−50
−60
−70
−80
−400
−200
0
200
400
Delay relative to trigger (ns)

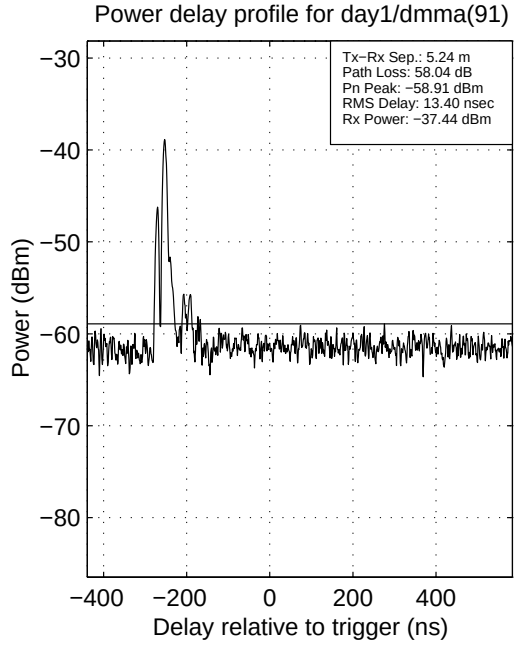
Power delay profile for day1/dmma(91)
Tx−Rx Sep.: 5.24 m
Path Loss: 58.04 dB
Pn Peak: −58.91 dBm
RMS Delay: 13.40 nsec
Rx Power: −37.44 dBm
Power (dBm)
−30
−40
−50
−60
−70
−80
−400
−200
0
200
400
Delay relative to trigger (ns)

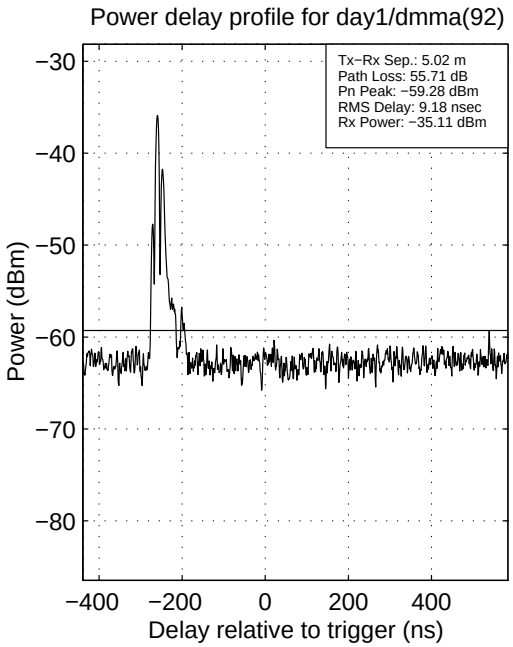
Power delay profile for day1/dmma(92)
Tx−Rx Sep.: 5.02 m
Path Loss: 55.71 dB
Pn Peak: −59.28 dBm
RMS Delay: 9.18 nsec
Rx Power: −35.11 dBm
Power (dBm)
−30
−40
−50
−60
−70
−80
−400
−200
0
200
400
Delay relative to trigger (ns)

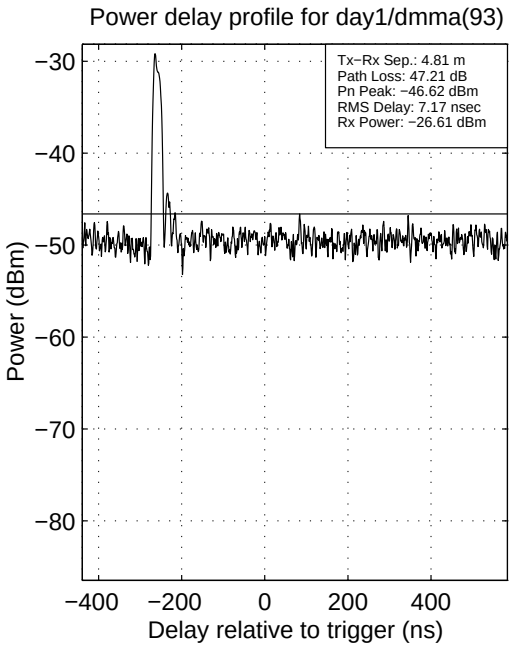
Power delay profile for day1/dmma(93)
Tx−Rx Sep.: 4.81 m
Path Loss: 47.21 dB
Pn Peak: −46.62 dBm
RMS Delay: 7.17 nsec
Rx Power: −26.61 dBm
Power (dBm)
−30
−40
−50
−60
−70
−80
−400
−200
0
200
400
Delay relative to trigger (ns)

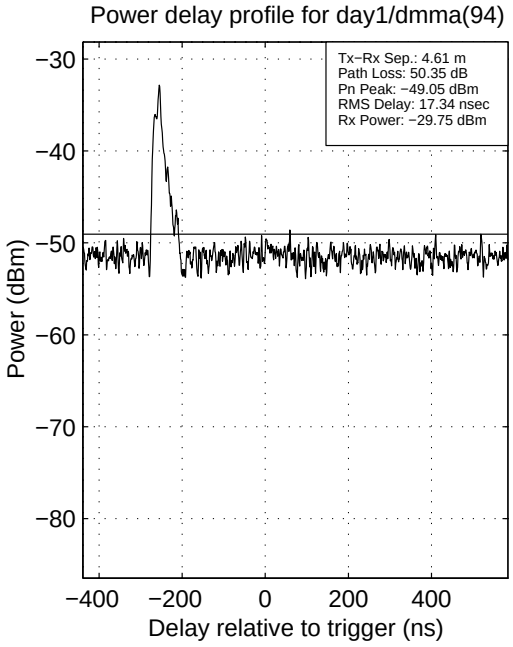
Power delay profile for day1/dmma(94)
Tx−Rx Sep.: 4.61 m
Path Loss: 50.35 dB
Pn Peak: −49.05 dBm
RMS Delay: 17.34 nsec
Rx Power: −29.75 dBm
Power (dBm)
−30
−40
−50
−60
−70
−80
−400
−200
0
200
400
Delay relative to trigger (ns)

Appendix C

Power Delay Profiles at Measurement Site 2

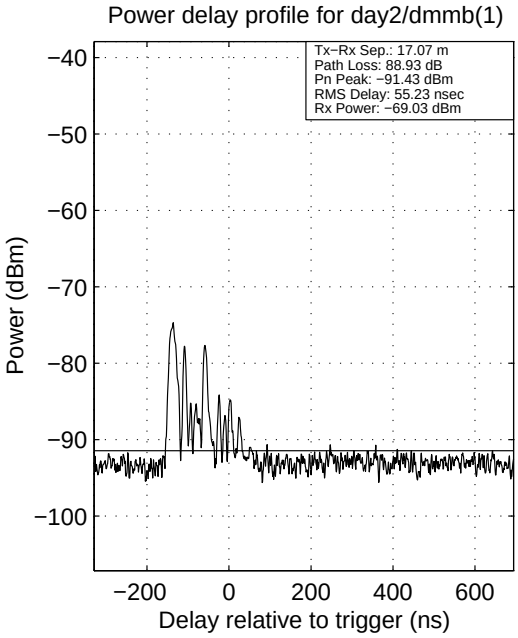
Power delay profile for day2/dmmb(1)
Tx−Rx Sep.: 17.07 m
Path Loss: 88.93 dB
Pn Peak: −91.43 dBm
RMS Delay: 55.23 nsec
Rx Power: −69.03 dBm
Power (dBm)
−40
−50
−60
−70
−80
−90
−100
−200
0
200
400
600
Delay relative to trigger (ns)

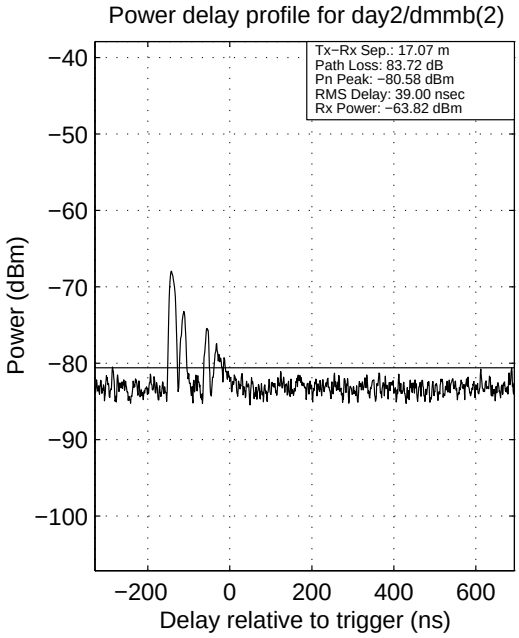
Power delay profile for day2/dmmb(2)
Tx−Rx Sep.: 17.07 m
Path Loss: 83.72 dB
Pn Peak: −80.58 dBm
RMS Delay: 39.00 nsec
Rx Power: −63.82 dBm
Power (dBm)
−40
−50
−60
−70
−80
−90
−100
−200
0
200
400
600
Delay relative to trigger (ns)

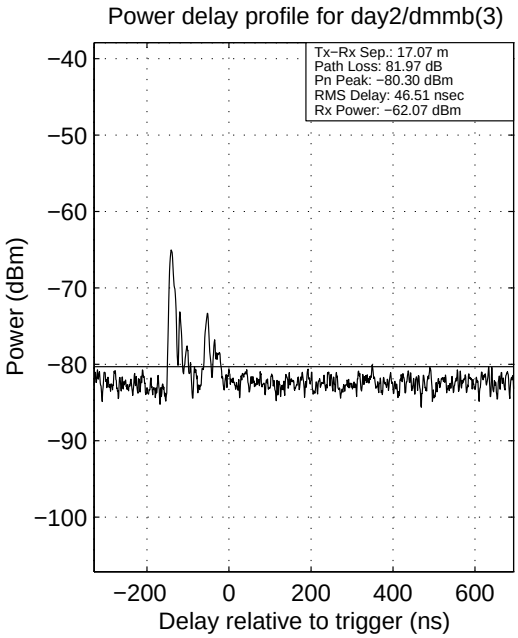
Power delay profile for day2/dmmb(3)
Tx−Rx Sep.: 17.07 m
Path Loss: 81.97 dB
Pn Peak: −80.30 dBm
RMS Delay: 46.51 nsec
Rx Power: −62.07 dBm
Power (dBm)
−40
−50
−60
−70
−80
−90
−100
−200
0
200
400
600
Delay relative to trigger (ns)

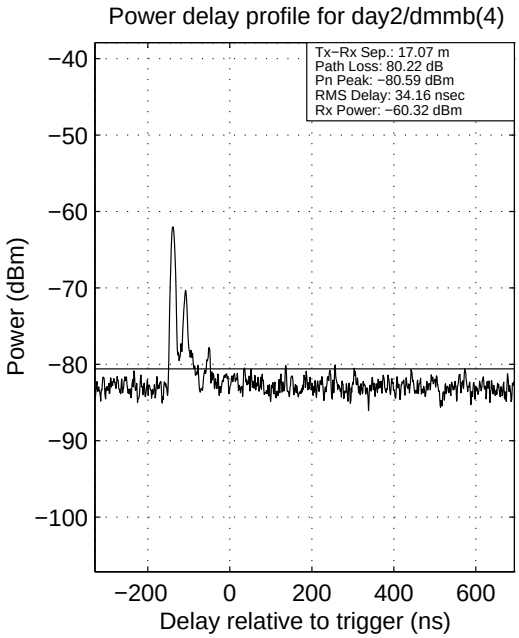
Power delay profile for day2/dmmb(4)
Tx−Rx Sep.: 17.07 m
Path Loss: 80.22 dB
Pn Peak: −80.59 dBm
RMS Delay: 34.16 nsec
Rx Power: −60.32 dBm
Power (dBm)
−40
−50
−60
−70
−80
−90
−100
−200
0
200
400
600
Delay relative to trigger (ns)

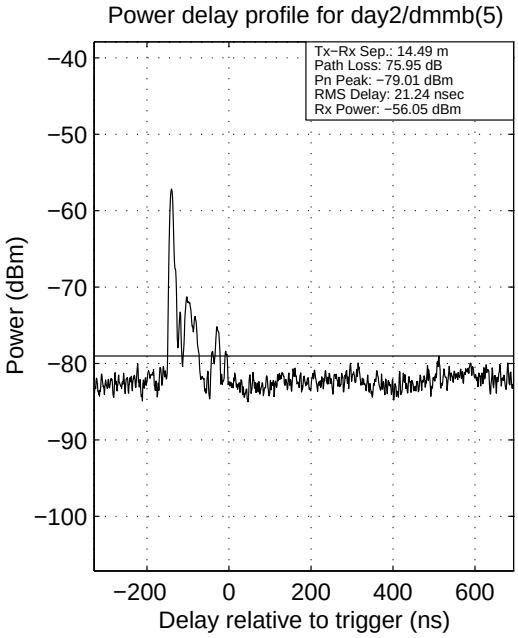
Power delay profile for day2/dmmb(5)
Tx−Rx Sep.: 14.49 m
Path Loss: 75.95 dB
Pn Peak: −79.01 dBm
RMS Delay: 21.24 nsec
Rx Power: −56.05 dBm
Power (dBm)
−40
−50
−60
−70
−80
−90
−100
−200
0
200
400
600
Delay relative to trigger (ns)

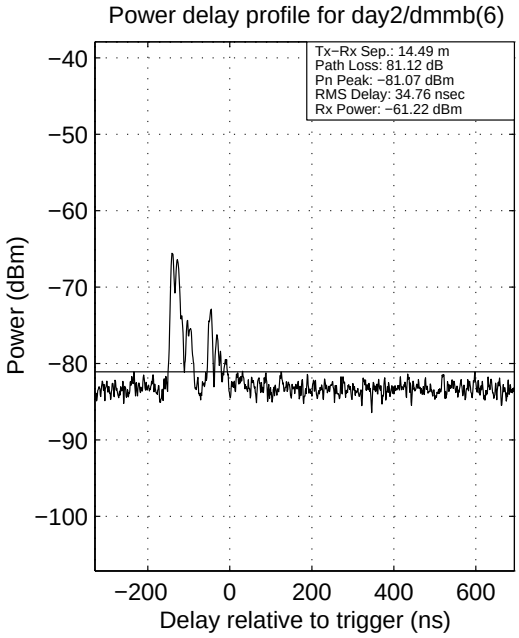
Power delay profile for day2/dmmb(6)
Tx−Rx Sep.: 14.49 m
Path Loss: 81.12 dB
Pn Peak: −81.07 dBm
RMS Delay: 34.76 nsec
Rx Power: −61.22 dBm
Power (dBm)
−40
−50
−60
−70
−80
−90
−100
−200
0
200
400
600
Delay relative to trigger (ns)

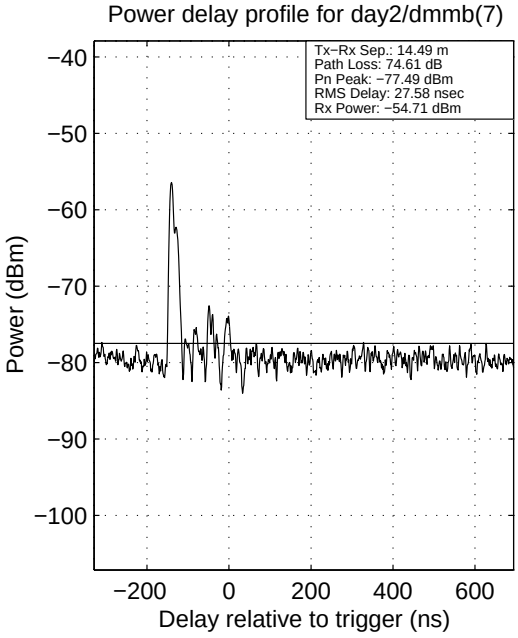
Power delay profile for day2/dmmb(7)
Tx−Rx Sep.: 14.49 m
Path Loss: 74.61 dB
Pn Peak: −77.49 dBm
RMS Delay: 27.58 nsec
Rx Power: −54.71 dBm
Power (dBm)
−40
−50
−60
−70
−80
−90
−100
−200
0
200
400
600
Delay relative to trigger (ns)

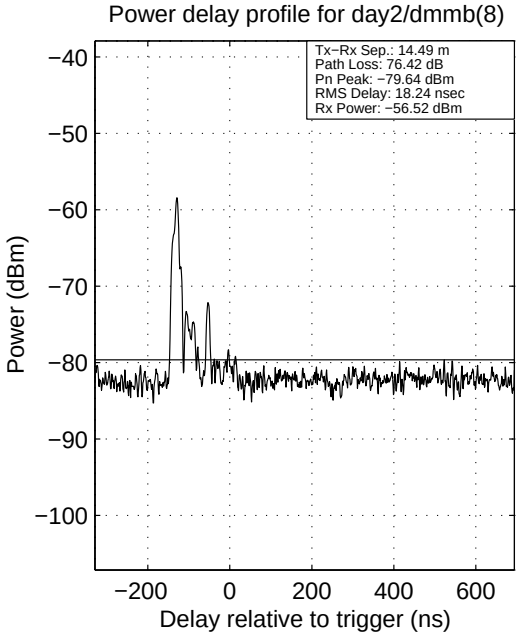
Power delay profile for day2/dmmb(8)
Tx−Rx Sep.: 14.49 m
Path Loss: 76.42 dB
Pn Peak: −79.64 dBm
RMS Delay: 18.24 nsec
Rx Power: −56.52 dBm
Power (dBm)
−40
−50
−60
−70
−80
−90
−100
−200
0
200
400
600
Delay relative to trigger (ns)

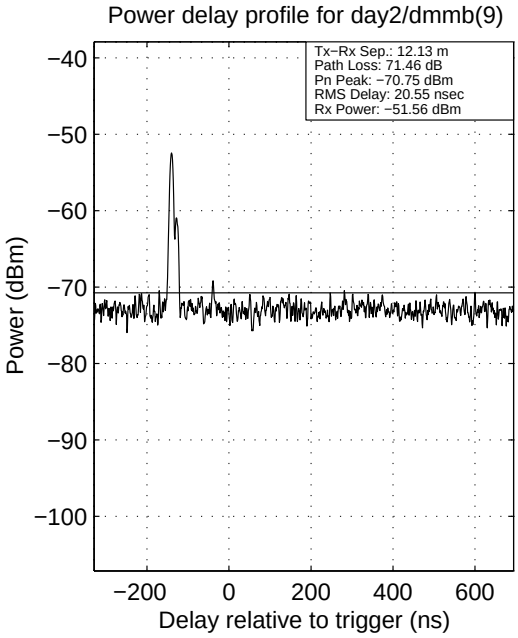
Power delay profile for day2/dmmb(9)
Tx−Rx Sep.: 12.13 m
Path Loss: 71.46 dB
Pn Peak: −70.75 dBm
RMS Delay: 20.55 nsec
Rx Power: −51.56 dBm
Power (dBm)
−40
−50
−60
−70
−80
−90
−100
−200
0
200
400
600
Delay relative to trigger (ns)

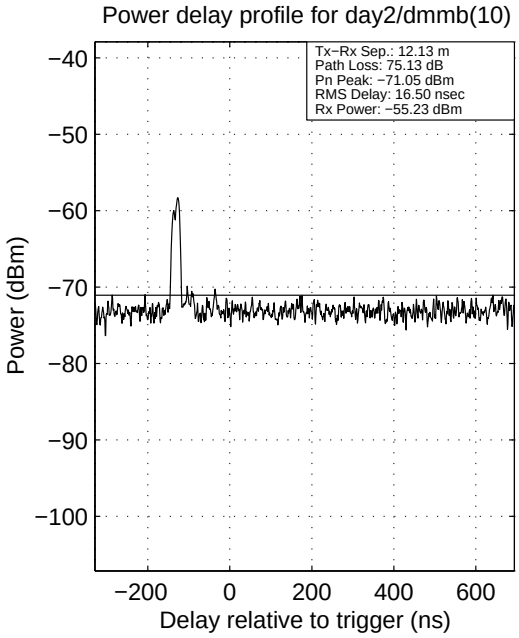
Power delay profile for day2/dmmb(10)
Tx−Rx Sep.: 12.13 m
Path Loss: 75.13 dB
Pn Peak: −71.05 dBm
RMS Delay: 16.50 nsec
Rx Power: −55.23 dBm
Power (dBm)
−40
−50
−60
−70
−80
−90
−100
−200
0
200
400
600
Delay relative to trigger (ns)

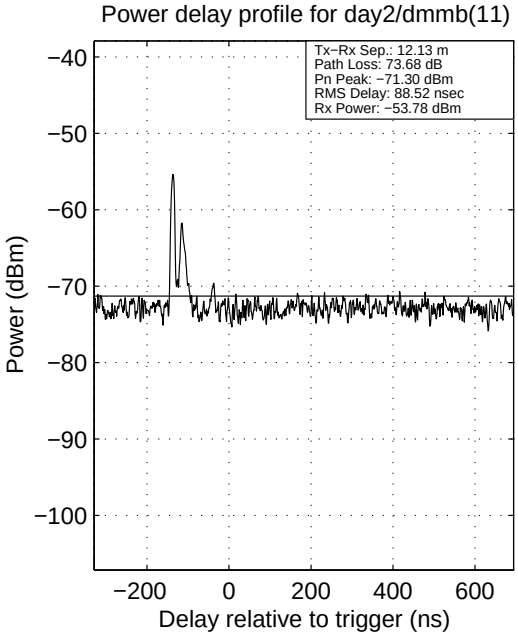
Power delay profile for day2/dmmb(11)
Tx−Rx Sep.: 12.13 m
Path Loss: 73.68 dB
Pn Peak: −71.30 dBm
RMS Delay: 88.52 nsec
Rx Power: −53.78 dBm
Power (dBm)
−40
−50
−60
−70
−80
−90
−100
−200
0
200
400
600
Delay relative to trigger (ns)

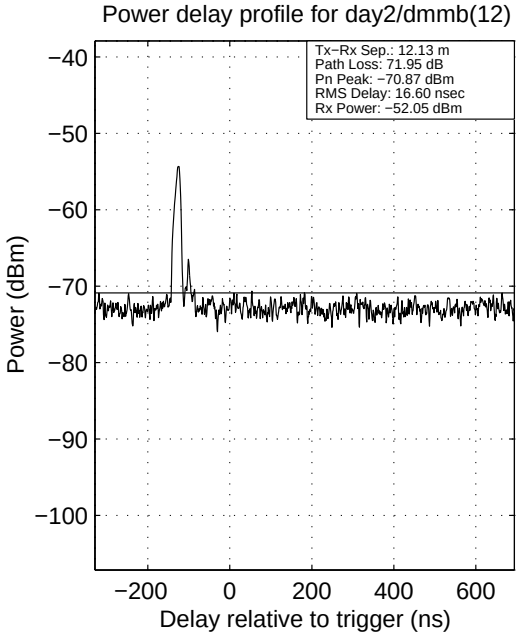
Power delay profile for day2/dmmb(12)
Tx−Rx Sep.: 12.13 m
Path Loss: 71.95 dB
Pn Peak: −70.87 dBm
RMS Delay: 16.60 nsec
Rx Power: −52.05 dBm
Power (dBm)
−40
−50
−60
−70
−80
−90
−100
−200
0
200
400
600
Delay relative to trigger (ns)

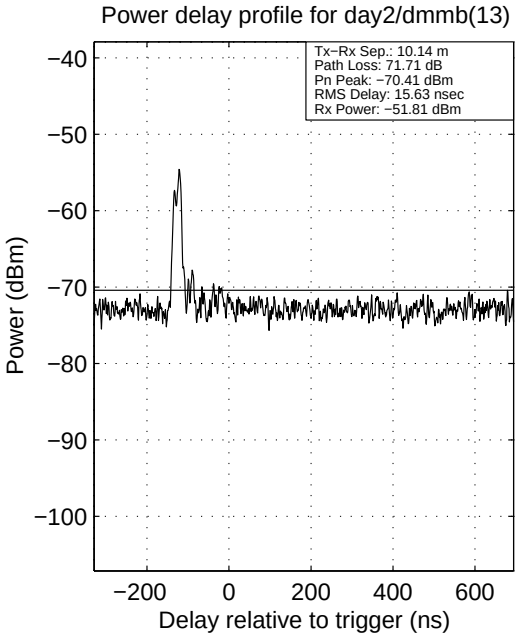
Power delay profile for day2/dmmb(13)
Tx−Rx Sep.: 10.14 m
Path Loss: 71.71 dB
Pn Peak: −70.41 dBm
RMS Delay: 15.63 nsec
Rx Power: −51.81 dBm
Power (dBm)
−40
−50
−60
−70
−80
−90
−100
−200
0
200
400
600
Delay relative to trigger (ns)

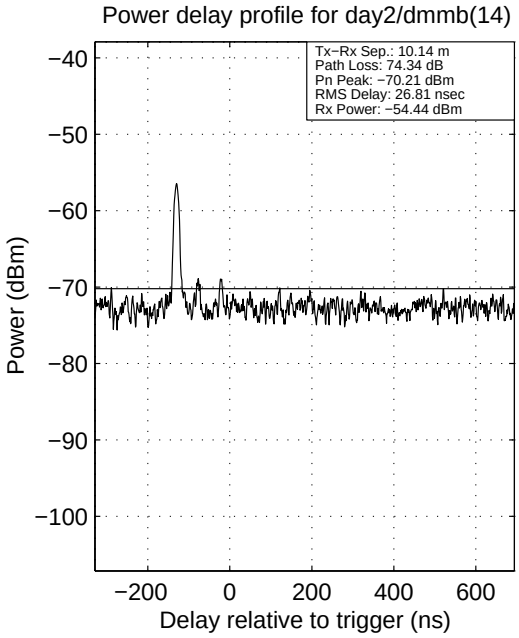
Power delay profile for day2/dmmb(14)
Tx−Rx Sep.: 10.14 m
Path Loss: 74.34 dB
Pn Peak: −70.21 dBm
RMS Delay: 26.81 nsec
Rx Power: −54.44 dBm
Power (dBm)
−40
−50
−60
−70
−80
−90
−100
−200
0
200
400
600
Delay relative to trigger (ns)

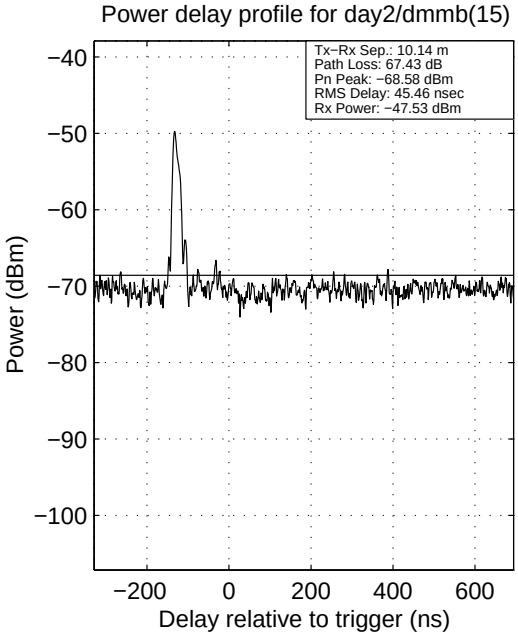
Power delay profile for day2/dmmb(15)
Tx−Rx Sep.: 10.14 m
Path Loss: 67.43 dB
Pn Peak: −68.58 dBm
RMS Delay: 45.46 nsec
Rx Power: −47.53 dBm
Power (dBm)
−40
−50
−60
−70
−80
−90
−100
−200
0
200
400
600
Delay relative to trigger (ns)

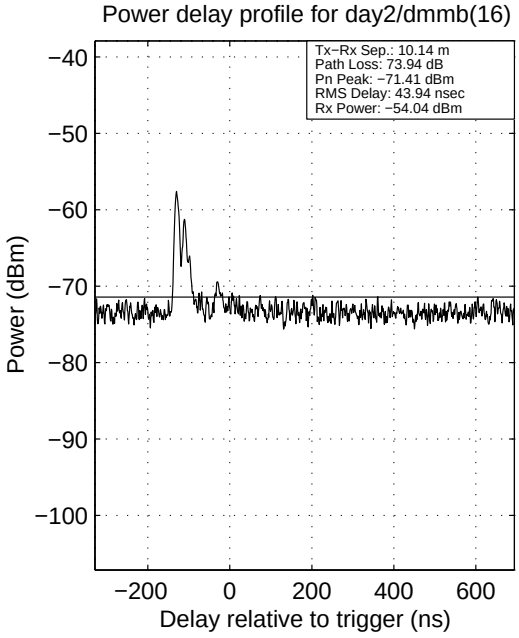
Power delay profile for day2/dmmb(16)
Tx−Rx Sep.: 10.14 m
Path Loss: 73.94 dB
Pn Peak: −71.41 dBm
RMS Delay: 43.94 nsec
Rx Power: −54.04 dBm
Power (dBm)
−40
−50
−60
−70
−80
−90
−100
−200
0
200
400
600
Delay relative to trigger (ns)

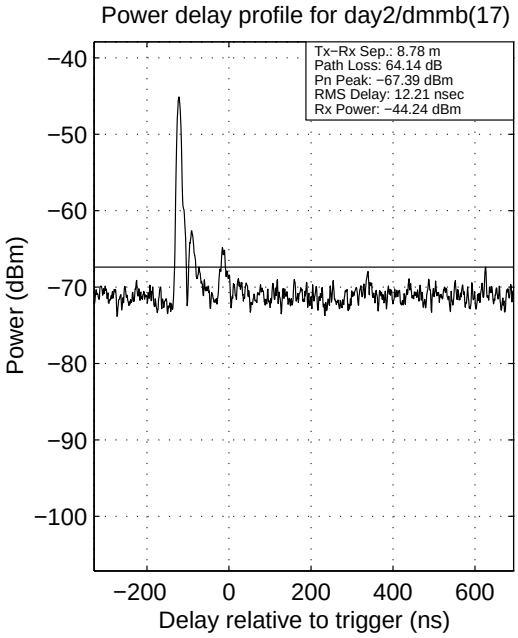
Power delay profile for day2/dmmb(17)
Tx−Rx Sep.: 8.78 m
Path Loss: 64.14 dB
Pn Peak: −67.39 dBm
RMS Delay: 12.21 nsec
Rx Power: −44.24 dBm
Power (dBm)
−40
−50
−60
−70
−80
−90
−100
−200
0
200
400
600
Delay relative to trigger (ns)

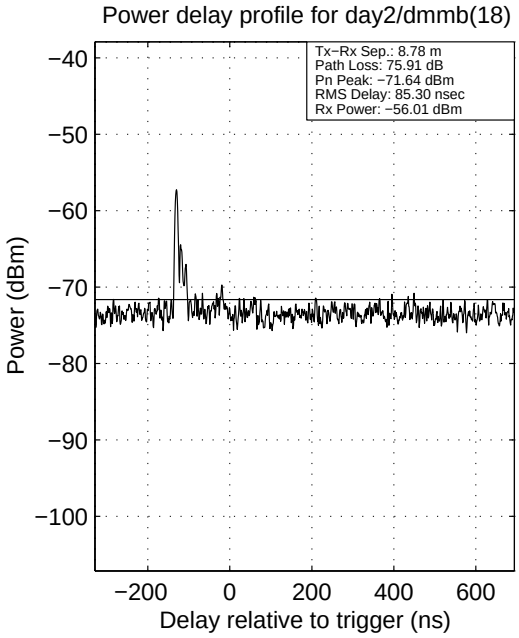
Power delay profile for day2/dmmb(18)
Tx−Rx Sep.: 8.78 m
Path Loss: 75.91 dB
Pn Peak: −71.64 dBm
RMS Delay: 85.30 nsec
Rx Power: −56.01 dBm
Power (dBm)
−40
−50
−60
−70
−80
−90
−100
−200
0
200
400
600
Delay relative to trigger (ns)

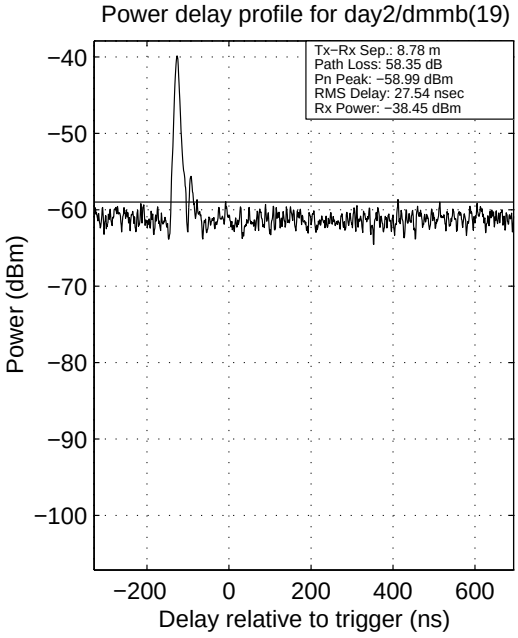
Power delay profile for day2/dmmb(19)
Tx−Rx Sep.: 8.78 m
Path Loss: 58.35 dB
Pn Peak: −58.99 dBm
RMS Delay: 27.54 nsec
Rx Power: −38.45 dBm
Power (dBm)
−40
−50
−60
−70
−80
−90
−100
−200
0
200
400
600
Delay relative to trigger (ns)

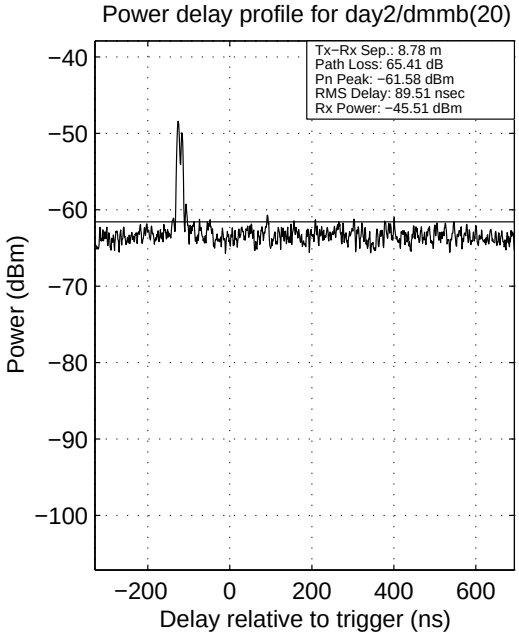
Power delay profile for day2/dmmb(20)
Tx−Rx Sep.: 8.78 m
Path Loss: 65.41 dB
Pn Peak: −61.58 dBm
RMS Delay: 89.51 nsec
Rx Power: −45.51 dBm
Power (dBm)
−40
−50
−60
−70
−80
−90
−100
−200
0
200
400
600
Delay relative to trigger (ns)

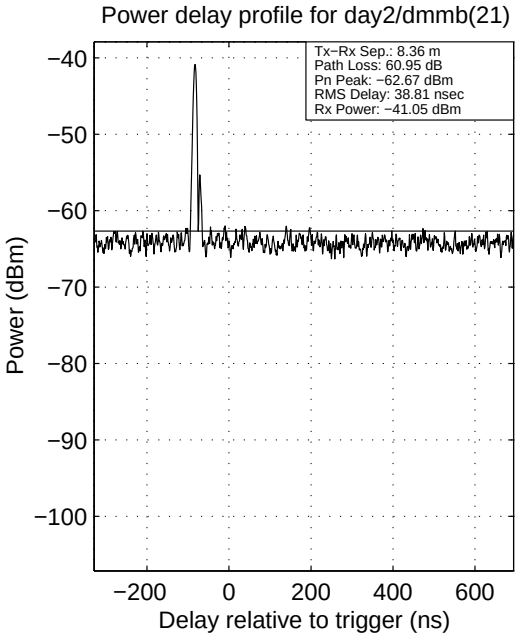
Power delay profile for day2/dmmb(21)
Tx−Rx Sep.: 8.36 m
Path Loss: 60.95 dB
Pn Peak: −62.67 dBm
RMS Delay: 38.81 nsec
Rx Power: −41.05 dBm
Power (dBm)
−40
−50
−60
−70
−80
−90
−100
−200
0
200
400
600
Delay relative to trigger (ns)

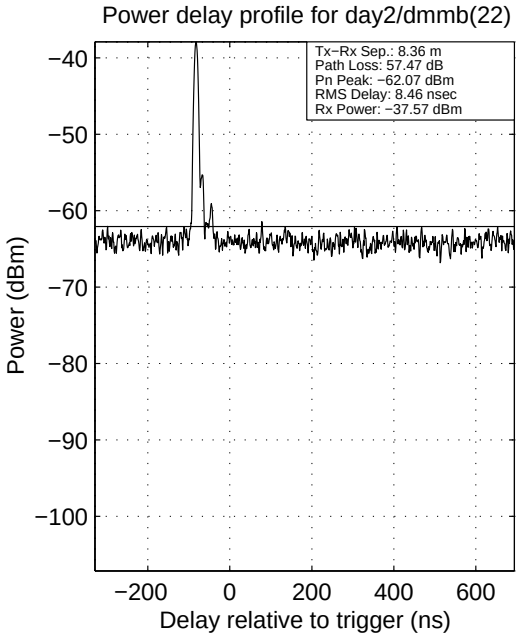
Power delay profile for day2/dmmb(22)
Tx−Rx Sep.: 8.36 m
Path Loss: 57.47 dB
Pn Peak: −62.07 dBm
RMS Delay: 8.46 nsec
Rx Power: −37.57 dBm
Power (dBm)
−40
−50
−60
−70
−80
−90
−100
−200
0
200
400
600
Delay relative to trigger (ns)

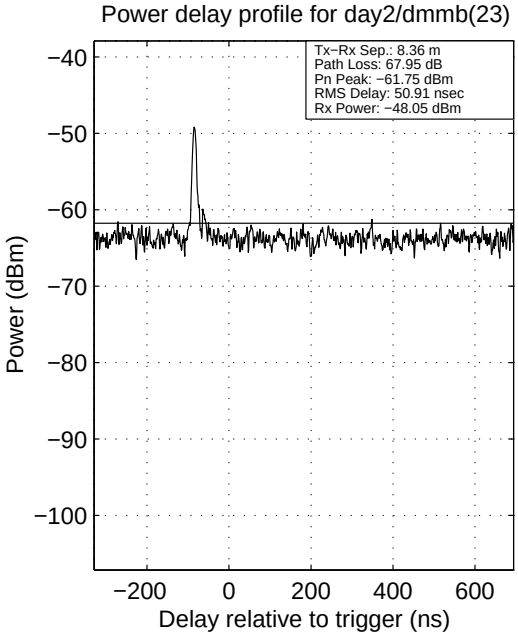
Power delay profile for day2/dmmb(23)
Tx−Rx Sep.: 8.36 m
Path Loss: 67.95 dB
Pn Peak: −61.75 dBm
RMS Delay: 50.91 nsec
Rx Power: −48.05 dBm
Power (dBm)
−40
−50
−60
−70
−80
−90
−100
−200
0
200
400
600
Delay relative to trigger (ns)

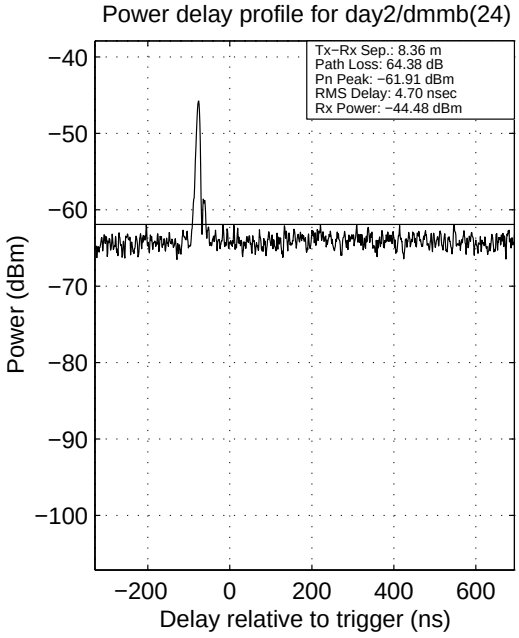
Power delay profile for day2/dmmb(24)
Tx−Rx Sep.: 8.36 m
Path Loss: 64.38 dB
Pn Peak: −61.91 dBm
RMS Delay: 4.70 nsec
Rx Power: −44.48 dBm
Power (dBm)
−40
−50
−60
−70
−80
−90
−100
−200
0
200
400
600
Delay relative to trigger (ns)

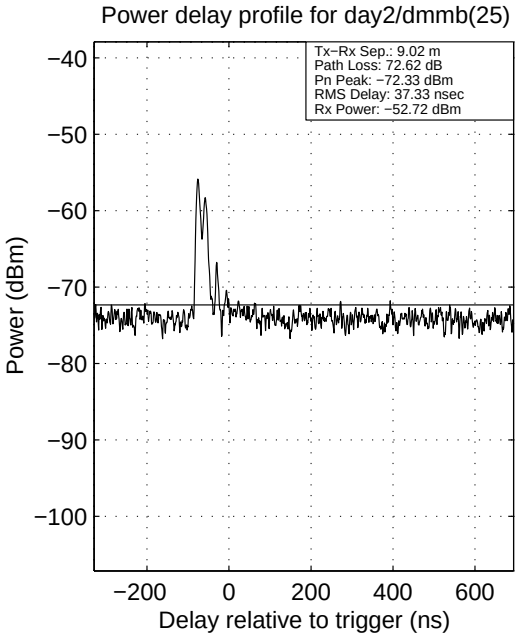
Power delay profile for day2/dmmb(25)
Tx−Rx Sep.: 9.02 m
Path Loss: 72.62 dB
Pn Peak: −72.33 dBm
RMS Delay: 37.33 nsec
Rx Power: −52.72 dBm
Power (dBm)
−40
−50
−60
−70
−80
−90
−100
−200
0
200
400
600
Delay relative to trigger (ns)

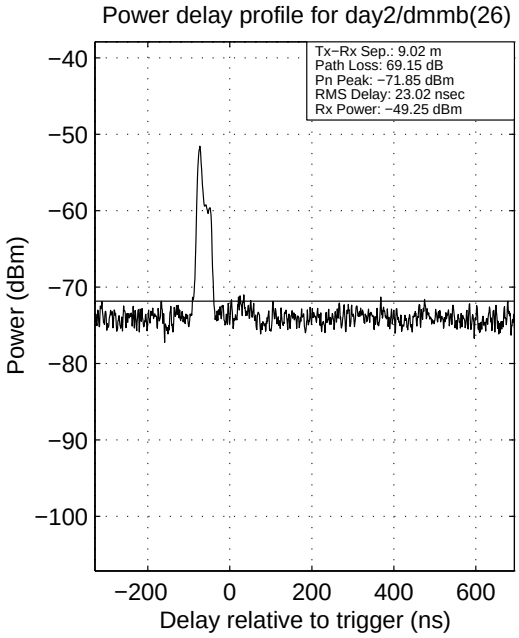
Power delay profile for day2/dmmb(26)
Tx−Rx Sep.: 9.02 m
Path Loss: 69.15 dB
Pn Peak: −71.85 dBm
RMS Delay: 23.02 nsec
Rx Power: −49.25 dBm
Power (dBm)
−40
−50
−60
−70
−80
−90
−100
−200
0
200
400
600
Delay relative to trigger (ns)

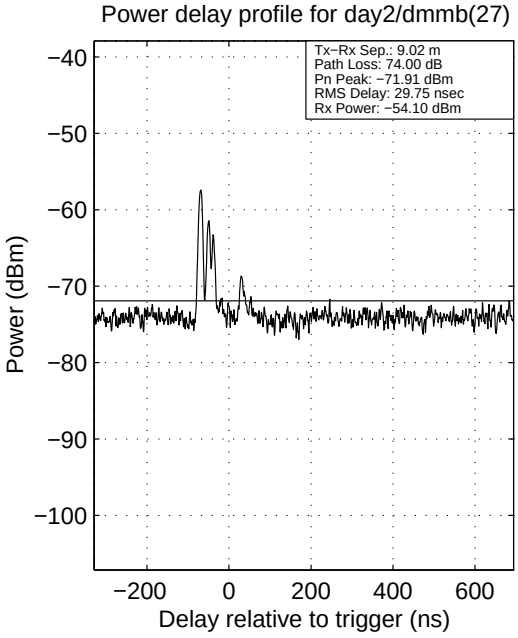
Power delay profile for day2/dmmb(27)
Tx−Rx Sep.: 9.02 m
Path Loss: 74.00 dB
Pn Peak: −71.91 dBm
RMS Delay: 29.75 nsec
Rx Power: −54.10 dBm
Power (dBm)
−40
−50
−60
−70
−80
−90
−100
−200
0
200
400
600
Delay relative to trigger (ns)

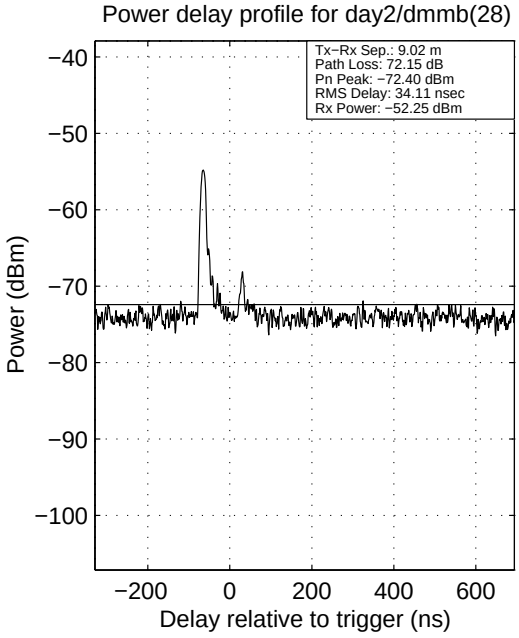
Power delay profile for day2/dmmb(28)
Tx−Rx Sep.: 9.02 m
Path Loss: 72.15 dB
Pn Peak: −72.40 dBm
RMS Delay: 34.11 nsec
Rx Power: −52.25 dBm
Power (dBm)
−40
−50
−60
−70
−80
−90
−100
−200
0
200
400
600
Delay relative to trigger (ns)

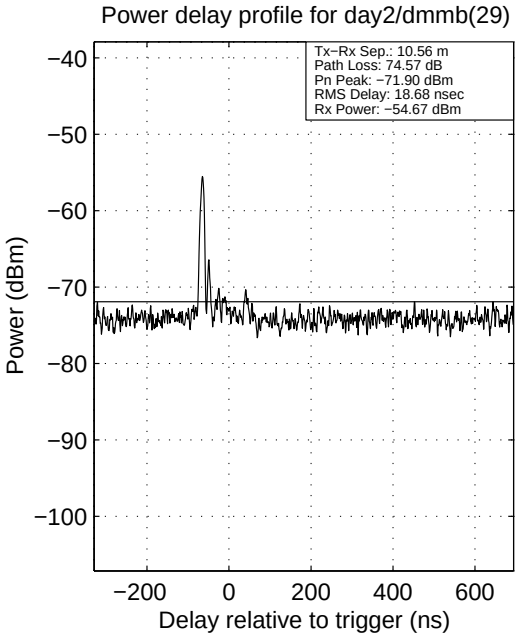
Power delay profile for day2/dmmb(29)
Tx−Rx Sep.: 10.56 m
Path Loss: 74.57 dB
Pn Peak: −71.90 dBm
RMS Delay: 18.68 nsec
Rx Power: −54.67 dBm
Power (dBm)
−40
−50
−60
−70
−80
−90
−100
−200
0
200
400
600
Delay relative to trigger (ns)

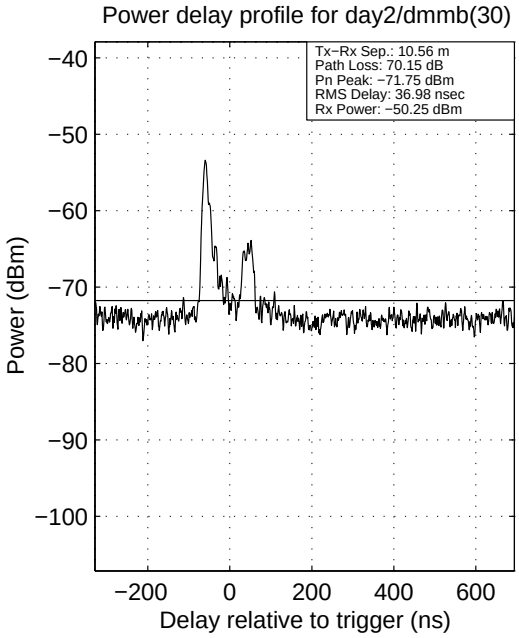
Power delay profile for day2/dmmb(30)
Tx−Rx Sep.: 10.56 m
Path Loss: 70.15 dB
Pn Peak: −71.75 dBm
RMS Delay: 36.98 nsec
Rx Power: −50.25 dBm
Power (dBm)
−40
−50
−60
−70
−80
−90
−100
−200
0
200
400
600
Delay relative to trigger (ns)

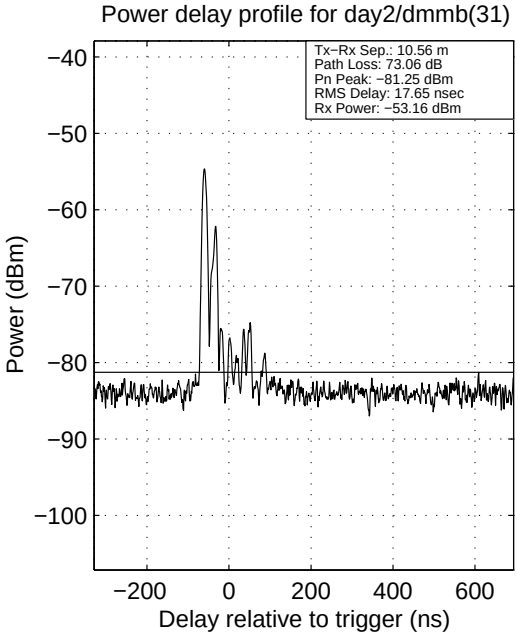
Power delay profile for day2/dmmb(31)
Tx−Rx Sep.: 10.56 m
Path Loss: 73.06 dB
Pn Peak: −81.25 dBm
RMS Delay: 17.65 nsec
Rx Power: −53.16 dBm
Power (dBm)
−40
−50
−60
−70
−80
−90
−100
−200
0
200
400
600
Delay relative to trigger (ns)

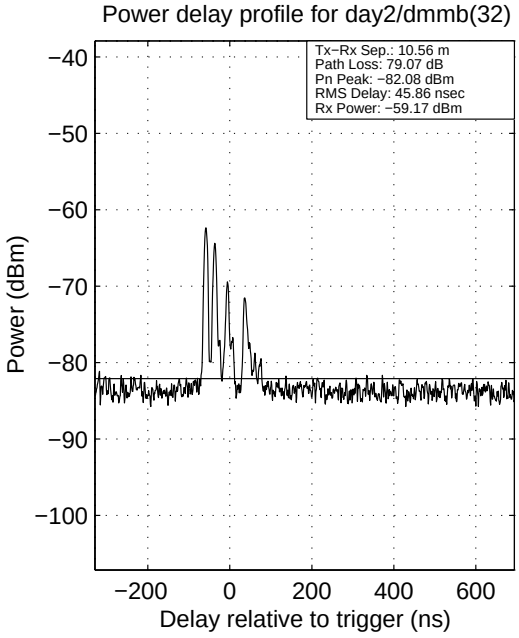
Power delay profile for day2/dmmb(32)
Tx−Rx Sep.: 10.56 m
Path Loss: 79.07 dB
Pn Peak: −82.08 dBm
RMS Delay: 45.86 nsec
Rx Power: −59.17 dBm
Power (dBm)
−40
−50
−60
−70
−80
−90
−100
−200
0
200
400
600
Delay relative to trigger (ns)

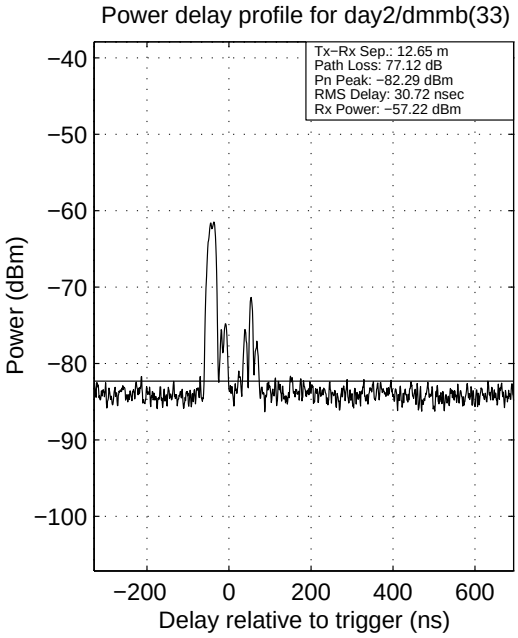
Power delay profile for day2/dmmb(33)
Tx−Rx Sep.: 12.65 m
Path Loss: 77.12 dB
Pn Peak: −82.29 dBm
RMS Delay: 30.72 nsec
Rx Power: −57.22 dBm
Power (dBm)
−40
−50
−60
−70
−80
−90
−100
−200
0
200
400
600
Delay relative to trigger (ns)

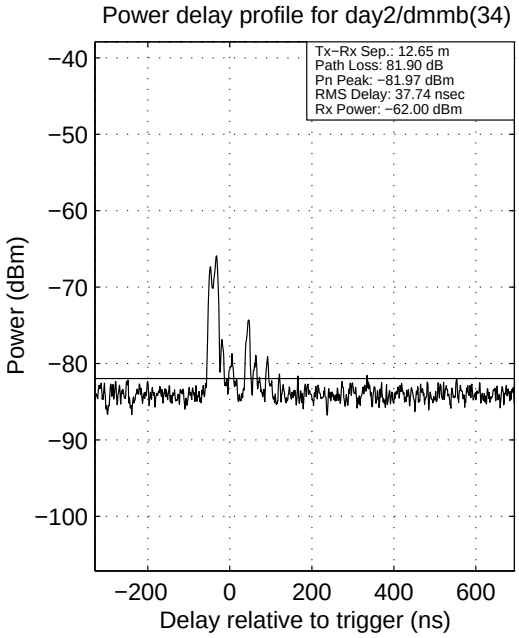
Power delay profile for day2/dmmb(34)
Tx−Rx Sep.: 12.65 m
Path Loss: 81.90 dB
Pn Peak: −81.97 dBm
RMS Delay: 37.74 nsec
Rx Power: −62.00 dBm
Power (dBm)
−40
−50
−60
−70
−80
−90
−100
−200
0
200
400
600
Delay relative to trigger (ns)

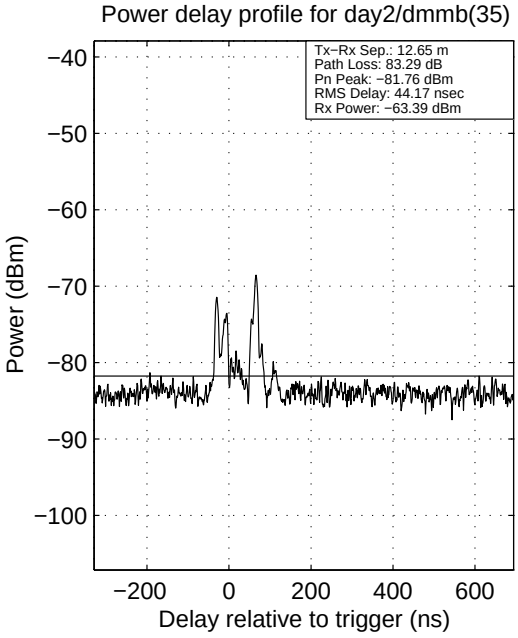
Power delay profile for day2/dmmb(35)
Tx−Rx Sep.: 12.65 m
Path Loss: 83.29 dB
Pn Peak: −81.76 dBm
RMS Delay: 44.17 nsec
Rx Power: −63.39 dBm
Power (dBm)
−40
−50
−60
−70
−80
−90
−100
−200
0
200
400
600
Delay relative to trigger (ns)

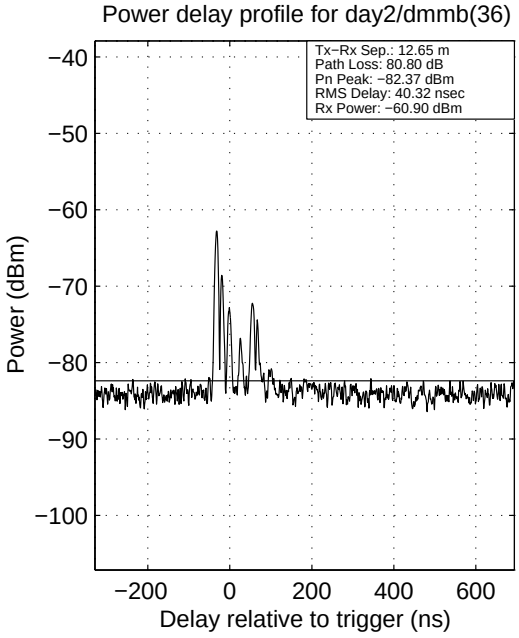
Power delay profile for day2/dmmb(36)
Tx−Rx Sep.: 12.65 m
Path Loss: 80.80 dB
Pn Peak: −82.37 dBm
RMS Delay: 40.32 nsec
Rx Power: −60.90 dBm
Power (dBm)
−40
−50
−60
−70
−80
−90
−100
−200
0
200
400
600
Delay relative to trigger (ns)

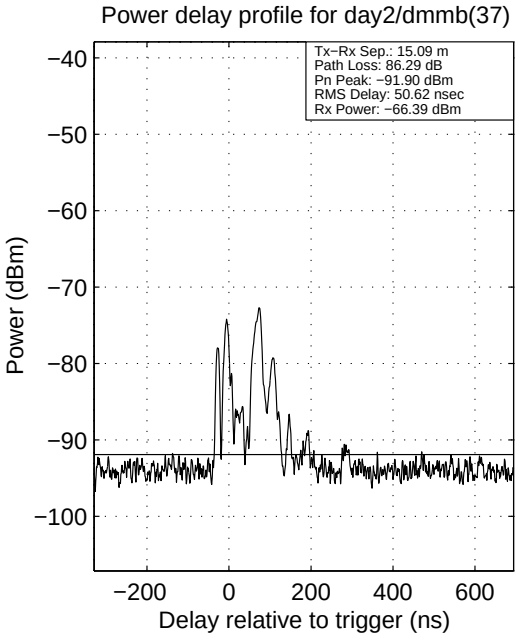
Power delay profile for day2/dmmb(37)
Tx−Rx Sep.: 15.09 m
Path Loss: 86.29 dB
Pn Peak: −91.90 dBm
RMS Delay: 50.62 nsec
Rx Power: −66.39 dBm
Power (dBm)
−40
−50
−60
−70
−80
−90
−100
−200
0
200
400
600
Delay relative to trigger (ns)

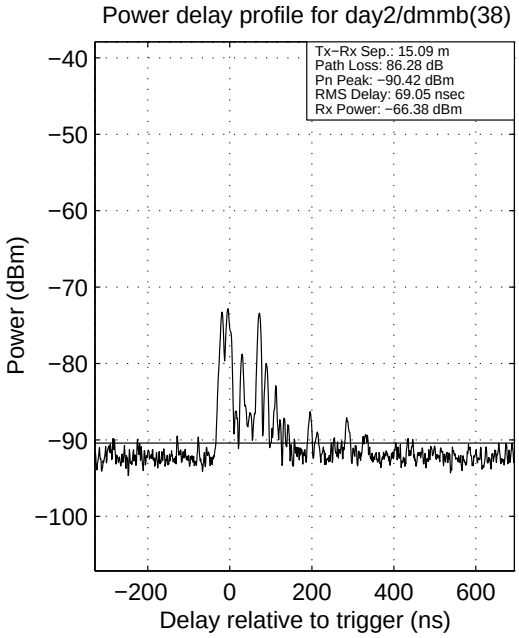
Power delay profile for day2/dmmb(38)
Tx−Rx Sep.: 15.09 m
Path Loss: 86.28 dB
Pn Peak: −90.42 dBm
RMS Delay: 69.05 nsec
Rx Power: −66.38 dBm
Power (dBm)
−40
−50
−60
−70
−80
−90
−100
−200
0
200
400
600
Delay relative to trigger (ns)

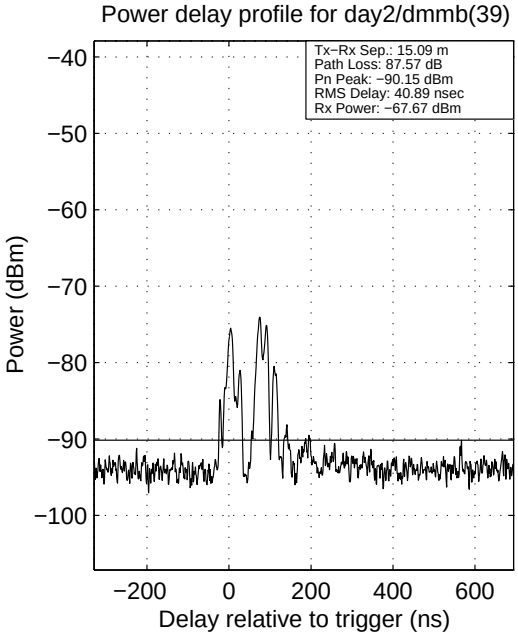
Power delay profile for day2/dmmb(39)
Tx−Rx Sep.: 15.09 m
Path Loss: 87.57 dB
Pn Peak: −90.15 dBm
RMS Delay: 40.89 nsec
Rx Power: −67.67 dBm
Power (dBm)
−40
−50
−60
−70
−80
−90
−100
−200
0
200
400
600
Delay relative to trigger (ns)

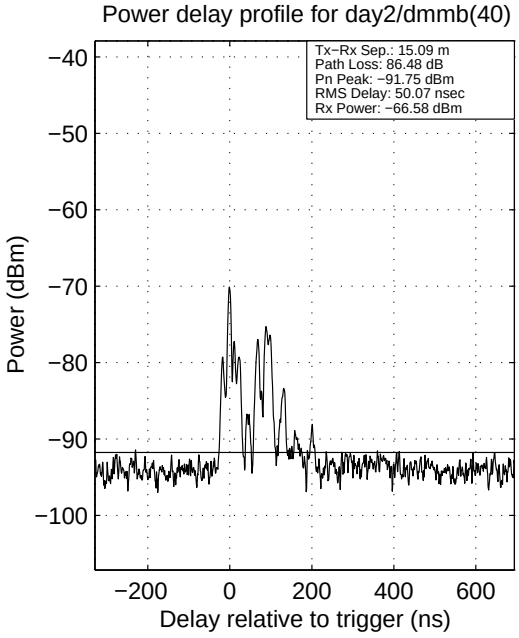
Power delay profile for day2/dmmb(40)
Tx−Rx Sep.: 15.09 m
Path Loss: 86.48 dB
Pn Peak: −91.75 dBm
RMS Delay: 50.07 nsec
Rx Power: −66.58 dBm
Power (dBm)
−40
−50
−60
−70
−80
−90
−100
−200
0
200
400
600
Delay relative to trigger (ns)

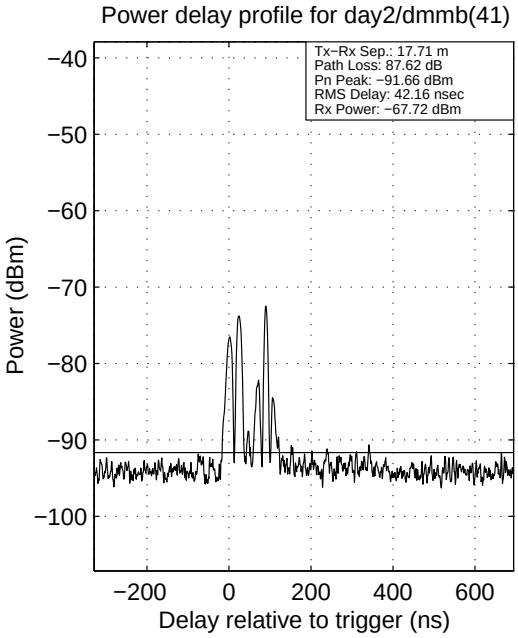
Power delay profile for day2/dmmb(41)
Tx−Rx Sep.: 17.71 m
Path Loss: 87.62 dB
Pn Peak: −91.66 dBm
RMS Delay: 42.16 nsec
Rx Power: −67.72 dBm
Power (dBm)
−40
−50
−60
−70
−80
−90
−100
−200
0
200
400
600
Delay relative to trigger (ns)

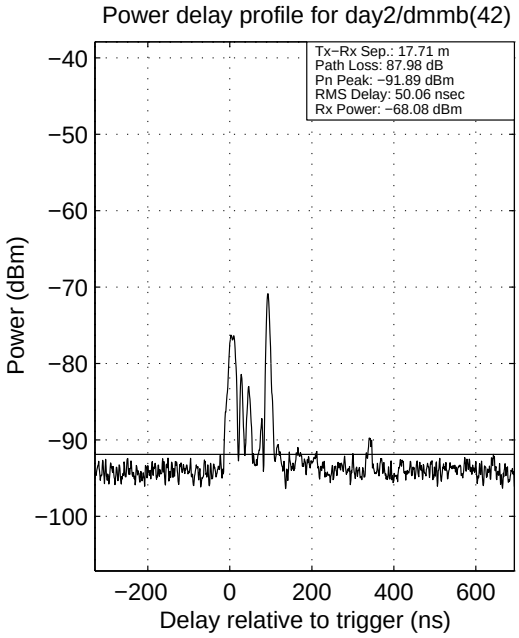
Power delay profile for day2/dmmb(42)
Tx−Rx Sep.: 17.71 m
Path Loss: 87.98 dB
Pn Peak: −91.89 dBm
RMS Delay: 50.06 nsec
Rx Power: −68.08 dBm
Power (dBm)
−40
−50
−60
−70
−80
−90
−100
−200
0
200
400
600
Delay relative to trigger (ns)

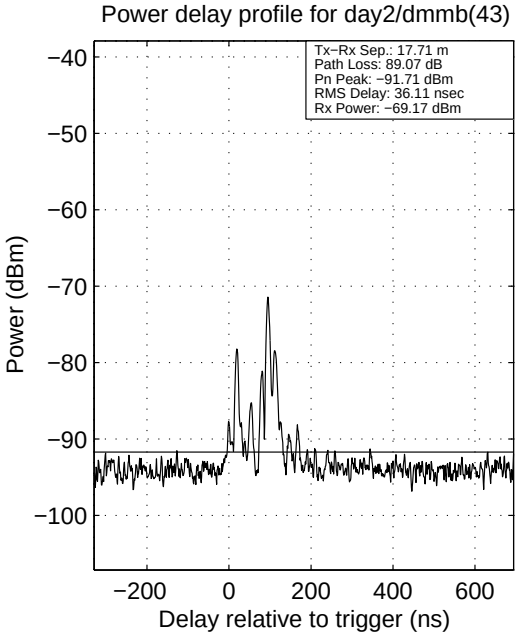
Power delay profile for day2/dmmb(43)
Tx−Rx Sep.: 17.71 m
Path Loss: 89.07 dB
Pn Peak: −91.71 dBm
RMS Delay: 36.11 nsec
Rx Power: −69.17 dBm
Power (dBm)
−40
−50
−60
−70
−80
−90
−100
−200
0
200
400
600
Delay relative to trigger (ns)

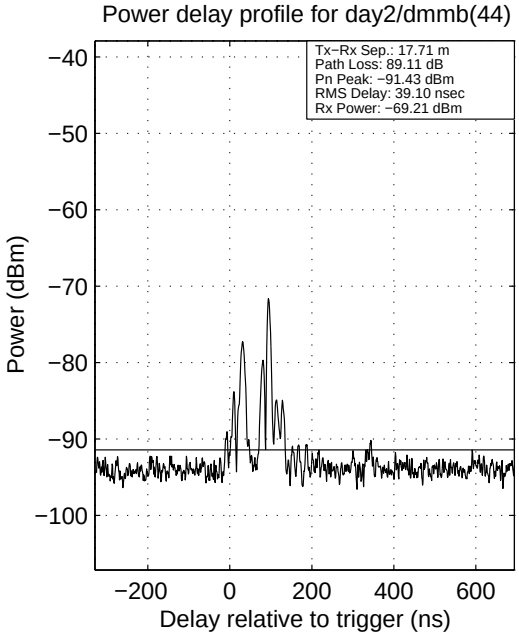
Power delay profile for day2/dmmb(44)
Tx−Rx Sep.: 17.71 m
Path Loss: 89.11 dB
Pn Peak: −91.43 dBm
RMS Delay: 39.10 nsec
Rx Power: −69.21 dBm
Power (dBm)
−40
−50
−60
−70
−80
−90
−100
−200
0
200
400
600
Delay relative to trigger (ns)

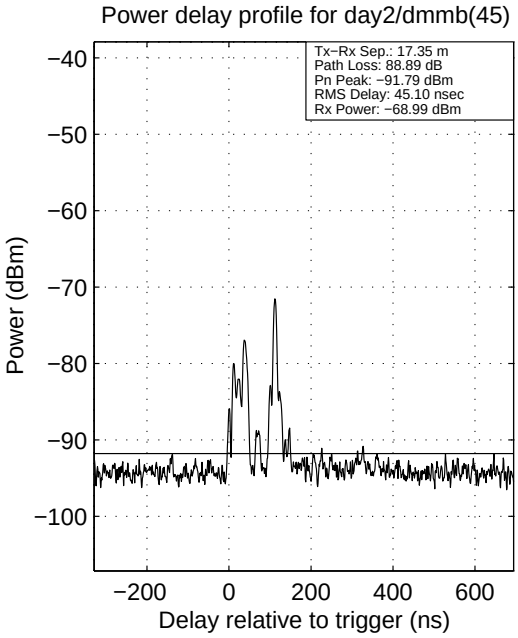
Power delay profile for day2/dmmb(45)
Tx−Rx Sep.: 17.35 m
Path Loss: 88.89 dB
Pn Peak: −91.79 dBm
RMS Delay: 45.10 nsec
Rx Power: −68.99 dBm
Power (dBm)
−40
−50
−60
−70
−80
−90
−100
−200
0
200
400
600
Delay relative to trigger (ns)

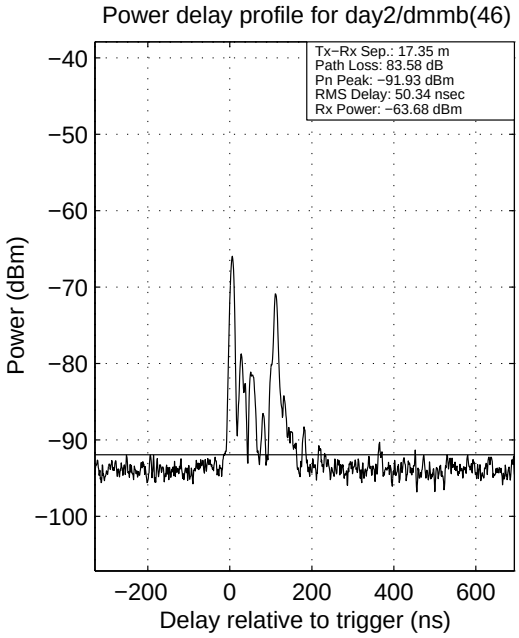
Power delay profile for day2/dmmb(46)
Tx−Rx Sep.: 17.35 m
Path Loss: 83.58 dB
Pn Peak: −91.93 dBm
RMS Delay: 50.34 nsec
Rx Power: −63.68 dBm
Power (dBm)
−40
−50
−60
−70
−80
−90
−100
−200
0
200
400
600
Delay relative to trigger (ns)

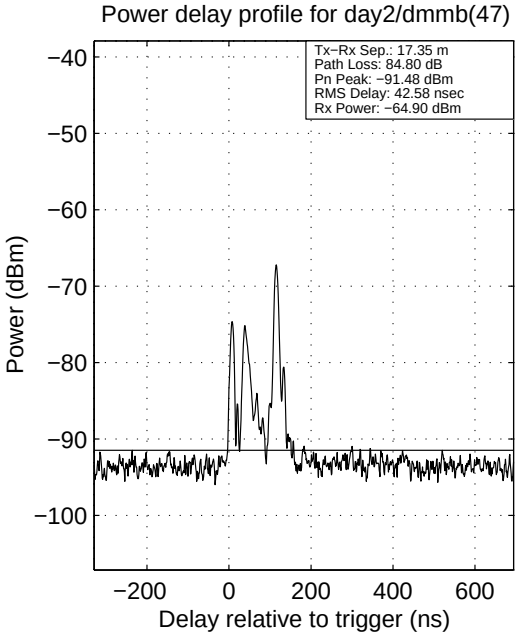
Power delay profile for day2/dmmb(47)
Tx−Rx Sep.: 17.35 m
Path Loss: 84.80 dB
Pn Peak: −91.48 dBm
RMS Delay: 42.58 nsec
Rx Power: −64.90 dBm
Power (dBm)
−40
−50
−60
−70
−80
−90
−100
−200
0
200
400
600
Delay relative to trigger (ns)

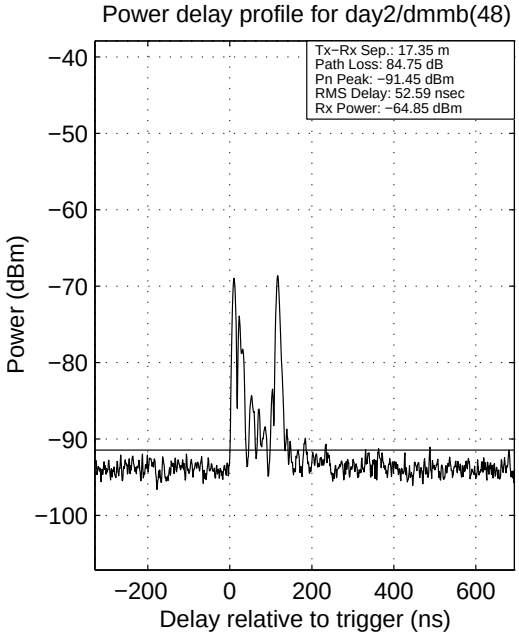
Power delay profile for day2/dmmb(48)
Tx−Rx Sep.: 17.35 m
Path Loss: 84.75 dB
Pn Peak: −91.45 dBm
RMS Delay: 52.59 nsec
Rx Power: −64.85 dBm
Power (dBm)
−40
−50
−60
−70
−80
−90
−100
−200
0
200
400
600
Delay relative to trigger (ns)

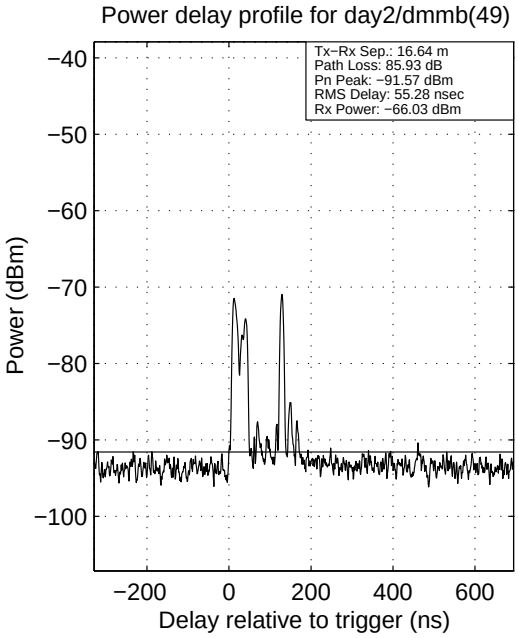
Power delay profile for day2/dmmb(49)
Tx−Rx Sep.: 16.64 m
Path Loss: 85.93 dB
Pn Peak: −91.57 dBm
RMS Delay: 55.28 nsec
Rx Power: −66.03 dBm
Power (dBm)
−40
−50
−60
−70
−80
−90
−100
−200
0
200
400
600
Delay relative to trigger (ns)

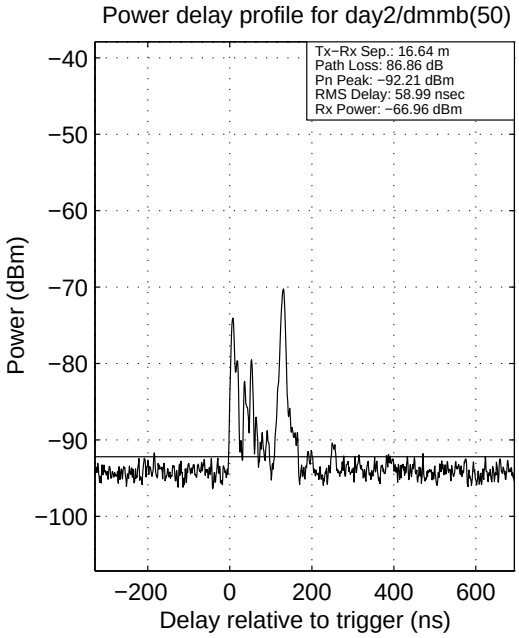
Power delay profile for day2/dmmb(50)
Tx−Rx Sep.: 16.64 m
Path Loss: 86.86 dB
Pn Peak: −92.21 dBm
RMS Delay: 58.99 nsec
Rx Power: −66.96 dBm
Power (dBm)
−40
−50
−60
−70
−80
−90
−100
−200
0
200
400
600
Delay relative to trigger (ns)

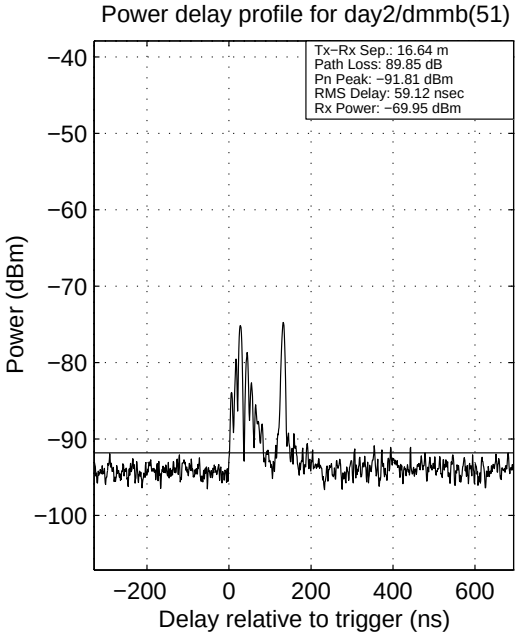
Power delay profile for day2/dmmb(51)
Tx−Rx Sep.: 16.64 m
Path Loss: 89.85 dB
Pn Peak: −91.81 dBm
RMS Delay: 59.12 nsec
Rx Power: −69.95 dBm
Power (dBm)
−40
−50
−60
−70
−80
−90
−100
−200
0
200
400
600
Delay relative to trigger (ns)

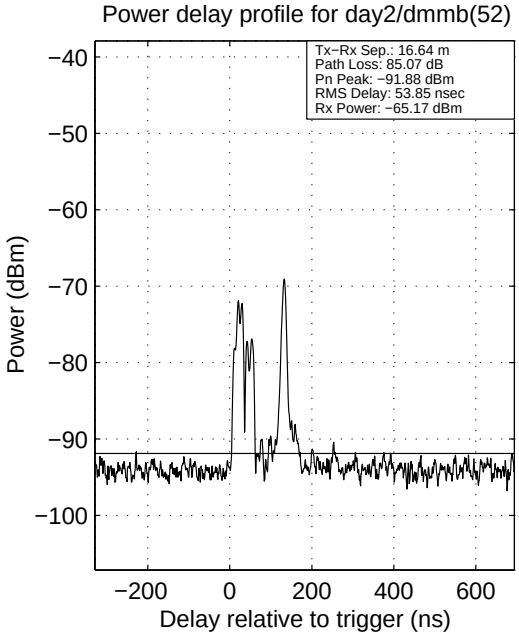
Power delay profile for day2/dmmb(52)
Tx−Rx Sep.: 16.64 m
Path Loss: 85.07 dB
Pn Peak: −91.88 dBm
RMS Delay: 53.85 nsec
Rx Power: −65.17 dBm
Power (dBm)
−40
−50
−60
−70
−80
−90
−100
−200
0
200
400
600
Delay relative to trigger (ns)

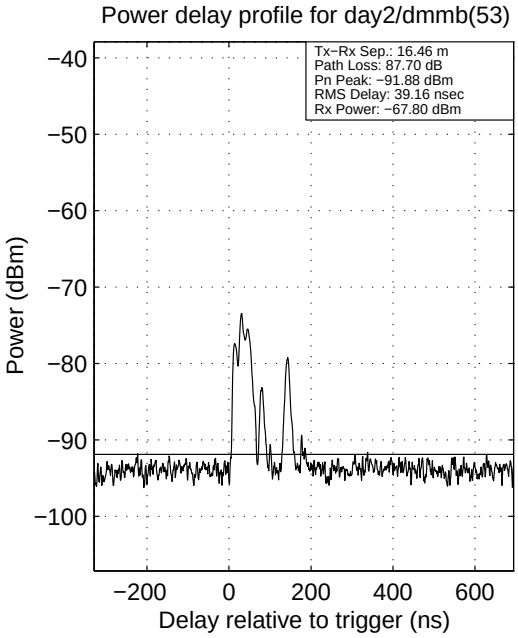
Power delay profile for day2/dmmb(53)
Tx−Rx Sep.: 16.46 m
Path Loss: 87.70 dB
Pn Peak: −91.88 dBm
RMS Delay: 39.16 nsec
Rx Power: −67.80 dBm
Power (dBm)
−40
−50
−60
−70
−80
−90
−100
−200
0
200
400
600
Delay relative to trigger (ns)

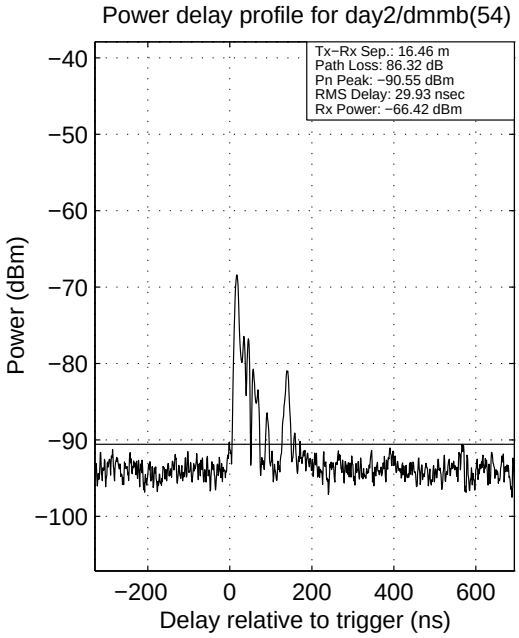
Power delay profile for day2/dmmb(54)
Tx−Rx Sep.: 16.46 m
Path Loss: 86.32 dB
Pn Peak: −90.55 dBm
RMS Delay: 29.93 nsec
Rx Power: −66.42 dBm
Power (dBm)
−40
−50
−60
−70
−80
−90
−100
−200
0
200
400
600
Delay relative to trigger (ns)

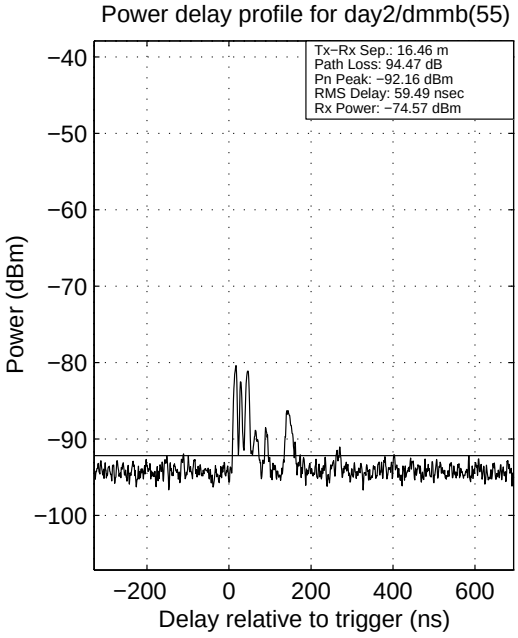
Power delay profile for day2/dmmb(55)
Tx−Rx Sep.: 16.46 m
Path Loss: 94.47 dB
Pn Peak: −92.16 dBm
RMS Delay: 59.49 nsec
Rx Power: −74.57 dBm
Power (dBm)
−40
−50
−60
−70
−80
−90
−100
−200
0
200
400
600
Delay relative to trigger (ns)

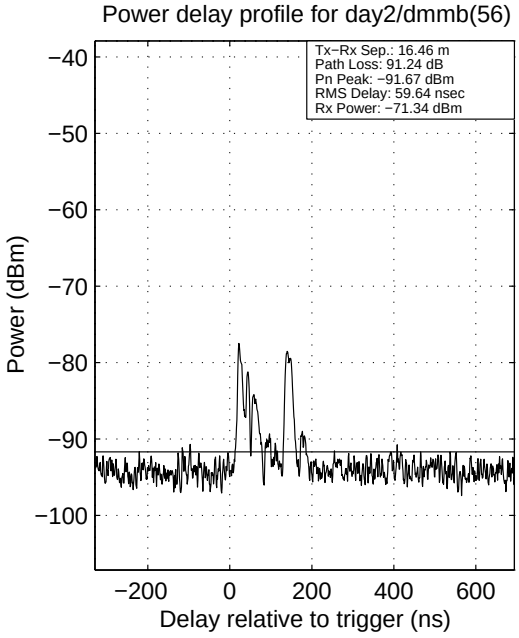
Power delay profile for day2/dmmb(56)
Tx−Rx Sep.: 16.46 m
Path Loss: 91.24 dB
Pn Peak: −91.67 dBm
RMS Delay: 59.64 nsec
Rx Power: −71.34 dBm
Power (dBm)
−40
−50
−60
−70
−80
−90
−100
−200
0
200
400
600
Delay relative to trigger (ns)

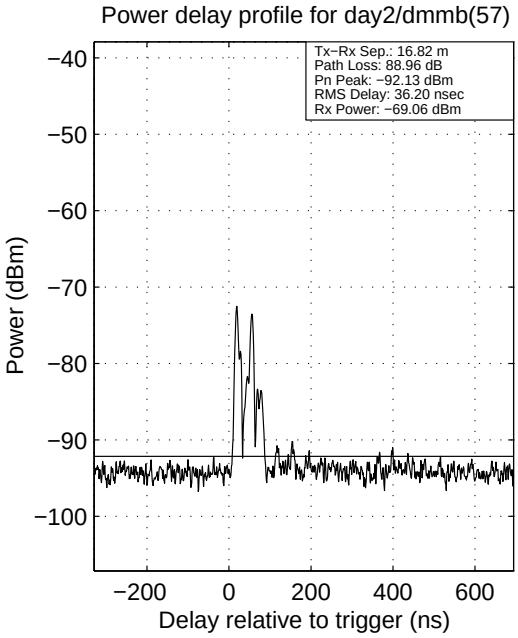
Power delay profile for day2/dmmb(57)
Tx−Rx Sep.: 16.82 m
Path Loss: 88.96 dB
Pn Peak: −92.13 dBm
RMS Delay: 36.20 nsec
Rx Power: −69.06 dBm
Power (dBm)
−40
−50
−60
−70
−80
−90
−100
−200
0
200
400
600
Delay relative to trigger (ns)

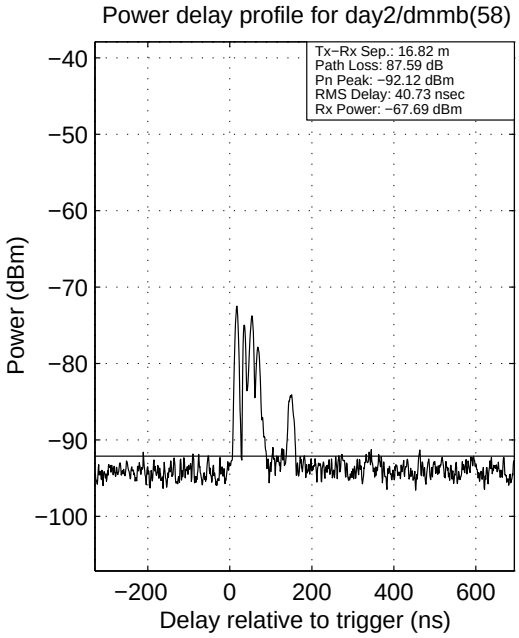
Power delay profile for day2/dmmb(58)
Tx−Rx Sep.: 16.82 m
Path Loss: 87.59 dB
Pn Peak: −92.12 dBm
RMS Delay: 40.73 nsec
Rx Power: −67.69 dBm
Power (dBm)
−40
−50
−60
−70
−80
−90
−100
−200
0
200
400
600
Delay relative to trigger (ns)

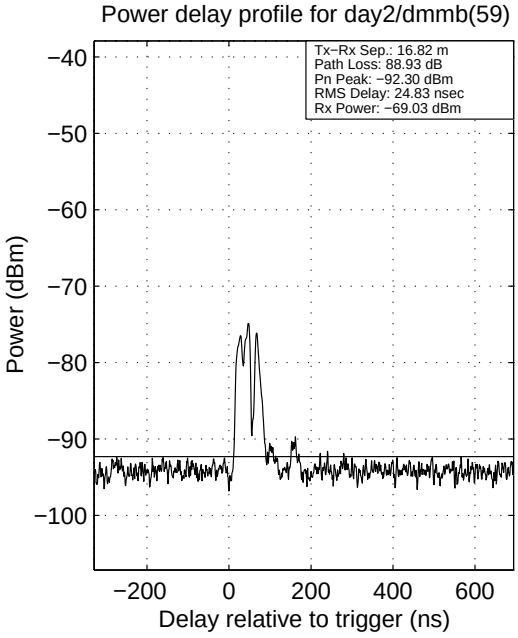
Power delay profile for day2/dmmb(59)
Tx−Rx Sep.: 16.82 m
Path Loss: 88.93 dB
Pn Peak: −92.30 dBm
RMS Delay: 24.83 nsec
Rx Power: −69.03 dBm
Power (dBm)
−40
−50
−60
−70
−80
−90
−100
−200
0
200
400
600
Delay relative to trigger (ns)

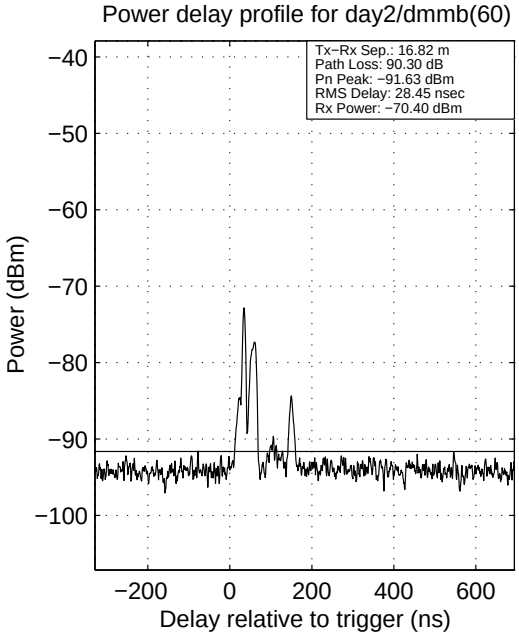
Power delay profile for day2/dmmb(60)
Tx−Rx Sep.: 16.82 m
Path Loss: 90.30 dB
Pn Peak: −91.63 dBm
RMS Delay: 28.45 nsec
Rx Power: −70.40 dBm
Power (dBm)
−40
−50
−60
−70
−80
−90
−100
−200
0
200
400
600
Delay relative to trigger (ns)

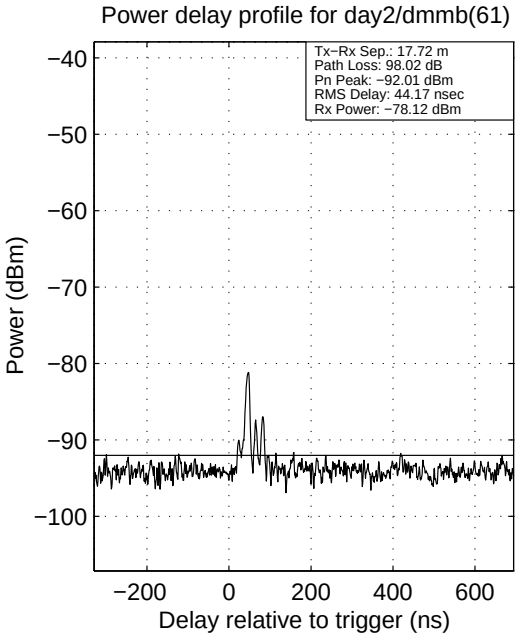
Power delay profile for day2/dmmb(61)
Tx−Rx Sep.: 17.72 m
Path Loss: 98.02 dB
Pn Peak: −92.01 dBm
RMS Delay: 44.17 nsec
Rx Power: −78.12 dBm
Power (dBm)
−40
−50
−60
−70
−80
−90
−100
−200
0
200
400
600
Delay relative to trigger (ns)

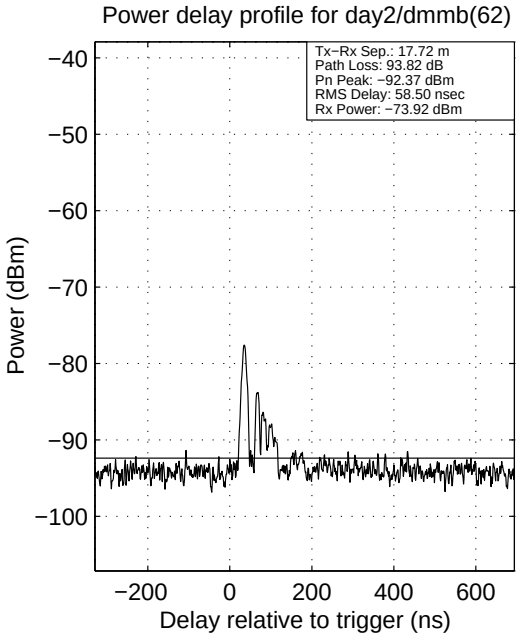
Power delay profile for day2/dmmb(62)
Tx−Rx Sep.: 17.72 m
Path Loss: 93.82 dB
Pn Peak: −92.37 dBm
RMS Delay: 58.50 nsec
Rx Power: −73.92 dBm
Power (dBm)
−40
−50
−60
−70
−80
−90
−100
−200
0
200
400
600
Delay relative to trigger (ns)

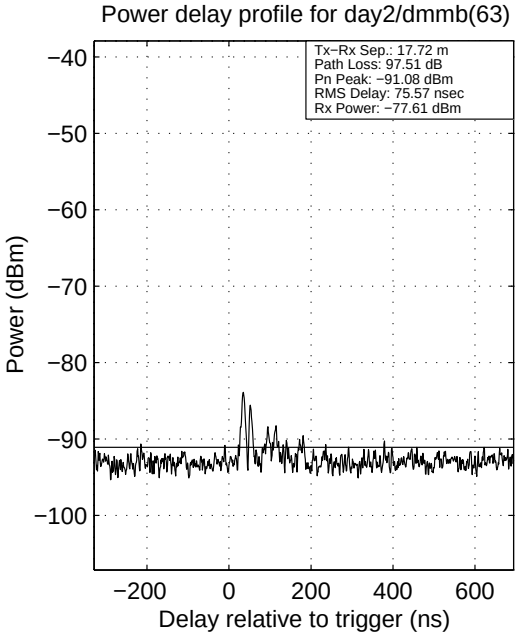
Power delay profile for day2/dmmb(63)
Tx−Rx Sep.: 17.72 m
Path Loss: 97.51 dB
Pn Peak: −91.08 dBm
RMS Delay: 75.57 nsec
Rx Power: −77.61 dBm
Power (dBm)
−40
−50
−60
−70
−80
−90
−100
−200
0
200
400
600
Delay relative to trigger (ns)

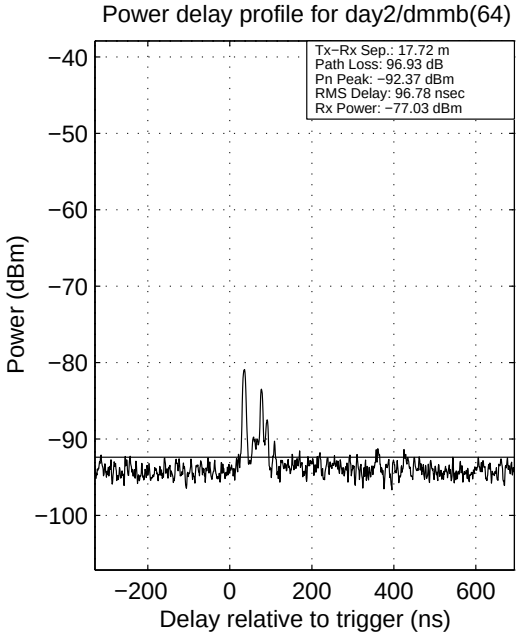
Power delay profile for day2/dmmb(64)
Tx−Rx Sep.: 17.72 m
Path Loss: 96.93 dB
Pn Peak: −92.37 dBm
RMS Delay: 96.78 nsec
Rx Power: −77.03 dBm
Power (dBm)
−40
−50
−60
−70
−80
−90
−100
−200
0
200
400
600
Delay relative to trigger (ns)

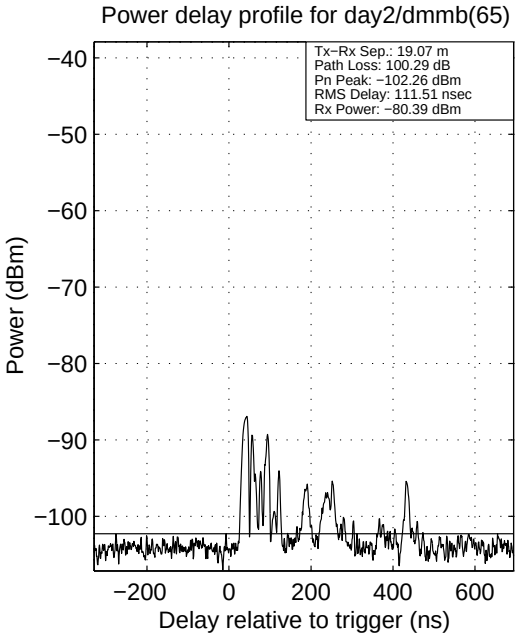
Power delay profile for day2/dmmb(65)
Tx−Rx Sep.: 19.07 m
Path Loss: 100.29 dB
Pn Peak: −102.26 dBm
RMS Delay: 111.51 nsec
Rx Power: −80.39 dBm
Power (dBm)
−40
−50
−60
−70
−80
−90
−100
−200
0
200
400
600
Delay relative to trigger (ns)

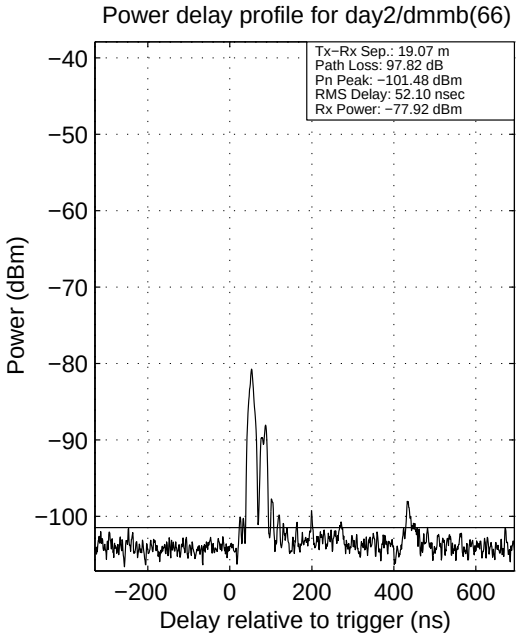
Power delay profile for day2/dmmb(66)
Tx−Rx Sep.: 19.07 m
Path Loss: 97.82 dB
Pn Peak: −101.48 dBm
RMS Delay: 52.10 nsec
Rx Power: −77.92 dBm
Power (dBm)
−40
−50
−60
−70
−80
−90
−100
−200
0
200
400
600
Delay relative to trigger (ns)

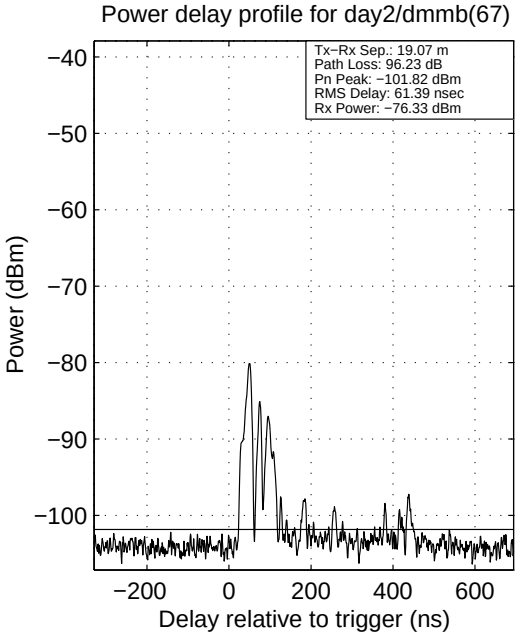
Power delay profile for day2/dmmb(67)
Tx−Rx Sep.: 19.07 m
Path Loss: 96.23 dB
Pn Peak: −101.82 dBm
RMS Delay: 61.39 nsec
Rx Power: −76.33 dBm
Power (dBm)
−40
−50
−60
−70
−80
−90
−100
−200
0
200
400
600
Delay relative to trigger (ns)

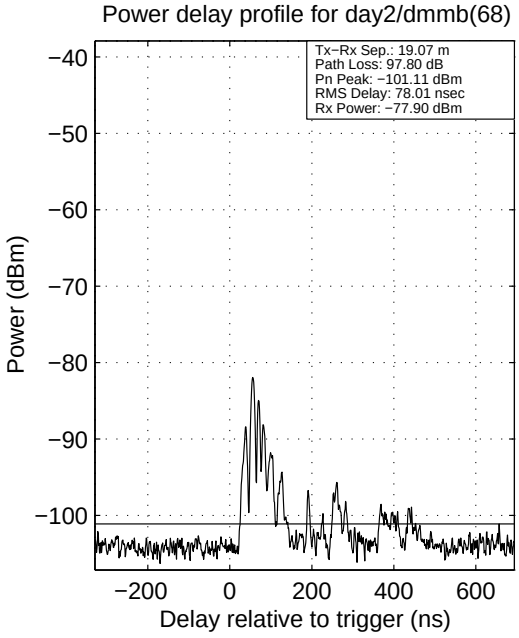
Power delay profile for day2/dmmb(68)
Tx−Rx Sep.: 19.07 m
Path Loss: 97.80 dB
Pn Peak: −101.11 dBm
RMS Delay: 78.01 nsec
Rx Power: −77.90 dBm
Power (dBm)
−40
−50
−60
−70
−80
−90
−100
−200
0
200
400
600
Delay relative to trigger (ns)

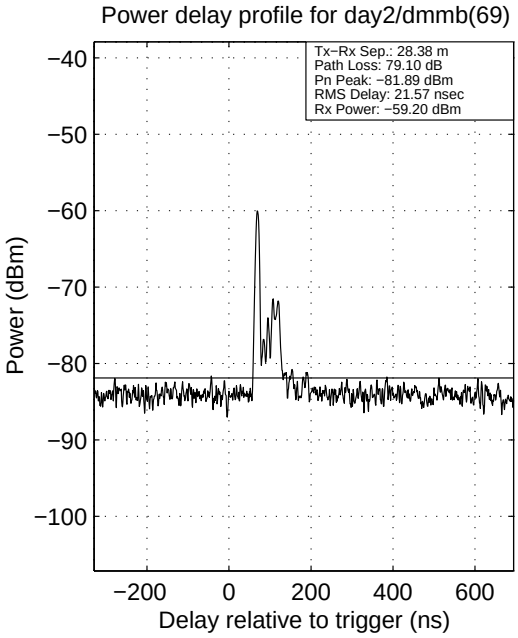
Power delay profile for day2/dmmb(69)
Tx−Rx Sep.: 28.38 m
Path Loss: 79.10 dB
Pn Peak: −81.89 dBm
RMS Delay: 21.57 nsec
Rx Power: −59.20 dBm
Power (dBm)
−40
−50
−60
−70
−80
−90
−100
−200
0
200
400
600
Delay relative to trigger (ns)

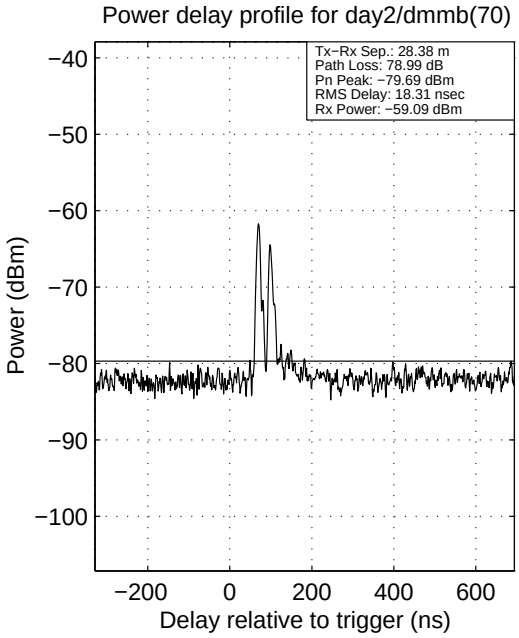
Power delay profile for day2/dmmb(70)
Tx−Rx Sep.: 28.38 m
Path Loss: 78.99 dB
Pn Peak: −79.69 dBm
RMS Delay: 18.31 nsec
Rx Power: −59.09 dBm
Power (dBm)
−40
−50
−60
−70
−80
−90
−100
−200
0
200
400
600
Delay relative to trigger (ns)

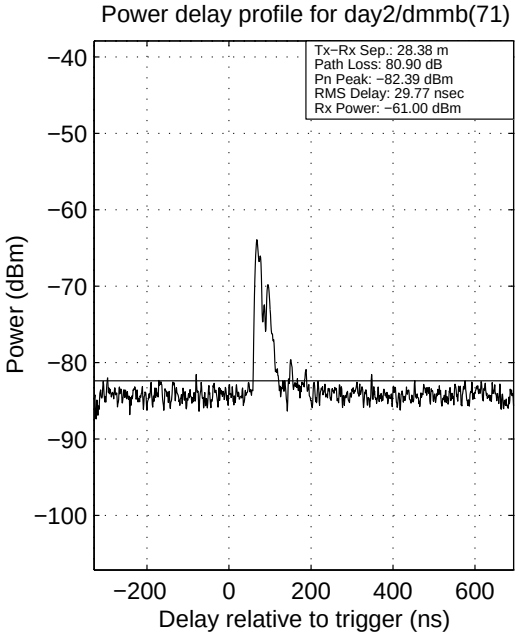
Power delay profile for day2/dmmb(71)
Tx−Rx Sep.: 28.38 m
Path Loss: 80.90 dB
Pn Peak: −82.39 dBm
RMS Delay: 29.77 nsec
Rx Power: −61.00 dBm
Power (dBm)
−40
−50
−60
−70
−80
−90
−100
−200
0
200
400
600
Delay relative to trigger (ns)

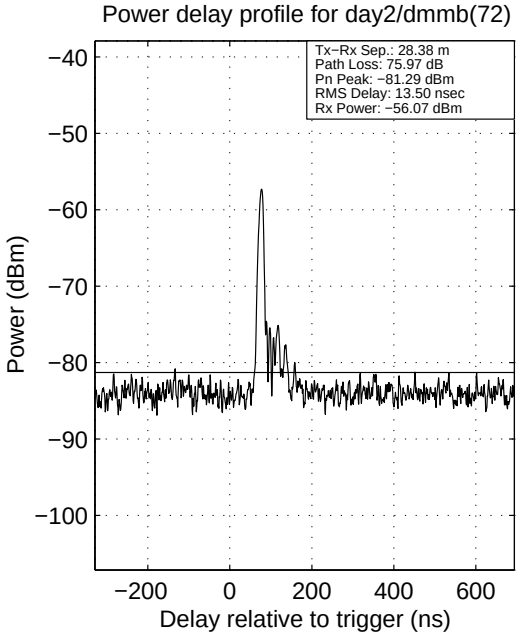
Power delay profile for day2/dmmb(72)
Tx−Rx Sep.: 28.38 m
Path Loss: 75.97 dB
Pn Peak: −81.29 dBm
RMS Delay: 13.50 nsec
Rx Power: −56.07 dBm
Power (dBm)
−40
−50
−60
−70
−80
−90
−100
−200
0
200
400
600
Delay relative to trigger (ns)

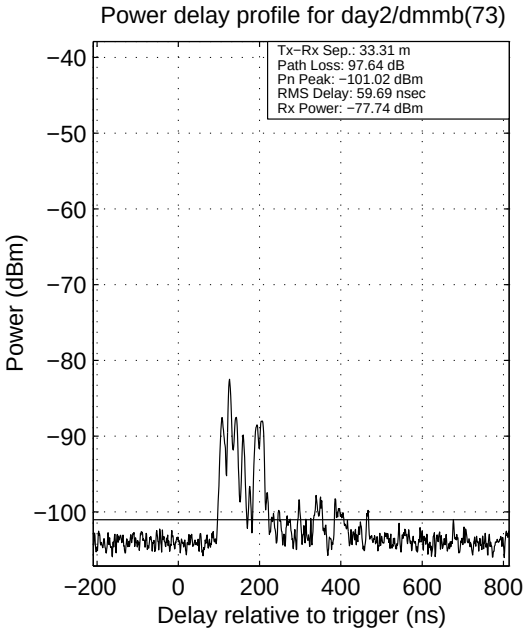
Power delay profile for day2/dmmb(73)
Tx−Rx Sep.: 33.31 m
Path Loss: 97.64 dB
Pn Peak: −101.02 dBm
RMS Delay: 59.69 nsec
Rx Power: −77.74 dBm
Power (dBm)
Delay relative to trigger (ns)

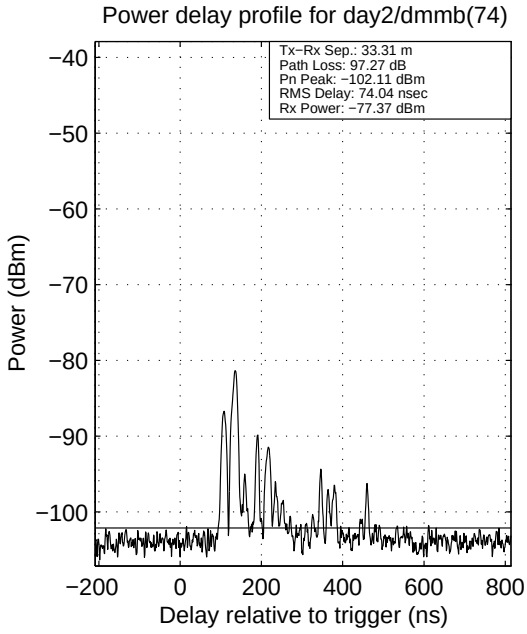
Power delay profile for day2/dmmb(74)
Tx−Rx Sep.: 33.31 m
Path Loss: 97.27 dB
Pn Peak: −102.11 dBm
RMS Delay: 74.04 nsec
Rx Power: −77.37 dBm
Power (dBm)
Delay relative to trigger (ns)

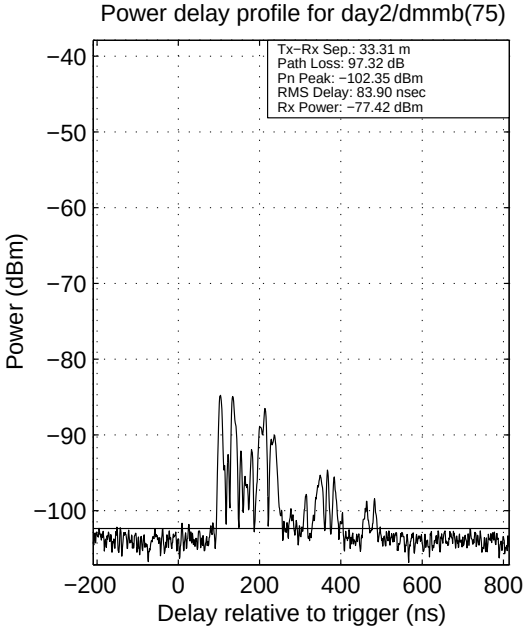
Power delay profile for day2/dmmb(75)
Tx−Rx Sep.: 33.31 m
Path Loss: 97.32 dB
Pn Peak: −102.35 dBm
RMS Delay: 83.90 nsec
Rx Power: −77.42 dBm
Power (dBm)
Delay relative to trigger (ns)

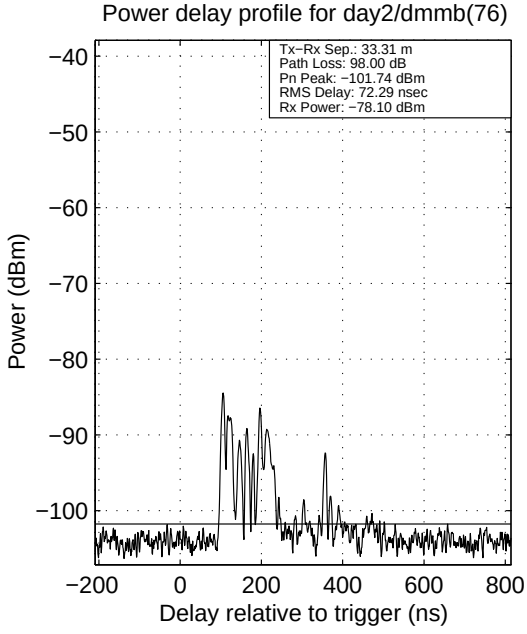
Power delay profile for day2/dmmb(76)
Tx−Rx Sep.: 33.31 m
Path Loss: 98.00 dB
Pn Peak: −101.74 dBm
RMS Delay: 72.29 nsec
Rx Power: −78.10 dBm
Power (dBm)
Delay relative to trigger (ns)

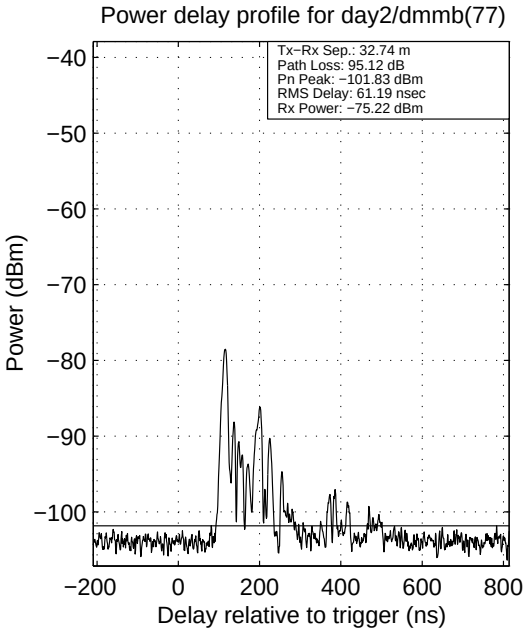
Power delay profile for day2/dmmb(77)
Tx−Rx Sep.: 32.74 m
Path Loss: 95.12 dB
Pn Peak: −101.83 dBm
RMS Delay: 61.19 nsec
Rx Power: −75.22 dBm
Power (dBm)
Delay relative to trigger (ns)

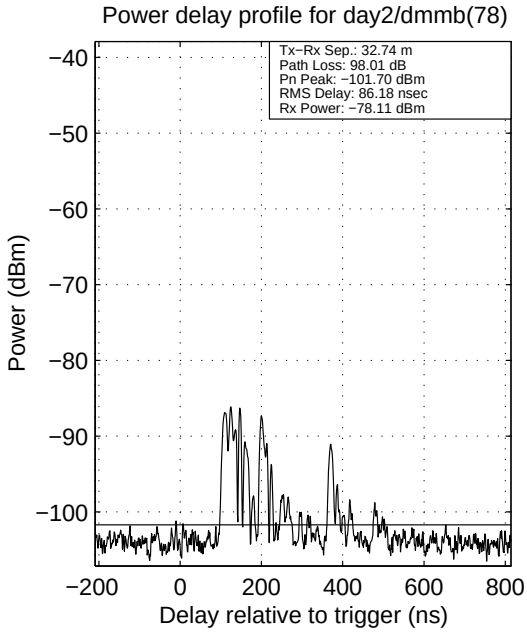
Power delay profile for day2/dmmb(78)
Tx−Rx Sep.: 32.74 m
Path Loss: 98.01 dB
Pn Peak: −101.70 dBm
RMS Delay: 86.18 nsec
Rx Power: −78.11 dBm
Power (dBm)
Delay relative to trigger (ns)

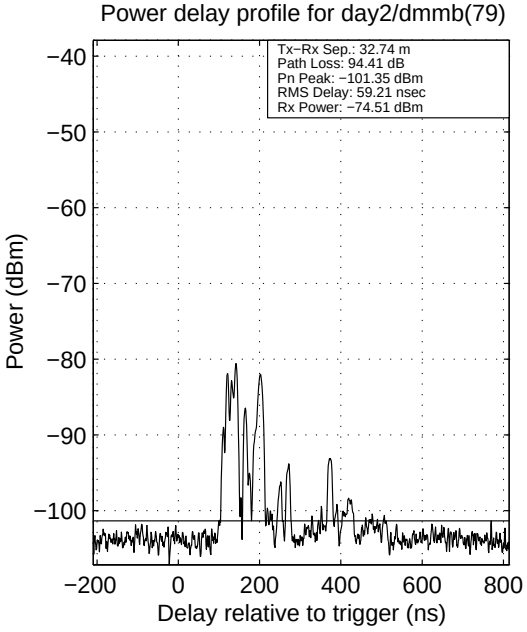
Power delay profile for day2/dmmb(79)
Tx−Rx Sep.: 32.74 m
Path Loss: 94.41 dB
Pn Peak: −101.35 dBm
RMS Delay: 59.21 nsec
Rx Power: −74.51 dBm
Power (dBm)
Delay relative to trigger (ns)

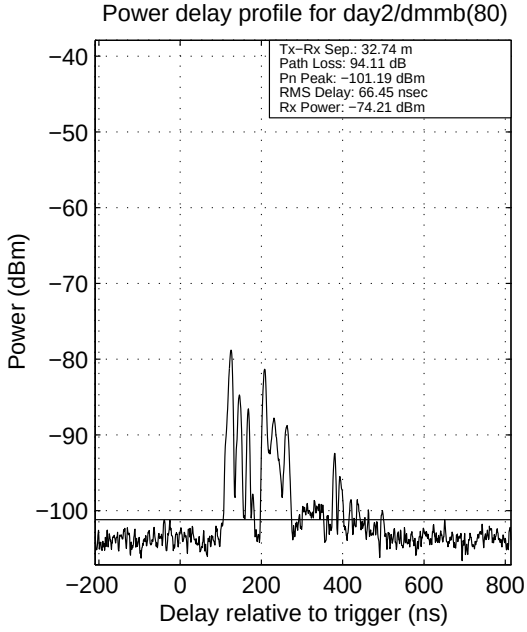
Power delay profile for day2/dmmb(80)
Tx−Rx Sep.: 32.74 m
Path Loss: 94.11 dB
Pn Peak: −101.19 dBm
RMS Delay: 66.45 nsec
Rx Power: −74.21 dBm
Power (dBm)
Delay relative to trigger (ns)

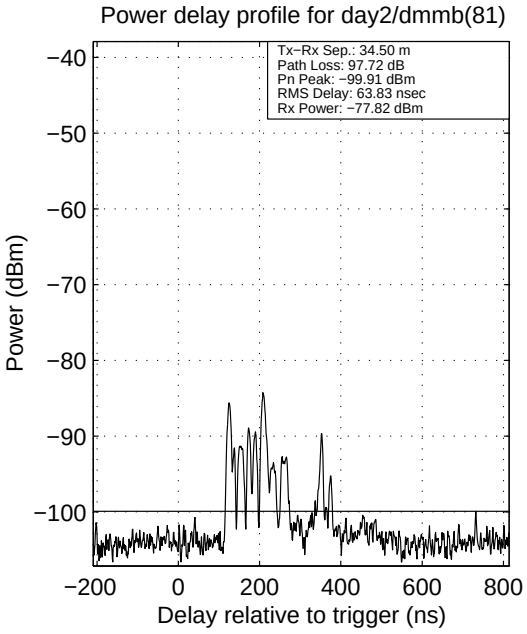
Power delay profile for day2/dmmb(81)
Tx−Rx Sep.: 34.50 m
Path Loss: 97.72 dB
Pn Peak: −99.91 dBm
RMS Delay: 63.83 nsec
Rx Power: −77.82 dBm
Power (dBm)
Delay relative to trigger (ns)

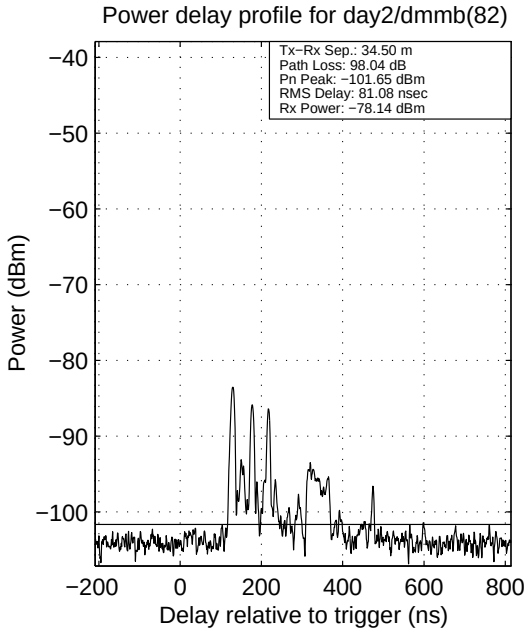
Power delay profile for day2/dmmb(82)
Tx−Rx Sep.: 34.50 m
Path Loss: 98.04 dB
Pn Peak: −101.65 dBm
RMS Delay: 81.08 nsec
Rx Power: −78.14 dBm
Power (dBm)
Delay relative to trigger (ns)

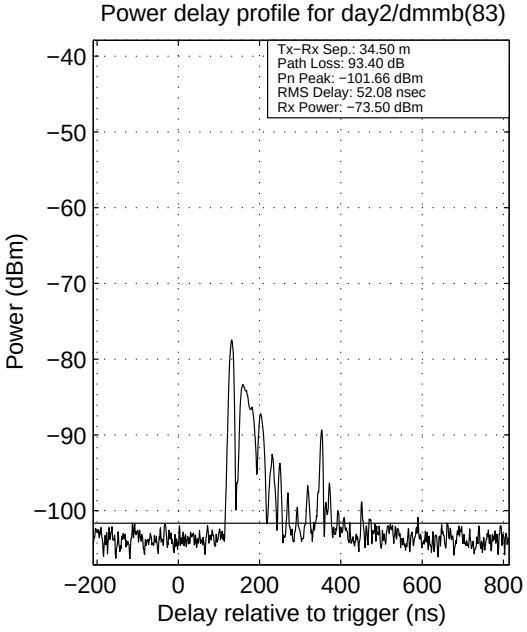
Power delay profile for day2/dmmb(83)
Tx−Rx Sep.: 34.50 m
Path Loss: 93.40 dB
Pn Peak: −101.66 dBm
RMS Delay: 52.08 nsec
Rx Power: −73.50 dBm
Power (dBm)
Delay relative to trigger (ns)

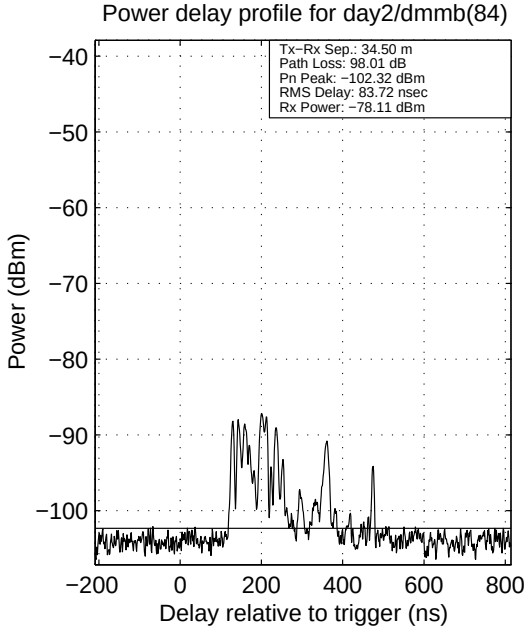
Power delay profile for day2/dmmb(84)
Tx−Rx Sep.: 34.50 m
Path Loss: 98.01 dB
Pn Peak: −102.32 dBm
RMS Delay: 83.72 nsec
Rx Power: −78.11 dBm
Power (dBm)
Delay relative to trigger (ns)

Appendix D

Power Delay Profiles at Measurement Site 3

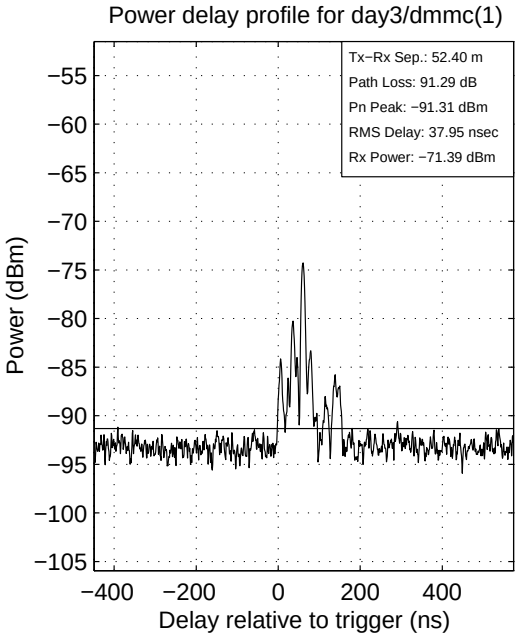
Power delay profile for day3/dmmc(1)
Tx−Rx Sep.: 52.40 m
Path Loss: 91.29 dB
Pn Peak: −91.31 dBm
RMS Delay: 37.95 nsec
Rx Power: −71.39 dBm
Power (dBm)
−55
−60
−65
−70
−75
−80
−85
−90
−95
−100
−105
−400
−200
0
200
400
Delay relative to trigger (ns)

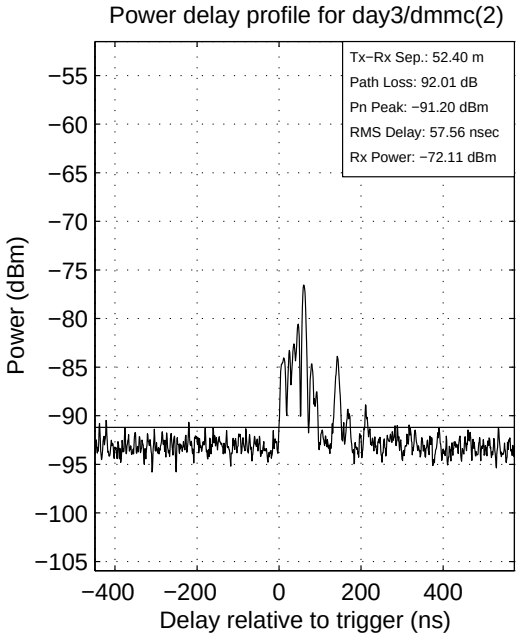
Power delay profile for day3/dmmc(2)
Tx−Rx Sep.: 52.40 m
Path Loss: 92.01 dB
Pn Peak: −91.20 dBm
RMS Delay: 57.56 nsec
Rx Power: −72.11 dBm
Power (dBm)
−55
−60
−65
−70
−75
−80
−85
−90
−95
−100
−105
−400
−200
0
200
400
Delay relative to trigger (ns)

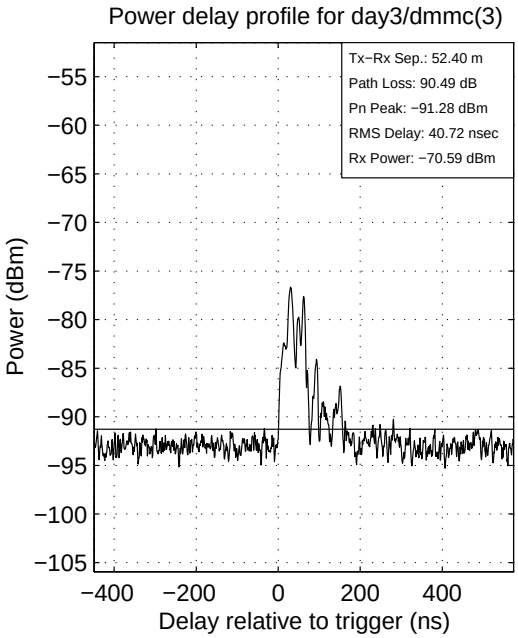
Power delay profile for day3/dmmc(3)
Tx−Rx Sep.: 52.40 m
Path Loss: 90.49 dB
Pn Peak: −91.28 dBm
RMS Delay: 40.72 nsec
Rx Power: −70.59 dBm
Power (dBm)
−55
−60
−65
−70
−75
−80
−85
−90
−95
−100
−105
−400
−200
0
200
400
Delay relative to trigger (ns)

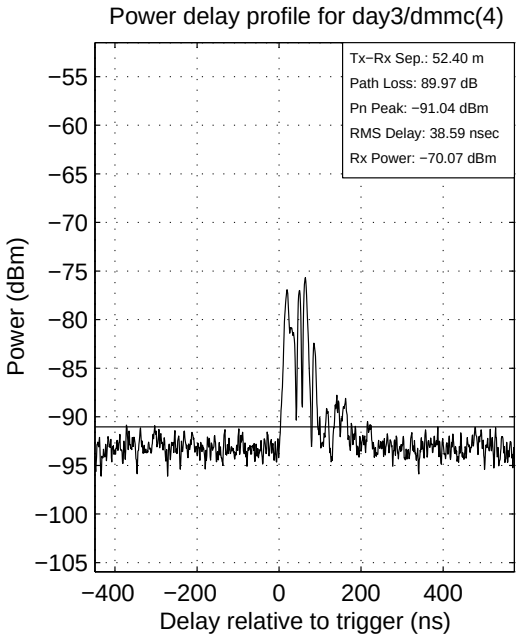
Power delay profile for day3/dmmc(4)
Tx−Rx Sep.: 52.40 m
Path Loss: 89.97 dB
Pn Peak: −91.04 dBm
RMS Delay: 38.59 nsec
Rx Power: −70.07 dBm
Power (dBm)
−55
−60
−65
−70
−75
−80
−85
−90
−95
−100
−105
−400
−200
0
200
400
Delay relative to trigger (ns)

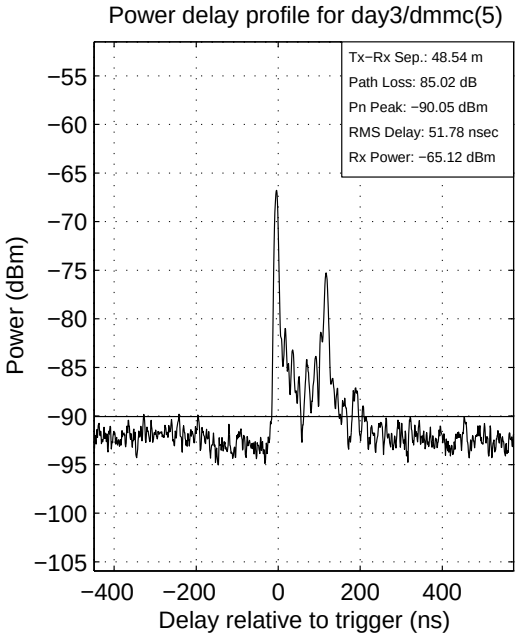
Power delay profile for day3/dmmc(5)
Tx−Rx Sep.: 48.54 m
Path Loss: 85.02 dB
Pn Peak: −90.05 dBm
RMS Delay: 51.78 nsec
Rx Power: −65.12 dBm
Power (dBm)
−55
−60
−65
−70
−75
−80
−85
−90
−95
−100
−105
−400
−200
0
200
400
Delay relative to trigger (ns)

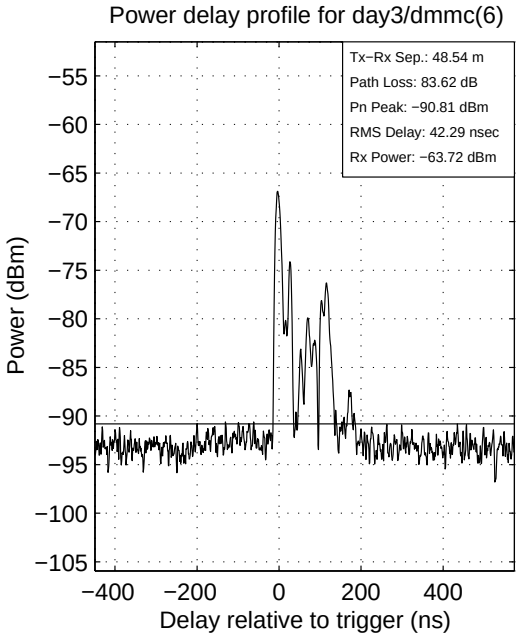
Power delay profile for day3/dmmc(6)
Tx−Rx Sep.: 48.54 m
Path Loss: 83.62 dB
Pn Peak: −90.81 dBm
RMS Delay: 42.29 nsec
Rx Power: −63.72 dBm
Power (dBm)
−55
−60
−65
−70
−75
−80
−85
−90
−95
−100
−105
−400
−200
0
200
400
Delay relative to trigger (ns)

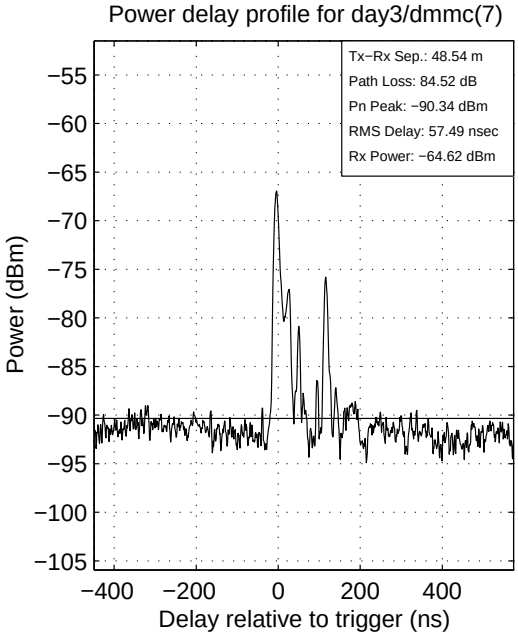
Power delay profile for day3/dmmc(7)
Tx−Rx Sep.: 48.54 m
Path Loss: 84.52 dB
Pn Peak: −90.34 dBm
RMS Delay: 57.49 nsec
Rx Power: −64.62 dBm
Power (dBm)
−55
−60
−65
−70
−75
−80
−85
−90
−95
−100
−105
−400
−200
0
200
400
Delay relative to trigger (ns)

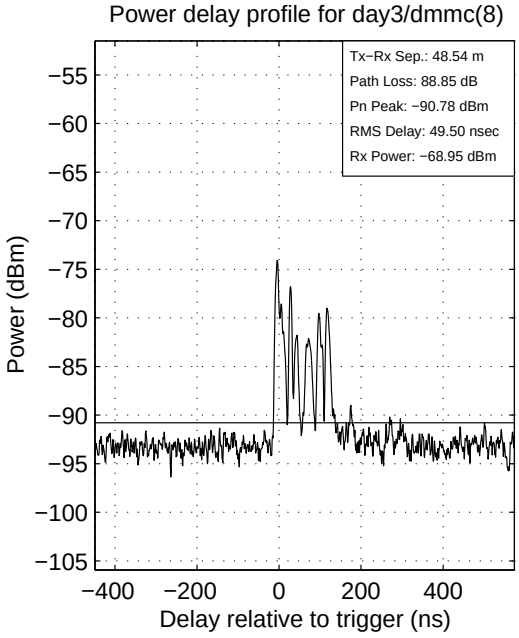
Power delay profile for day3/dmmc(8)
Tx−Rx Sep.: 48.54 m
Path Loss: 88.85 dB
Pn Peak: −90.78 dBm
RMS Delay: 49.50 nsec
Rx Power: −68.95 dBm
Power (dBm)
−55
−60
−65
−70
−75
−80
−85
−90
−95
−100
−105
−400
−200
0
200
400
Delay relative to trigger (ns)

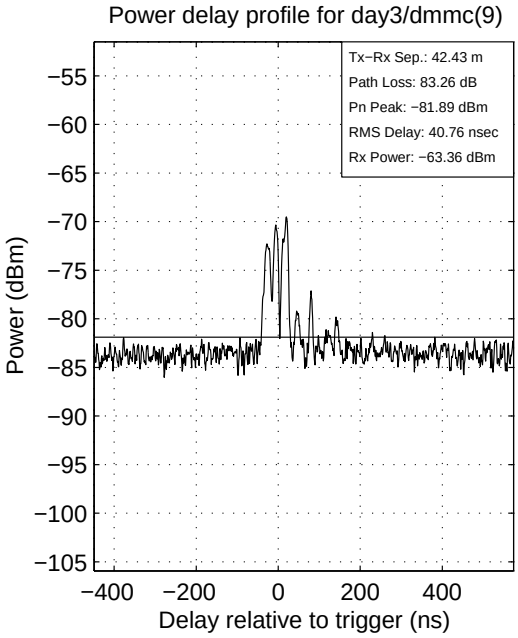
Power delay profile for day3/dmmc(9)
Tx−Rx Sep.: 42.43 m
Path Loss: 83.26 dB
Pn Peak: −81.89 dBm
RMS Delay: 40.76 nsec
Rx Power: −63.36 dBm
Power (dBm)
−55
−60
−65
−70
−75
−80
−85
−90
−95
−100
−105
−400
−200
0
200
400
Delay relative to trigger (ns)

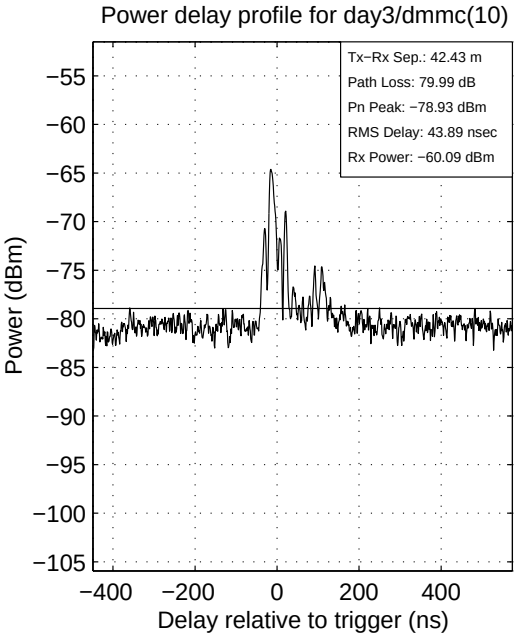
Power delay profile for day3/dmmc(10)
Tx−Rx Sep.: 42.43 m
Path Loss: 79.99 dB
Pn Peak: −78.93 dBm
RMS Delay: 43.89 nsec
Rx Power: −60.09 dBm
Power (dBm)
−55
−60
−65
−70
−75
−80
−85
−90
−95
−100
−105
−400
−200
0
200
400
Delay relative to trigger (ns)

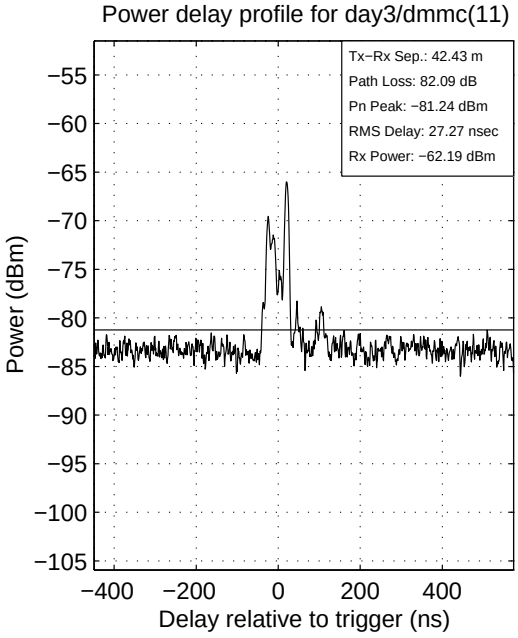
Power delay profile for day3/dmmc(11)
Tx−Rx Sep.: 42.43 m
Path Loss: 82.09 dB
Pn Peak: −81.24 dBm
RMS Delay: 27.27 nsec
Rx Power: −62.19 dBm
Power (dBm)
−55
−60
−65
−70
−75
−80
−85
−90
−95
−100
−105
−400
−200
0
200
400
Delay relative to trigger (ns)

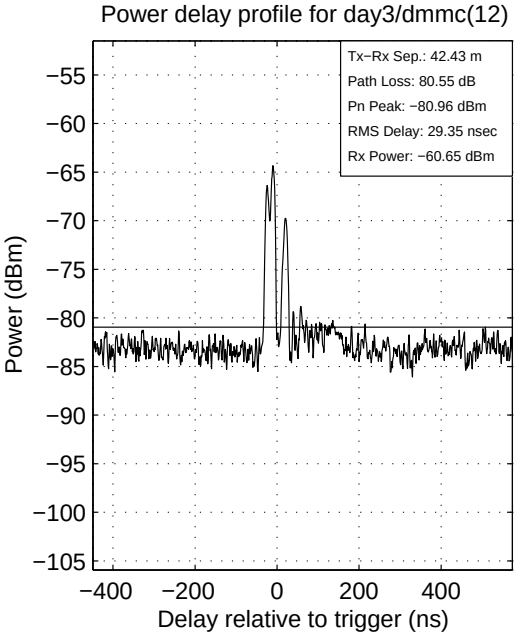
Power delay profile for day3/dmmc(12)
Tx−Rx Sep.: 42.43 m
Path Loss: 80.55 dB
Pn Peak: −80.96 dBm
RMS Delay: 29.35 nsec
Rx Power: −60.65 dBm
Power (dBm)
−55
−60
−65
−70
−75
−80
−85
−90
−95
−100
−105
−400
−200
0
200
400
Delay relative to trigger (ns)

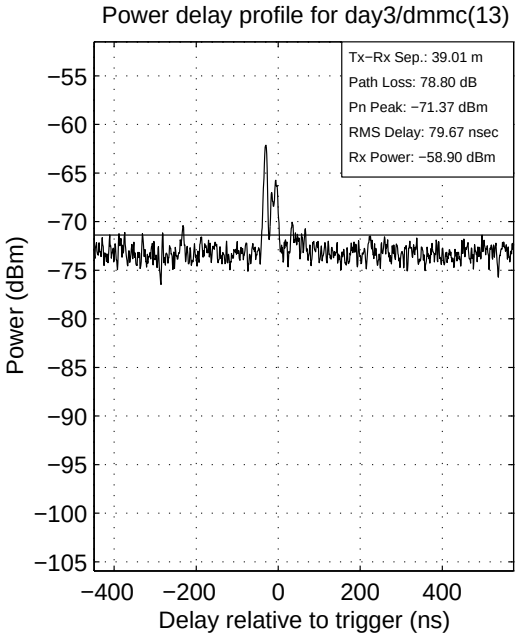
Power delay profile for day3/dmmc(13)
Tx−Rx Sep.: 39.01 m
Path Loss: 78.80 dB
Pn Peak: −71.37 dBm
RMS Delay: 79.67 nsec
Rx Power: −58.90 dBm
Power (dBm)
−55
−60
−65
−70
−75
−80
−85
−90
−95
−100
−105
−400
−200
0
200
400
Delay relative to trigger (ns)

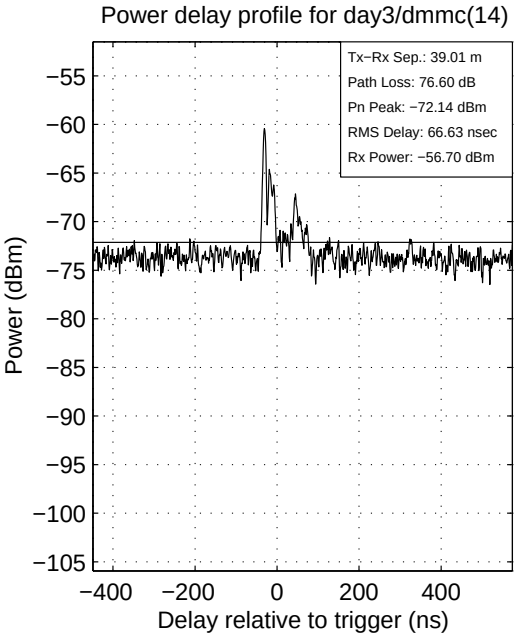
Power delay profile for day3/dmmc(14)
Tx−Rx Sep.: 39.01 m
Path Loss: 76.60 dB
Pn Peak: −72.14 dBm
RMS Delay: 66.63 nsec
Rx Power: −56.70 dBm
Power (dBm)
−55
−60
−65
−70
−75
−80
−85
−90
−95
−100
−105
−400
−200
0
200
400
Delay relative to trigger (ns)

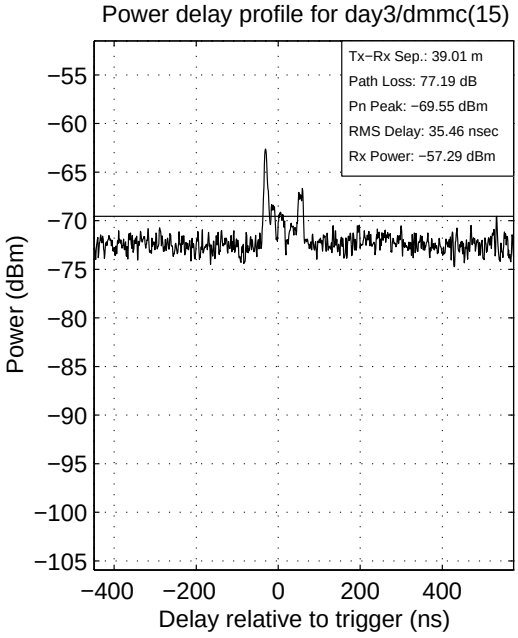
Power delay profile for day3/dmmc(15)
Tx−Rx Sep.: 39.01 m
Path Loss: 77.19 dB
Pn Peak: −69.55 dBm
RMS Delay: 35.46 nsec
Rx Power: −57.29 dBm
Power (dBm)
−55
−60
−65
−70
−75
−80
−85
−90
−95
−100
−105
−400
−200
0
200
400
Delay relative to trigger (ns)

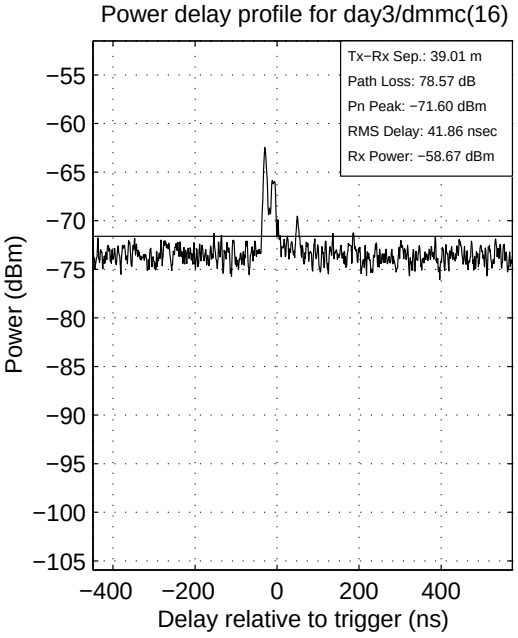
Power delay profile for day3/dmmc(16)
Tx−Rx Sep.: 39.01 m
Path Loss: 78.57 dB
Pn Peak: −71.60 dBm
RMS Delay: 41.86 nsec
Rx Power: −58.67 dBm
Power (dBm)
−55
−60
−65
−70
−75
−80
−85
−90
−95
−100
−105
−400
−200
0
200
400
Delay relative to trigger (ns)

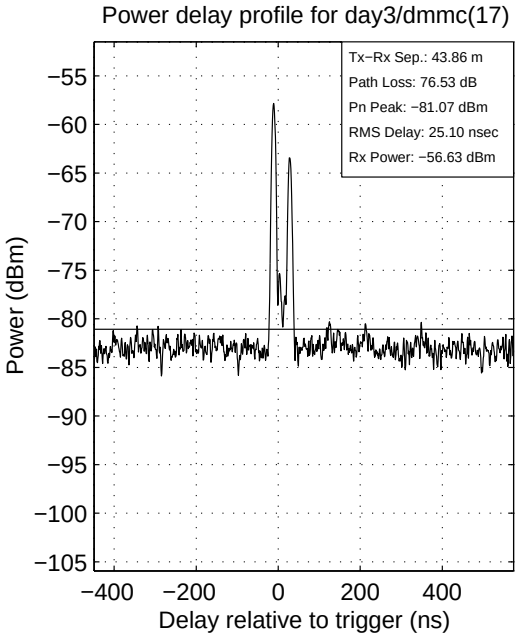
Power delay profile for day3/dmmc(17)
Tx−Rx Sep.: 43.86 m
Path Loss: 76.53 dB
Pn Peak: −81.07 dBm
RMS Delay: 25.10 nsec
Rx Power: −56.63 dBm
Power (dBm)
−55
−60
−65
−70
−75
−80
−85
−90
−95
−100
−105
−400
−200
0
200
400
Delay relative to trigger (ns)

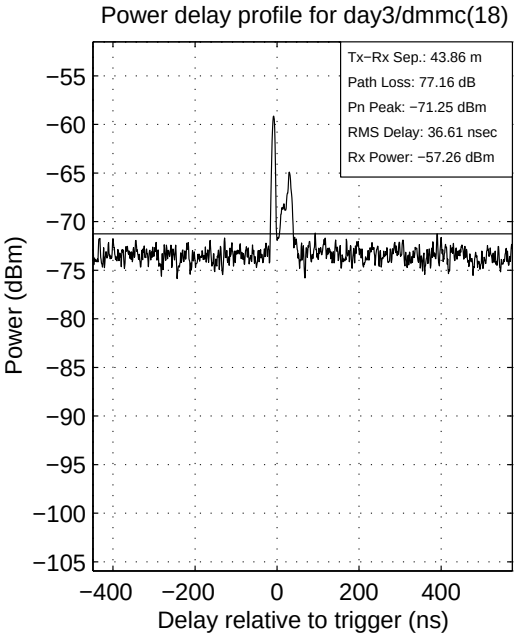
Power delay profile for day3/dmmc(18)
Tx−Rx Sep.: 43.86 m
Path Loss: 77.16 dB
Pn Peak: −71.25 dBm
RMS Delay: 36.61 nsec
Rx Power: −57.26 dBm
Power (dBm)
−55
−60
−65
−70
−75
−80
−85
−90
−95
−100
−105
−400
−200
0
200
400
Delay relative to trigger (ns)

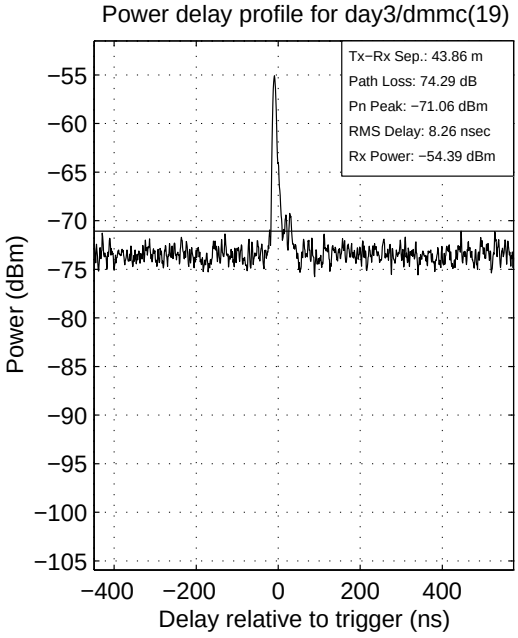
Power delay profile for day3/dmmc(19)
Tx−Rx Sep.: 43.86 m
Path Loss: 74.29 dB
Pn Peak: −71.06 dBm
RMS Delay: 8.26 nsec
Rx Power: −54.39 dBm
Power (dBm)
−55
−60
−65
−70
−75
−80
−85
−90
−95
−100
−105
−400
−200
0
200
400
Delay relative to trigger (ns)

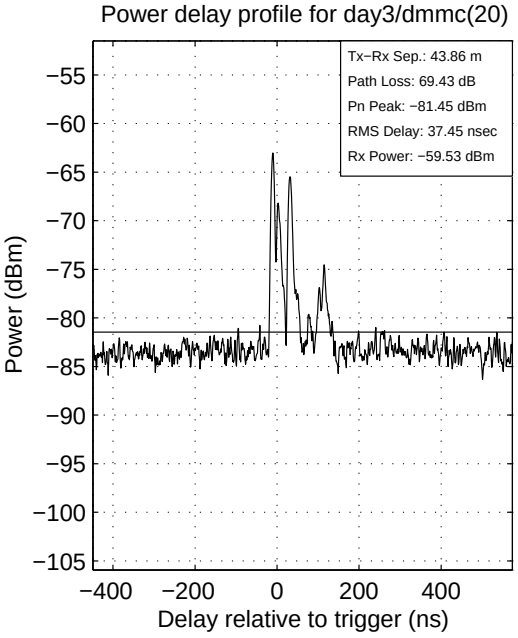
Power delay profile for day3/dmmc(20)
Tx−Rx Sep.: 43.86 m
Path Loss: 69.43 dB
Pn Peak: −81.45 dBm
RMS Delay: 37.45 nsec
Rx Power: −59.53 dBm
Power (dBm)
−55
−60
−65
−70
−75
−80
−85
−90
−95
−100
−105
−400
−200
0
200
400
Delay relative to trigger (ns)

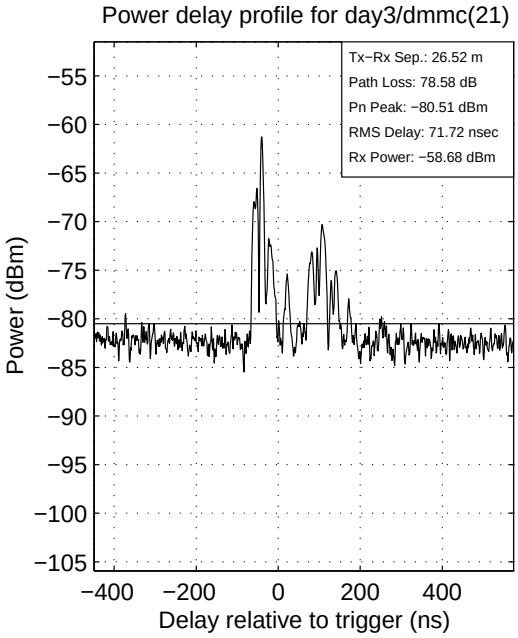
Power delay profile for day3/dmmc(21)
Tx−Rx Sep.: 26.52 m
Path Loss: 78.58 dB
Pn Peak: −80.51 dBm
RMS Delay: 71.72 nsec
Rx Power: −58.68 dBm
Power (dBm)
−55
−60
−65
−70
−75
−80
−85
−90
−95
−100
−105
−400
−200
0
200
400
Delay relative to trigger (ns)

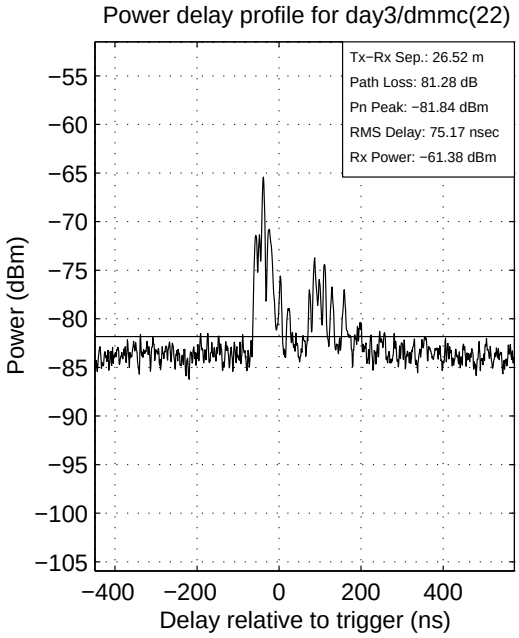
Power delay profile for day3/dmmc(22)
Tx−Rx Sep.: 26.52 m
Path Loss: 81.28 dB
Pn Peak: −81.84 dBm
RMS Delay: 75.17 nsec
Rx Power: −61.38 dBm
Power (dBm)
−55
−60
−65
−70
−75
−80
−85
−90
−95
−100
−105
−400
−200
0
200
400
Delay relative to trigger (ns)

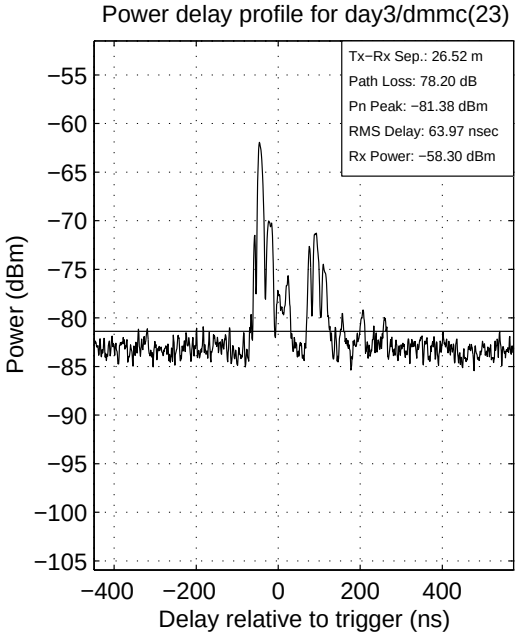
Power delay profile for day3/dmmc(23)
Tx−Rx Sep.: 26.52 m
Path Loss: 78.20 dB
Pn Peak: −81.38 dBm
RMS Delay: 63.97 nsec
Rx Power: −58.30 dBm
Power (dBm)
−55
−60
−65
−70
−75
−80
−85
−90
−95
−100
−105
−400
−200
0
200
400
Delay relative to trigger (ns)

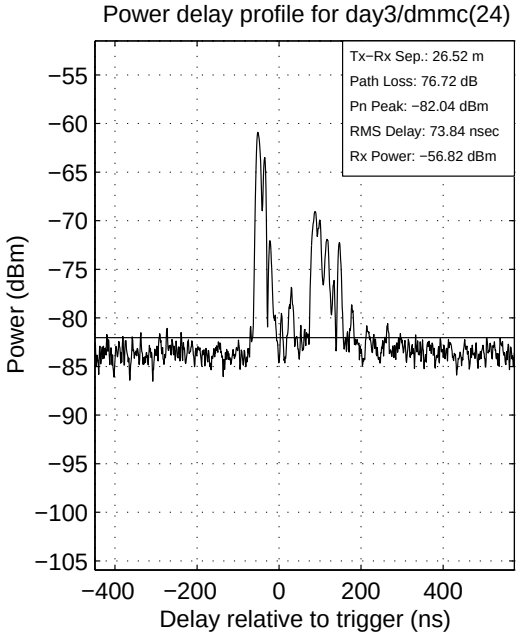
Power delay profile for day3/dmmc(24)
Tx−Rx Sep.: 26.52 m
Path Loss: 76.72 dB
Pn Peak: −82.04 dBm
RMS Delay: 73.84 nsec
Rx Power: −56.82 dBm
Power (dBm)
−55
−60
−65
−70
−75
−80
−85
−90
−95
−100
−105
−400
−200
0
200
400
Delay relative to trigger (ns)

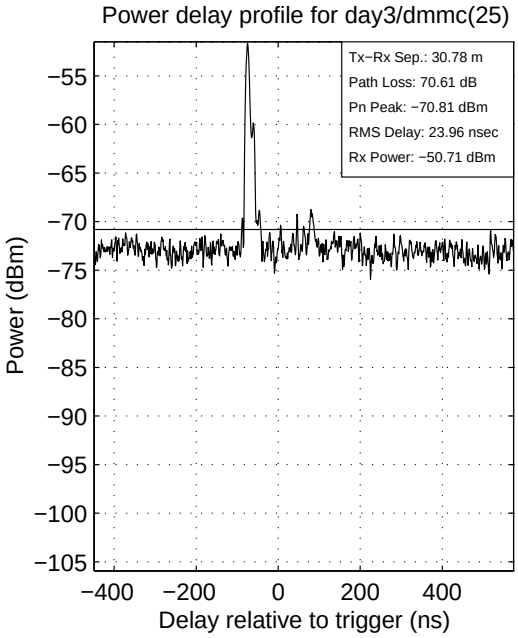
Power delay profile for day3/dmmc(25)
Tx−Rx Sep.: 30.78 m
Path Loss: 70.61 dB
Pn Peak: −70.81 dBm
RMS Delay: 23.96 nsec
Rx Power: −50.71 dBm
Power (dBm)
−55
−60
−65
−70
−75
−80
−85
−90
−95
−100
−105
−400
−200
0
200
400
Delay relative to trigger (ns)

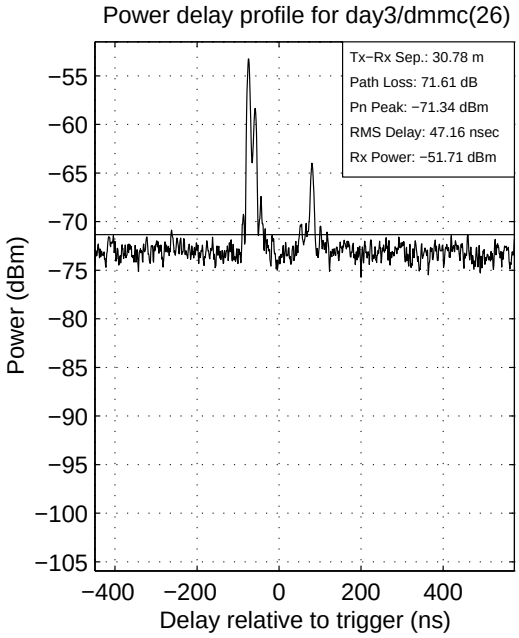
Power delay profile for day3/dmmc(26)
Tx−Rx Sep.: 30.78 m
Path Loss: 71.61 dB
Pn Peak: −71.34 dBm
RMS Delay: 47.16 nsec
Rx Power: −51.71 dBm
Power (dBm)
−55
−60
−65
−70
−75
−80
−85
−90
−95
−100
−105
−400
−200
0
200
400
Delay relative to trigger (ns)

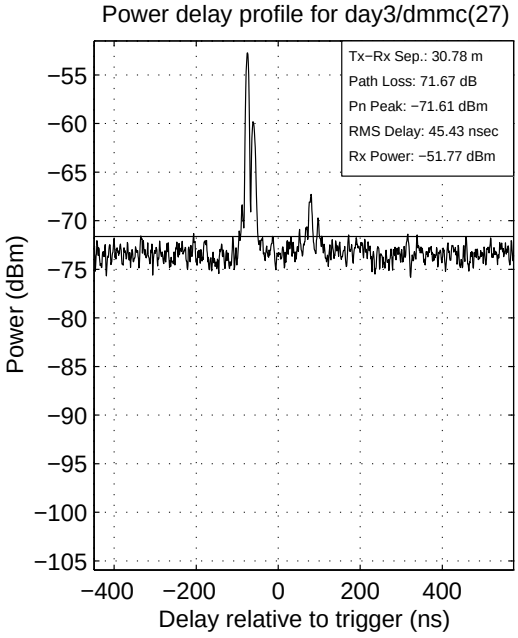
Power delay profile for day3/dmmc(27)
Tx−Rx Sep.: 30.78 m
Path Loss: 71.67 dB
Pn Peak: −71.61 dBm
RMS Delay: 45.43 nsec
Rx Power: −51.77 dBm
Power (dBm)
−55
−60
−65
−70
−75
−80
−85
−90
−95
−100
−105
−400
−200
0
200
400
Delay relative to trigger (ns)

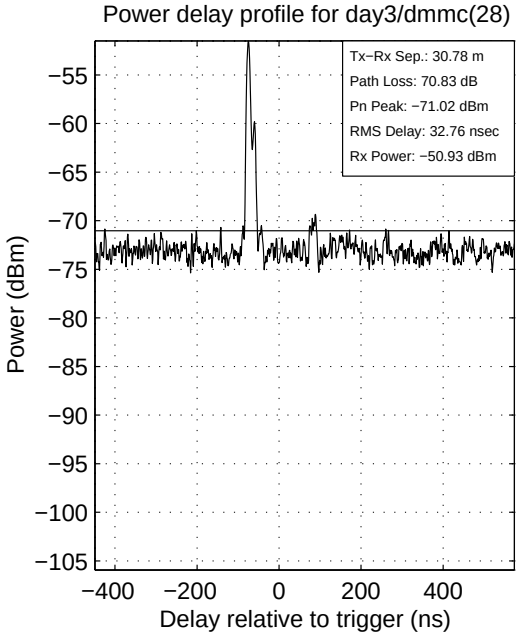
Power delay profile for day3/dmmc(28)
Tx−Rx Sep.: 30.78 m
Path Loss: 70.83 dB
Pn Peak: −71.02 dBm
RMS Delay: 32.76 nsec
Rx Power: −50.93 dBm
Power (dBm)
−55
−60
−65
−70
−75
−80
−85
−90
−95
−100
−105
−400
−200
0
200
400
Delay relative to trigger (ns)

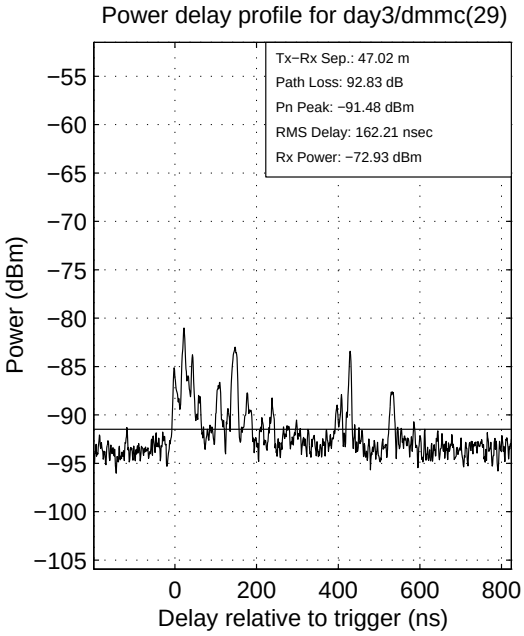
Power delay profile for day3/dmmc(29)
Tx−Rx Sep.: 47.02 m
Path Loss: 92.83 dB
Pn Peak: −91.48 dBm
RMS Delay: 162.21 nsec
Rx Power: −72.93 dBm
Power (dBm)
−55
−60
−65
−70
−75
−80
−85
−90
−95
−100
−105
0
200
400
600
800
Delay relative to trigger (ns)

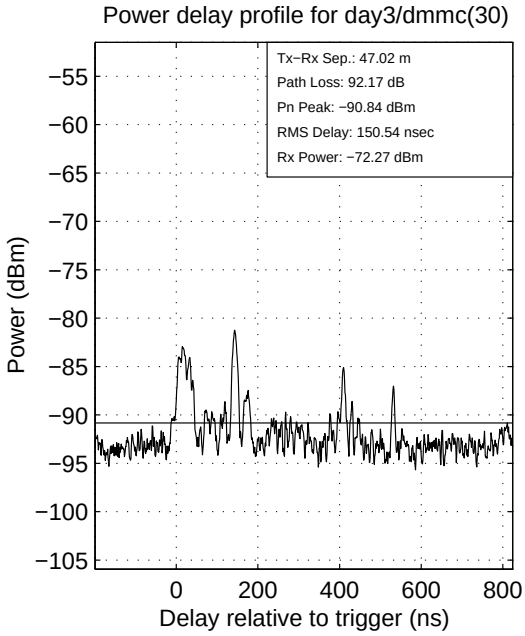
Power delay profile for day3/dmmc(30)
Tx−Rx Sep.: 47.02 m
Path Loss: 92.17 dB
Pn Peak: −90.84 dBm
RMS Delay: 150.54 nsec
Rx Power: −72.27 dBm
Power (dBm)
−55
−60
−65
−70
−75
−80
−85
−90
−95
−100
−105
0
200
400
600
800
Delay relative to trigger (ns)

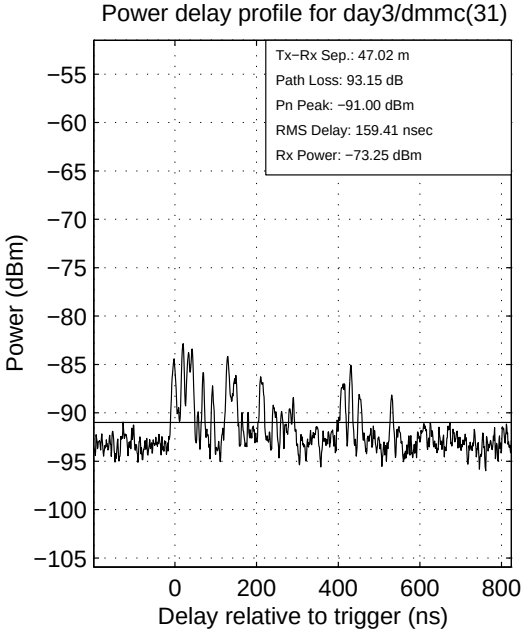
Power delay profile for day3/dmmc(31)
Tx−Rx Sep.: 47.02 m
Path Loss: 93.15 dB
Pn Peak: −91.00 dBm
RMS Delay: 159.41 nsec
Rx Power: −73.25 dBm
Power (dBm)
−55
−60
−65
−70
−75
−80
−85
−90
−95
−100
−105
0
200
400
600
800
Delay relative to trigger (ns)

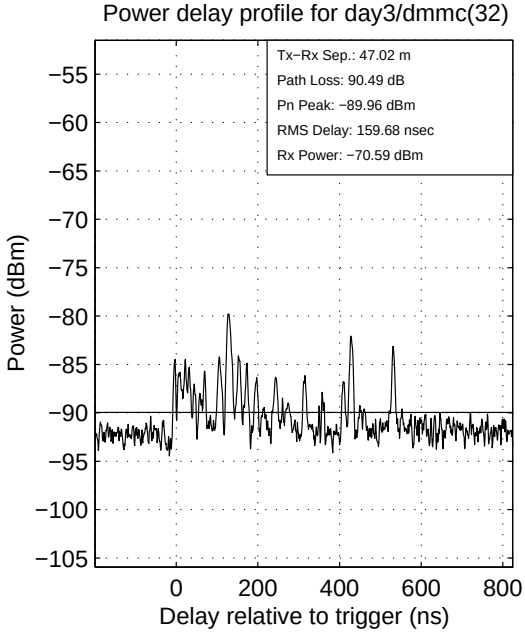
Power delay profile for day3/dmmc(32)
Tx−Rx Sep.: 47.02 m
Path Loss: 90.49 dB
Pn Peak: −89.96 dBm
RMS Delay: 159.68 nsec
Rx Power: −70.59 dBm
Power (dBm)
−55
−60
−65
−70
−75
−80
−85
−90
−95
−100
−105
0
200
400
600
800
Delay relative to trigger (ns)

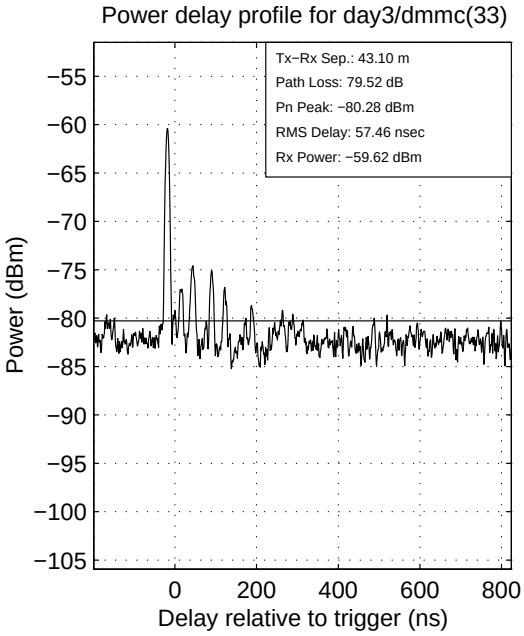
Power delay profile for day3/dmmc(33)
Tx−Rx Sep.: 43.10 m
Path Loss: 79.52 dB
Pn Peak: −80.28 dBm
RMS Delay: 57.46 nsec
Rx Power: −59.62 dBm
Power (dBm)
−55
−60
−65
−70
−75
−80
−85
−90
−95
−100
−105
0
200
400
600
800
Delay relative to trigger (ns)

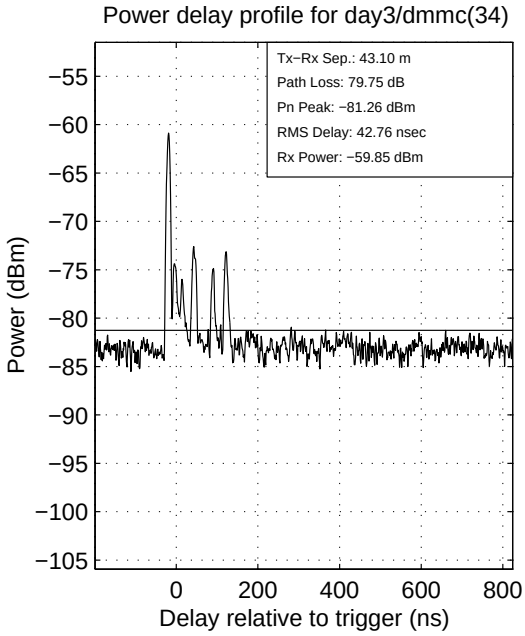
Power delay profile for day3/dmmc(34)
Tx−Rx Sep.: 43.10 m
Path Loss: 79.75 dB
Pn Peak: −81.26 dBm
RMS Delay: 42.76 nsec
Rx Power: −59.85 dBm
Power (dBm)
−55
−60
−65
−70
−75
−80
−85
−90
−95
−100
−105
0
200
400
600
800
Delay relative to trigger (ns)

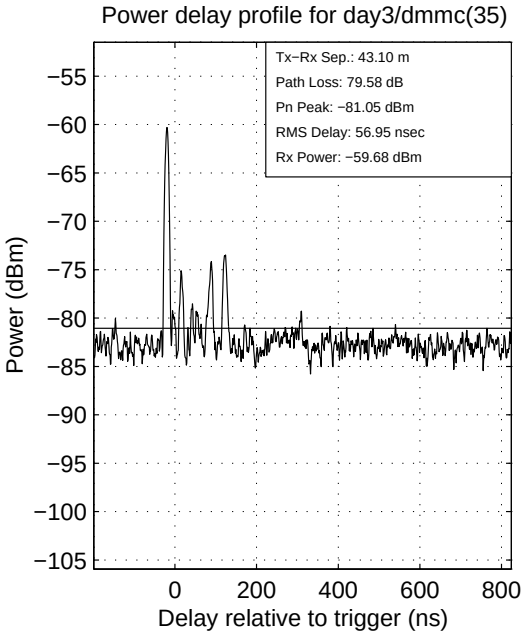
Power delay profile for day3/dmmc(35)
Tx−Rx Sep.: 43.10 m
Path Loss: 79.58 dB
Pn Peak: −81.05 dBm
RMS Delay: 56.95 nsec
Rx Power: −59.68 dBm
Power (dBm)
−55
−60
−65
−70
−75
−80
−85
−90
−95
−100
−105
0
200
400
600
800
Delay relative to trigger (ns)

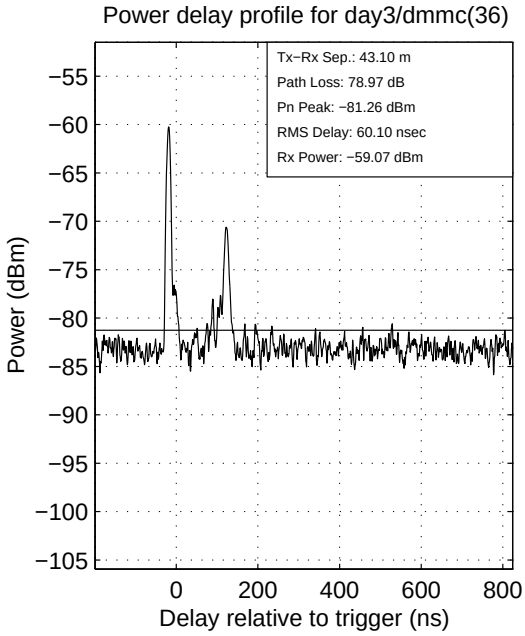
Power delay profile for day3/dmmc(36)
Tx−Rx Sep.: 43.10 m
Path Loss: 78.97 dB
Pn Peak: −81.26 dBm
RMS Delay: 60.10 nsec
Rx Power: −59.07 dBm
Power (dBm)
−55
−60
−65
−70
−75
−80
−85
−90
−95
−100
−105
0
200
400
600
800
Delay relative to trigger (ns)

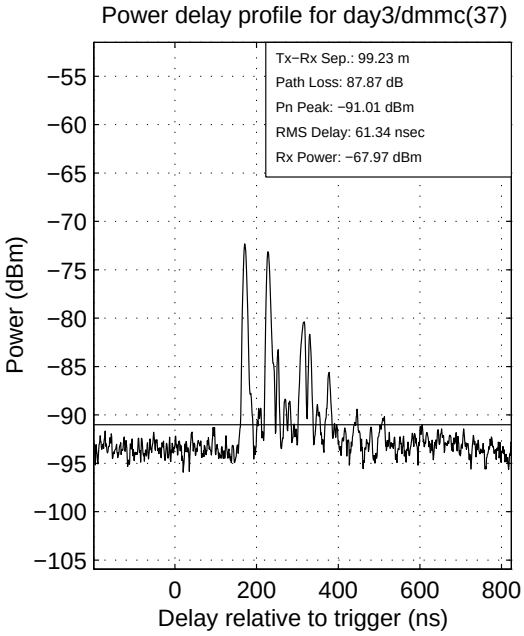
Power delay profile for day3/dmmc(37)
Tx−Rx Sep.: 99.23 m
Path Loss: 87.87 dB
Pn Peak: −91.01 dBm
RMS Delay: 61.34 nsec
Rx Power: −67.97 dBm
Power (dBm)
−55
−60
−65
−70
−75
−80
−85
−90
−95
−100
−105
0
200
400
600
800
Delay relative to trigger (ns)

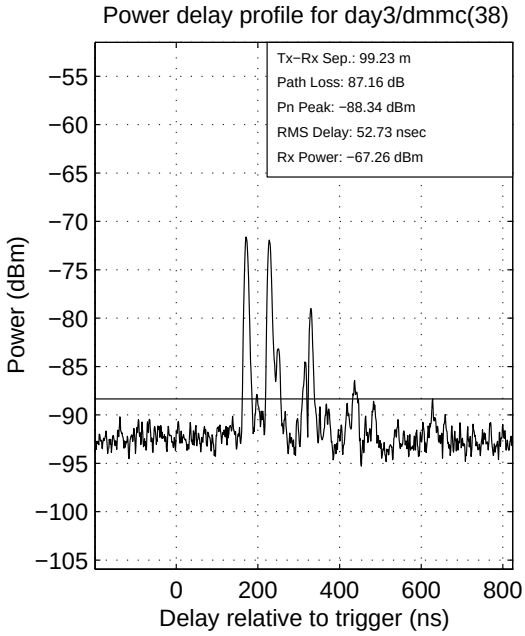
Power delay profile for day3/dmmc(38)
Tx−Rx Sep.: 99.23 m
Path Loss: 87.16 dB
Pn Peak: −88.34 dBm
RMS Delay: 52.73 nsec
Rx Power: −67.26 dBm
Power (dBm)
−55
−60
−65
−70
−75
−80
−85
−90
−95
−100
−105
0
200
400
600
800
Delay relative to trigger (ns)

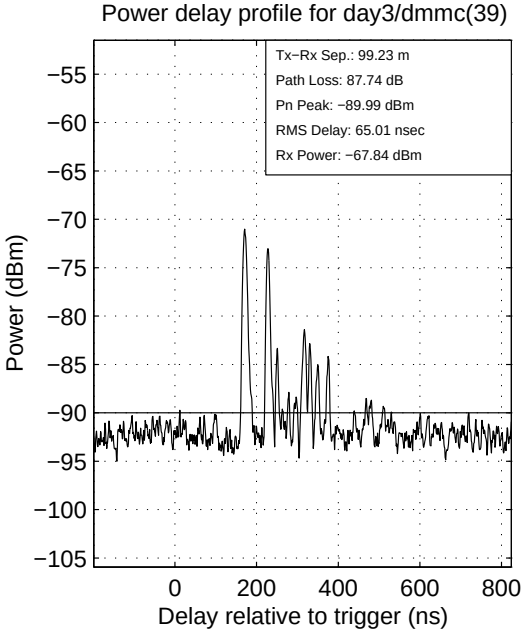
Power delay profile for day3/dmmc(39)
Tx−Rx Sep.: 99.23 m
Path Loss: 87.74 dB
Pn Peak: −89.99 dBm
RMS Delay: 65.01 nsec
Rx Power: −67.84 dBm
Power (dBm)
−55
−60
−65
−70
−75
−80
−85
−90
−95
−100
−105
0
200
400
600
800
Delay relative to trigger (ns)

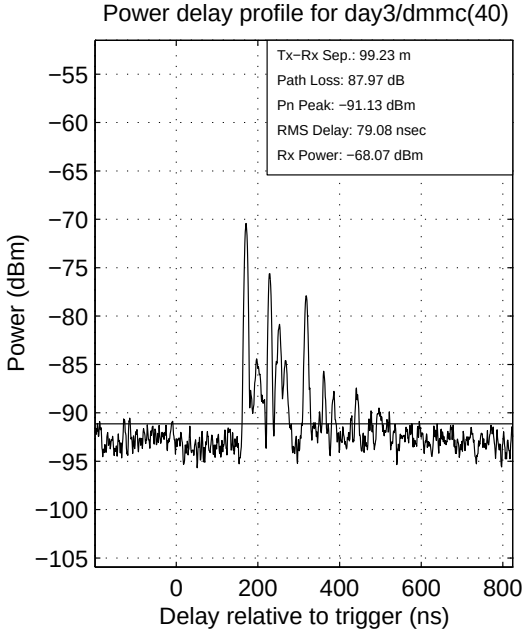
Power delay profile for day3/dmmc(40)
Tx−Rx Sep.: 99.23 m
Path Loss: 87.97 dB
Pn Peak: −91.13 dBm
RMS Delay: 79.08 nsec
Rx Power: −68.07 dBm
Power (dBm)
−55
−60
−65
−70
−75
−80
−85
−90
−95
−100
−105
0
200
400
600
800
Delay relative to trigger (ns)

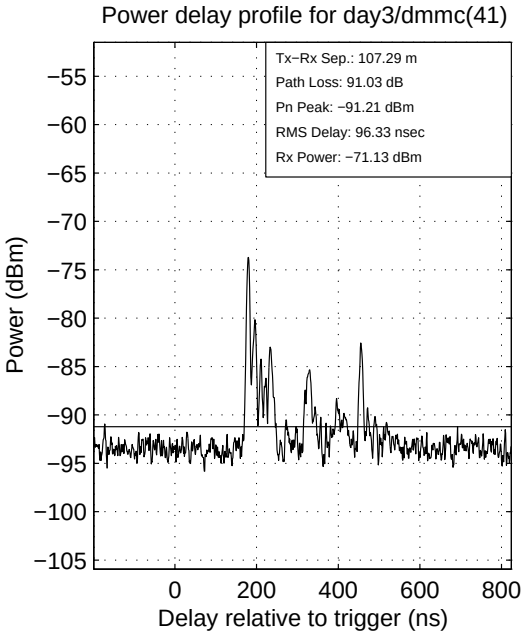
Power delay profile for day3/dmmc(41)
Tx−Rx Sep.: 107.29 m
Path Loss: 91.03 dB
Pn Peak: −91.21 dBm
RMS Delay: 96.33 nsec
Rx Power: −71.13 dBm
Power (dBm)
−55
−60
−65
−70
−75
−80
−85
−90
−95
−100
−105
0
200
400
600
800
Delay relative to trigger (ns)

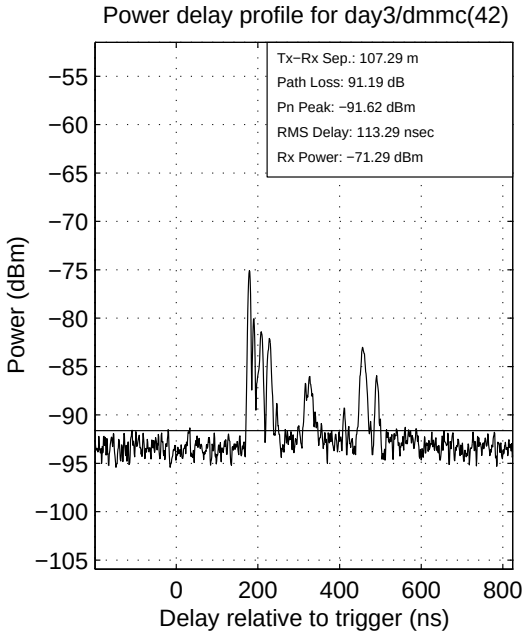
Power delay profile for day3/dmmc(42)
Tx−Rx Sep.: 107.29 m
Path Loss: 91.19 dB
Pn Peak: −91.62 dBm
RMS Delay: 113.29 nsec
Rx Power: −71.29 dBm
Power (dBm)
−55
−60
−65
−70
−75
−80
−85
−90
−95
−100
−105
0
200
400
600
800
Delay relative to trigger (ns)

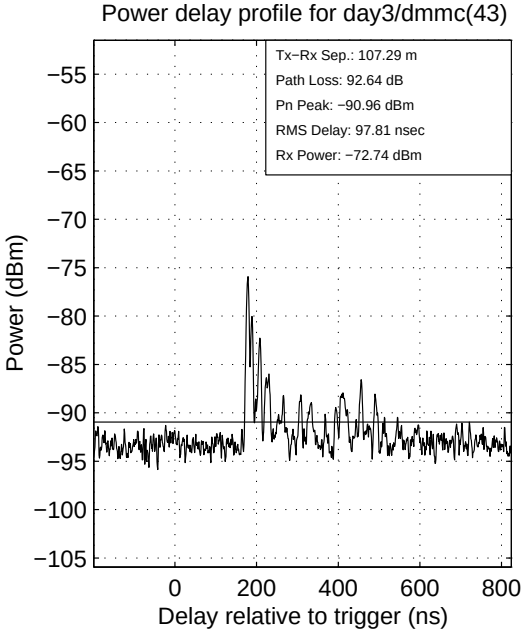
Power delay profile for day3/dmmc(43)
Tx−Rx Sep.: 107.29 m
Path Loss: 92.64 dB
Pn Peak: −90.96 dBm
RMS Delay: 97.81 nsec
Rx Power: −72.74 dBm
Power (dBm)
−55
−60
−65
−70
−75
−80
−85
−90
−95
−100
−105
0
200
400
600
800
Delay relative to trigger (ns)

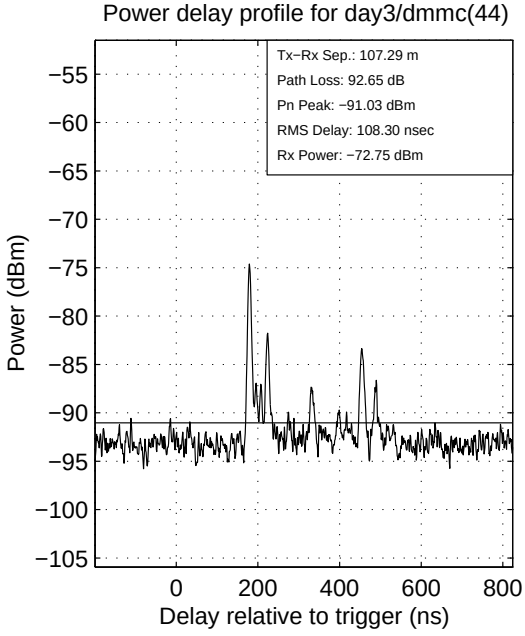
Power delay profile for day3/dmmc(44)
Tx−Rx Sep.: 107.29 m
Path Loss: 92.65 dB
Pn Peak: −91.03 dBm
RMS Delay: 108.30 nsec
Rx Power: −72.75 dBm
Power (dBm)
−55
−60
−65
−70
−75
−80
−85
−90
−95
−100
−105
0
200
400
600
800
Delay relative to trigger (ns)

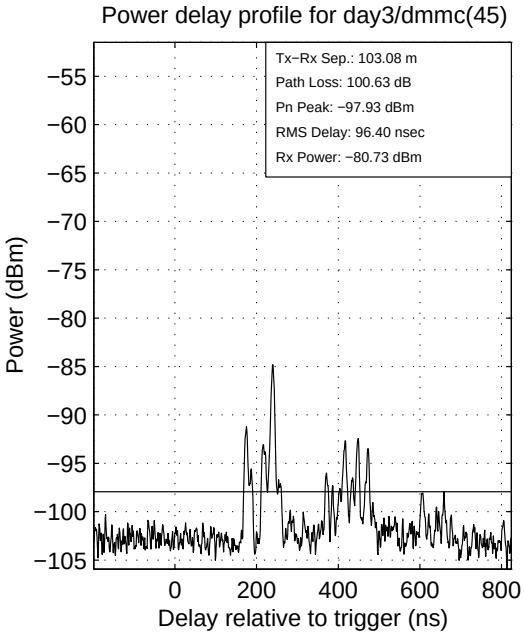
Power delay profile for day3/dmmc(45)
Tx−Rx Sep.: 103.08 m
Path Loss: 100.63 dB
Pn Peak: −97.93 dBm
RMS Delay: 96.40 nsec
Rx Power: −80.73 dBm
Power (dBm)
−55
−60
−65
−70
−75
−80
−85
−90
−95
−100
−105
0
200
400
600
800
Delay relative to trigger (ns)

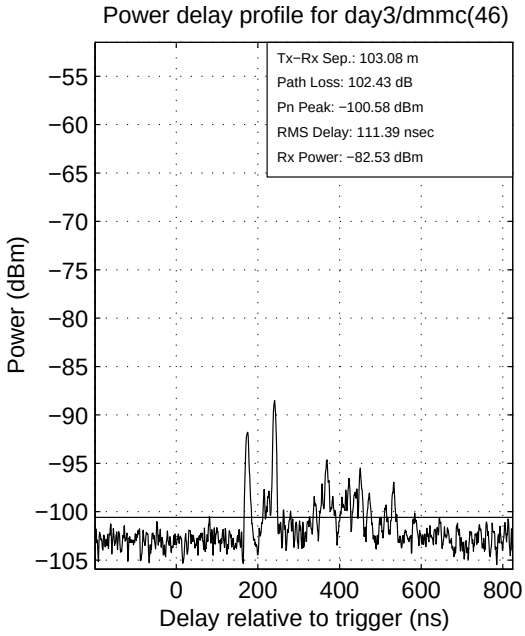
Power delay profile for day3/dmmc(46)
Tx−Rx Sep.: 103.08 m
Path Loss: 102.43 dB
Pn Peak: −100.58 dBm
RMS Delay: 111.39 nsec
Rx Power: −82.53 dBm
Power (dBm)
−55
−60
−65
−70
−75
−80
−85
−90
−95
−100
−105
0
200
400
600
800
Delay relative to trigger (ns)

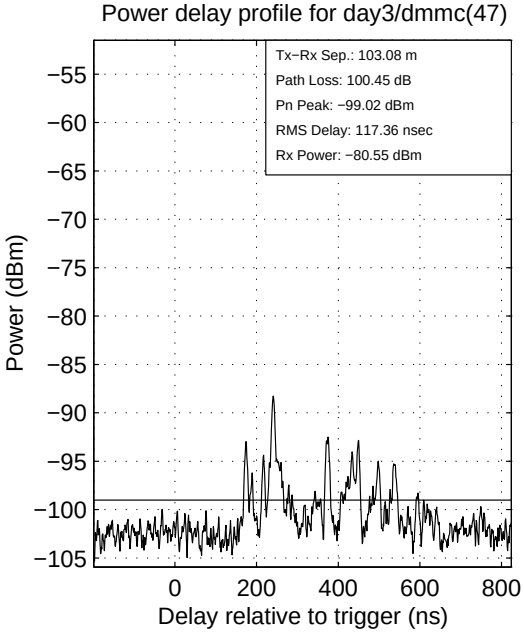
Power delay profile for day3/dmmc(47)
Tx−Rx Sep.: 103.08 m
Path Loss: 100.45 dB
Pn Peak: −99.02 dBm
RMS Delay: 117.36 nsec
Rx Power: −80.55 dBm
Power (dBm)
−55
−60
−65
−70
−75
−80
−85
−90
−95
−100
−105
0
200
400
600
800
Delay relative to trigger (ns)

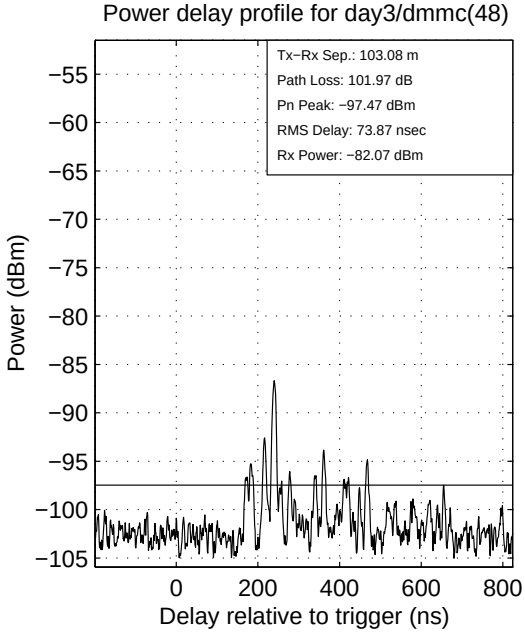
Power delay profile for day3/dmmc(48)
Tx−Rx Sep.: 103.08 m
Path Loss: 101.97 dB
Pn Peak: −97.47 dBm
RMS Delay: 73.87 nsec
Rx Power: −82.07 dBm
Power (dBm)
−55
−60
−65
−70
−75
−80
−85
−90
−95
−100
−105
0
200
400
600
800
Delay relative to trigger (ns)

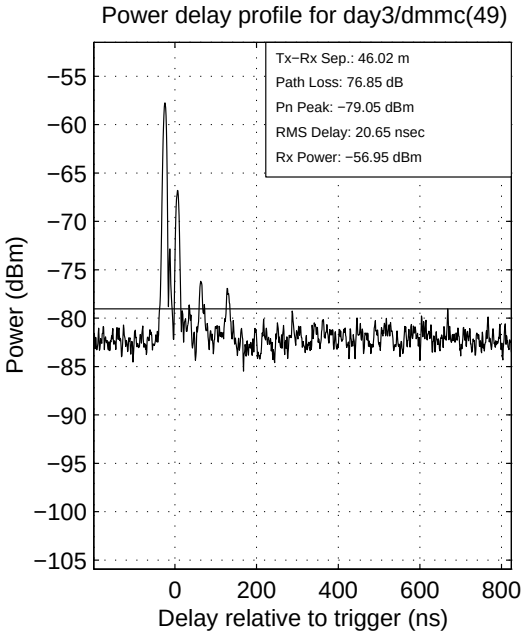
Power delay profile for day3/dmmc(49)
Tx−Rx Sep.: 46.02 m
Path Loss: 76.85 dB
Pn Peak: −79.05 dBm
RMS Delay: 20.65 nsec
Rx Power: −56.95 dBm
Power (dBm)
−55
−60
−65
−70
−75
−80
−85
−90
−95
−100
−105
0
200
400
600
800
Delay relative to trigger (ns)

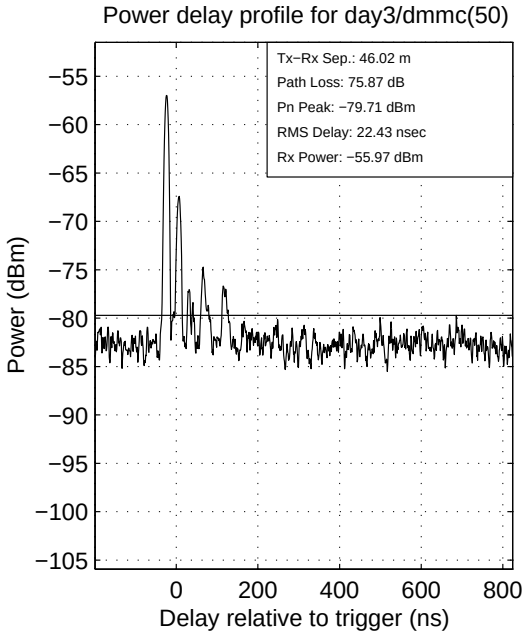
Power delay profile for day3/dmmc(50)
Tx−Rx Sep.: 46.02 m
Path Loss: 75.87 dB
Pn Peak: −79.71 dBm
RMS Delay: 22.43 nsec
Rx Power: −55.97 dBm
Power (dBm)
−55
−60
−65
−70
−75
−80
−85
−90
−95
−100
−105
0
200
400
600
800
Delay relative to trigger (ns)

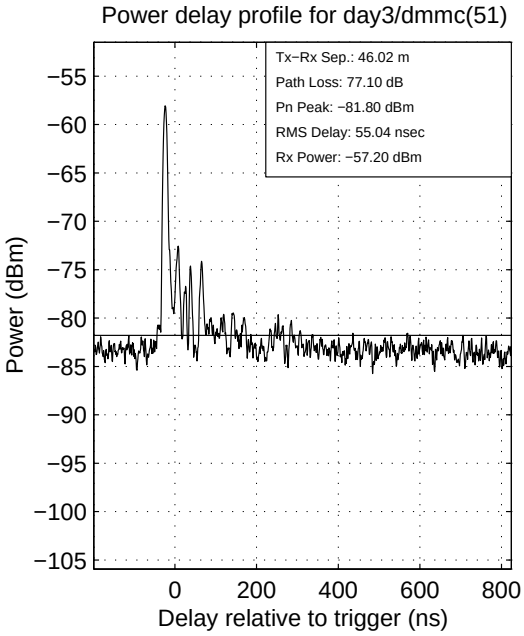
Power delay profile for day3/dmmc(51)
Tx−Rx Sep.: 46.02 m
Path Loss: 77.10 dB
Pn Peak: −81.80 dBm
RMS Delay: 55.04 nsec
Rx Power: −57.20 dBm
Power (dBm)
−55
−60
−65
−70
−75
−80
−85
−90
−95
−100
−105
0
200
400
600
800
Delay relative to trigger (ns)

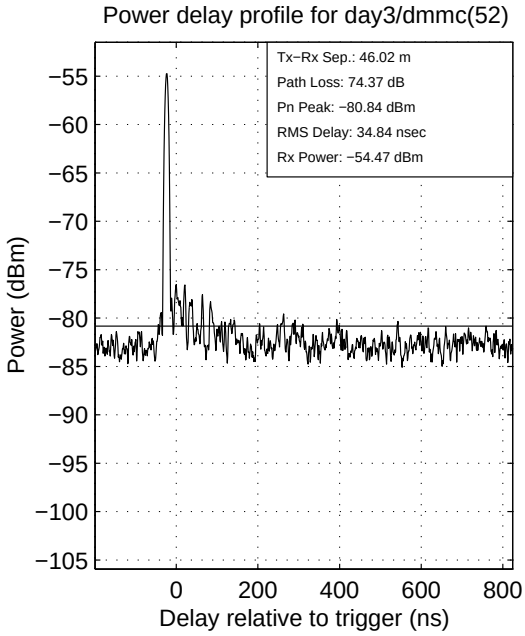
Power delay profile for day3/dmmc(52)
Tx−Rx Sep.: 46.02 m
Path Loss: 74.37 dB
Pn Peak: −80.84 dBm
RMS Delay: 34.84 nsec
Rx Power: −54.47 dBm
Power (dBm)
−55
−60
−65
−70
−75
−80
−85
−90
−95
−100
−105
0
200
400
600
800
Delay relative to trigger (ns)

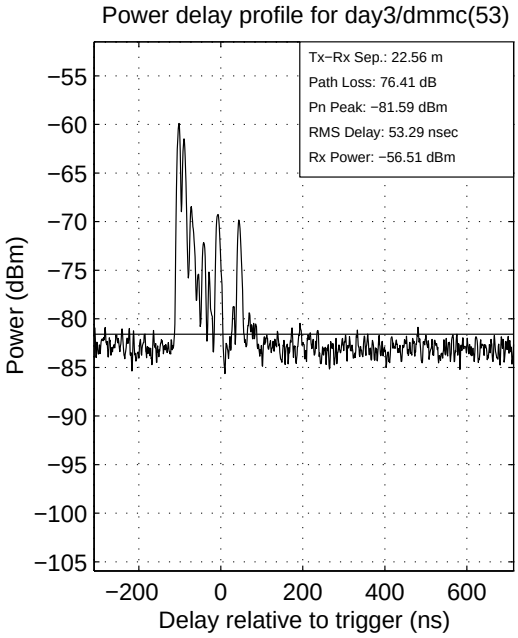
Power delay profile for day3/dmmc(53)
Tx−Rx Sep.: 22.56 m
Path Loss: 76.41 dB
Pn Peak: −81.59 dBm
RMS Delay: 53.29 nsec
Rx Power: −56.51 dBm
Power (dBm)
−55
−60
−65
−70
−75
−80
−85
−90
−95
−100
−105
−200
0
200
400
600
Delay relative to trigger (ns)

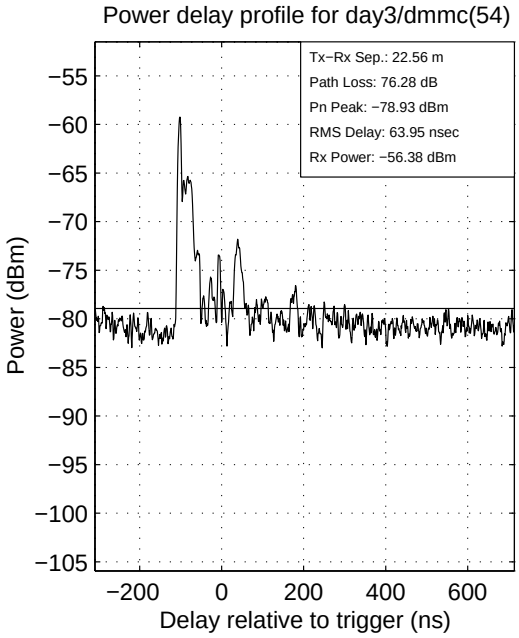
Power delay profile for day3/dmmc(54)
Tx−Rx Sep.: 22.56 m
Path Loss: 76.28 dB
Pn Peak: −78.93 dBm
RMS Delay: 63.95 nsec
Rx Power: −56.38 dBm
Power (dBm)
−55
−60
−65
−70
−75
−80
−85
−90
−95
−100
−105
−200
0
200
400
600
Delay relative to trigger (ns)

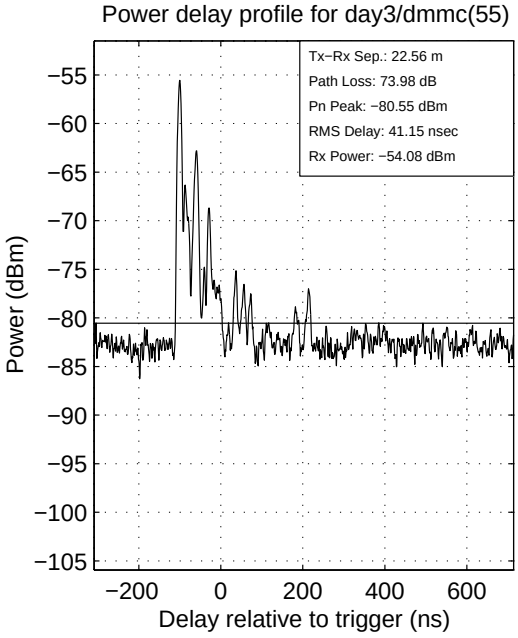
Power delay profile for day3/dmmc(55)
Tx−Rx Sep.: 22.56 m
Path Loss: 73.98 dB
Pn Peak: −80.55 dBm
RMS Delay: 41.15 nsec
Rx Power: −54.08 dBm
Power (dBm)
−55
−60
−65
−70
−75
−80
−85
−90
−95
−100
−105
−200
0
200
400
600
Delay relative to trigger (ns)

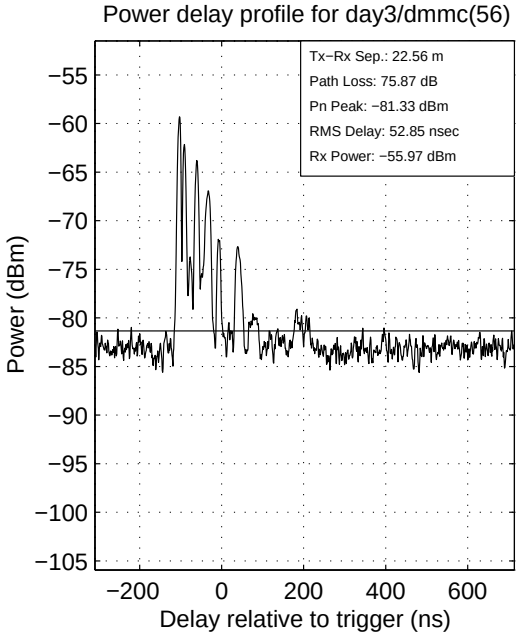
Power delay profile for day3/dmmc(56)
Tx−Rx Sep.: 22.56 m
Path Loss: 75.87 dB
Pn Peak: −81.33 dBm
RMS Delay: 52.85 nsec
Rx Power: −55.97 dBm
Power (dBm)
−55
−60
−65
−70
−75
−80
−85
−90
−95
−100
−105
−200
0
200
400
600
Delay relative to trigger (ns)

Bibliography

[1] H. Van der Hoek, "The new DECT standard for cordless communications," *Telecommunications Magazine*, pp. 35–38, April 1993.

[2] L. B. Lopes, "On the radio link performance of the Digital European Cordless Telecommunications (DECT) system," in *IEEE Globecom*, vol. 2, pp. 1013–1017, 1990.

[3] D. E. Fague, B. Madsen, C. Karmel, and A. Dao, "Performance evaluation of a low cost, solid state radio front end for DECT," in *Proceedings of IEEE Vehicular Technology Conference*, vol. 1, (Piscataway, N.J.), pp. 512–515, IEEE, 1994.

[4] ETSI, "Radio equipment and systems (RES–3): Digital European Cordless Telecommunications (DECT) common interface," vol. ETS 300 175-1 to ETS 300 175-9, October 1992.

[5] V. Werbus, A. Veloso, and A. Villanueva, "DECT – cordless functionality in new generation Alcatel PABXs," *Electrical Communications*, pp. 172–180, 2nd Quarter 1993.

[6] J. D. Gibson, *The Mobile Communications Handbook*. Florida: CRC Press, 1996.

[7] R. J. Mulder, "DECT, a universal cordless access system," *Phillips Telecommunications Review*, vol. 49, pp. 68–73, September 1991.

[8] P. H. G. van de Berg and F. B. Brouwer, "The architecture and performance of a dect–pcs implementation," in *Proceedings of IEEE Vehicular Technology Conference*, vol. 2, (Piscataway, N.J.), pp. 1074–1078, IEEE, 1994.

[9] National Semiconductor, "Specification for the DECT ARi1 interface to the radio frequency front end," *Application Note 908*, September 1993.

[10] Sierra Semiconductor Corporation, "SC14401 – DECT terminal processor with CODEC," *Reference Manual*, vol. Rev 0.1, 1993.

[11] RTX Research, "DECT radio transceiver module RTX 1901/1902," *Technical Documentation*, vol. Revision A, May 1995.

[12] National Semiconductor, "LMX2411 baseband processor for radio communications," *National Products for Wireless Communications Manual*, pp. 2.3–2.10, 1996.

[13] R. Mohindra, "Isolator for DECT open loop modulation," *RF Design*, pp. 30–35, January 1996.

[14] National Semiconductor, "LMX2315 PLLatinum 1.2 GHz frequency synthesizer for RF personal communications," *National Products for Wireless Communications Manual*, pp. 1.22–1.39, 1996.

[15] National Semiconductor, "LMX2216 0.1 GHz to 2.0 GHz low noise amplifier/mixer for RF personal communications," *National Products for Wireless Communications Manual*, pp. 1.105–1.115, 1996.

[16] National Semiconductor, "LMX2240 intermediate frequency receiver," *National Products for Wireless Communications Manual*, pp. 1.116–1.125, 1996.

[17] T. S. Rappaport, *Wireless Communications: Principles and Practice*. N.J.: Prentice Hall, 1996.

[18] M. R. Heath, "Propagation measurements at 1.76 GHz for Digital European Cordless Telecommunications," in *IEEE Globecom*, vol. 2, pp. 604.2.1–604.2.4, 1990.

[19] D. M. Devasirvatham, "Multipath time delay spread in the digital portable radio environment," *IEEE Communications Magazine*, vol. 25, pp. 13–21, June 1987.

[20] D. M. Devasirvatham and R. R. Murray, "Two frequency radiowave propagation measurements in a small city for low power personal communications," *Bellcore*, vol. TM-25043, pp. 1–17, June 1995.

[21] L. B. Lopes, "Performance of the DECT system in fading dispersive channels," *Electronic Letters*, vol. 26, pp. 1416–1417, August 1990.

[22] U. Kauschke, "Propagation and system performance simulations for the short range DECT system in microcellular urban roads," in *IEEE Transactions on Vehicular Technology*, vol. 44, pp. 253–260, May 1995.

[23] G. Schultes and et. al., "Performance of the Siemens DECT – prototype Gigaset 95x in a dispersive indoor environment," in *Proceedings of the IEEE Vehicular Technology Conference*, vol. 2, (Piscataway, N.J.), pp. 1079–1082, IEEE Press, 1994.

[24] P. Nobles, D. Ashworth, and F. Halsall, "Indoor radiowave propagation measurements at frequencies up to 20 GHz," in *Proceedings of the IEEE Vehicular Technology Conference*, (Piscataway, N.J.), pp. 873–877, IEEE Press, 1994.

[25] S. J. Howard and K. Pahlavan, "Measurement and analysis of the indoor radio channel in the frequency domain," *IEEE Transactions on Instrumentation and Measurement*, vol. 39, pp. 751–755, October 1990.

[26] G. Schultes and I. Crohn, "Measured performance of DECT transmission in low dispersive indoor radio channel," *Electronic Letters*, vol. 28, pp. 1625–1627, August 1992.

[27] P. E. Mogensen and S. Petersen, "Antenna configuration measurements for DECT micro–cells," in *PIMRC*, vol. 2, pp. 1532–1536, 1994.

[28] L. B. Lopes and S. Safavi, "Relationship between performance and timing recovery mechanisms for a DECT link in dispersive channels," *Electronic Letters*, vol. 29, pp. 2173–2174, December 1993.

[29] Alta Group, *SPW - The User's Guide and Tutorial Release Notes/Installation Guide*. CA: Cadence Design Systems, Inc., 1995.

[30] R. E. Ziemer and R. L. Peterson, *Introduction to Digital Communications*. New York: Macmillan Publishing Company, 1992.

[31] W. H. Press, S. A. Teukolsky, W. T. Vetterling, and B. P. Flannery, *Numerical Recipes in C*. New York: Cambridge University Press, 2nd ed., 1992.

[32] F. Dominique, "Design and development of a frequency hopper based on the DECT system for the 902–928 MHz ISM band," Master's thesis, Virginia Polytechnic Institute and State University, VA, December 1995.

[33] M. LaCon, "Designing a DECT telephone tests your receiver knowledge," *Electronic Design News*, pp. 149–158, October 1995.

[34] M. C. Jeruchim, P. Balaban, and K. S. Shanmugan, *Simulation of Communication Systems*. New York: Plenum Press, 1992.

[35] M. J. Gans, "A power spectral theory of propagation in the mobile radio environment," *IEEE Transactions on Vehicular Technology*, vol. 21, pp. 27–38, February 1972.

[36] Alta Group, *SPW - Communications Library Reference Release Notes*. CA: Cadence Design Systems, Inc., 1995.

[37] V. Fung, T. S. Rappaport, and B. Thoma, "Bit error rate simulation for $\pi/4$ DQPSK mobile radio communications using two–ray and measurement–based impulse response models," *IEEE Journal on Selected Areas in Communications*, vol. 11, pp. 393–405, April 1993.

[38] L. Dossi, G. Tartara, and F. Tallone, "Statistical analysis of measured impulse response functions of 2.0 GHz indoor radio channel," in *Proceedings of the IEEE Vehicular Technology Conference*, (Chicago), pp. 1153–1157, 1995.

[39] W. Newhall, T. S. Rappaport, and D. Sweeney, "A spread spectrum sliding correlator system for propagation measurements," *RF Design*, pp. 40–54, April 1996.

[40] W. G. Newhall, K. J. Saldanha, and T. S. Rappaport, "Propagation time delay spread measurements at 915 MHz in a large train yard," in *Proceedings of the IEEE Vehicular Technology Conference*, vol. 2, (Piscataway, N.J.), pp. 864–868, IEEE Press, April 1996.

[41] L. Couch, *Digital and Analog Communication Systems*. New York: Macmillan Publishing Company, fourth ed., 1993.

[42] M. K. Simon and C. C. Wang, "Differential detection of GMSK in a mobile radio environment," *IEEE Transactions on Vehicular Technology*, vol. 33, pp. 307–320, November 1984.

[43] G. Schultes, E. Bonek, P. Weger, and W. Herzog, "Basic performance of a direct conversion DECT receiver," *Electronic Letters*, vol. 26, pp. 1746–1748, October 1990.

[44] W. C. Y. Lee, *Mobile Communications Engineering*. New York: McGraw–Hill, 1982.

[45] I. Crohn, G. Schultes, R. Gahleitner, and E.Bonek, "Irreducible error performance of a digital portable communication system in a controlled time-dispersion indoor channel," *IEEE Journal on Selected Areas in Communications*, vol. 11, pp. 1024–1033, September 1993.

[46] A. F. Molisch, J. Fuhl, and P. Proksch, "Error floor of MSK modulation in a mobile-radio channel with two independent fading paths," *IEEE Transactions on Vehicular Technology*, vol. 45, pp. 303–309, May 1996.

[47] S. Safavi, L. B. Lopes, P. E. Mogensen, and F. Frederiksen, "A hierarchy of receiver options for DECT systems," in *PIMRC 95*, vol. 3, pp. 1351–1356, July 1995.

[48] S. Y. Seidel and T. S. Rappaport, "Site-specific propagation prediction for wireless in-building personal communication system design," *IEEE Transactions on Vehicular Technology*, vol. 43, pp. 879–891, November 1994.

[49] J. B. Anderson, T. S. Rappaport, and S. Yoshida, "Propagation measurements and models for wireless communications channels," *IEEE Communications Magazine*, pp. 42–49, January 1995.

[50] K. R. Schaubach, "Microcellular radio channel prediction using ray tracing," Master's thesis, Virginia Polytechnic Institute and State University, VA, August 1992.

[51] P. E. Mogensen and C. M. Verholt, "Measurement results from using DECT in a RLL application," in *Proceedings of the IEEE Vehicular Technology Conference*, (Piscataway, N.J.), pp. 1065–1068, IEEE Press, 1994.

[52] B. Ramamurthi and C. Mathiazhagan, "DECT–based wireless local loop system," in *Proceedings of the ICPWC*, (Piscataway, N.J.), pp. 55–59, IEEE Press, 1994.

[53] P. E. Mogensen and S. Petersen, "Practical considerations of using antenna diversity in DECT," in *Proceedings of the IEEE Vehicular Technology Conference*, (Piscataway, N.J.), pp. 1532–1536, IEEE Press, 1994.

[54] J. Wigard, P. E. Mogensen, F. Frederiksen, and O. Norklit, "Evaluation of optimum diversity combining in DECT," in *PIMRC 95*, vol. 3, pp. 505–511, July 1995.

Vita

Kevin Joseph Saldanha was born on October 20, 1972 in Bombay, India. He received the Bachelor of Engineering degree in Electronics Engineering with distinction in June 1994 from the University of Bombay. He joined Virginia Tech in Fall 1994. He is the co-author of one conference paper and two articles. Kevin joined the MPRG in January 1995 as a Graduate Research Assistant where his work concentrated on analyzing the performance of DECT. His areas of interest are digital communications, digital signal processing, and RF propgation and planning.